



THESIS

3

(1995)



This is to certify that the

dissertation entitled


CHARACTERIZATION OF METALLOPORPHYRIN SINGLET EXCITED STATE  
VIBRATIONS THROUGH PICOSECOND RAMAN SPECTROSCOPY AND  
NATURAL ORBITAL CALCULATIONS

presented by

Douglas H. Kreszowski

has been accepted towards fulfillment  
of the requirements for

Ph. D. degree in Chemistry



Major professor

Date 12 May 1995



**LIBRARY**  
**Michigan State**  
**University**

PLACE IN RETURN BOX to remove this checkout from your record.  
TO AVOID FINES return on or before date due.

DATE DUE	DATE DUE	DATE DUE
_____	_____	_____
_____	_____	_____
_____	_____	_____
_____	_____	_____
_____	_____	_____
_____	_____	_____
_____	_____	_____

MSU Is An Affirmative Action/Equal Opportunity Institution

c:\circ\data\due.pm3-p.1

# CHARACTERIZATION OF METALLOPORPHYRIN SINGLET EXCITED STATE VIBRATIONS THROUGH PICOSECOND RAMAN SPECTROSCOPY AND NATURAL ORBITAL CALCULATIONS

By

Photosynthesis in bacteria proceeds through photochemical reactions in a special pair bacteriochlorophyll dimer (BCl<sub>2</sub>). Douglas H. Kreszowski has been a member of the Center. The dimer resides in the excited singlet electronic state ( $S_1$ ) following the initial electron transfer to bacteriopheophytin A (BPh<sub>A</sub>), and its configuration in the triplet state following electron transfer is unknown. Thus, a picosecond laser system was developed that can pump time-resolved Raman techniques to characterize structural changes in the dimer, as well as to investigate vibrationally excited species. This both can be used to study the reaction centers, and the limited knowledge about the structure of the reaction centers in the initial experiments on model porphyrins. The center is currently a member of the Center.

A DISSERTATION

Submitted to  
Michigan State University  
in partial fulfillment of the requirements  
for the degree of  
DOCTOR OF PHILOSOPHY  
Department of Chemistry

1995

had not been addressed in either theory or experiment, so further experiments were

## CHARACTERIZATION OF METALLOPORPHYRIN SINGLET EXCITED STATE VIBRATIONS THROUGH PICOSECOND RAMAN SPECTROSCOPY AND NATURAL ORBITAL CALCULATIONS

By Douglas H. Kreszowski

using natural orbital calculations that take into account configuration interaction between

Photosynthesis in bacteria proceeds through photoexcitation of the special pair

bacteriochlorophyll dimer (BChl<sub>2</sub>) that is lodged within the reaction center. This dimer

resides in the excited singlet electronic state ( $S_1$ ) during the initial electron transfer to

bacteriopheophytin A (BPh<sub>A</sub>), and its conformation at the time of electron transfer is

unknown. Thus, a picosecond laser system was developed that can utilize time-resolved

Raman techniques to characterize structures of singlet state intermediates, as well as to

investigate vibrationally excited species. Due both to the complexity of the reaction

centers, and the limited knowledge about singlet excited states, it became necessary to do

initial experiments on model porphyrins. The  $S_1$  state of zinc(II) octaethylporphyrin

(ZnOEP) displayed Raman spectra that are dominated by totally symmetric modes, that

generally shift down in frequency, and have increased linewidths within the core modes.

This dominance of totally symmetric modes suggest that, contrary to triplet excited states,

the  $S_1$  state lacks significant Jahn-Teller distortion. The experimental results are in

agreement with theoretical predictions that configuration interaction (CI) in singlet states

will act to diminish Jahn-Teller distortion. The downshift in frequencies of core vibrations

( $\nu_4$ ,  $\nu_2$ ,  $\nu_3$ ) suggest an overall expansion of the porphyrin ring in the  $S_1$  state. This issue

had not been addressed in either theory or experimentation, so further experiments were done involving ZnOEP, ZnOEP-*d4*, ZnOEP- $^{15}\text{N}_4$ , zinc(II) etioporphyrin (ZnEtio), and magnesium octaethylporphyrin (MgOEP). These additional experiments led us to conclude that mode composition changes do not significantly contribute to the  $S_1$  state of these porphyrins. To assist in the interpretation, composite orbital diagrams were drawn using natural orbital calculations that take into account configuration interaction between electronic transitions. The diagrams predict the experimentally observed ring expansion as well as a small  $b_{1g}$  distortion in lower singlet excited states. We conclude that this predicted structural inhomogeneity is reflected by the observed increased linewidths, and that both the increased linewidth and the ring expansion are consequences of extensive configuration interaction between the  $a_{1u}e_g$  and  $a_{2u}e_g$  transitions.

Copyright by

DOUGLAS H KRESZOWSKI

1995



## ACKNOWLEDGMENTS

My diverse list of acknowledgements include: I thank Professor Jerry Baircock for his guidance and financial support (defense research grant NIH GM23480). I also appreciate Professor George Leroy's contribution as second reader of my guidance committee. I thank Professor's Jeff Leathers and Eugene Lepp for serving on my guidance committee. Dr. Geun Deumun deserves special thanks for his collaborative contributions within portions of this thesis. He was an advisor in the project. Dr. Tom Carter was vital in both technical and with experimental assistance and help with computer related operations. I thank Scott To my mother and my father, for help in designing and implementing the shutter driver. Likewise, I thank Tom Baker, Tom Monke, and Sam Jackson for their skilled support involving fabrication of the microscope mount, spectrometer and optics mounts. And my friends, Jeff, Scott, and Chris, Keta, Manfred, and Scott, deserve credit for their service in the laboratory. Professor Jim Harrison was of tremendous help in the technical discussions. Professor Chris Chang's contributions of images and fluorescence microscopy studies are greatly appreciated. Professor Costas Vrethlis's technical discussions was also valuable input during my early graduate years. I thank Rob Richards and Keta for room and boarding during my last year of research. Lastly, I thank all other laboratory and schoolmates for teaching me the balance between vision and practicality.

his g

app

com

gud

con

Car

rela

and

la

spe

Ma

Pr

Pr

an

va

an

so

## ACKNOWLEDGMENTS

My diverse list of acknowledgements include: I thank Professor Jerry Babcock for his guidance and financial support (federal research grant NIH GM25480). I also appreciate Professor George Leroy's contributions as second reader of my guidance committee. I thank Professor's Jeff Ledford and Eugene Legoff for serving on my guidance committee. Dr. Geurt Deinum deserves special thanks for his collaborative contributions within portions of this thesis, for he was an asset to the project. Dr. Tom Carter was vital in both technical aid with experimental apparatus and help with computer related operations. I thank Scott Sanderson of the electronics shop for help in designing and implementing the shutter driver. Likewise, I thank Russ Geyer, Dick Menke, and Sam Jackson for their skilled support involving equipment fabrications for detector mounts, spectrometer and optics mounts, and many other items. The glass shop members, Keki, Manfred, and Scott, deserve credit for their support in glassware related projects. Professor Jim Harrison was of immeasurable help with the natural orbital calculations. Professor Chris Chang's contributions of isotopes and chlorins to our porphyrin studies are greatly appreciated. Professor Costas Varotsis's technical discussions was also valuable input during my early graduate years. I thank Rob Richards and Kitz for room and boarding during my last year of research. Lastly, I thank all other labmates and schoolmates for teaching me the balance between vision and practicality.

CHAPTER 4 VIBRATIONAL ANALYSIS OF ZINC(II)  
OCTAETHYLPORPHYRIN IN THE LOWEST EXCITED  
SINGLET STATE

TABLE OF CONTENTS

Abstract.....	113
I. Introduction.....	114
II. Materials and Methods.....	120
III. Results.....	125
IV. Discussion.....	137
List of References.....	138
LIST OF TABLES.....	ix
LIST OF FIGURES.....	x
CHAPTER 5 STRUCTURAL PERTURBATIONS FROM NATURAL ORBITAL CALCULATIONS	
CHAPTER 1 INTRODUCTION TO TIME-RESOLVED RAMAN SPECTROSCOPY	153
Abstract.....	1
I. Introduction.....	2
II. Reaction Centers.....	4
III. Ultrafast Raman Spectroscopy Applications.....	14
Instrumental Techniques.....	15
Vibrational Relaxation Processes.....	16
Photochemical Systems.....	17
Photobiological Systems.....	19
IV. Metalloporphyrin Structure and Dynamics.....	22
List of References.....	35
APPENDIX A	
CHAPTER 2 INSTRUMENTATION	
Abstract.....	43
I. Experimental Apparatus.....	44
II. Flowing Liquid Jet Assembly.....	60
III. Quasi-Simultaneous Accumulation.....	70
List of References.....	78
CHAPTER 3 RAMAN SPECTRA OF METALLOPORPHYRIN EXCITED STATES	
Abstract.....	81
I. Introduction.....	82
II. Materials and Methods.....	83
III. Results.....	87
IV. Discussion.....	107
List of References.....	110

# **CHAPTER 4 VIBRATIONAL ANALYSIS OF ZINC(II) OCTAETHYLPORPHYRIN IN THE LOWEST EXCITED SINGLET STATE**

Abstract.....	113
I. Introduction.....	114
II. Materials and Methods .....	120
III. Results .....	122
IV. Discussion .....	137
List of References .....	148

# **CHAPTER 5 STRUCTURAL PREDICTIONS FROM NATURAL ORBITAL CALCULATIONS**

Abstract.....	153
I. Introduction.....	154
II. Calculations.....	160
III. Results and Discussion.....	172
IV. Future Work.....	199
List of References .....	203

APPENDIX A.....	206
-----------------	-----

Table 5.1 Molecular orbital energies of metalloporphyrins.....	181
--	-----

Table 5.2 Screened potential wavefunctions of metalloporphyrins.....	183
--	-----



Ta

Ta

Ta

Ta

Ta

Ta

Ta

# LIST OF TABLES

Table 2.1	Flow Rate Requirements for Sample Replenishment.	66
Table 2.2	Flowing Jet Restrictions on Temporal Delay.	67
Table 3.1	Raman shifts, polarizations and assignments of the observed Raman modes of ZnOEP in its ground and $S_1$ and $T_1$ excited states in tetrahydrofuran and pyridine.	96
Table 4.1	Vibrational Frequencies ( $\text{cm}^{-1}$ ), isotope shifts ( $\text{cm}^{-1}$ ), and polarizations of ZnOEP, ZnEtio and MgOEP in the ground state, ( $S_0$ ), and the lowest excited singlet state, ( $S_1$ ).	128
Table 4.2	Predictions based on shifts of vibrational frequencies of ZnTPP and ZnOEP anions, and ZnOEP and CuTPP cations compared with the measured values of shifts in the $S_1$ state.	145
Table 5.1	Molecular orbital energies of metalloporphyrin. <sup>a</sup>	161
Table 5.2	Screened potential wavefunctions of low-lying excited state metalloporphyrin. <sup>a</sup>	163
Figure 1.5	Metalloporphyrin in absorption and fluorescence excited states. The spectra are taken with a spectrofluorometer.	27
Figure 2.5	zinc(II) octaethylporphyrin in methanol solution. The $S_0$ and $T_1$ spectra are taken with reference to results of Radziszewski, J. Kirmayer, C., Houten, D. W. <i>J. Am. Chem. Soc.</i> 1989, 111, 6500-6501.	37
Figure 3.6	Molecular orbital coefficients for the HOMO and LUMO orbitals involved in lower electronic state transitions (as calculated <i>ab initio</i> by Sekino, H.; Kobayashi, H. <i>J. Chem. Phys.</i> 1987, 86(9), 5045-5052).	29

Figure 1.7 Raman spectrum of zinc(II) octaethylporphyrin in tetrahydrofuran. Taken with glass jar tube in a backscattering apparatus at room temperature (1877 triple spectrometer, 1200 grooves/mm,  $\lambda = 413.1$  nm, 10 mW, exposure time 60 seconds). Solvent peaks are marked by an asterisk.

## LIST OF FIGURES

Figure 2.1	Instrumentation used for time-resolved picosecond Raman experiment SHG, second harmonic generator using KTP crystal	46
Figure 1.1	Representation of coupled electron and proton transfer in bacterial photosynthesis. Photoexcitation of the special pair dimer (BChl <sub>2</sub> ) results in electron transfer through bacteriopheophytin A (BPh <sub>A</sub> ) and quinone A (Q <sub>A</sub> ) to reduce quinone (Q <sub>B</sub> ), which triggers proton transfer across the membrane. Diagram taken from Okamura, M. Y.; Feher, G. <i>Annu. Rev. Biochem.</i> <b>1992</b> , 61, 861-896.	7
Figure 1.2	Reaction center structure of <i>Rps. viridis</i> . Structure taken from Deisenhofer, J.; Epp, O.; Miki, R.; Huber, R.; Michel, H. <i>Nature(London)</i> <b>1985</b> , 318, 618-624.	9
Figure 1.3	Electron transfer reactions in reaction centers of photosynthetic bacteria. Transfer times for forward and recombination rates are taken from Feher, G.; Allen, J. P.; Okamura, M. Y.; Rees, D. C. <i>Nature</i> <b>1989</b> , 339, 111-116.	12
Figure 1.4	a) Structural Diagram of a D <sub>4h</sub> metalloporphyrin. X and Y indicates positions for peripheral substitution. Pyrrole core carbons are assigned to a, b, and m positions to permit interpretation of Raman peaks. b) Compositions of porphyrin in-plane "skeletal" modes deemed important in S <sub>1</sub> state studies within this thesis.	24
Figure 1.5	Metalloporphyrin absorption characteristics for ground and excited states. The spectra are simulated to represent those of zinc(II) octaethylporphyrin in methylene chloride. The S <sub>1</sub> and T <sub>1</sub> spectra are taken with reference to results of Rodriguez, J.; Kirmaier, C.; Holten, D. W. <i>J. Am. Chem. Soc.</i> <b>1989</b> , 111, 6500-6501.	27
Figure 1.6	Molecular orbital coefficients for the HOMO and LUMO orbitals involved in lower electronic state transitions (as calculated <i>ab initio</i> by Sekino, H.; Kobayashi, H. <i>J. Chem. Phys.</i> <b>1987</b> , 86(9), 5045-5052.	29

Figure 1.7	Raman spectrum of zinc(II) octaethylporphyrin in tetrahydrofuran. Taken with glass nmr tube in a backscattering apparatus at room temperature (1877 triple spectrometer, 1200 grooves/mm, resolution $\lambda = 413.1$ nm, 10 mW, exposure time 60 seconds). Solvent peaks are marked by an asterisk.	33
Figure 2.1	Instrumentation used for time-resolved picosecond Raman experiment SHG: second harmonic generator using KTP crystal; THG: third harmonic generator using BBO crystal; Shutter driver: homebuilt device to control mechanical shutters; PI/CCD: princeton instruments charge coupled device detector; OPTICS: a collimating lens (focus length = 2.5 inch, diameter = 2 inch), and a focusing lens (focus length = 12 inch, diameter = 2 inch).	46
Figure 2.2	Laser dye efficiency curves for a) stilbene 420 in ethylene glycol	48
Figure 2.12	b) pyrromethene 567 in propyl phenyl ether (PPH), and	73
Figure 3.1	c) rhodamine 6G in ethylene glycol. Data were collected by delivering 1 W 355 nm and 2 W 532 nm pulses from a Coherent 76-s Antares laser to a pair of Coherent 702 dye lasers with the cavity dumper drivers operated at 3.825 MHz.	86
Figure 2.3	Pulse energies from Coherent 702 dye lasers as a function of repetition rate for a) pyrromethene 567 in propyl phenyl ether b) rhodamine 6G in ethylene glycol and c) stilbene 420 in ethylene glycol. The pulse energy dependence was done at the efficiency curve maxima of each dye, with 2 W 532 nm and 1 W 355 nm pump pulses. The actual repetition rate equals 38.25 MHz/Repetition divisor.	51
Figure 2.4	Spectral response curves for optical filters 520DFD22-50S and 505FD64-50S. The responsivity of the 520FD22-50S is shown at incident beam angles of $0^\circ$ and $45^\circ$ to display the angle dependence of transmission.	53
Figure 2.5	Experimental setup initially used in determining zero-time overlap through a modified transient absorption experiment	56
Figure 2.6	DODC iodide transient absorption. a) Simulated absorption spectra representing optical behavior of DODC iodide. b) Time-averaged voltage pulse of "blue" laser showing intensity decrease when in temporal overlap with "red" pulses (as seen on Tektronix DSA 602 oscilloscope).	58
Figure 2.7	Flowing jet cell assembly used in high repetition rate picosecond Raman experiments.	63

Fig

Fig

Fig

Fi

Fi

Fi

Y



Figure 2.8	Knife-edge technique used for determining beam waist size.	65
Figure 2.4	a) Experimental setup used with 5X microscope objective(569-199). b) Plots of beam intensity versus changes in razor edge translation taken at four vertical positions. The vertical positions are listed in reference to the position that gave the minimal beam waist value of 13 $\mu\text{m}$ .	91
Figure 2.9	Molecular excitations expected under rapid flowing jet setup.	69
Figure 2.10	Simultaneous method implementing mechanical shutters (SI and SII) within laser beam pathways.	72
Figure 2.11	Schematic of shutter driver. a) voltage transformer. b) analog switching permitting shutter operation.	74
Figure 2.12	Partitions of time intervals generated by shutter driver.	75
Figure 3.1	Instrumentation used for time-resolved nanosecond Raman experiments. HG: hamonic generators giving 2 <sup>nd</sup> and 3 <sup>rd</sup> harmonic wavelengths; Dye Laser: optionally used to generate wavelengths not accessible by Raman shifter; H <sub>2</sub> Raman shifter: 1st anti-stokes of 532 nm used (435.7 nm); PBP: Pellin-Broca prism used to separate the stokes lines coming from the Raman shifter; 1459 Illuminator: mirrors used to direct Raman scatter into Spex 1877 Triplemate.	86
Figure 3.2	Time resolved resonance Raman spectra of ZnOEP in THF in (a) low wavenumber region and (b) in the high wavenumber region. The pump and probe beams were at 572 nm and 450 nm, respectively. The time evolution of the Raman scattering is represented by spectra obtained at time delays between the pump and probe pulse of 100 ps, 800 ps, 2 ns, and 27 ns. The concentration of ZnOEP was $5 \cdot 10^{-4}$ M. The spectra of the ground state (gs) and the solvent (dotted line) were obtained in the absence of the pump pulse.	89
Figure 3.3	Time resolved resonance Raman difference spectra of ZnOEP in THF in (a) low-wavenumber and (b) high-wavenumber range. Experimental spectra from Figure 3.2 were acquired "quasi-simultaneously". The ground state features observed in Figure 3.2 at various delays for high and low frequencies have been subtracted out such that no negative peaks appear. The peak positions of the vibrational modes are collected in Table 3.1. The low intensities observed at 669 $\text{cm}^{-1}$ and 753 $\text{cm}^{-1}$ suggest that the intensities of ground state features in the excited state spectra are minimal.	91

Figure 3.3	Time-resolved resonance Raman difference spectra of ZnOEP in pyridine taken at (a) low and (b) high wavenumber regions. Spectra are shown for all polarizations, parallel polarization, and perpendicular polarization. Qualitative assignments to symmetries of vibrational modes are labeled as either totally symmetric (P) or nontotally symmetric (DP). Solvent spectra (dotted lines) are obtained in the absence of a pump pulse and peaks are marked by an asterisk.	104
Figure 3.4	Time-resolved resonance Raman difference spectra taken at 100 ps in (a) low and (b) high wavenumber regions. Spectra are shown for all polarizations, parallel polarization, and perpendicular polarization. Qualitative assignments to symmetries of vibrational modes are labeled as either totally symmetric (P) or nontotally symmetric (DP). Solvent spectra (dotted lines) are obtained in the absence of a pump pulse and peaks are marked by an asterisk.	93
Figure 3.5	Time-resolved resonance Raman difference spectra taken at 27 nanoseconds in (a) low and (b) high wavenumber regions. Spectra are shown for all polarizations, parallel polarization, and perpendicular polarization. Qualitative assignments to symmetries of vibrational modes are labeled as either totally symmetric (P) or nontotally symmetric (DP). Solvent spectra (dotted lines) are obtained in the absence of a pump pulse and peaks are marked by an asterisk.	95
Figure 3.6	Time-resolved resonance Raman difference spectra taken using nanosecond Q-switched Nd:YAG laser pulses as pump and probe. Spectra are shown for (a) ground state (g.s.), (b) time delay between pump and probe of 13 ns, (c) scaled difference spectrum, (d) parallel polarization, and (e) perpendicular polarization. The wavelength of the pump pulse was 532 nm, and the probe wavelength was 437.5 nm. The ground state spectrum was taken in the absence of a pump pulse. The concentration of ZnOEP was $5 \cdot 10^{-3}$ M in THF.	99
Figure 3.7	Time-resolved resonance Raman difference spectra of ZnOEP in pyridine in (a) low-wavenumber and (b) high-wavenumber range. The ground state features observed in Figure 3.7 at various delays for high and low frequencies have been subtracted out such that no negative peaks appear by using techniques identical to that used in Figure 3.2. Solvent spectra acquired immediately after the experiment were used to subtract out the strong solvent features which obscure the 27 ns spectrum. The peak positions of the vibrational modes are collected in Table 3.1. Asterisks mark artifacts arising from subtraction of the pyridine solvent features.	101
Figure 4.5	Parallel and perpendicular (—) Raman difference spectra of ZnOEP (n.a.), ZnOEP- $d_6$ , ZnOEP- $^{15}\text{N}_4$ , ZnEP1 (n.a.) and MgOEP (n.a.). Other than the polarizer, conditions were identical to those used in Figure 4.4.	132

Figure 3.8	Time-resolved resonance Raman difference spectra of ZnOEP in pyridine taken at 100 ps in (a) low and (b) high wavenumber regions. Spectra are shown for all polarizations, and parallel and perpendicular polarizations. Qualitative assignments to symmetries of vibrational modes are labeled as either totally symmetric (P), or nontotally symmetric (DP). Asterisks mark artifacts arising from subtraction of the pyridine solvent features.	104
Figure 3.9	Time-resolved resonance Raman difference spectra of ZnOEP in pyridine taken at 27 ns in (a) low and (b) high wavenumber regions. Spectra are shown for all polarizations, and parallel and perpendicular polarizations. Qualitative assignments to symmetries of vibrational modes are labeled as either totally symmetric (P), or nontotally symmetric (DP). Asterisks mark artifacts arising from subtraction of the pyridine solvent features.	106
Figure 4.1	a) Metalloporphyrin absorption characteristics for ground and excited states of zinc(II) octaethylporphyrin (ZnOEP) in methylene chloride. The $S_1$ and $T_1$ spectra are taken with reference to results of Rodriguez, J.; Kirmaier, C.; Holten, D. W. <i>J. Am. Chem. Soc.</i> <b>1989</b> , 111, 6500-6501. b) Energy level diagram representing observed energy levels for ZnOEP.	118
Figure 4.2	Ground state Raman spectra of ZnOEP (n.a.), ZnOEP- $d_4$ , ZnOEP- $^{15}\text{N}_4$ , ZnEPI (n.a.) and MgOEP (n.a.). The probe beam was at 450 nm. Each porphyrin was dissolved in tetrahydrofuran. The concentration for all porphyrins was $5 \cdot 10^{-3}$ M, except ZnEPI, which was $1 \cdot 10^{-3}$ M.	124
Figure 4.3	Parallel and perpendicular(---) Raman spectra of ZnOEP (n.a.), ZnOEP- $d_4$ , ZnOEP- $^{15}\text{N}_4$ , ZnEPI (n.a.) and MgOEP (n.a.). Other than the polarizer, conditions were the same as those described in Figure 4.2.	127
Figure 4.4	Raman difference spectra of ZnOEP (n.a.), ZnOEP- $d_4$ , ZnOEP- $^{15}\text{N}_4$ , ZnEPI (n.a.) and MgOEP (n.a.). The pump pulse was set at 572 nm, except for MgOEP, which used 575 nm, and preceded the probe pulse (450 nm) by 100 ps. Porphyrins were dissolved in tetrahydrofuran to approximately $5 \cdot 10^{-4}$ M.	130
Figure 4.5	Parallel and perpendicular(---) Raman difference spectra of ZnOEP (n.a.), ZnOEP- $d_4$ , ZnOEP- $^{15}\text{N}_4$ , ZnEPI (n.a.) and MgOEP (n.a.). Other than the polarizer, conditions were identical to those used in Figure 4.4.	132



Figure 4.6	Relative isotopic shifts in ground and excited states (from Table 4.1).	135
Figure 5.1	Molecular orbitals for the HOMO, $a_{2u}$ and $a_{1u}$ , LUMO, $e_{gx}$ and $e_{gy}$ , and the next two lowest unoccupied states, $b_{1u}$ and $b_{2u}$ , of porphine as defined by Longuet-Higgins, H. C.; Rector, C. W.; Platt, J. R. <i>J. Chem. Phys.</i> <b>1950</b> , 18(9), 1174-1181.	158
Figure 5.2	Labeling sequence used for natural orbital calculations.	174
Figure 5.3	Composite orbital diagrams for atom electron densities of singlet states of metalloporphin.	176
Figure 5.4	Composite orbital diagrams for atom electron densities of triplet states of metalloporphin.	178
Figure 5.5	Composite orbital difference diagrams for atom electron densities of lowest excited states of metalloporphin.	180
Figure 5.6	Composite orbital difference diagrams for atom electron densities of second lowest excited states of metalloporphin.	182
Figure 5.7	Composite orbital bond order diagram for the singlet ground state of metalloporphin.	184
Figure 5.8	Composite orbital bond order diagrams for the two lowest singlet excited states of metalloporphin.	186
Figure 5.9	Composite orbital bond order diagrams for the two lowest triplet excited states of metalloporphin.	188
Figure 5.10	Composite orbital bond order difference diagrams for the lowest singlet and triplet excited states of metalloporphin.	190
Figure 5.11	Composite orbital bond order difference diagrams for the second lowest singlet and triplet excited states of metalloporphin.	192
Figure 5.12	Metalloporphin bond density changes in first and second excited states. Positive values suggest bond compression, whereas negative values suggest bond stretching.	199
Figure 5.13	Representative distortions in $S_1$ , $T_1$ , $S_2$ , and $T_2$ excited electronic states.	201

## 1. INTRODUCTION

Free energy consumed by biological systems is ultimately generated from solar energy that is trapped by the process of photosynthesis. Photosynthesis in green plants results in evolution of oxygen through a deceptively simple redox equation:

### CHAPTER 1

## INTRODUCTION TO TIME-RESOLVED RAMAN SPECTROSCOPY

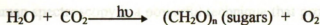
**ABSTRACT**  $\text{H}_2\text{O} + \text{CO}_2 \xrightarrow{\text{light}} (\text{CH}_2\text{O})_n (\text{sugars}) + \text{O}_2$

The reaction center in photosynthesis initiates charge transfer processes while its special pair chlorophyll dimer resides in an excited singlet electronic state ( $S_1$ ). The role of structural effects in this charge transfer step has been elusive but can be obtained through vibrational spectroscopy. In this thesis, a picosecond Raman system was developed to study these photosynthetically active chlorophyll pigments, and porphyrins were used to study structural changes in excited states of biologically relevant molecules. Since two-pulsed picosecond Raman spectroscopy underwent large developments during my tenure as a graduate student, and structural knowledge about excited states of metalloporphyrins was relatively unknown, this chapter provides relevant background information that will be helpful in perusing Chapter 2 through Chapter 5. Bacterial reaction centers, the original focus of this project, are discussed in detail. A synopsis of the relevant uses of ultrafast time-resolved Raman spectroscopy (picosecond) on biological and model systems is discussed. Detailed understanding of structural changes in the  $S_1$  state of model porphyrins requires a detailed understanding of dynamic and structural behavior of ground state porphyrins. Thus, a section has been included in this chapter that summarizes the extensive literature background on metalloporphyrins.



## I. INTRODUCTION

Free energy consumed by biological systems is ultimately generated from solar energy that is trapped by the process of photosynthesis. Photosynthesis in green plants results in evolution of oxygen through a deceptively simple redox equation:



The actual mechanism is quite complex and requires the interplay of many proteins and smaller molecules, involving coupled proton and electron transfer reactions.<sup>1</sup> Purple photosynthetic bacteria are a well studied example of photosynthesis that generates free energy but does not evolve oxygen. The research project described in this thesis concerns understanding the mechanism of primary charge separation within reaction centers such as those of purple photosynthetic bacteria.<sup>2</sup>

The bacterial reaction center contains two closely associated bacteriochlorophyll molecules that form a bacteriochlorophyll dimer (BChl<sub>2</sub>). This dimeric species can be photoexcited into its singlet excited state (S<sub>1</sub>). The bacteriochlorophyll dimer is still in the S<sub>1</sub> state when it becomes the initial electron donor in rapid electron transfer to a bacteriopheophytin (BPh).<sup>3-6</sup> This charge transfer initiates a series of chemical reactions that eventually result in conversion of CO<sub>2</sub> into organic compounds and generation of free energy. Protein x-ray crystallography has shown that reaction center components for bacteria such as *Rb. sphaeroides* and *Rps. viridis* are highly organized structures.<sup>7</sup> The structures of the redox intermediates in this series of chemical reactions are known to

regulate electron transfer rates.<sup>7</sup> Likewise, the initial electron transfer rate to BPh is influenced by the structure of the BChl<sub>2</sub> dimer.<sup>7</sup> However, the structure of the initial S<sub>1</sub> state of the dimer has not been found by using x-ray crystallography, and must be accessed with other physical techniques. The method we have selected for this purpose is time-resolved resonance Raman spectroscopy.

Resonance Raman spectroscopy is a powerful technique that probes molecular vibrations coupled to electronic transitions. When the monochromatic laser frequency is brought into resonance with an electronic transition of a species of interest, dramatic enhancements in scattered intensity are observed for the selected molecular species. Time-resolved resonance Raman spectroscopy is even more selective and can be used to measure conformational and structural changes of transient species and excited electronic states.<sup>8</sup> This technique can be appropriate for bacterial reaction center studies, but its application at Michigan State University first required development of a picosecond time-resolved resonance Raman system capable of studying S<sub>1</sub> states.

Investigation of primary charge separation in reaction centers through application of time-resolved resonance Raman spectroscopy is the overriding goal of this project. However, the initial experiments with the newly developed picosecond Raman instrumentation were carried out on porphyrin model compounds. This was done for several reasons. Inherent in the resonance Raman technique is the fact that structural changes observed are localized. In the case of  $\pi\pi^*$  resonance Raman within the porphyrin ring, many structural similarities with the BChl<sub>2</sub> dimer exist. Moreover, porphyrins are worthy of studies not only for their relevance to biological systems,<sup>1,9,10,11</sup> but also for

technology driven applications such as solar energy systems,<sup>12,13</sup> development of molecular electronic switches,<sup>14</sup> and medical utilization in photodynamic therapy.<sup>15</sup> The universal feature of these applications is that all involve fundamental processes such as vibrational and electronic relaxation, photodissociation, and photoinduced energy and electron transfer. This introductory chapter, as well as the remainder of the thesis, demonstrates that these fundamental processes can be investigated by Raman spectroscopy. Since, at this point in time, very little is known about the vibrational properties of singlet excited electronic states of metalloporphyrins, much less the actual reaction centers, it became necessary to use the relative simplicity of model porphyrins to aid in the analysis of excited state structures.

This chapter gives a brief introduction to the bacterial photosynthetic system that will be studied by using the Raman instrumentation described in this thesis in future projects. Ultrafast time-resolved Raman spectroscopy has seen extensive development in the last few years, so a brief resume of current results on biological and model systems are included. The structural changes that are observed in the  $S_1$  state are best understood in relation to the structural behavior of ground state porphyrins, so a section summarizes the basic structure and dynamics of metalloporphyrins within the context of absorption and Raman spectroscopies.

## II. REACTION CENTERS

Photosynthesis is the process whereby light energy is transformed into chemical energy. Two classes of organisms perform photosynthesis: green plants, which evolve core of the reaction center. A third protein subunit,  $H_L$ , contains only one

oxygen, and photosynthetic bacteria, which do not. Green plants contain two photosystems, I (PSI) and II (PSII). Bacterial photosynthesis bears similarities to that of green plants, but is simpler and contains only one photosystem. In purple photosynthetic bacteria, a light-driven proton pump coupled to electron transfer drives the conversion of light energy to chemical energy. The bacterial reaction center plays a critical role in this process by absorbing photons, performing the initial rapid electron transfers, and providing the initial site for proton uptake reactions. The coupling between electron transfer and proton transfer is displayed in Figure 1.1. The initial photoexcitation of the special pair dimer (BChl<sub>2</sub>), results in subsequent electron transfers through a bacteriopheophytin (BPh<sub>A</sub>), and then quinone A (Q<sub>A</sub>) to produce doubly reduced quinone B (Q<sub>B</sub>), which is bound near the cytoplasmic side of the membrane. Two protons bind to Q<sub>B</sub><sup>2-</sup>, and the doubly reduced quinone then dissociates from the reaction center, and is reoxidized by the cytochrome b/c<sub>1</sub> complex, releasing protons on the periplasmic side of the membrane. The net result is proton transport across the membrane. The proton transfer is driven by electron transfer occurring within the reaction center. The redox centers and chromophores of the reaction center from *Rps. viridis*<sup>16</sup> (Figure 1.2) are typical of bacterial reaction centers and include the following cofactors: four bacteriochlorophylls, two bacteriopheophytins, two quinones, and one nonheme Fe<sup>2+</sup>. These species are bound into two homologous protein subunits, L and M, that are not shown in Figure 1.2.<sup>17,18</sup> The arrangement of the cofactors in Figure 1.2 imply an apparent C<sub>2</sub> symmetry between subunits L and M.

The L and M subunits each have five membrane-spanning helices that form the core of the reaction center. A third protein subunit, H, contains only one



# REACTION CENTER

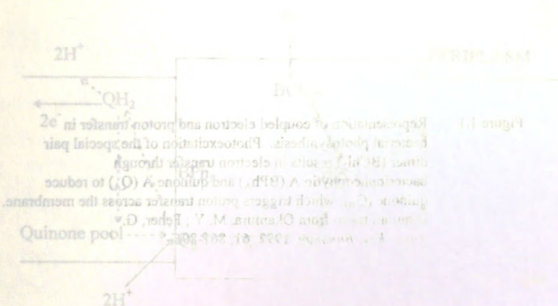


Figure 11. Representation of coupled electron and proton transfer in photosynthetic reaction center. Photooxidation of the special pair of chlorophylls results in electron transfer through bacteriochlorophyll A (BChl<sub>A</sub>) and bacteriochlorophyll B (BChl<sub>B</sub>) to reduce quinone (Q), which triggers proton transfer across the membrane. (From M. V. Fagan, D. G. ...)



**Figure 1.1** Representation of coupled electron and proton transfer in bacterial photosynthesis. Photoexcitation of the special pair dimer ( $\text{BChl}_2$ ) results in electron transfer through bacteriopheophytin A ( $\text{BPh}_A$ ) and quinone A ( $\text{Q}_A$ ) to reduce quinone ( $\text{Q}_B$ ), which triggers proton transfer across the membrane. Diagram taken from Okamura, M. Y.; Feher, G. *Annu. Rev. Biochem.* 1992, 61, 861-896.

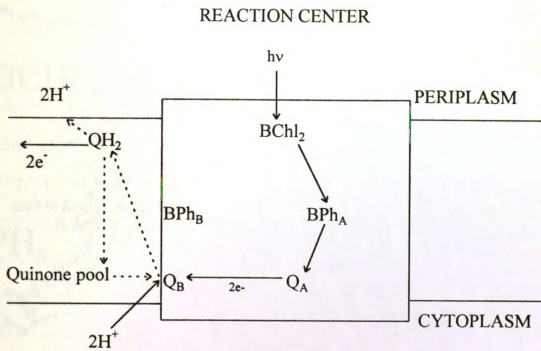


Figure 1.1

## BACTERIAL REACTION CENTER

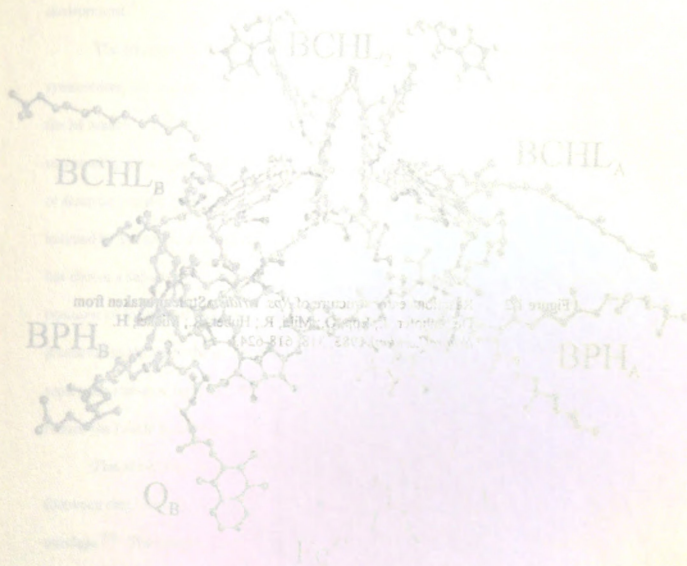


Figure 1.2

**Figure 1.2**      **Reaction center structure of *Rps. viridis*. Structure taken from Deisenhofer, J.; Epp, O.; Miki, R.; Huber, R.; Michel, H. *Nature(London)* 1985, 318, 618-624.**

## BACTERIAL REACTION CENTER

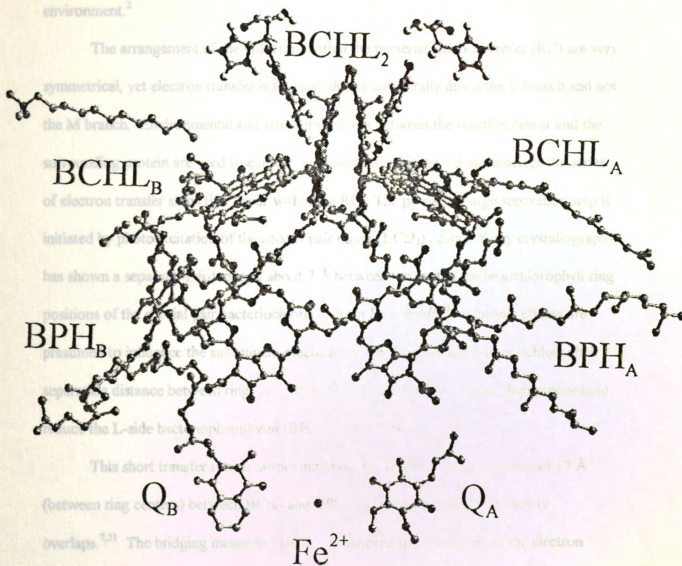


Figure 1.2



mem

comp

pro

envi

sym

the

su

of

in

ha

p

p

s

n

membrane-spanning helix and is asymmetrically located on the cytoplasmic side of the complex overlaying the  $Q_A \text{ Fe}^{2+}$  complex. Subunit H behaves as a cap over  $Q_A$  and promotes proton transfer association with  $Q_B$  by shielding  $Q_A$  from the aqueous environment.<sup>2</sup>

The arrangement of the cofactors within the bacterial reaction center (RC) are very symmetrical, yet electron transfer is favored almost unilaterally down the L branch and not the M branch. Environmental and structural factors between the reaction center and the surrounding protein are used to explain this selectivity. Figure 1.3 summarizes the series of electron transfer steps that occur within the RC. The primary charge separation step is initiated by photoexcitation of the special pair dimer ( $\text{BChl}_2$ ). Since X-ray crystallography has shown a separation distance of about 7 Å between the central bacteriochlorophyll ring positions of the special pair bacteriochlorophylls in *Rps. viridis*,<sup>16</sup> excitonic effects are presumed to influence the subsequent electron transfer (the average bacteriochlorophyll separation distance between rings is ~3.0 Å).<sup>19,20</sup> The special pair dimer then proceeds to reduce the L-side bacteriopheophytin ( $\text{BPh}_A$ ) within 3 psec.

This short transfer time is surprising given the relatively large distance of 17 Å (between ring centers) between  $\text{BChl}_2$  and  $\text{BPh}_A$  and their small electron density overlaps.<sup>7,21</sup> The bridging monomer,  $\text{BChl}_A$ , is believed to be involved in the electron transfer mechanism.<sup>21,22,23,24</sup> One proposal suggests a two-step sequential mechanism, in which  $\text{BChl}_A^-$  serves as a transient intermediate state that has not been observed using femtosecond spectroscopy. An alternative mechanism, called superexchange, proposes

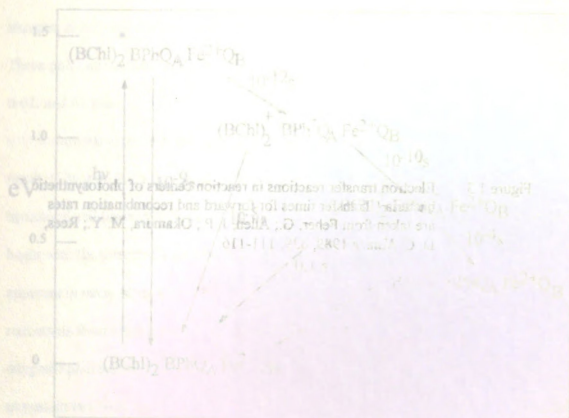


Figure 1.1

**Figure 1.3**      **Electron transfer reactions in reaction centers of photosynthetic bacteria. Transfer times for forward and recombination rates are taken from Feher, G.; Allen, J. P.; Okamura, M. Y.; Rees, D. C. *Nature* 1989, 339, 111-116.**

that electronic overlap between  $\text{BChl}_2^+$  and  $\text{BPhQA}$  is enhanced by a factor of 10.

$\text{BChl}_2^+ \text{BChl}_2$ .

Electron transfer from  $\text{BPhQA}$  to  $\text{Q}_B$  proceeds at a rate of  $10^{-10}$  s.

electron to  $\text{Q}_B$  within a millisecond to complete the charge separation process.

interacts in the proton transport process. The redox potential of  $\text{Q}_B$  is 0.1 V.

regulation of environmental differences between different

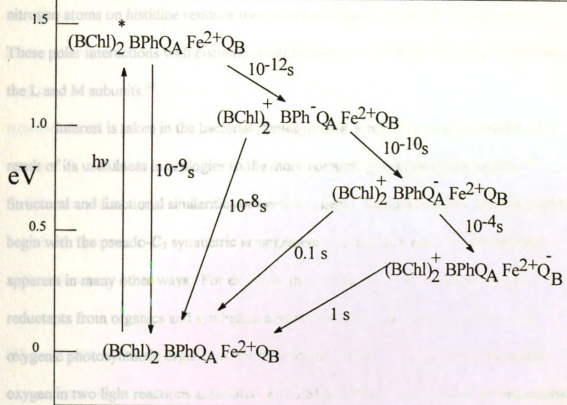


Figure 1.3

of proteins that enclose the reaction center of PSI. These structural similarities

suggest that PSI may have evolved from green photosynthetic bacteria, whereas PSII

probably arose from purple photosynthetic bacteria.<sup>32</sup> In any case, PSI and purple bacteria

appear to have a common ancestor.<sup>33</sup> The differences that exist in comparisons of



that

BCh

elec

inte

reg

mit

The

the

res

St.

be

ap

re

on

on

of

o:

su

p

a

that electronic overlap between  $\text{BChl}_2^*$  and  $\text{BPhA}$  is enhanced by a virtual state to the  $\text{BChl}_2^+ \text{BChl}_A^-$  ~~interacts between bacterial reaction centers and those of oxygenic~~ photosynthesis. Electron transfer from  $\text{BPhA}$  to  $\text{Q}_A$  proceeds in  $\sim 200$  psec.  $\text{Q}_A$  transfers an ~~electron to~~ electron to  $\text{Q}_B$  within a millisecond to complete the charge separation process.  $\text{Q}_B$  then interacts in the proton transport process. The function of the non-heme iron appears to be regulation of environmental differences between the two quinones. The iron is ligated to nitrogen atoms on histidine residues that in turn are ligated to protein subunits L and M. These polar interactions with histidine residues appear to stabilize the tertiary structure of the L and M subunits.<sup>25</sup> ~~Resonance Raman spectroscopy provides evidence that each quinone binds in a specific~~ structure. Interest is taken in the bacterial photosynthetic reaction center, particularly as a result of its usefulness in analogies to the more complex green plant photosystem.<sup>26</sup> Structural and functional similarities between oxygenic and non-oxygenic reaction centers begin with the pseudo- $\text{C}_2$  symmetric arrangement of chromophores,<sup>27,28</sup> but are also apparent in many other ways. For example, the simpler bacterial organisms obtain reductants from organics and synthesize sugars through a single light reaction. The oxygenic photosynthetic organisms not only fix the carbon, but also evolve molecular oxygen in two light reactions associated with PSI and PSII. The L and M protein subunits of bacterial reaction centers have been shown to have significant homology with the dimer of proteins that enclose the reaction center of PSII.<sup>29,30,31</sup> These structural similarities suggest that PSI may have evolved from green photosynthetic bacteria, whereas PSII probably arose from purple photosynthetic bacteria.<sup>32</sup> In any case, PSI and purple bacteria appear to have a common ancestor.<sup>33</sup> The differences that exist in comparisons of ~~methods~~

quan

differe

phot

this

high

sen

evi

rea

str

su

by

co

o

**E**

v

quantum yield and energy conversion efficiency have been speculated to be due to the differing environments between bacterial reaction centers and those of oxygenic photosynthetic organisms. The bacterial organisms operate near unity quantum yield, but this is done at the expense of energy conversion efficiency ( $\sim 30\%$ ).<sup>7</sup> Plant systems have higher energy conversion efficiency but a lesser quantum yield ( $\sim 90\%$ ).<sup>34</sup>

These structural homologies suggest that calculated electron transfer kinetics are sensitive to the structures of the associated intermediates. Additionally, experimental evidence suggests that structural changes occur during charge separation.<sup>35,36</sup> For these reasons, a time-resolved Raman spectroscopic apparatus that could monitor both time and structure of BChl<sub>2</sub> was designed. As will be shown in the following chapters, this was successfully applied to BChl<sub>2</sub> like porphyrin molecules.<sup>37,38,39</sup> Structural changes incurred by BPh (and BChl<sub>A</sub>) upon reduction can also be monitored via Raman spectroscopy. This combined dynamical information should give quantitative understanding of the mechanism of the initial electron transfer step.

### III. ULTRAFAST RAMAN SPECTROSCOPY APPLICATIONS

Time-resolved Raman spectroscopy combines the vibrational and structural information gained through the Raman process with the ability to probe transient species in photophysical and photobiological processes. Resonance Raman spectroscopy takes advantage of the high selectivity and increased sensitivity gained by tuning the probe laser wavelength to an electronic transition of interest. While the time resolution can include time ranges from microseconds to sub-picoseconds, this review of experimental methods

will

Ram

to b

**Inst**

lase

lith

con

tita

use

pic

las

ha

g

co

P

P

r

c

R



will be limited to recent applications that use picosecond time-resolved spontaneous Raman spectroscopy and gives a general overview of the techniques, and the applications to biological and model systems.

### **Instrumental Techniques**

For time-resolved picosecond Raman spectroscopy, lamp-pumped solid state lasers, such as neodymium-yttrium-aluminum-garnet (Nd:YAG) or neodymium-yttrium-lithium-fluoroborate (Nd:YLF) lasers are the most commonly used laser systems, often in conjunction with dye lasers and/or amplifiers. Laser pumped solid state lasers, such as titanium sapphire lasers, have been more recently developed and are becoming increasingly used for picosecond pulse generation. Currently, the most common approach for picosecond Raman experiments involves spatially and temporally overlapping two pulsed lasers with pulse widths in the range 4-30 psec.<sup>8,40,41</sup> Single pulse picosecond experiments have also been done.<sup>42a,42b,43</sup>

Pulse repetition rates and pulse energies used in ultrafast Raman spectroscopy vary greatly among experimental setups. The choice of amplification scheme requires a compromise between the need for higher peak power and the need for moderate average power. High average power enhances high collection of Raman scattered light, but high pulse energies can also destroy the sample through non-linear processes. The high repetition rate (70 to 80 MHz) characteristic of source lasers like Nd:YAG or Nd:YLF can generate 50 Hz or near KHz repetition rates when used with various amplifiers.<sup>40,42,44</sup> However, amplified and slower repetition rate picosecond lasers bring higher pulse

ener

thos

the

picc

hun

det

em,

res

col

vis

me

Th

sy

**V**

v

r

**V**

**P**

energies. Typical pulse energies for 50 Hz systems are on the order of 100's of  $\mu\text{J}$ , while those with KHz amplification produce 5 to 20  $\mu\text{J}$ . Some research groups have neglected the use of low repetition rate amplifiers and retained the MHz repetition rates of picosecond lasers. The MHz systems typically have pulse energies on the order of tens to hundreds of nanojoules.<sup>41</sup> Single grating spectrometers and charge coupled device (CCD) detectors or intensified photodiode array (IPDA) detectors are the most commonly employed collection and detection devices used in these picosecond time-resolved resonance Raman spectroscopy experiments. Different combinations of these lasers and collection/detection devices have been used for various research projects. In order to visualize the general impact of time-resolved Raman spectroscopy on research systems more clearly, the following discussion will be divided into broadly based topic areas. These areas include studies done on vibrational relaxation processes, photochemical systems, and photobiological systems.

### **Vibrational Relaxation Processes**

Vibrational relaxation is a molecular process whereby excess energy from a vibrationally excited molecule is dissipated to its surroundings. Information on vibrational relaxation can be obtained in different ways through time-resolved Raman spectroscopy. Vibrational relaxation of vibrational modes is expressed as a sum of contributions from population decay time,  $T_1$ , and pure dephasing time,  $T_2^*$ :

$$T_2^{-1} = (2T_1)^{-1} + (T_2^*)^{-1}$$

Tim

pop

que

ref:

ofia

pres

mo

*tran*

the

**Ph**

Ra

pro

gro

all

and

tran

pa

spe



Time-resolved spontaneous anti-stokes Raman spectroscopy can obtain information on the population lifetime ( $T_1$ ) of vibrational modes. This is of paramount importance for questions addressing state-selective chemistry. The decay time of vibrational modes are reflected by their intrinsic linewidth. Raman bands of electronically excited molecules are often much broader than those of ground state molecules.<sup>37,38,39,45,46,47</sup> This indicates the presence of additional mechanisms for vibrational dephasing in electronically excited molecules. As an example, the vibrational dephasing in the C=C stretching mode of  $S_1$  *trans*-stilbene was explained within a dephasing model that supported theories addressing the isomerization process from *trans*-stilbene to *cis*-stilbene.<sup>48</sup>

### Photochemical Systems

The ideal excited electronic state to be studied with time-resolved resonance Raman spectroscopy should have the following traits: the excited state should be produced in a photochemically simple process, the extinction coefficients of both the ground and excited electronic state should be large, and preferably the excited state should allow resonance Raman excitation in the near ultraviolet region. The strong absorption and selective resonance Raman in the ultraviolet region would give high signal-to-noise transient Raman spectra. Delocalized  $\pi\pi^*$  transitions have all these qualities and are particularly pliable for time-resolved resonance Raman studies.

Studies of  $\pi\pi^*$  excitation of *trans*-stilbene are especially amenable since the spectroscopic properties are reasonably well understood.<sup>49,50</sup> The time and solvent

dependent changes of band shapes for C=C and C-Ph stretches have been noted for stilbene.<sup>50</sup> These experiments have also been done with structural analogues such as paraphenylenes, biphenyl, and terphenyl.<sup>49,51,52</sup>

The  $\pi\pi^*$  transitions of polyenes are also amenable to Raman studies. In an attempt to understand the pericyclic rearrangements relevant to vitamin D photochemistry, Mathies and coworkers monitored several of these polyenes via picosecond ultraviolet time-resolved stokes and anti-stokes Raman spectroscopy.<sup>44b,53,54,55,56</sup> Their studies on 1,3,5-cycloheptatriene (CHT) first determined the kinetics of a sigmatropic shift on the CHT ring.<sup>55,56</sup> Later experiments on CHT characterized Raman scattering from an electronically excited state populated by internal conversion from the initially prepared electronic excited state, and vibrationally unrelaxed and relaxed ground states.<sup>44b,55</sup> In conjunction with resonance Raman analysis results,<sup>56,44b</sup> they concluded that ring planarization of the polyene transpired prior to all pericyclic nuclear rearrangements. Ensuing picosecond Raman results determined reaction dynamics on ring-openings of 1,3-cyclohexadiene (CHD) and  $\alpha$ -phellandrene ( $\alpha$ -PHE).<sup>57</sup> Photoexcitation of these polyenes resulted in a ring-opening that occurred in a conrotatory (i.e. with a twisting of terminal groups in the same direction) fashion. The conrotatory movements were shown to agree with the orbital symmetry predictions of Hoffmann and Woodward.<sup>58</sup> Interestingly, the time-resolved Raman results on 1,3,5-cyclooctatriene (COT) show disrotatory rotation upon photoexcitation of the ring.<sup>44b</sup> However, these results are also consistent with orbital symmetry predictions.<sup>59</sup> Overall, their work is a good example of the utility of time-resolved stokes and anti-stokes Raman scattering for characterizing structural and

v

e

(j

P

di

pr

m

on

wi

as

im,

an

sin,

wh

con

sta

the

of r

bact

vibrational relaxation kinetics of these photoproducts. Furthermore, this linking of experimental results to theoretical predictions was implemented within this thesis (particularly within Chapter 4 and Chapter 5).

### Photobiological Systems

Picosecond time-resolved resonance Raman studies have also been applied to directly measure biological systems such as carotenoids, bacteriorhodopsin, and heme proteins. As noted earlier, single pulse picosecond experiments have been done on metalloporphyrins. Two-pulse picosecond Raman experiments on metalloporphyrins have only recently been completed, and are discussed in detail in Chapter 2 through Chapter 5 within this thesis.

Time-resolved Raman spectra have been obtained for photobiological systems such as  $\beta$ -carotene and other membrane-bound carotenoids. Carotenoids are of biological importance since they perform as energy absorbers in the wavelength region 400-600 nm, and subsequently transfer energy to chlorophylls and bacteriochlorophylls through their singlet excited states. Essentially, carotenoids complement the chlorophyll chromophores, which are basically non-absorptive between the Soret and Q bands. Hashimoto *et al.*<sup>60,61</sup> concluded from their time-resolved studies on carotenoids, that the lowest singlet excited state was  $2^1A_g$ , not the  $1^1B_u$  orbital. Subsequent studies of carotenoids have looked into the relaxation of the  $2^1A_g$  state to form a vibrationally excited  $1^1A_g$  ground state. This is of relevance since the vibrationally excited ground state is thought to transfer energy to bacteriochlorophyll.<sup>62,63</sup>



Another photobiological system that has attracted interest involves photocyclic reactions in retinal proteins, such as the protein bacteriorhodopsin. Bacteriorhodopsin (BR) is an integral protein in the purple membrane of *Halobacterium halobium* that, upon photoexcitation, undergoes isomerization at the all-*trans* retinal protonated Schiff base prosthetic group.<sup>64,65</sup> This protein then behaves as a light-driven transmembrane proton pump.<sup>66</sup> The reversible photocycle has generic labels for the numerous intermediates (I, J, K, L, M, N, O) that are involved in the isomerization of all-*trans* BR and pump protons across a membrane and drive ATP synthesis.<sup>67</sup> Time-resolved picosecond Raman studies were essential in identifying the different conformations of early intermediates such as J and K. Atkinson and coworkers initially identified the resonance Raman features of these species, and established that neither J nor K contained all-*trans* retinal, but were both conformationally distinct species.<sup>68</sup> They concluded that the primary BR photocycle event must include a configurational change in the retinal chromophore. Subsequently, Mathies and coworkers evaluated the structure and dynamics of the J and K intermediates of bacteriorhodopsin by using Stokes and anti-Stokes Raman.<sup>69</sup> They concluded that isomerization induced several subtle changes that resulted in a greater  $\pi$ -electron delocalization over the polyene. Strong mode intensities for the anti-Stokes Raman spectrum of the J intermediate were used to interpret J as a highly twisted chromophore that is vibrationally excited, but cools upon formation of K. As judged by the out-of-plane vibrational modes, K is a more planar intermediate and shows adjustment to protein changes in the local environment within 3 picoseconds.

photochemical systems have been studied rather effectively,<sup>49-50</sup> and certain



photochemical Oxygen binding to heme proteins, such as hemoglobin and myoglobin, are another example of the successful application of picosecond Raman spectroscopy to biological systems. Time-resolved studies by Findsen *et al.*,<sup>70</sup> Dasgupta *et al.*,<sup>71</sup> and Rousseau *et al.*<sup>72</sup> all indicate time dependent Raman frequency shifts between photolyzed heme protein and stable deoxy-heme protein. Interpretations of these changes were drawn mostly from the  $\nu_4$  and iron-histidine stretching frequencies. They correlated these shifts to bond distance changes in the central core of the heme. The collective results of these studies suggest a recombination rate for the heme proteins that proceeds in the following manner. The initial unligated photoexcited state of the heme protein forms within 50 fsec.<sup>8</sup> The protein relaxes to its vibrationally excited ground state in less than 2.5 psec.<sup>73</sup> The vibrationally excited bands in deoxy-hemoglobin have been studied by Lingle *et al.*<sup>74,75</sup> using stokes and anti-stokes time-resolved Raman.

After vibrational cooling is complete, the  $\nu_4$  mode, which initially shifted down upon photoexcitation, slowly increases in frequency from ~10 psec to 10 nsec.<sup>76</sup> This suggests a second slower relaxation process in the protein. This relaxation process has been attributed to a more global protein motion that induces a tilt in the proximal histidine relative to the heme plane.<sup>76</sup> This theory is supported by correlation between iron-histidine and  $\nu_4$  stretching frequencies for a variety of heme structures.<sup>70</sup> Clearly, time-resolved vibrational information such as provided by Raman is essential to perform this type of structural analysis.

While the previous discussion shows that excited electronic states of photochemical systems have been studied rather effectively,<sup>49-59</sup> and certain

pho

few

life

him

trip

exp

the

dis

V.

ur

m

di

m

ne

pr

st

ar

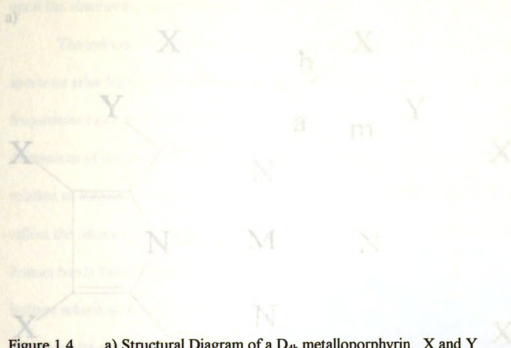
fr

ri

photobiological systems like bacteriorhodopsin have also been analyzed,<sup>64-69</sup> at this time few studies had been done with singlet excited states of porphyrins. Since excited state lifetimes of iron porphyrins are on the order of a picosecond,<sup>73</sup> heme protein studies were limited to studying conformational changes of electronically relaxed proteins.<sup>8,70-76</sup> While triplet excited states were accessible by nanosecond pulsed lasers,<sup>77</sup> picosecond experiments on metalloporphyrins had been limited to d,d excited states,<sup>42c,43</sup> Since this thesis presents the first picosecond results on singlet excited electronic states,<sup>37,38,39</sup> a brief discussion of porphyrin structure and dynamics is in order.

## V. METALLOPORPHYRIN STRUCTURE AND DYNAMICS

Figure Porphyrins are aromatic macrocycles with four pyrrole rings connected by unsaturated methine bridges at the four corners of a square (Figure 1.4a). The conjugated macrocycle of a  $D_{4h}$  metalloporphyrin shows three unique carbon sites that are distinguished by labels as  $C_a$ ,  $C_m$ , and  $C_b$ . This permits the assignment of vibrational modes to observed Raman frequencies (Figure 1.4b). A typical porphyrin has 69 non-substituent vibrational modes, but five were of particular interest in this research project. These five, the  $\nu_4$ ,  $\nu_3$ ,  $\nu_2$ ,  $\nu_{10}$ , and  $\nu_{11}$  modes, predominantly reflect vibrational stretching (and stretching force constants) between different combinations of the  $C_a$ ,  $C_b$ , and  $C_m$  atoms. An empirical correlation has been found between the vibrational frequencies of the five modes listed in Figure 1.4b and the overall size of the porphyrin ring.<sup>78</sup> Hence, these modes are commonly called the porphyrin "core size" skeletal mode



**Figure 1.4** a) Structural Diagram of a  $D_{4h}$  metalloporphyrin. X and Y indicates positions for peripheral substitution. Pyrrole core carbons are assigned to a, b, and m positions to permit interpretation of Raman peaks. b) Compositions of porphyrin in-plane "skeletal" modes deemed important in  $S_1$  state studies within this thesis.

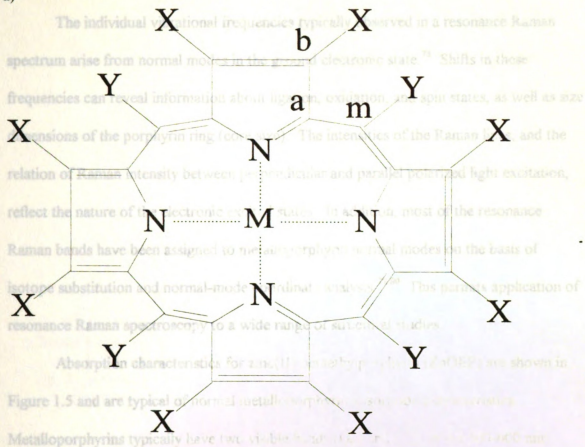
**Figure 1.4**





frequencies. Moreover, these porphyrin resonance Raman features are very dependent upon the absorption characteristics.

a)



b)

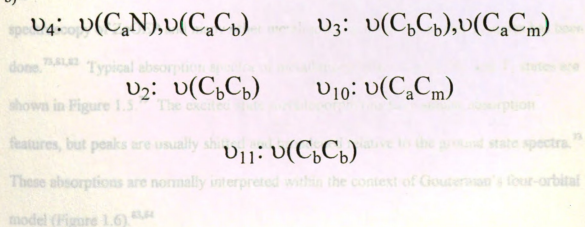


Figure 1.4

Gouterman assumed an idealized  $D_{4h}$  symmetry for the porphyrin ring, with excited electronic transitions from the two nearly degenerate  $a_{1g}$  and  $a_{2g}$  HOMO's into the

fre

up

sp

fre

dir

rel

re

Ra

isc

re

Fig

M

reg

sp

do

sh

fe

Th

mc

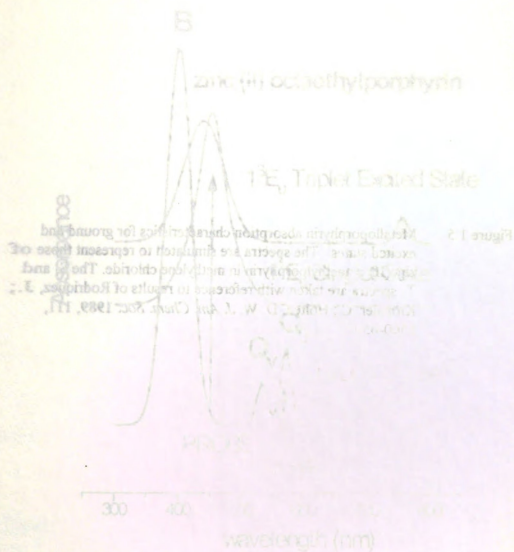
ele

frequencies. Moreover, these porphyrin resonance Raman features are very dependent upon the absorption characteristics.

The individual vibrational frequencies typically observed in a resonance Raman spectrum arise from normal modes in the ground electronic state.<sup>78</sup> Shifts in these frequencies can reveal information about ligation, oxidation, and spin states, as well as size dimensions of the porphyrin ring (core size). The intensities of the Raman lines, and the relation of Raman intensity between perpendicular and parallel polarized light excitation, reflect the nature of the electronic excited states. In addition, most of the resonance Raman bands have been assigned to metalloporphyrin normal modes on the basis of isotope substitution and normal-mode coordinate analysis.<sup>79,80</sup> This permits application of resonance Raman spectroscopy to a wide range of structural studies.

Absorption characteristics for zinc(II) octaethylporphyrin (ZnOEP) are shown in Figure 1.5 and are typical of normal metalloporphyrin absorption characteristics. Metalloporphyrins typically have two visible bands ( $Q_{0,0}$  and  $Q_{0,1}$ ) in the 500-600 nm region and have an intense band called the Soret near 400 nm. Transient absorption spectroscopy of ZnOEP and many other metalloporphyrins in the  $S_1$  and  $T_1$  states has been done.<sup>73,81,82</sup> Typical absorption spectra of metalloporphyrin in the  $S_0$ ,  $S_1$ , and  $T_1$  states are shown in Figure 1.5.<sup>73</sup> The excited state metalloporphyrins have similar absorption features, but peaks are usually shifted and broadened relative to the ground state spectra.<sup>73</sup> These absorptions are normally interpreted within the context of Gouterman's four-orbital model (Figure 1.6).<sup>83,84</sup>

Gouterman assumed an idealized  $D_{4h}$  symmetry for the porphyrin ring, with excited electronic transitions from the two nearly degenerate  $a_{1u}$  and  $a_{2u}$  HOMO 's into the



**Figure 1.5** Metalloporphyrin absorption characteristics for ground and excited states. The spectra are simulated to represent those of zinc(II) octaethylporphyrin in methylene chloride. The  $S_1$  and  $T_1$  spectra are taken with reference to results of Rodriquez, J.; Kirmaier, C.; Holten, D. W. *J. Am. Chem. Soc.* **1989**, 111, 6500-6501.



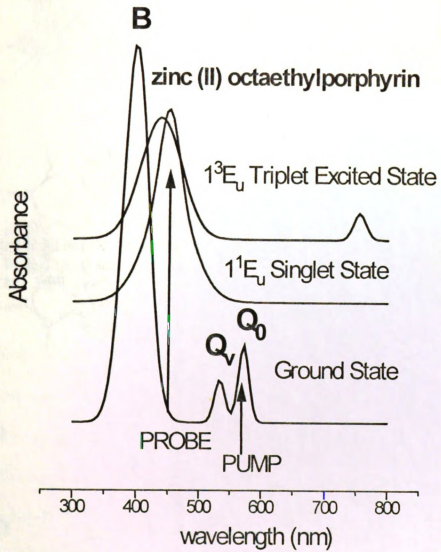


Figure 1.5



**Figure 1.6** Molecular orbital coefficients for the HOMO and LUMO orbitals involved in lower electronic state transitions (as calculated *ab initio* by Sekino, H.; Kobayashi, H. *J. Chem. Phys.* **1987**, 86(9), 5045-5052.

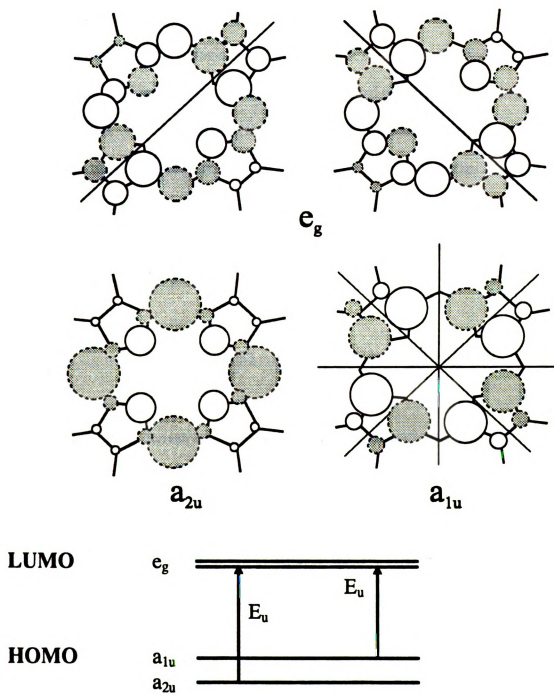


Figure 1.6

d

'(

tr

tr

b

s

+

c

s

v

l

s

s

s

s

s

s

s

s

s

s

s



degenerate  $e_g$  LUMO pair. The lowest singlet excited state configurations  $^1(a_{1u}, e_g)$  and  $^1(a_{2u}, e_g)$  are of the same  $E_u$  symmetry and have nearly the same energies. As a result, these transitions have strong electronic interactions and mix by configuration interaction. The transition dipole moments add up for the Soret band, and nearly cancel for the weaker  $Q_0$  band transition. Vibronic mixing of the B and  $Q_{0,0}$  produces the  $Q_{0,1}$  sideband. The symmetries of the vibrational modes that actively couple the  $E_u$  states are  $A_{1g} + A_{2g} + B_{1g} + B_{2g}$ . A coordinate operator with any one of these symmetries will be active in vibronic coupling, and is quantified by the derivative of the electric dipole moment for the excited state with respect to the normal coordinate:

$$\delta m_e / \delta Q = m_s \langle s | \delta H / \delta Q / e \rangle / h(\nu_s - \nu_e)$$

where  $\delta H / \delta Q$  is the derivative of the Hamiltonian with respect to the normal mode,  $h$  is Planck's constant,  $e$  and  $s$  are excited and mixing state wavefunctions,  $\nu_e$  is the excited state frequency,  $\nu_s$  and  $m_s$  are the frequency and electric dipole moment of the excited state, and  $\nu_s$  and  $m_s$  are the frequency and electric dipole moment of the mixing state.

The ground state Raman spectra of metalloporphyrins are explained by using the following formalism. Treating the substituent groups at the *meso* and  $\beta$  positions as point masses, the metalloporphyrin with  $N = 37$  atoms has 71 in-plane vibrations ( $2N-3$ ), 35 of which are Raman-active.<sup>85</sup>

$$\Gamma_{\text{in-plane}} = 9A_{1g} + 8A_{2g} + 9B_{1g} + 9B_{2g} + 18E_u$$

Likewise, there are 34 out-of-plane vibrations (N-3).<sup>85</sup>

$$\Gamma_{\text{out-of-plane}} = 3A_{1u} + 6A_{2u} + 5B_{1u} + 4B_{2u} + 8E_g$$

The resonance Raman frequencies below 1000 cm<sup>-1</sup> are dominated by the out-of-plane bending or ring deformation porphyrin modes, and modes involving the heavy-atom metal center. The resonance Raman bands in the 1000 to 1700 cm<sup>-1</sup> range are the in-plane stretching C-C and C-N modes and are sensitive to the inner porphyrin environment, responding according to Badger's rule.<sup>78,86</sup>

These modes are found to be affected by conditions such as the porphyrin core size and metal complex spin state, metal oxidation state, porphyrin ring oxidation and reduction, and  $\pi$  backbonding and doming effects. These modes are resonantly enhanced by  $\pi\pi^*$  electronic transitions.

Since most of the spectra that are presented in Chapter 3 and Chapter 4 were taken with Raman excitation wavelengths between 420 to 460 nm, consider the Raman spectrum of Zn(II) octaethylporphyrin in tetrahydrofuran (Figure 1.7). The porphyrin was excited at 413.1 nm with a krypton ion laser and illustrates effects of Soret enhancement upon porphyrin Raman spectra. The totally symmetric bands become relatively more enhanced when excited near the Soret. Specifically, the strongest band in resonance Raman spectra excited near resonance with the Soret is  $\nu_4$ , the C $\alpha$ -N stretching mode. This mode is often called the  $\pi$  electron density marker or oxidation state marker because its frequency is

**Figure 1.7** Raman spectrum of zinc(II) octaethylporphyrin in tetrahydrofuran. Taken with glass nmr tube in a backscattering apparatus at room temperature (1877 triple spectrometer, 1200 grooves/mm,  $\lambda = 413.1$  nm, 10 mW, exposure time 60 seconds). Solvent peaks are marked by an asterisk.

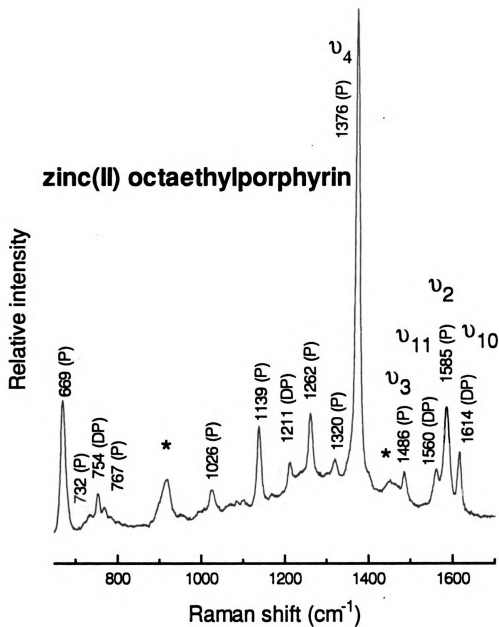


Figure 1.7

res

ox

sta

rel

Go

(su

po

th

th

ar

at

bo

re

sp

sp

hz

w

st

no

ar

ur

responsive to shifts with electron density changes.<sup>85</sup> The  $\nu_4$  frequency is dependent on the oxidation state of the central metal atom, and typically increases with increase in oxidation state for a given metal. Macrocycle cation and anion radicals show frequency shifts relative to neutral metalloporphyrins that agree with electron occupancy arguments using Gouterman's four orbital model (Figure 1.6).<sup>78b,86</sup> The HOMO for octaethylporphyrins (substitution at the  $\beta$  position) is the  $a_{1u}$  orbital from Figure 1.6, whereas *meso* substituted porphyrins, such as tetraphenylporphin, have  $a_{2u}$  as the HOMO.<sup>78b,88-90</sup> Similar effects on the Raman spectra are observed with  $\pi$  backbonding but this occurs when d electrons on the metal contribute to the  $\pi^*$  orbitals of the porphyrin ring.<sup>84</sup> Doming effects (ruffling) are smaller but occur when the pyrrole nitrogens follow out-of-plane motion of the central atom.<sup>84</sup> Changing the metal complex spin state from low-spin to high-spin lengthens the bond length to the metal, enlarging the core size and reducing the vibrational frequencies.

The aim of this work at the outset was to develop an appropriate picosecond time-resolved apparatus capable of monitoring excited electronic states using Raman spectroscopy. This introduction has shown that picosecond time-resolved Raman spectroscopy has worked well for other chemical and biological systems, and porphyrins have the optical characteristics that make them suitable for similar studies. The intention was to use this apparatus to characterize the vibrational and structural properties in  $S_1$  states of metalloporphyrins. Since vibrational characterization of model porphyrins had not been previously addressed, this was a necessary prerequisite to bacteriochlorophyll analysis. Once this characterization is complete, this experiment can be applied towards understanding of the primary charge separation step in bacterial reaction centers.



## LIST OF REFERENCES

- (1) Deisenhofer, J.; Norris, J. R. in *The Photosynthetic Reaction Center*; Academic Press, Inc.: California, 1993, Vol 1.
- (2) Okamura, M. Y.; Feher, G. *Annu. Rev. Biochem.* **1992**, 61, 861-896.
- (3) Breton, J.; Vermeglio, A. in *The Photosynthetic Bacterial Reaction Center: Structure and Dynamics*; Plenum: New York 1988.
- (4) Norris, J. R.; Schiffer, M. *Chem. Eng. News* **1990**, 68(31), 22-28.
- (5) Michel-Beyerle, M. E. in *Reaction Centers of Photosynthetic Bacteria*; Springer-Verlag: New York, 1990, Vol I.
- (6) Mitchell, P. *Nature* **1961**, 191, 144-48.
- (7) Feher, G.; Allen, J. P.; Okamura, M. Y.; Rees, D. C. *Nature* **1989**, 111-116.
- (8) Hamaguchi, H. and Gustafson, T. L. *Ann. Rev. Phys. Chem.* **1994**, 45, 593-622.
- (9) (a) Lutz, ; Robert, B., in *Biological Applications of Raman Spectroscopy*; Spiro, T. G., Ed.; John Wiley & Sons: New York, 1988, pp 347-413. (b) Rutherford, A. W.; Zimmerman, J.-L.; Boussac, A. in *The Photosystems: Structure, Function and Molecular Biology*; Barber, J., Ed.; Elsevier: Amsterdam, 1992, pp 125-158.
- (10) (a) Wilkström, M.; Krab, K.; Saraste, M. in *Cytochrome Oxidase-A Synthesis*; Academic Press: New York, 1981. (b) Babcock, G. T. in *Biological Applications of Raman Spectroscopy*; Spiro, T. G., Ed.; John Wiley & Sons: New York, 1988, pp 293-346.
- (11) (a) Rousseau, D. L.; Friedman, J. M. in *Biological Applications of Raman Spectroscopy*; Spiro, T. G., Ed.; John Wiley & Sons: New York, 1988, pp 133-217. (b) Cartling, B. in *Biological Applications of Raman Spectroscopy*; Spiro, T. G., Ed.; John Wiley & Sons: New York, 1988, pp 217-248. (c) Champion, P. M. in *Biological Applications of Raman Spectroscopy*; Spiro, T. G., Ed.; John Wiley & Sons: New York, 1988, pp 249-292.

- (12) (a) Harriman, A.; Porter, G.; Richoux, M.-C. *J. Chem. Soc. Faraday Trans 2* **1981**, 77, 833-844. (b) Kalyanasundaram, K.; Neumann-Spallart, M. *J. Phys. Chem.* **1982**, 86, 5163-5169. (c) Kay, A.; Grätzel, M. *J. Phys. Chem.* **1993**, 97, 6272-6277.
- (13) (a) Wasielewski, M. R. *Chem. Rev.* **1992**, 92, 435-461. (b) Wasielewski, M. R. in *The Photosynthetic Reaction Center*; Deisenhofer, J.; Norris, J. R., Eds.; Academic Press, Inc.: California, Vol II, 1993, pp 465-512. (c) Gust, D.; Moore, T. A. in *The Photosynthetic Reaction Center*; Deisenhofer, J.; Norris, J. R., Eds.; Academic Press, Inc.: California, Vol II, 1993, pp 387-418.
- (14) (a) Carter, F. L. in *Molecular Electronic Devices*; Dekker: New York, 1982, Vol I. (b) Hopfield, J. J.; Onuchic, J. N.; Beratan, D. N. *Science* **1988**, 241, 817-823. (c) Parthenopoulos, D. A.; Rentzepis, P. M. *ibid* **1989**, 245, 843. (d) O'Neil, M. P.; Niemczyk, M. P.; Svec, W. A.; Gosztola, D.; Gaines, G. L.; Wasielewski, M. R. *Science* **1992**, 257, 63-65.
- (15) (a) Jori, G. *Radiat. Phys. Chem.* **1987**, 30, 375. (b) Borland, C. F.; Mcgarvey, D. J.; Morgan, A. R.; Truscott, T. G. *J. Photochem. Photobiol. B: Biology* **1988**, 2, 427. (c) Schermann, G.; Völcker, A.; Seikel, K.; Schmidt, R.; Brauer, H.-D.; Montforts, F.-P. *Photochem. Photobiol.* **1990**, 51, 45-52. (d) Mironov, A. F.; Seylanov, J. A.; Pizhik, V. M.; Deruzhenko, I. V.; Ju Nockel, A. *J. Photochem. Photobiol. B: Biology* **1992**, 16, 341.
- (16) Deisenhofer, J.; Epp, O.; Miki, R.; Huber, R.; Michel, H. *Nature(London)* **1985**, 318, 618-624.
- (17) Feher, G.; Okamura, M. Y. in *The Photosynthetic Bacteria*; Plenum: New York, 1978.
- (18) Parson, W. W. in *Photosynthesis*; Elsevier: Amsterdam, 1987, pp 43-61.
- (19) Kasha, M. *Radiat. Research* **1963**, 20, 55-71.
- (20) (a) Gregory, A. R.; Henneker, W. H.; Siebrand, W.; Zgierski, M. Z. *J. Chem. Phys.* **1975**, 63(12), 5475-5489. (b) Netzel, T. L.; Kroger, P.; Chang, C. K.; Fujita, I.; Fajer, J. *Chem. Phys. Lett.* **1979**, 67, 223-228. (c) Lalonde, D. E.; Petke, J. D.; Maggiora, G. M. *J. Phys. Chem.* **1988**, 92(16) 4746-4752. (d) Hunter, C. A.; Sanders, J. K. M.; Stone, A. *J. Chem. Phys.* **1989**, 133, 395-404. (e) Won, Y.; Friesner, R. A.; Johnson, M. R.; Sessler, J. L. *Photosynth. Res.* **1989**, 22(3), 201-210. (f) Tran-Thi, T. H.; Lipskier, J. F.; Maillard, P.; Momenteau, M.; Lopez-Castillo, J.-M.; Jay-Gerin, J.-P. *J. Phys. Chem.* **1992**, 96, 1073-1082. (g) Helennius, V. M.; Hynninen, P. H.; Korppi-Tommola, J. E. I. *Proc. SPIE-Int. Soc. Opt. Eng.* **1993**, 1921(Laser Spectroscopy of Biomolecules), 86-93.

- (21) Marcus, R. A. *Chem. Phys. Lett.* **1987**, 133, 471-477.
- (22) Bixon, M.; Jortner, J.; Michel-Beyerle, M. E.; Ogrodnik, A.; Lersch, W. *Chem. Phys. Lett.* **1988**, 140, 626-630.
- (23) Fischer, S. F.; Scherer, P. O. *J. Chem. Phys.* **1987**, 115, 151-158.
- (24) Creighton, S.; Hwang, J. K.; Warshel, A.; Parson, W. W.; Norris, J. *Biochemistry* **1986**, 27, 774-781.
- (25) Schiffer, M., Norris, J. R. *The Photosynthetic Reaction Center*; Deisenhofer, J.; Norris, J. R., Eds.; Academic Press Inc.: New York, 1993; Vol 1, pp 1-10.
- (26) Rutherford, A. W. *Biochim. Biophys. Acta.* **1985**, 14, 15-17.
- (27) Debus, R. J.; *Biochim. Biophys. Acta.*, **1992**, 1102, 269-352.
- (28) Deisenhofer, J.; Epp, O.; Miki, K.; Huber, R.; Michel, H. *Nature (London)*, **1985**, 318, 618-624.
- (29) Youvan, D. C.; Bylina, E. J.; Alberti, M.; Begusch, H.; Hearst, J. E. *Cell*, **1984**, 37, 949-957.
- (30) Deisenhofer, J.; Epp, O.; Mrochaix, J. D.; Dron, M.; Rahire, M.; Malnoe, P. *Plant. Mol. Biol.* **1984**, 3, 363-370.
- (31) Michel, H.; Deisenhofer, J. *Biochemistry*, **1988**, 27, 1-7.
- (32) Seibert, M. in *The Photosynthetic Reaction Center*; Deisenhofer, J.; Norris, J. R., Eds.; Academic Press Inc.: New York, 1993; Vol 1, pp 319-347.
- (33) Nitschke, W.; Rutherford, A. W. *Trends Biochem. Sci.* **1991**, 16, 241-245.
- (34) Babcock, G. T.; Ghanotakis, D. F.; Ke, B.; Diner, B. A. *Biochim. Biophys. Acta.* **1983**, 723(2), 276-286.
- (35) Kleinfeld, K.; Okamura, M. Y.; Feher, G. *Biochemistry*, **1984**, 23, 5780-5786.
- (36) Kirmaier, C.; Holten, D. *Photosynth. Res.* **1987**, 13, 225-260.
- (37) Kreszowski, D. H.; Deinum, G.; Babcock, G. T. *Biophys. J.* **1994**, 66(2), a374.
- (38) Kreszowski, D. H.; Deinum, G.; Babcock, G. T. *J. Am. Chem. Soc.* **1994**, 116, 7463-7464.

(3)

(4)

(4)

(4)

(4)

(4)

(4)

(4)

- (39) Deinum, G.; Kreszowski, D. H.; Chang, C. K.; Babcock, G. T. *submitted to J. Am. Chem. Soc.*
- (40) (a) Reed, R. A.; Purrello, R.; Prendegast, K.; Spiro, T. G. *J. Phys. Chem.* **1991**, 95, 9720-9727. (b) Phillips, D. L.; Rodier, M.-J.; Myers, A. B. *Chem. Phys.* **1993**, 175, 1-12. (c) Rodgers, K. R.; Su, L.; Subramanian, S.; Spiro, T. G. *Biochemistry* **1993**, 32, 4547-4551. (d) Myers, A. B.; Philips, D. L.; Ci, X.; Westerfield, C.; Rodier, J.-M. *Proc. SPIE-Int Soc.* **1993**, pp 1-12.
- (41) (a) Gustafson, T. L.; Iwata, K.; Weaver, W. L. in *Ultrafast Phenomena VII*; Harris, C. B.; Ippen, E. P.; Mourou, G. A.; Zewail, A. H., Eds.; Springer-Verlag: New York, 1990 (b) Hayashi, H.; Kolaczowski, S. V.; Noguchi, T.; Blanchard, D.; Atkinson, G. H. *J. Am. Chem. Soc.* **1990**, 112, 4664-4670. (c) Noguchi, T.; Kolaczowski, S.; Gartner, W.; Atkinson, G. H. *J. Phys. Chem.* **1990**, 94, 4920-4926. (d) Hayashi, H.; Brack, T. L.; Noguchi, T.; Tasumi, M.; Atkinson, G. H. *J. Phys. Chem.* **1991**, 95, 6797-6802. (e) Noguchi, T.; Hayashi, H.; Tasumi, M.; Atkinson, G. H. *J. Phys. Chem.* **1991**, 95, 3167-3172. (f) Iwata, K.; Hamaguchi, H. *Chem. Phys. Lett.* **1992**, 196, 462-468.
- (42) (a) Findsen, E. W.; Shelnut, J. A.; Ondrias, M. R., *J. Phys. Chem.* **1988**, 92, 307-314. (b) Apanasevich, P. A.; Kruglik, S. G.; Kvach, V. V.; Orlovich, V. A. in *Time Resolved Vibrational Spectroscopy V*; Takahashi, H., Ed.; Springer-Verlag: Berlin, 1992. (c) Courtney, S. H.; Jedju, T. M.; Friedman, J. M.; Alden, R. G.; Ondrias, M. R. *Chem. Phys. Lett.* **1989**, 164(1), 39-43. (d) Alden, R. G.; Sparks, L. D.; Ondrias, M. R.; Crawford, B. A.; Shelnut, J. A. *J. Phys. Chem.* **1990**, 94, 1440-1443.
- (43) (a) Turner, J.; Spiro, T. G.; Nagumo, M.; Nicol, M.; El-Sayed, M. A. *J. Am. Chem. Soc.* **1980**, 102, 3238-3239. (b) Turner, J.; Strong, J. D.; Spiro, T. G.; Nagumo, M.; El-Sayed, M. A. *Proc. Natl. Acad. Sci.* **1981**, 78, 1313-1317. (c) Nagumo, M.; Nicol, M.; El-Sayed, M. A. *J. Phys. Chem.* **1981**, 85, 2435-2438. (d) Hsieh, C.-L.; Nagumo, M.; Nicol, M.; El-Sayed, M. A. *J. Phys. Chem.* **1981**, 85, 2714-2717. (e) Hsieh, C.-L.; El-Sayed, M. A.; Nicol, M.; Nagumo, M.; Lee, J. H. *Photochem. Photobiol.* **1983**, 38, 83-94. (f) El-Sayed, M. A. *Pure Appl. Chem.* **1985**, 57, 187-193.
- (44) (a) Reid, R. J.; Doig, S. J.; Wickham, S. D.; Mathies, R. A. *J. Am. Chem. Soc.* **1993**, 115, 4754-4763. (b) Reid, P. J.; Lawless, M. K.; Wickham, S. D.; Mathies, R. A. *J. Phys. Chem.* **1994**, 98, 5597-5606.
- (45) Weaver, W. L.; Huston, L. A.; Iwata, K.; Gustafson, T. L.; *J. Phys. Chem.* **1992**, 96, 8956-8961.
- (46) Butler, R. M.; Lynn, M. A.; Gustafson, T. L. *J. Phys. Chem.* **1993**, 97, 2609-2617.

- (47) Ishibashi, T.; Hamaguchi, H. *J. Spectrosc. Soc. Jpn.* **1990**, 40, 222-226.
- (48) Hamaguchi, H.; Iwata, K. *Chem. Phys. Lett.* **1993**, 208, 465-470.
- (49) Gustafson, T. L.; Roberts, D. M.; Chernoff, D. A. *J. Chem. Phys.* **1983**, 79, 1559-1564.
- (50) Hamaguchi, H.; Kato, C.; Tasumi, M. *Chem. Phys. Lett.* **1983**, 100, 3-7.
- (51) Iwata, K.; Yamaguchi, S.; Hamaguchi, H. *Rev. Sci. Instrum.* **1993**, 64, 2140-2146.
- (52) Kato, C.; Hamaguchi, H.; Tasumi, M. *Chem. Phys. Lett.* **1985**, 120, 183-187.
- (53) Reid, P. J.; Doig, S. J.; Mathies, R. A. *J. Phys. Chem.* **1990**, 94, 8396-8399.
- (54) Reid, P. J.; Doig, S. J.; Mathies, R. A. *Chem. Phys. Lett.* **1989**, 156, 163-168.
- (55) Reid, P. J.; Wickham, S. D.; Mathies, R. A. *J. Phys. Chem.* **1992**, 96, 5720-5724.
- (56) Reid, P. J.; Shreve, A. P.; Mathies, R. A. *J. Phys. Chem.* **1993**, 97, 12691-12699.
- (57) Reid, P. J.; Doig, S. J.; Wickham, S. D.; Mathies, R. A. *J. Am. Chem. Soc.* **1993**, 115, 4753-4763.
- (58) Woodward, R. B.; Hoffmann, R. in *The Conservation of Orbital Symmetry*; Verlag Chemie International: Weinheim, 1981, 3rd edition.
- (59) (a) Goldfarb, T. D.; Linquist, L. *J. Am. Chem. Soc.* **1967**, 89, 4588. (b) Datta, P.; Goldfarb, T. D.; Boikess, R. S. *J. Am. Chem. Soc.* **1969**, 91, 5429.
- (60) Hashimoto, H.; Koyama, Y.; Hirata, Y.; Mataga, N. *J. Phys. Chem.* **1991**, 95, 3072-3076.
- (61) Kuki, M.; Hashimoto, H.; Koyama, Y. *Chem. Phys. Lett.* **1990**, 165, 417-422.
- (62) Hayashi, H.; Noguchi, T.; Tasumi, M.; Atkinson, G. H. *Biophys. J.* **1991**, 60, 252-260.
- (63) Hayashi, H.; Tasumi, M.; Atkinson, G. H. *Chem. Phys. Lett.* **1991**, 178, 388-392.
- (64) Birge, R. R. *Annu. Rev. Biophys. Bioenerg.* **1981**, 10, 315.
- (65) Smith, S. O.; Lugtenburg, J.; Mathies, R. A. *J. Membrane Biol.* **1985**, 85, 95.
- (66) Stockenheis, W.; Bogomolni, R. A. *Annu. Rev. Biochem.* **1982**, 51, 587.



(67)

(68)

(69)

(70)

(71)

(72)

(73)

(74)

(75)

(76)

(77)

- (67) Mathies, R. A.; Lin, S. W.; Ames, J. B.; Pollard, W. T. *Annu. Rev. Biophys. Chem.* **1991**, 20, 491-518.
- (68) Atkinson, G. H.; Brack, T. L.; Blanchard, D.; Rumbles, G. *Chem. Phys.* **1989**, 131, 1-15.
- (69) (a) Smith, S. O.; Pardo, J. A.; Lugtenberg, J.; Mathies, R. A. *J. Phys. Chem.* **1987**, 91, 804-819. (b) Mathies, R. A.; Brito-Cruz, C. H.; Pollard, T. W.; Shank, C. V. *Science* **1988**, 240, 777-779. (c) Doig, S. J.; Reid, P. J.; Mathies, R. A. *J. Phys. Chem.* **1991**, 95, 6372-6379.
- (70) Findsen, E. W.; Scott, T. W.; Chance, M. R.; Friedman, J. M.; Ondrias, M. R. *J. Am. Chem. Soc.* **1985**, 107, 3355-3357.
- (71) Dasgupta, S.; Spiro, T. G.; Johnson, C. K.; Dalickas, G. A.; Hochstrasser, R. M. *Biochemistry* **1985**, 24, 5295-5297.
- (72) Rousseau, D. L.; Argade, P. V. *Proc. Natl. Acad. Sci. USA* **1986**, 83, 1310-1314.
- (73) Rodriguez, J.; Kirmaier, C.; Holten, D. W. *J. Am. Chem. Soc.* **1989**, 111, 6500-6501.
- (74) Lingle, R. J.; Xu, X.; Zhu, H.; Yu, S. C.; Hopkins, J. B.; Straub, K. D. *J. Am. Chem. Soc.* **1991**, 113, 3992-3994.
- (75) Lingle, R. J.; Xu, X.; Zhu, H.; Yu, S. C.; Hopkins, J. B. *J. Phys. Chem.* **1991**, 95, 9320-9331.
- (76) Petrich, J. W.; Martin, J. L.; Houde, D.; Poyart, C.; Orszag, A. *Biochemistry* **1987**, 26, 7914.
- (77) (a) Walters, V. A.; de Paula, J. C.; Babcock, G. T.; Leroi, G. E. *J. Am. Chem. Soc.* **1989**, 111, 8300-8302. (b) Nam, H. H.; Walters, V. A.; de Paula, J. C.; Babcock, G. T.; Leroi, G. E. In *Proceedings of the XIIIth International Conference on Raman Spectroscopy*; Durig, J.R.; Sullivan, J.F., Eds.; Wiley and Sons: New York, 1990, p 618. (c) Reed, R. A.; Purello, R.; Prendegast, K.; Spiro, T. G. *J. Phys. Chem.* **1991**, 95, 9720-9727. (d) Sato, S.; Asano-Someda, M.; Kitagawa, T. *Chem. Phys. Lett.* **1992**, 189, 443-447. (e) Kumble, R.; Hu, S.; Loppnow, G. R.; Vitols, S. E.; Spiro, T. G. *J. Phys. Chem.* **1993**, 97, 10521-10523. (f) Kreszowski, D. H.; Babcock, G. T. *Biophys. J.* **1993**, 64, a276. (g) Bell, S. E. J.; Al-Obaidi, A. H. R.; Hegarty, M.; Hester, R. E.; McGarvey, J. J. *J. Phys. Chem.* **1993**, 97, 11599-11602.

- (78) (a) Sarma, Y. A. *Spectrochimica Acta*. **1989**, 45a(6), 649-652. (b) Oertling, W. A.; Salehi, A.; Chang, C. K.; Babcock, G. T. *J. Phys. Chem.* **1989**, 93, 1311-1319.
- (79) Procyk, A. D.; Bocian, D. F. *Annu. Rev. Phys. Chem.* **1992**, 43, 465-496.
- (80) (a) Abe, M.; Kitagawa, T.; Kyogoku, Y. *J. Chem. Phys.* **1978**, 69, 4526-4534. (b) Li, X.-Y.; Czernuszewicz, R. S.; Kincaid, J. R.; Stein, P.; Spiro, T. G. *J. Phys. Chem.* **1990**, 94, 47-61.
- (81) (a) Tait, C. D.; Holten, D.; Barley, M.; Dolphin, D. D.; James, B. R. *J. Am. Chem. Soc.* **1985**, 107(7), 1930-1934. (b) Apanasevich, P. A.; Chirvonyi, V. S.; Kruglik, S. G.; Kvach, V. V.; Orlovich, V. A. *Proc. SPIE-Int. Soc. Opt. Eng.* **1991**, 1403(Laser Appl. Life Sci., Pt. 1) pp 195-211. (c) Apanasevich, P. A.; Chirvonyi, V. S.; Kruglik, S. G.; Kvach, V. V.; Orlovich, V. A. *Proc. SPIE-Int. Soc. Opt. Eng.* **1991**, 1403(Laser Appl. Life Sci., Pt. 1) pp 240-242. (d) Loppnow, G. R.; Melamed, D.; Leheny, A. R.; Hamilton, A. D.; Spiro, T. G. *J. Phys. Chem.* **1993**, 97(35), 8969-8975. (e) Gentemann, S.; Abaneze, J.; Garcia-Ferrer, R.; Knapp, S.; Potzena, J. A.; Schugar, H. J.; Holten, D. *J. Am. Chem. Soc.* **1994**, 116(1), 281-289.
- (82) Irvine, M. P.; Harrison, R. J.; Strahand, M. A.; Beddard, G. S. *Ber. Bunsenges. Phys. Chem.* **1985**, 89, 226-232.
- (83) Gouterman, M. *J. Mol. Spectroscopy* **1961**, 6, 138-163.
- (84) Sekino, H.; Kobayashi, H. *J. Chem. Phys.* **1987**, 86(9), 5045-5052.
- (85) Spiro, T. G.; Czernuszewicz, R. S.; Li, X.-Y. *Coord. Chem. Rev.* **1990**, 100, 541-571.
- (86) (a) Spaulding, L. D.; Chang, C. C.; Yu, N.-T.; Felton, R. H. *J. Am. Chem. Soc.* **1975**, 97, 2517-2524. (b) Choi, S.; Spiro, T. G.; Langry, K. C.; Smith, K. M. *J. Am. Chem. Soc.* **1982**, 104, 4337-4344. (c) Choi, S.; Spiro, T. G.; Langry, K. C.; Smith, K. M.; Budd, L. D.; Lamar, G. N. *J. Am. Chem. Soc.* **1982**, 104, 4345-4353.
- (87) (a) Czernuszewicz, R. S.; Macor, K. A.; Li, X.-Y.; Kincaid, J. R.; Spiro, T. G. *J. Am. Chem. Soc.* **1989**, 111, 3860-3869. (b) Perng, J.-H.; Bocian, D. F. *J. Phys. Chem.* **1992**, 96, 4804-4811.
- (88) (a) Salehi, A.; Oertling, W. A.; Babcock, G. T.; Chang, C. K. *J. Am. Chem. Soc.* **1986**, 108, 5630-5631. (b) Oertling, W. A.; Salehi, A.; Chung, Y.-C.; Leroi, G. E.; Chang, C. K.; Babcock, G. T. *J. Phys. Chem.* **1987**, 91, 5887-5898. (c) Salehi, A.; Oertling, W. A.; Babcock, G. T.; Chang, C. K. *Inorg. Chem.* **1987**, 26, 4296-4298.

- (89) (a) Donohoe, R. J.; Duchowski, J. K.; Bocian, D. F. *J. Am. Chem. Soc.* **1988**, 110, 6119-6124 (b) Czernuszewicz, R. S.; Macor, K. A.; Li, X.-Y.; Kincaid, J. R.; Spiro, T. G. *J. Am. Chem. Soc.* **1989**, 111, 3860-3869. (c) Macor, K. A.; Czernuszewicz, R. S.; Spiro, T. G. *Inorg. Chem.* **1990**, 29, 1996-2000. (d) Duchowski, J. K.; Bocian, D. F. *J. Am. Chem. Soc.* **1990**, 112, 3312-3318. (e) Perng, J.-H.; Duchowski, J. K.; Bocian, D. F. *J. Phys. Chem.* **1990**, 94, 6684-6691. (f) Duchowski, J. K.; Bocian, D. F. *Inorg. Chem.* **1990**, 29, 4158-4160. (g) Duchowski, J. K.; Bocian, D. F. *J. Am. Chem. Soc.* **1990**, 112, 8807-8811.
- (90) (a) Gurinovich, G. P.; Gurinovich, I. F.; Ksenofontova, N. M.; Terekhov, S. N. *J. Appl. Spectrosc.* **1985**, 43, 758-763. (b) Teraoka, J.; Hashimoto, S.; Sugimoto, H.; Mori, M.; Kitagawa, T. *J. Am. Chem. Soc.* **1987**, 109, 180-184. (c) Donohoe, R. J.; Atamian, M.; Bocian, D. F. *J. Am. Chem. Soc.* **1987**, 109, 5593-5599. (d) Gurinovich, G. P.; Gurinovich, I. F.; Ivashin, N. V.; Sinyakov, G. N.; Shulga, A. M. *J. Mol. Struct.* **1988**, 172, 317-343. (e) Atamian, M.; Donohoe, R. J.; Lindsey, J. S.; Bocian, D. F. *J. Phys. Chem.* **1989**, 93, 2236-2243. (f) Reed, R. A. Purrello, R.; Prendergast, K.; Spiro, T. G. *J. Phys. Chem.* **1991**, 95, 9720-9727.

## CHAPTER 2

### INSTRUMENTATION

#### ABSTRACT

Time-resolved resonance Raman techniques applied to electronically excited porphyrins has thus far been limited mostly to time-resolution in the nanosecond range, and, correspondingly, the techniques that have been used typically involve low repetition rate pulsed lasers. The research project described here extends time-resolved resonance Raman to the picosecond regime, and opens up the ability to probe more dynamic processes, such as vibrational relaxation in electronically excited molecules. This project involved taking advantage of the high repetition rate characteristics of picosecond lasers described in the experimental apparatus section. A rapidly flowing glass free jet cell similar to that developed by Atkinson *et. al.* (Atkinson, G. H.; Brack, T. L.; Blanchard, D.; Rumbles, G. *Chem. Phys.* **1989**, 131, 1-15) was used in conjunction with a microscope objective to refresh the sample between individual flashes in a series of laser pulses. Implementation of a “quasi-simultaneous” technique analogous in purpose to that of Sato *et. al.* (Sato, S.-I.; Kamogawa, K.; Aoyagi, K.; Kitagawa, K. *J. Phys. Chem.* **1992**, 96, 10676-10681) was useful in dealing with the difference spectra associated with time-resolved techniques. Spectrum Basic programs were written to process the data accumulated through this technique.

## **I. EXPERIMENTAL APPARATUS**

The experimental apparatus used for picosecond transient experiments is shown schematically in Figure 2.1. An actively mode-locked Q-switched Coherent 76-s Nd:YAG laser with built-in second harmonic frequency-mixing capabilities uses a standard KTP crystal to generate 70 psec full-width-half-maximum, 76.5 MHz, 532 nm second harmonic pulses. The output is directed through a Coherent third harmonic generator by using a BBO crystal that mixes 1064 nm and 532 nm wavelengths to generate 355 nm. The 532 nm and 355 nm pulses are directed into two identical Coherent 702 tunable pulse dye lasers with variable tuning ranges dependent upon dye selection. Photoacoustically driven cavity dumpers on the 702 dye lasers are enabled by Coherent 7200 cavity dumper drivers that permit selection of variable pulse repetition rates (38.25 MHz divisible by any integer between 4 and 259). One Coherent 702 dye laser initially used rhodamine 6G (R6G) dissolved in ethylene glycol and permitted a tuning range of 570-630 nm. Recent characterization of pyrromethene laser dyes for ultrafast pulse generation suggests exceptionally efficient power generation.<sup>1</sup> For this reason, in later experiments we implemented pyrromethene 567, which was dissolved in propyl phenyl ether (PPH), and has a tuning range of 550-600 nm. The other 702 dye laser used stilbene 420 dissolved in ethylene glycol with tunability from 420-470 nm. All dyes and the PPH were purchased from Exciton Corporation (P.O. Box 3126 Overlook Station, Dayton, Ohio 45431). Figure 2.2 displays relative efficiencies as a function of emission wavelength for the dyes used in our time-resolved experiments. R6G and pyrromethene 567 were pumped with ~2 W of 532 nm, while the stilbene 420 was synchronously pumped with ~1 W of 355 nm.



**Figure 2.1**      **Instrumentation used for time-resolved picosecond Raman experiment SHG: second harmonic generator using KTP crystal; THG: third harmonic generator using BBO crystal; Shutter driver: homebuilt device to control mechanical shutters; PI/CCD: princeton instruments charge coupled device detector; OPTICS: a collimating lens (focus length = 2.5 inch, diameter = 2 inch), and a focusing lens ( focus length = 12 inch, diameter = 2 inch).**

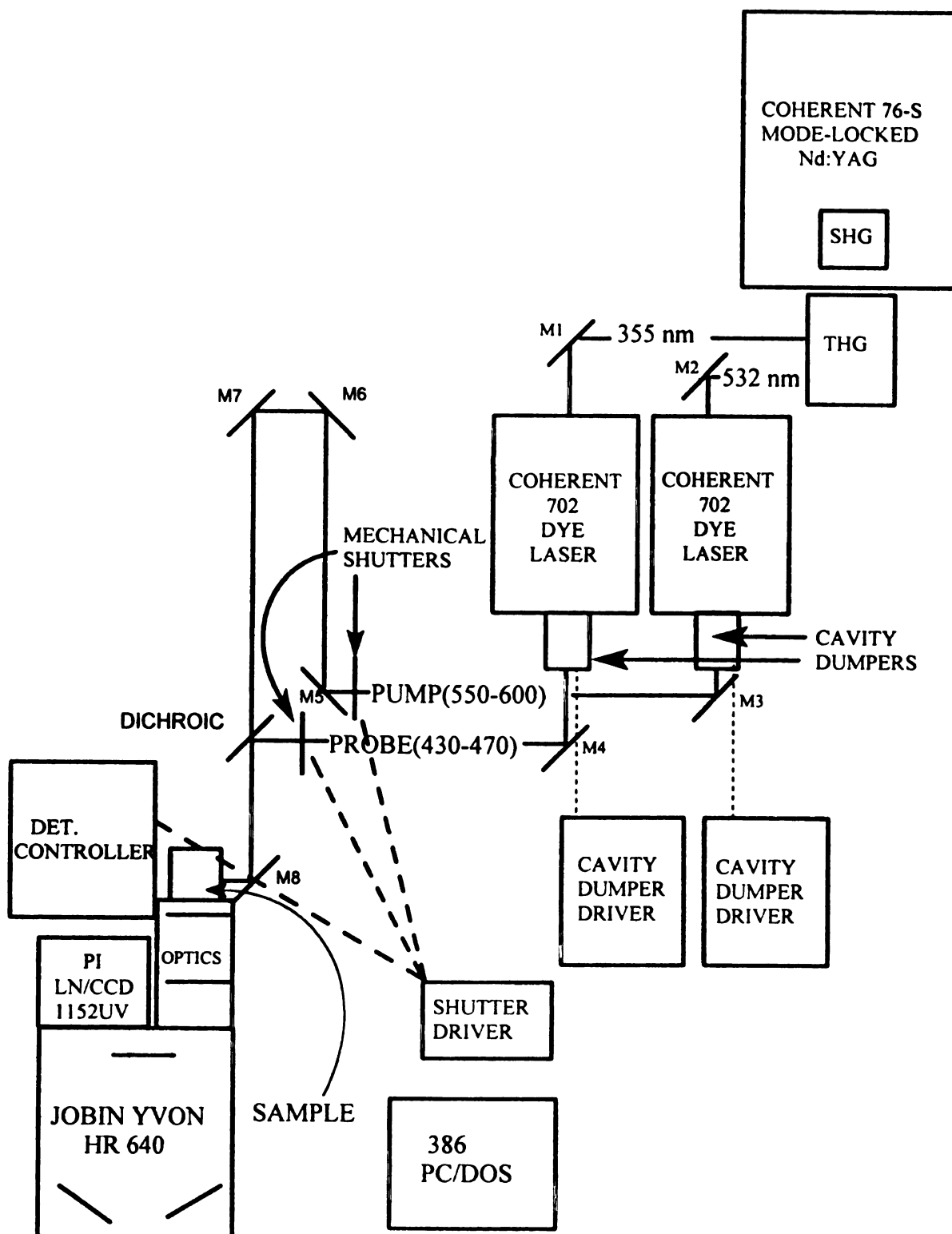


Figure 2.1

**Figure 2.2** Laser dye efficiency curves for a) stilbene 420 in ethylene glycol b) pyrromethene 567 in propyl phenyl ether (PPH), and c) rhodamine 6G in ethylene glycol. Data were collected by delivering 1 W 355 nm and 2 W 532 nm pulses from a Coherent 76-s Antares laser to a pair of Coherent 702 dye lasers with the cavity dumper drivers operated at 3.825 MHz .

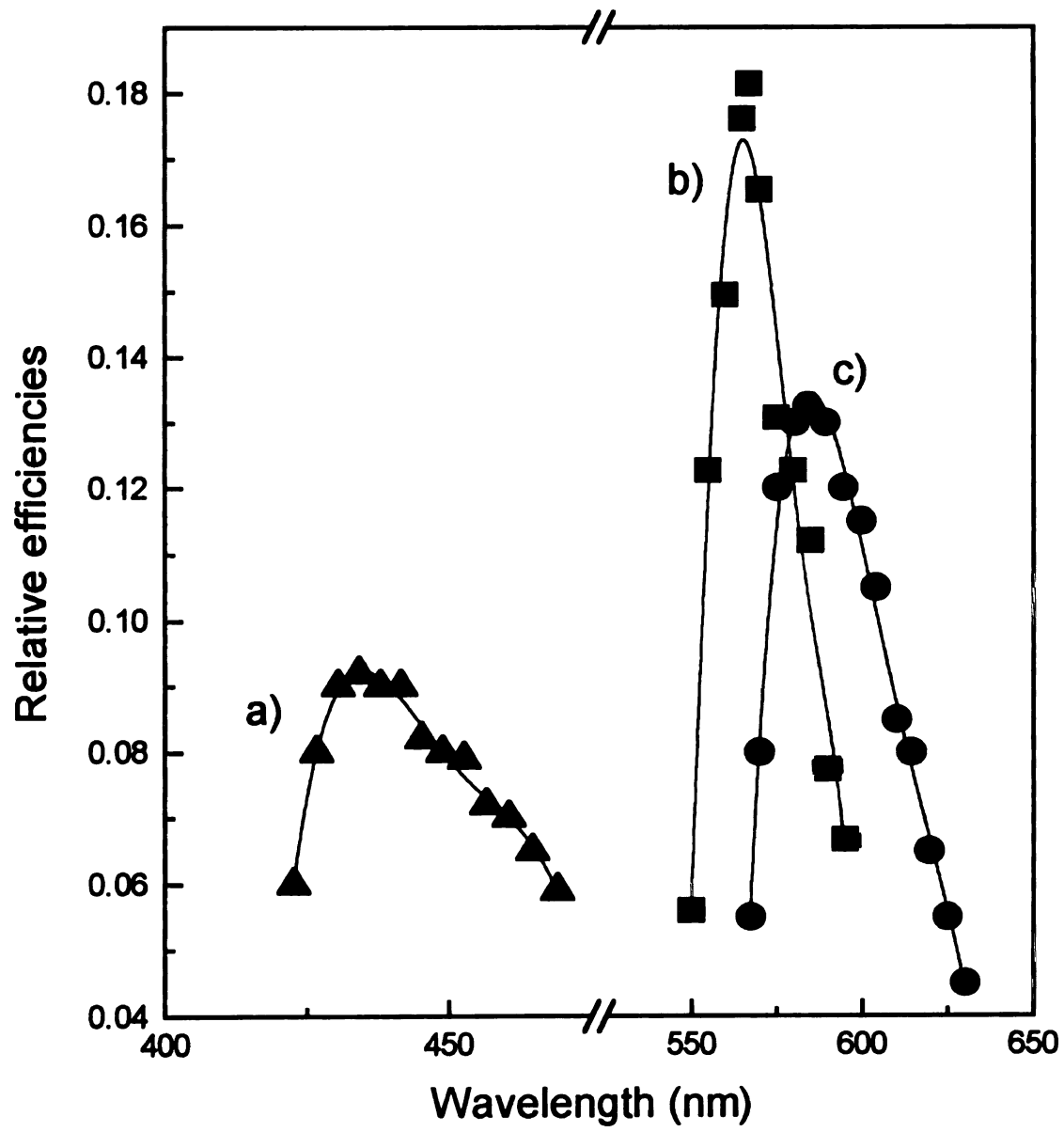


Figure 2.2

The relative efficiency is defined as dye laser output power (mW) divided by pumping power (mW). Readings were taken with a Coherent 210 power meter. It should be noted that dye laser companies normally specify dye efficiencies for continuous wave lasers, whereas these efficiencies were taken at 3.825 MHz and thus appear comparatively lower. Brief comparisons with the dye lasers set in continuous wave mode agreed with documented laser efficiencies. The “red” pulses generated from either R6G or pyromethene 567 act as the pump beam in promoting molecules into electronic excited states. The “blue” pulses from the stilbene 420 were used as the probe beam and take Stokes Raman spectra of the resultant excited state. The pulse energy dependence upon cavity dumper repetition rate for the 702 dye lasers is shown in Figure 2.3, where pulse energy (in nJ) reaches a maximum and then plateaus around 1.27 MHz.

Two identical Inrad model 5-14B autocorrelators, (purchased from Coherent), monitor the pulse shape coming out of the dye lasers with cross-correlation full-width-half-maximum of 7 psec. The cross-correlation shape has the general appearance of a gaussian profile.

The two beams were spatially overlapped at a dichroic filter (yellow subtractive, 520FD22-50S, 1.0 mm thickness) and directed into the sample compartment. The dichroic filter was purchased from the Andover Corporation (4 Commercial Drive, Salem, New Hampshire 03079), and its spectral characteristics are shown in Figure 2.4. The temporal delay between the pump and probe beams can be controlled both electronically through the cavity dumper drivers, and spatially through an optical delay line. The relative temporal position of pump and probe beams can be altered in 26.4 or 13.2 ns steps using electronic delay switches on either 7200 Coherent cavity dumper driver. Finer delays can

**Figure 2.3** Pulse energies from Coherent 702 dye lasers as a function of repetition rate for a) pyrromethene 567 in propyl phenyl ether b) rhodamine 6G in ethylene glycol and c) stilbene 420 in ethylene glycol. The pulse energy dependence was done at the efficiency curve maxima of each dye, with 2 W 532 nm and 1 W 355 nm pump pulses. The actual repetition rate equals 38.25 MHz/Repetition divisor.



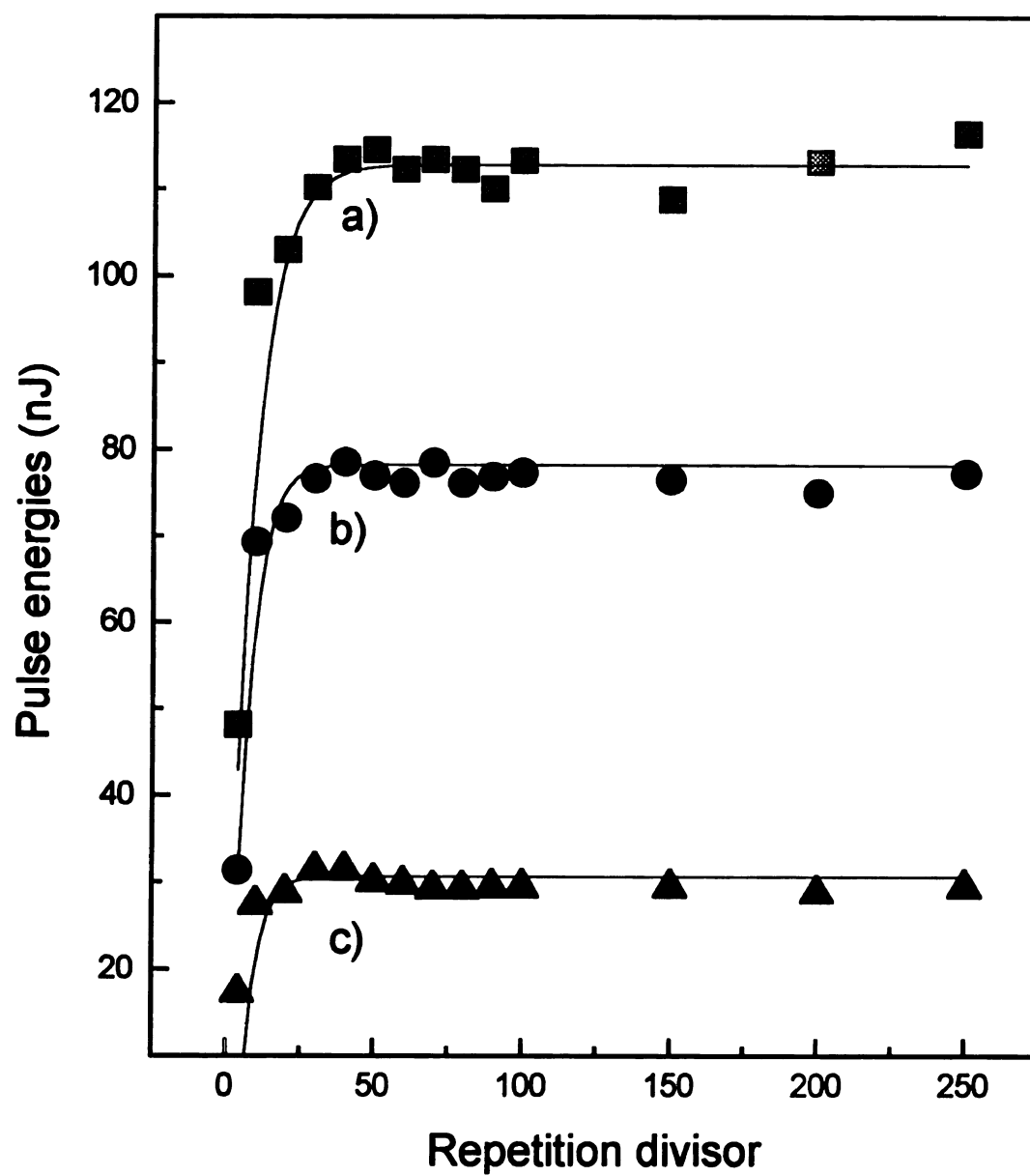


Figure 2.3

**Figure 2.4** Spectral response curves for optical filters 520DFD22-50S and 505FD64-50S. The responsivity of the 520FD22-50S is shown at incident beam angles of  $0^\circ$  and  $45^\circ$  to display the angle dependence of transmission.

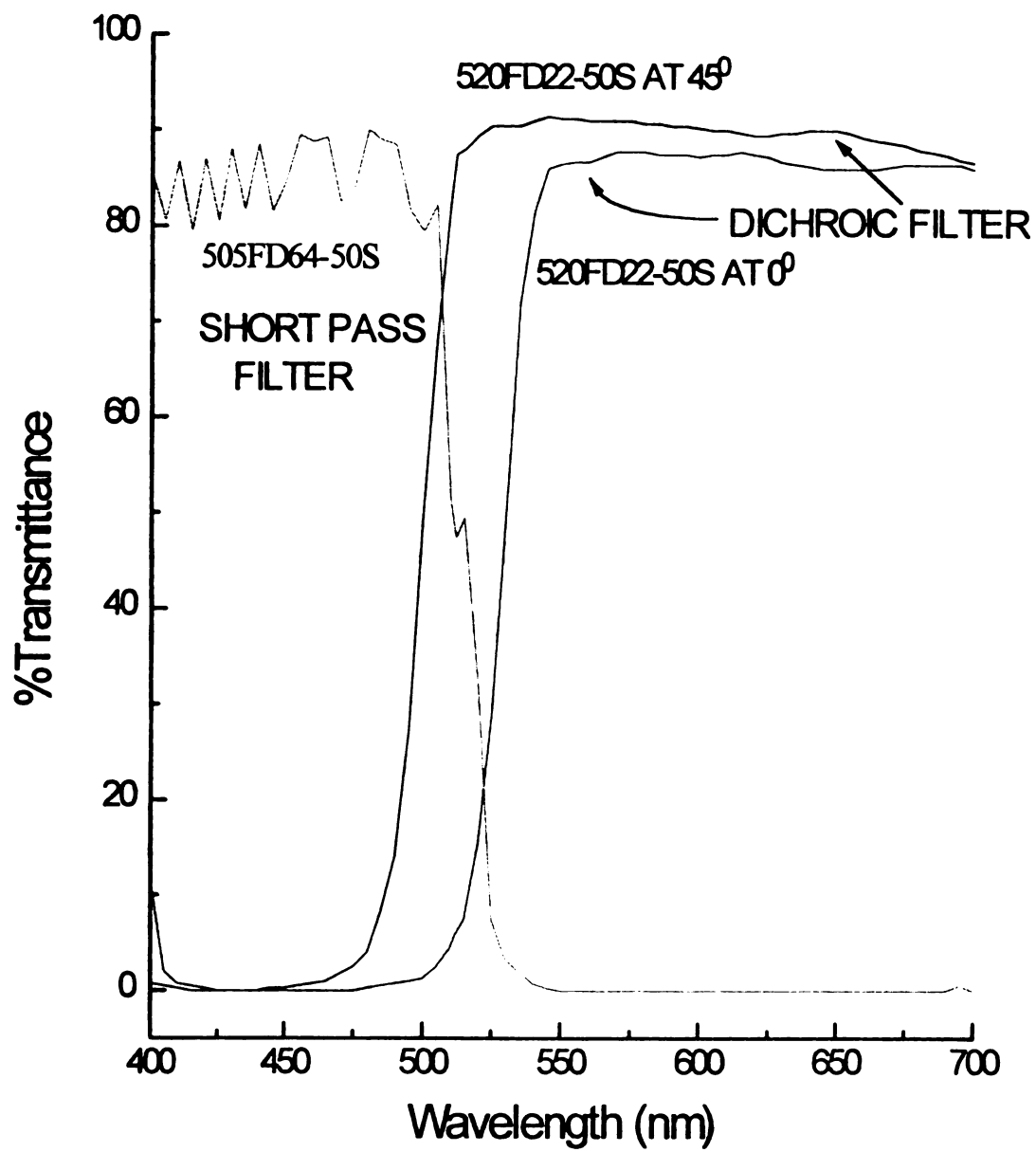


Figure 2.4

be

Ki

Cit

fas

we

ave

a te

tran

exc

pul

gro

and

iod

nm

Fig

tigh

bea

was

is st

deia

by th

be achieved through directing the pump beam down an optical delay line controlled by a Klinger CC1.1 programmable motor-driven translation stage (Klinger Scientific, Garden City, New York 11530). The time delay was monitored by sending the two beams into a fast Hewlett-Packard 4220 photodiode detector with a rise time  $<1$  nsec. The two pulses were distinguished on a Tektronix DSA 602A Digitizing Signal Analyzer scope with averaging and difference detection capabilities, and real time accumulation up to 1 GHz.

When finer time resolution near zero-time overlap was desired, it was obtained by a technique we loosely term “zero-time measurements”. Essentially, we use a simplified transient absorption experiment in which we pump a molecule into an electronically excited state with a “red” pulse, and monitor the intensity of the “blue” pulse. This blue pulse is absorbed by the time-dependent electronic excited state but not by the electronic ground state. Initially, the experimental apparatus used was that described in Figure 2.5, and DODC iodide was used as a reference sample (purchased from Exciton). DODC iodide is a commonly used laser dye that has strong ground state optical absorption at 580 nm and broadband excited state absorption around 450 nm, similar to the simulated plot in Figure 2.6. Its excited state lifetime is  $\sim 2$  nsec.<sup>2</sup> The two spatially overlapped beams are tightly focused onto the sample, the pump beam intensity is filtered out, and the probe beam intensity is directed into the Hewlett-Packard 4220 photodiode. The short pass filter was purchased from Andover (505FD64-50S, blue dichroic), and its spectral dependence is shown in Figure 2.4. The probe pulse intensity can be monitored as a function of pump delay on the optical delay line. A sudden decrease in probe intensity indicated absorption by the excited state and zero-time overlap. In later experiments, we monitored zinc(II)

**Figure 2.5** Experimental setup initially used in determining zero-time overlap through a modified transient absorption experiment.



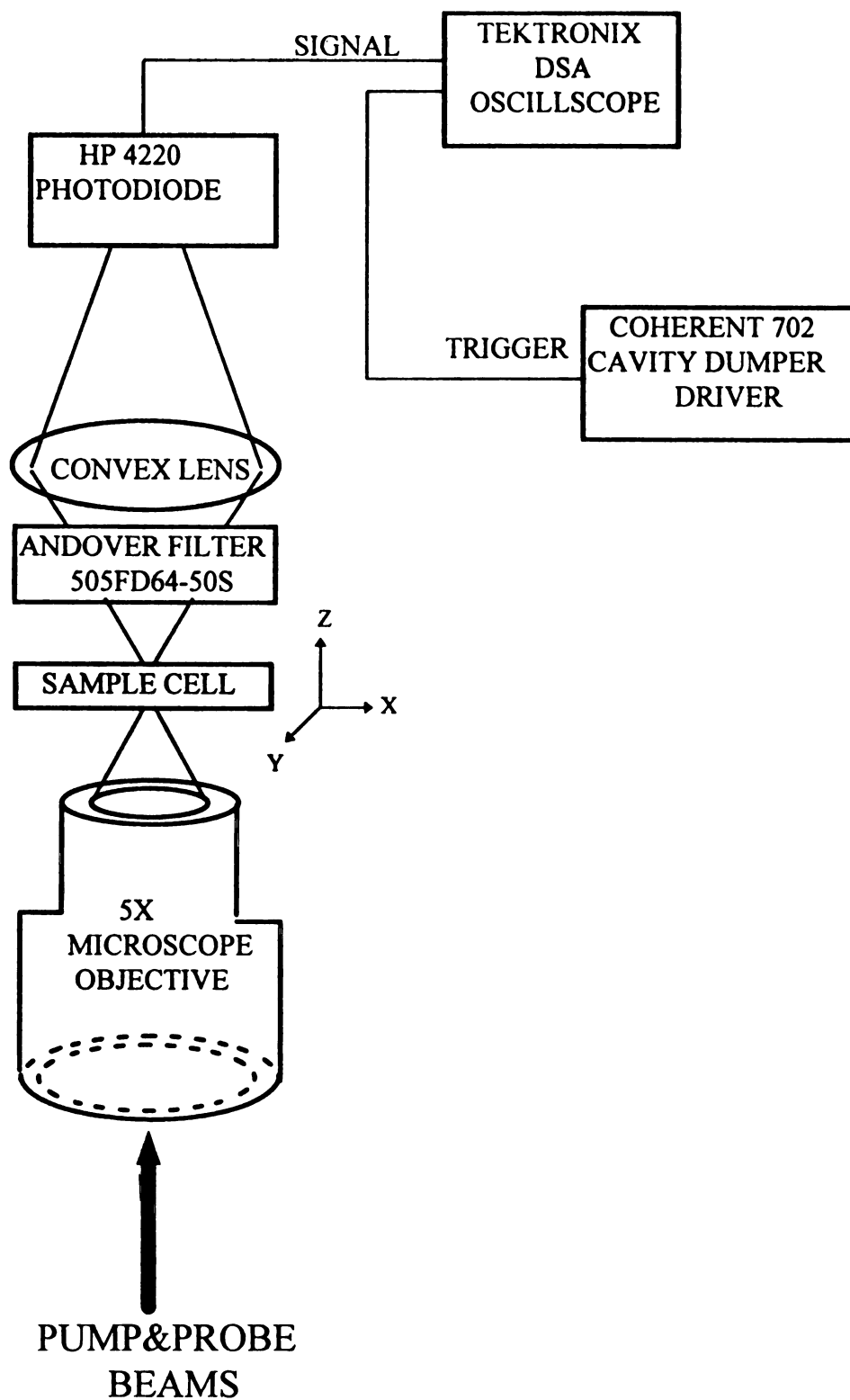
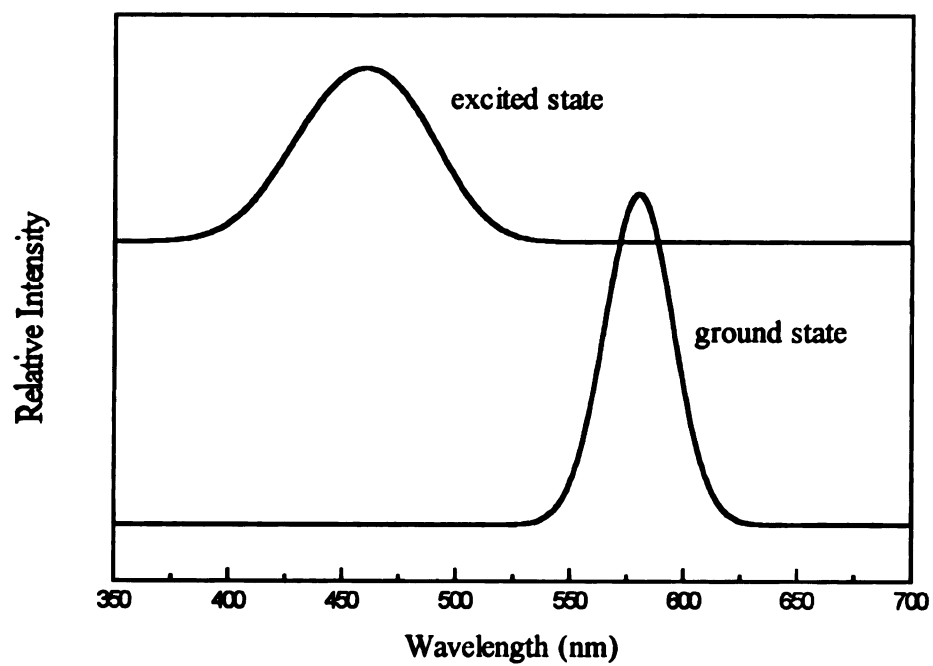


Figure 2.5

**Figure 2.6** DODC iodide transient absorption. a) Simulated absorption spectra representing optical behavior of DODC iodide.  
b) Time-averaged voltage pulse of “blue” laser showing intensity decrease when in temporal overlap with “red” pulses (as seen on Tektronix DSA 602 oscilloscope).

a)



b)

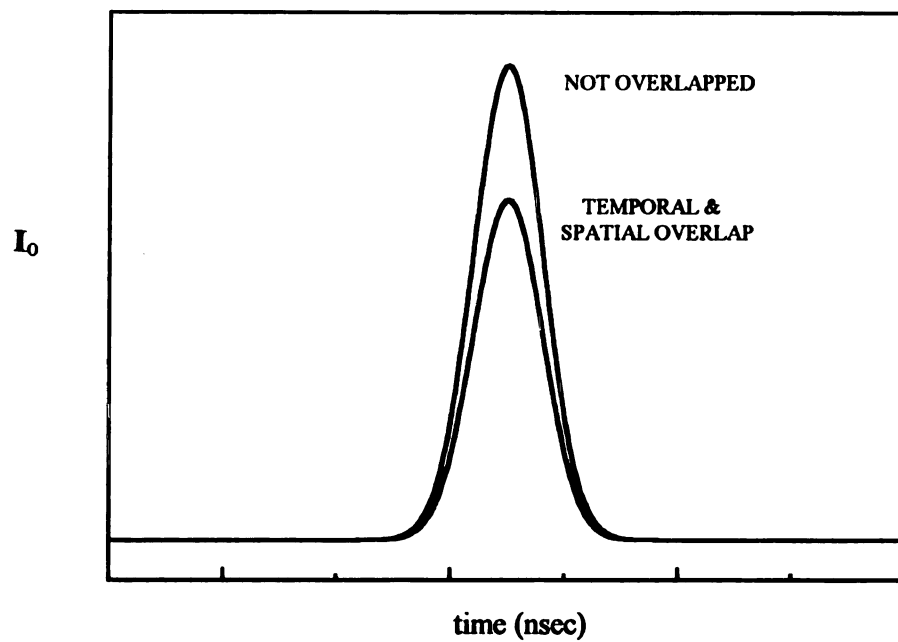


Figure 2.6

octaethylporphyrin through either a similar transient absorption setup or the actual time-resolved Raman experiment to determine zero time. Each of these protocols performed this zero time determination well, and enabled determination to within  $\sim 18$  psec (270 counts on the Klinger programmable counter).

Scattering from the sample was collected through lenses designed to match the  $f/\#$  of 5.6 for the Jobin Yvon HR640 single grating monochromator. The monochromator used a 2400 gr/mm grating and is of 0.64 meter focal length with a spectral resolution of approximately  $7\text{ cm}^{-1}$  under typical experimental conditions. A charge coupled device (Princeton Instruments, model LN/CCD 1152UV) was used to detect the Raman spectrum.

Absorption spectra were recorded prior to and following the Raman studies to confirm the integrity of the samples. UV/Vis spectra were recorded on a Perkin-Elmer Lambda 5 spectrometer (resolution of 0.25 nm,  $\pm 0.3$  nm wavelength accuracy, and stray light of less than 0.001% at 370 nm).

Solvents used in these experiments were usually organics such as tetrahydrofuran or pyridine, which were of reagent quality, purchased from Aldrich, and purified by distillation, if necessary. The Raman spectra were observed through 90 degree scattering and the sample was replenished by using a rapid flowing liquid jet system that was kept at a constant temperature by cooling the sample reservoir either in or above dry ice.

## II. FLOWING LIQUID JET ASSEMBLY

Selecting an appropriate technique for monitoring time-resolved Raman spectroscopy of liquid solutions can be critical. Several approaches exist. Dual-beam flow experiments use continuous wave lasers which monitor intermediates on microsecond and millisecond time scales.<sup>3</sup> Nanosecond pulsed lasers operating at 10 Hz have also been used for similar delay regions.<sup>4,5</sup> These approaches do not have the time resolution we desire, which can only be offered by picosecond lasers. These lasers can function at 50 Hz or near KHz repetition rates when used with various amplifiers.<sup>6,7</sup> Other research groups have neglected the use of low repetition rate amplifiers and retained the MHz repetition rates of picosecond lasers.<sup>8</sup> We have selected to omit low repetition rate amplification and use the megahertz repetition rates and nanojoule pulse energies which are intrinsic in cavity-dumped picosecond dye lasers synchronously pumped by a mode-locked cw Nd:YAG laser. High repetition rate lasers offer several advantages over comparable low repetition rate systems.<sup>9</sup> The average power available is sufficient to generate resonance Raman from intermediates with good signal-to-noise without the high pulse energies associated with multiphoton processes. The high repetition rates utilized provide improved signal averaging capabilities as long as the sample is not exposed to multiple excitations by consecutive pulses. The stability of the picosecond laser system can be optimized for high repetition rate, low peak power operation.

For time-resolved experiments on singlet and triplet electronic states of porphyrins it is essential that the ground state does not bleach through multiple excitations by consecutive pulses. To avoid multiple excitations we replenished the sample between

pairs of pump-probe pulses by using a small irradiated volume and a rapidly flowing sample. A high speed rotary pump (Gelber Industries (1136 Lloyd Rd., Wickliffe, Ohio 44092), Micropump 415 motor with a 120 magnet drive gear pump) flowed sample at a rate of  $\sim 1.0$  ml/sec through a  $300\text{ }\mu\text{m}$  diameter glass nozzle (Figure 2.7). This flow rate was used since the jet quality for our chosen organic solutions were acceptable at this rate and this rate was sufficient to avoid multiple excitations when the irradiated volume is small enough. To reduce the volume of sample optically pumped and sampled, both laser beams were spatially overlapped at a dichroic lens and then focused on the sample by using a 5X microscope objective (569-199, by W. Nuhsbaum, 3918 West Main Street, Mchenry, Illinois 60050, achromatically corrected at 546.1 nm, with a working distance of 6.2 mm and depth of focus  $\sim 280\text{ }\mu\text{m}$ ). The beam diameter of this microscope objective can be measured by several techniques.<sup>10</sup> The knife-edge technique was selected for its ease of application.<sup>11</sup>

The knife edge experimental setup is shown in Figure 2.8a. A razor blade was attached to a differential micrometer and translated horizontally across the laser beam spot. Resultant beam intensities (read in mV) were monitored at incremental positions by using a Tektronix DSA 602 oscilloscope and a Hewlett-Packard 4420 photodiode. The pulse intensity is plotted versus relative translation distance in Figure 2.8b. The pulse intensity of the unobstructed beam ( $I_0$ ), drops rapidly once the razor beam translates into the beam pathway. The beam waist ( $\omega_0$ ) is determined by measuring the horizontal translation difference between the 12%  $I_0$  and 86.4%  $I_0$  distances (the  $1/e^2$  values).<sup>11,12</sup> Plots were generated with the razor blade at several different vertical positions so as to

**Figure 2.7**      **Flowing jet cell assembly used in high repetition rate picosecond Raman experiments.**



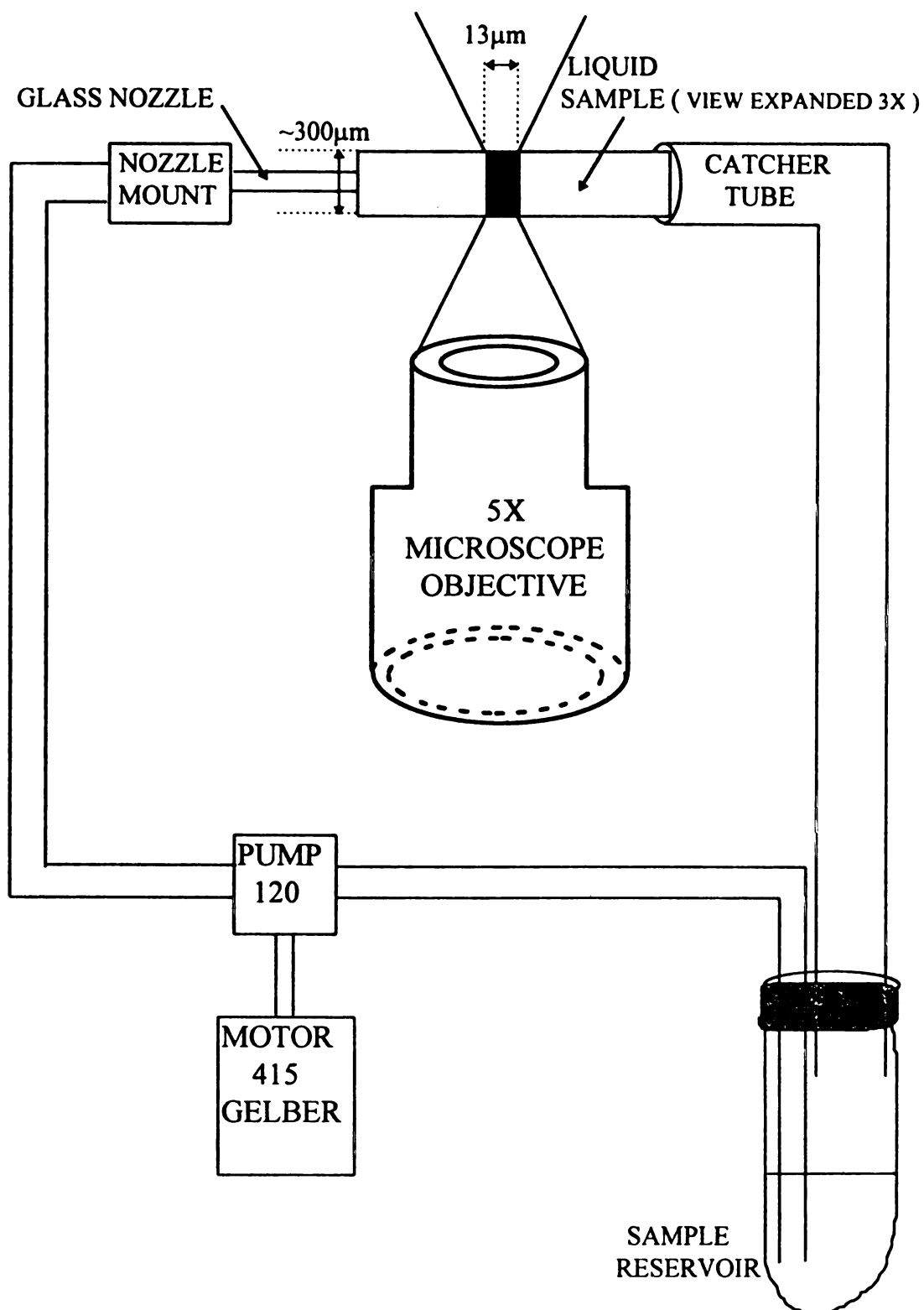


Figure 2.7

**Figure 2.8** Knife-edge technique used for determining beam waist size.  
a) Experimental setup used with 5X microscope objective(569-199).  
b) Plots of beam intensity versus changes in razor edge translation taken at four vertical positions. The vertical positions are listed in reference to the position that gave the minimal beam waist value of 13  $\mu\text{m}$ .

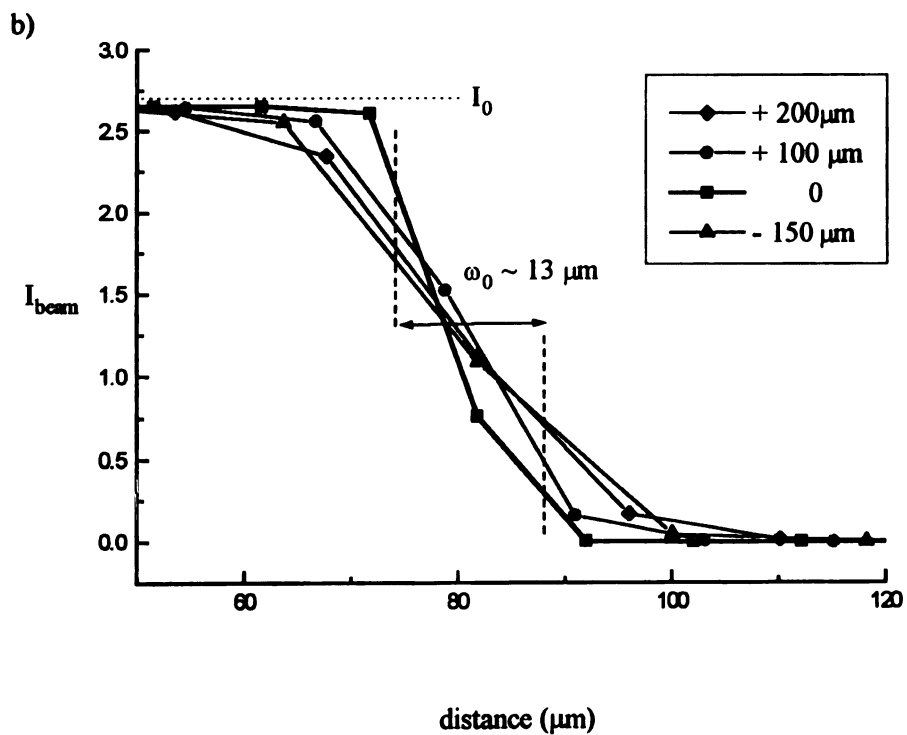
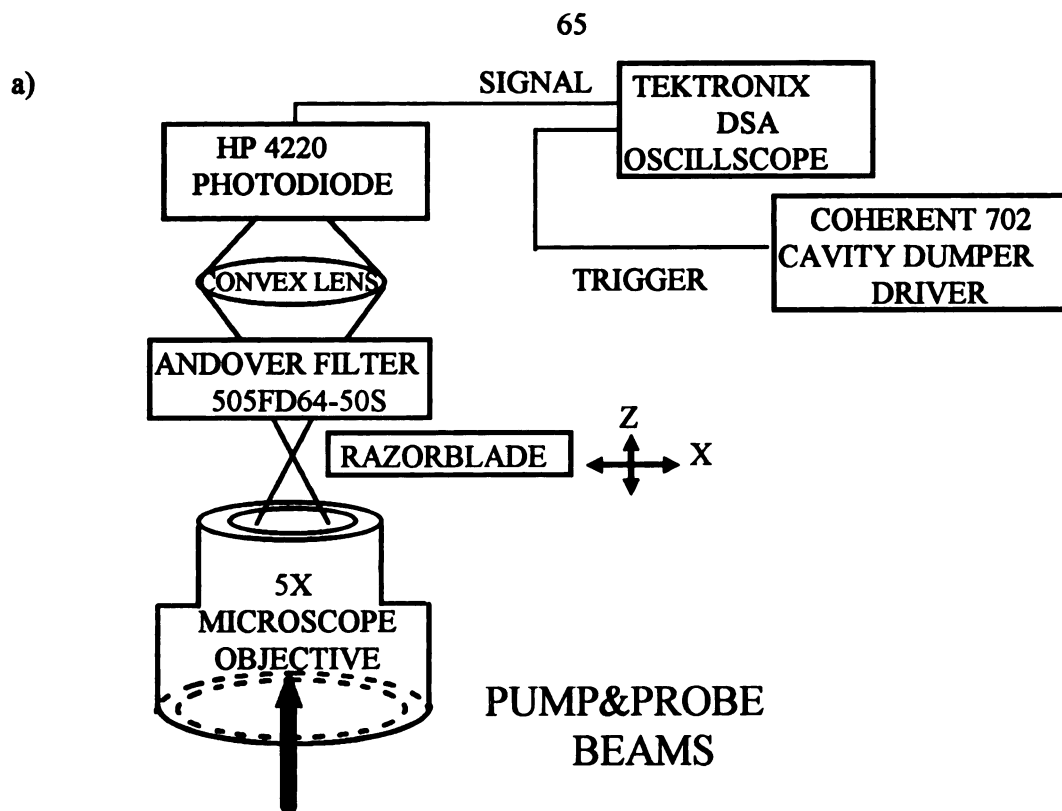


Figure 2.8

ensure convergence of the beam waist to the true beam diameter. This was reflected by the strongest slope, which gave a measured beam waist value of  $\sim 13 \mu\text{m}$ .

With this beam diameter the flow rates necessary for sample regeneration at individual repetition rates can be calculated and are listed in Table 2.1.

**Table 2.1** Flow Rate Requirements for Sample Replenishment.

<b>+N</b>	<b>Repetition Rate</b>	<b>Pulse Train Gap</b>	<b>meters/sec</b>	<b>ml/sec at 100% sample replenishment</b>
10	3.825 MHz	261.4 nsec	38.25	2.704
30	1.275 MHz	783.8 nsec	12.75	0.901
40	0.956 MHz	1.051 $\mu\text{sec}$	9.560	0.676
50	0.765 MHz	1.305 $\mu\text{sec}$	7.650	0.541
100	382.5 KHz	2.614 $\mu\text{sec}$	3.825	0.270
200	191.2 KHz	5.228 $\mu\text{sec}$	1.913	0.135

Application of rapid flowing jet systems to spectroscopy requires consideration not only of sample replenishment between pulses but also inherent restrictions on time delay measurements owing to sample movement between the initial excitation by the pump pulse and the delayed arrival of the probe pulse. Calculations in Table 2.2, using the typical experimental flow rate of  $\sim 1.0 \text{ ml/sec}$ , show the feasibility of time-resolved experiments out to a time delay of about 350 nsec.

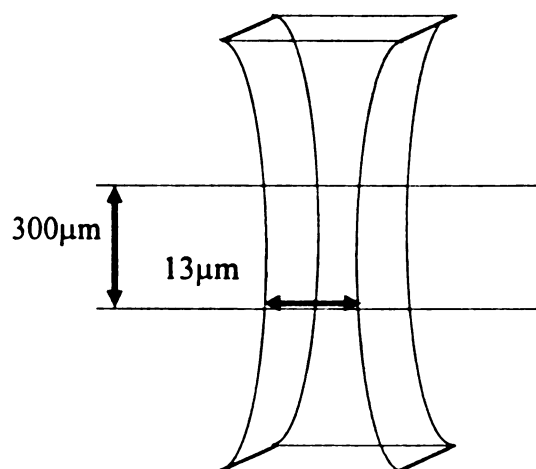
Table 2.2      Flowing Jet Restrictions on Temporal Delay.

<b>Delay time between pump and probe (nsec)</b>	<b>%Same Sample pump and probe</b>
0.1	99.99
0.8	99.89
10	98.58
26.4	96.26
50	92.92
200	71.70
350	50.47

After establishing the presence of singlet and triplet excited electronic state spectra with the glass nozzle, we alternatively used a Spectra-Physiks dye laser nozzle. This nozzle had a rectangular opening 200  $\mu\text{m}$  by 2 mm which brings the liquid to a focus  $\sim 1.5$  cm beyond the nozzle opening. We originally were concerned about possible lack of sample replenishment between pulse pairs, but failed to observe any presence of photoaccumulated product at the flow speeds and repetition rates used for our experimentation (normally 1.27 MHz and  $\sim 1.0$  ml/sec). The rectangular flowing cell gave us some advantages in minimizing background scattering from surface reflections at the air-liquid interface.

Operating with repetition rates of 1.27 MHz or less, pulse energies of the pump and probe lasers were typically  $\sim 45$  nJ and  $\sim 15$  nJ at the sample. The corresponding peak powers are  $\sim 6.5$  KW and  $\sim 2.1$  KW. Under the experimental conditions that involved high repetition rates lasers and a tightly focusing microscopic objective, as described above, the flux densities are  $\sim 55$  mJ/cm<sup>2</sup> for the pump and  $\sim 20$  mJ/cm<sup>2</sup> for the probe. These flux densities, particularly for the pump, are comparable with other published values for time-resolved Raman spectroscopy on porphyrin-like molecules.<sup>13</sup> Under these conditions it is reasonable to carry out a calculation to determine the number of molecules that are excited, and to calculate what percentage of molecules are excited. Figure 2.9 shows that

**Figure 2.9**      **Molecular excitations expected under rapid flowing jet setup.**



Under typical experiment conditions of pulse energy 40 nJ and  $\lambda_{\text{exc}} = 572 \text{ nm}$ .

$$\# \text{ PHOTONS ABSORBED} = (I_{\text{abs}}) \cdot (\lambda_{\text{exc}}) / hc$$

$$= ((\lambda_{\text{exc}}) \cdot (I_0) \cdot (1 - 10^{-\epsilon Cl})) / hc$$

$$= \frac{(572 \cdot 10^{-9} \text{ m}) \cdot (40 \cdot 10^{-9} \text{ J}) \cdot \{1 - 10^{-(30 \text{ mM}^{-1} \text{ cm}^{-1}) \cdot (0.5 \text{ mM}) \cdot (300 \cdot 10^{-4} \text{ cm})}\}}{(6.6256 \cdot 10^{-34} \text{ J} \cdot \text{s}) \cdot (3.00 \cdot 10^8 \text{ m/s})}$$

$$= \boxed{7.43 \cdot 10^{10} \text{ photons}}$$

$$\# \text{ MOLECULES} = \text{Volume enclosed} \cdot \text{Concentration} \cdot \text{Avagadro's number}$$

$$= \pi \cdot (\text{beam radius})^2 \cdot (l) \cdot (C) \cdot (N_A)$$

$$= \pi \cdot (6.5 \cdot 10^{-5} \text{ dm})^2 \cdot (300 \cdot 10^{-5} \text{ dm}) \cdot (5 \cdot 10^{-4} \text{ M}) \cdot (6.022 \cdot 10^{23})$$

$$= \boxed{1.20 \cdot 10^{10} \text{ molecules}}$$

Figure 2.9

under the typical experimental parameters of the rapid flowing jet experiment there are  $\sim 10^{10}$  molecules enclosed within the laser beam. A sufficient number of photons are present in each laser pulse to excite virtually all molecules even at higher porphyrin concentrations.

### III. QUASI-SIMULTANEOUS ACCUMULATION

Even under optimal conditions, transient Raman spectra are dominated by ground state and solvent features. Subtraction of ground state and solvent features ideally leaves only transient features. However, for the long time exposures required for pump/probe experiments that involve difference spectra determination, instabilities contribute noise to the difference spectrum. Laser power fluctuations and temperature differences in optical components become significant and reduce sensitivity and reproducibility of experimental data.<sup>14</sup> A technique has been applied that addresses these problems and improves signal-to-noise in the difference spectrum. A rapid series of short time sample accumulations are subsequently summed up to generate the long time exposure, in an approach similar to that applied by Sato *et. al.*,<sup>15</sup> and called the “quasi-simultaneous” technique.<sup>16,17</sup> As illustrated in Figure 2.10, two external mechanical shutters (Uniblitz VS14 models, from A.W. Vincent Associates, 1255-T University Avenue, Rochester, New York 14607, with total opening time 4.0 msec, closing time 3.0 msec, and capable of withstanding laser energy up to 10 W/mm<sup>2</sup>), are placed in the pathway of the pump and probe beams. These shutters are driven by a device constructed by the Michigan State Chemistry Department electronics shop and appropriately called the shutter driver. The schematic of the shutter driver is given in Figure 2.11.



**Figure 2.10** Simultaneous method implementing mechanical shutters (SI and SII) within laser beam pathways.

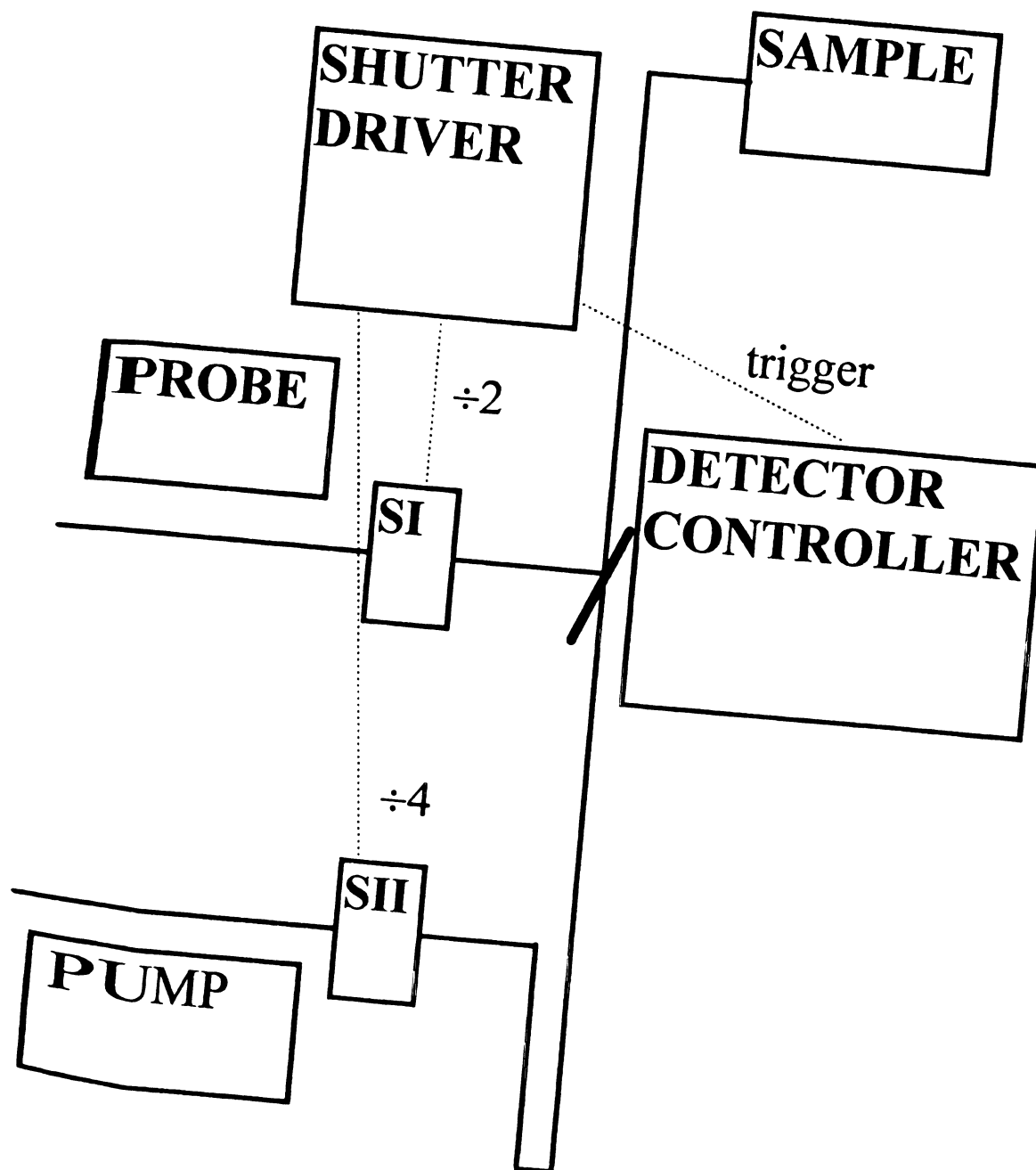


Figure 2.10

**Figure 2.11** Schematic of shutter driver. a) voltage transformer.  
b) analog switching permitting shutter operation.

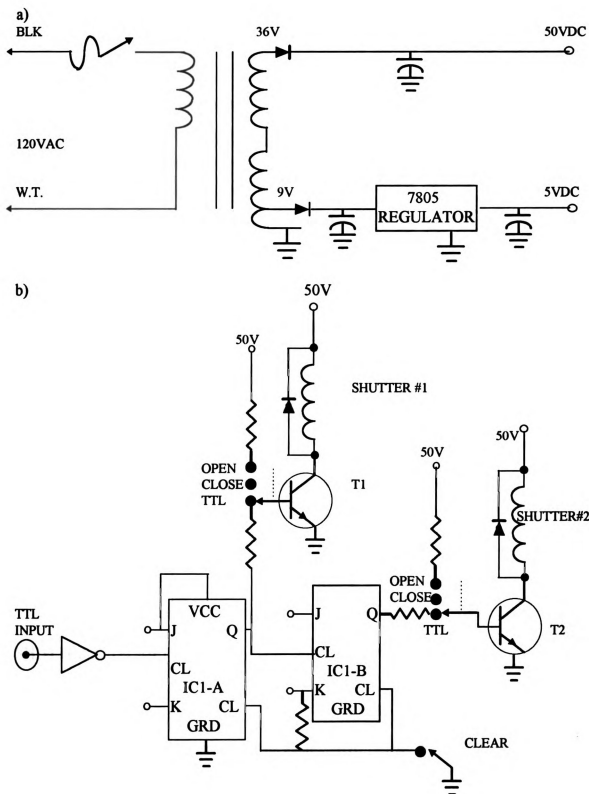


Figure 2.11

The shutter driver transforms incoming 120 VAC into 50 VDC and 5 VDC. The 5 VDC supplies two IC analog voltage switches while the 50 VDC is used to power the two mechanical shutters.

A TTL pulse is inverted prior to entering IC1-A. The pulse is alternately transmitted to IC1-B, an identical analog switch in series with IC1-A. The alternate pulse from IC1-A also actuates transistor 1 (T1), which permits opening of shutter #1. IC1-B performs a similar function for transistor 2 (T2) and shutter #2. Since IC1-B receives a TTL pulse only every other cycle, the net result is that shutter #2 opens and closes half as often as shutter #1. Thus, the shutter driver permits four possible combinations of shutter switching, and these switchings are regulated by a TTL input pulse. This TTL pulse originates from the NOTSCAN outlet from the Princeton Instruments ST130 controller, and changes with every closing of the internal mechanical shutter associated with the CCD detector. The shutter driver is sequenced to produce four partitions of time intervals, such as shown in Figure 2.12, which can be sequenced with the CSMA software.

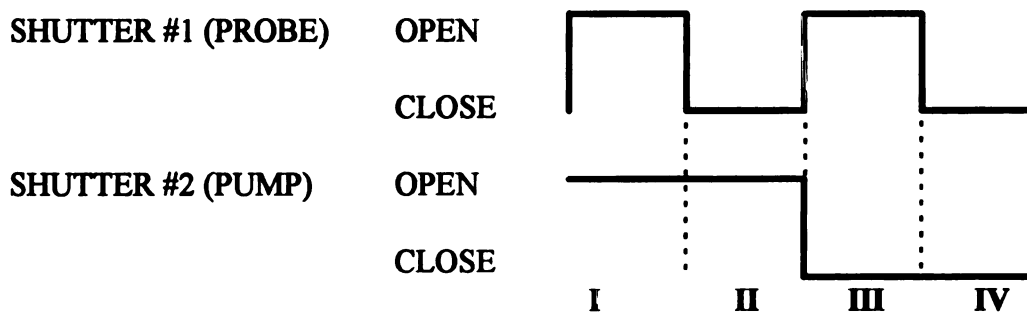


Figure 2.12 Partitions of time intervals generated by shutter driver.

These time intervals can be varied, but typically were run between 0.5-3 minutes. Partition I has both shutters open and exposes the sample to both pump and probe beams. Partition II has one shutter closed and consequently records the pump only spectrum. In partition III the other shutter closes while the first one reopens and the probe only spectrum is recorded. Partition IV has both shutters closed and dark counts are recorded.

Post data processing subsequently divides the accumulated spectra into pump&probe, pump, probe, and dark spectra. The software associated with Princeton Instruments detection systems is called CSMA (v3.0), and uses a programming language called Spectrum Basic, which has written programs that perform the operations essential to data acquisition, spectral processing, image processing, and reviewing acquired data.<sup>18</sup> It was necessary to write three additional programs to assist in processing of data accumulated through the “quasi-simultaneous” technique. These programs are written in Spectrum Basic and are listed in Appendix A.

Initially a program called Separate.pro was created to process spectra acquired by using only one external mechanical shutter. The standard procedure is to first collect continuously a series of short exposures independently stored into an even number of frames selected by prompts from the CSMA software. The Separate.pro is a post-processing program that separates even frames from odd frames, then adds up and stores the individual frames into two newly created data files.

Quartiles.pro is a similar post-processing program that enables the use of two external mechanical shutters and permits differentiation of consecutive data frames into four separate data files. The only restriction is that the total number of selected frames must be an integral number of four.

Additionally, it was useful to write a program that can edit the occasional bad frame in an otherwise good series of spectra. Frmedit.pro is a modification of Replay.pi which will perform this function.<sup>18</sup> The usual sequence after starting this program is to first type “Alt-M” to assume manual control over replay of frames in the unprocessed

spec

and

fran

reta

con

sim

use

pun

sam

con

met

prol

The

ene

exp

wel

cha

Mic

spectra. If one wishes to save the current frame displayed, one types “s” to save. The up and down arrows, or “Pgup” or “Pgdn”, will move the displayed spectra to subsequent frames. The “s” key must be hit for each frame you wish to store, and it is important to retain the proper sequence of frames stored. When editing is finished, typing “Esc” completes the process and terminates the program. The application of the “quasi-simultaneous” method, along with some post-data processing, was found to be especially useful in taking difference spectra.

This combination of features, a tunable pair of high repetition rate synchronously pumped picosecond pulsed dye lasers, a flowing liquid cell that adequately refreshes the sample, and a data processing technique that minimizes fluctuations, represents the first combination of these techniques applied to studying Raman spectroscopy of metalloporphyrins. The dye lasers offer broad selectable wavelengths for both pump and probe beams. Time resolution of intermediates can be applied to within ~18 picoseconds. The post-processing programs in conjunction with the high average powers and low pulse energies of the dye lasers permit favorable signal-to-noise levels. Completion of this experimental setup provides the flexibility to study shorter lived electronic species,<sup>19</sup> as well as a wider range of processes including vibrational relaxation.<sup>19,20,21</sup> The following chapters detail some of the initial applications of picosecond Raman spectroscopy at Michigan State University.



(1)

(2)

(3)

(4)

(5)

(6)

(7)

## LIST OF REFERENCES

- (1) O'Neil, M. P. *Optics Letters* **1993**, 18(1), 37-38.
- (2) (a) Schafer, F. P.; Schmidt, W.; Marth, K.; *Appl. Phys. Lett.* **1967**, 24A, 280. (b) Maeda, M.; Miyazoe, Y.; *Jpn. J. Appl. Phys.* **1972**, 11(5), 692.
- (3) (a) Han, S.; Ching, Y-C.; Rousseau, D. L. *J. Am. Chem. Soc.* **1990**, 112, 9446-9451. (b) Ames, J. B.; Raap, J.; Lugtenburg, J.; Mathies, R. A. *Biochemistry* **1992**, 31, 12546-12554. (c) Han, Y.; Ching, Y-C.; Rousseau, D. L. *Nature*, **1992**, 348, 89-90. (d) Ogura, T.; Takahashi, S.; Hirota, S.; Shinzawa-Itoh, K.; Yoshikawa, S.; Appelman, E. H.; Kitagawa, T. *J. Am. Chem. Soc.* **1993**, 115, 8527-8536.
- (4) (a) Findsen, E. W.; Shelnut, J. A.; Ondrias, M. R. *J. Phys. Chem.* **1988**, 92, 307-314 (b) Kaminaka, S.; Kitagawa, T. *J. Am. Chem. Soc.* **1992**, 114, 3256-3260. (d) Bell, S. E. J.; Al-Obaidi, A. H. R.; Hegarty, M.; Hester, R. E.; McGarvey, J. J. *J. Phys. Chem.* **1993**, 97, 11599-11602.
- (5) (a) Babcock, G. T.; Jean, J. M.; Johnston, L. N.; Palmer, G.; Woodruff, W. H. *J. Am. Chem. Soc.* **1984**, 106, 8305-8306. (b) Walters, V. A.; dePaula, J. C.; Babcock, G. T.; Leroi, G. E. *J. Am. Chem. Soc.* **1989**, 111, 8300-8302. (c) Varotsis, C.; Babcock, G. T. *Biochemistry* **1990**, 29(32) 7357-7361. (d) Varotsis, C.; Woodruff, W. H.; Babcock, G. T. *J. Biol. Chem.* **1990**, 265(19), 11131-11136. (e) Varotsis, C.; Zhang, Y.; Appelman, E. H.; Babcock, G. T. *Proc. Natl. Acad. Sci. USA* **1993**, 90, 237-241.
- (6) (a) Courtney, S. H.; Jedju, T. M.; Friedman, J. M.; Alden, R. G.; Ondrias, M. R. *Chem. Phys. Lett.* **1989**, 164(1), 39-43. (b) Alden, R. G.; Sparks, L. D.; Ondrias, M. R.; Crawford, B. A.; Shelnut, J. A. *J. Phys. Chem.* **1990**, 94, 1440-1443. (c) Reid, R. J.; Doig, S. J.; Wickham, S. D.; Mathies, R. A. *J. Am. Chem. Soc.* **1993**, 115, 4754-4763. (d) Reid, P. J.; Lawless, M. K.; Wickham, S. D.; Mathies, R. A. *J. Phys. Chem.* **1994**, 98, 5597-5606.
- (7) (a) Reed, R. A.; Purrello, R.; Prendegast, K.; Spiro, T. G. *J. Phys. Chem.* **1991**, 95, 9720-9727. (b) Phillips, D. L.; Rodier, M-J.; Myers, A. B. *Chem. Phys.* **1993**, 175, 1-12. (c) Rodgers, K. R.; Su, L.; Subramanian, S.; Spiro, T. G. *Biochemistry* **1993**, 32, 4547-4551. (d) Myers, A. B.; Philips, D. L.; Ci, X.; Westerfield, C.; Rodier, J-M *Proc. SPIE-Int Soc.* **1993**, 1-12.

- (8) (a) Gustafson, T. L.; Iwata, K.; Weaver, W. L. in *Ultrafast Phenomena VII*; Harris, C. B.; Ippen, E. P.; Mourou, G. A.; Zewail, A. H., Eds.; Springer-Verlag: New York, 1990. (b) Hayashi, H.; Kolaczowski, S. V.; Noguchi, T.; Blanchard, D.; Atkinson, G. H. *J. Am. Chem. Soc.* **1990**, *112*, 4664-4670. (c) Noguchi, T.; Kolaczowski, S.; Gartner, W.; Atkinson, G. H. *J. Phys. Chem.* **1990**, *94*, 4920-4926. (d) Hayashi, H.; Brack, T. L.; Noguchi, T.; Tasumi, M.; Atkinson, G. H. *J. Phys. Chem.* **1991**, *95*, 6797-6802. (e) Noguchi, T.; Hayashi, H.; Tasumi, M.; Atkinson, G. H. *J. Phys. Chem.* **1991**, *95*, 3167-3172. (f) Iwata, K.; Hamaguchi, H. *Chem. Phys. Lett.* **1992**, *196*, 462-468. (g) Weaver, W. L.; Huston, L. A.; Iwata, K.; Gustafson, T. L.; *J. Phys. Chem.* **1992**, *96*, 8956-8961. (h) Butler, R. M.; Lynn, M. A.; Gustafson, T. L. *J. Phys. Chem.* **1993**, *97*, 2609-2617.
- (9) Atkinson, G. H.; Brack, T. L.; Blanchard, D.; Rumbles, G. *Chem. Phys.* **1989**, *131*, 1-15.
- (10) (a) Yoshida, A.; Asakura, T. *Opt. Laser Technol.* **1976**, *8*, 273. (b) Shayler, P. J.; *Appl. Opt.* **1978**, *17*, 2673-2675. (c) Sasaki, A.; Yamada, F.; Masui, T. *Jpn. J. Appl. Phys.* **1978**, *17*, 1163-1164. (d) Dickson, L. D. *Opt. Eng.* **1979**, *18*, 70. (e) Mccally, R. L.; *Appl. Opt.* **1982**, *23*, 2227-2229 (f) Liu, J. M.; *Opt. Lett.* **1982**, *7*, 196-198. (g) Kimura, S.; Munakata, C. *App. Opt.* **1988**, *27*, 84-88.
- (11) (a) Arnaud, J. A.; Hubbard, W. M.; Mandeville, G. D.; de la Claviere, B.; Franke, E. A.; Franke, J. M. *Appl. Opt.* **1971**, *10*, 2775. (b) Skinner, D. R.; Whitcher, R. E. *J. Phys. E.* **1972**, *5*, 237. (c) Suzaki, Y.; Tachibana, A. *Appl. Opt.* **1975**, *14*, 2809. (d) Firester, A. H.; Heller, M. E.; Sheng, P. *Appl. Opt.* **1977**, *16*, 1971. (e) Schneider, M. B.; Webb, W. W. *Appl. Opt.* **1981**, *20*, 1382.
- (12) Karim, M. A. in *Electro-Optical Devices and Systems*; Karim, M. A. Ed.; Kent: Cambridge, 1990, pp 189-195.
- (13) (a) Sato, S-I.; Asano-Someda, M.; Kitagawa, T. *Chem. Phys. Lett.* **1992**, *189*, 443-447. (b) de Paula, J. C.; Walters, V. A.; Nutaitis, C.; Lind, J.; Hall, K. *J. Phys. Chem.* **1992**, *96*(26), 10591-10594. (c) Kumble, R.; Hu, S.; Loppnow, G.; Vitols, S. E.; Spiro, T. G. *J. Phys. Chem.* **1993**, *97*, 10521-10523.
- (14) Diller, R.; Stockburger, M. *Biochemistry* **1988**, *27*, 7641.
- (15) Sato, S-I.; Kamogawa, K.; Aoyagi, K.; Kitagawa, T. *J. Phys. Chem.* **1992**, *96*, 10676-10681.
- (16) Nakagawa, M.; Maeda, A.; Ogura, T.; Kitagawa, T. *J. Mol. Struct.* **1991**, *242*, 221-234.
- (17) Muench, R.; Schaack, G.; Winterfeldt, V. *J. Phys. E.* **1982**, *15*, 776-781.

- (18) See Princeton Instruments manual (CSMA User's Manual, v3.0) for a complete listing of programs that were available at that time.
- (19) (a) Alden, R. G.; Schneebeck, M. C.; Ondrias, M. R.; Courtney, S. H.; Friedman, J. M. *J. Raman Spectrosc.* **1992**, 23, 569-574. (b) Schneebeck, M. C.; Vigil, L. E.; Ondrias, M. R. *Chem. Phys. Lett.* **1993**, 215, 251-6. (c) Qian, J.; Schultz, S.; Bradburn, G. R.; Jean, J. M. *J. Phys. Chem.* **1993**, 97, 10638-10644. (d) Markel, F.; Ferris, N. S.; Gould, I. R.; Myers, A. B. *J. Am. Chem. Soc.* **1992**, 114, 6208-6219. (e) Iwata, K.; Hamaguchi, H. *Springer Proc. Phys.* 1994, 74(Time-Resolved Vibrational Spectroscopy VI), pp 85-88. (f) Moore, J. N.; Matousek, P.; Parker, A. W.; Toner, W. T.; Towrie, M.; Hester, R. E. *Springer Proc. Phys.* 1994, 74(Time-Resolved Vibrational Spectroscopy VI), pp 89-92.
- (20) (a) Rodriguez, J.; Holten, D. *J. Chem. Phys.* **1989**, 91, 3525-3531. (b) Rodriguez, J.; Holten, D. *J. Chem. Phys.* **1990**, 92, 5944-5949. (c) Bilsel, O.; Rodriguez, J.; Holten, D. *J. Chem. Phys.* **1990**, 94, 3508-3512. (d) Rodriguez, J.; Kirmaier, C.; Holten, D. *J. Chem. Phys.* **1991**, 94, 6020-6029.
- (21) Vos, M. H.; Rappaport, F.; Lambry, J.-C.; Breton, J.; Martin, J.-L. *Nature* **1993**, 363, 320-325.

## CHAPTER 3

### RAMAN SPECTRA OF METALLOPORPHYRIN EXCITED STATES

#### ABSTRACT

Picosecond time-resolved resonance Raman measurements on Zn(II) octaethylporphyrin are reported. The lowest excited singlet state ( $S_1$ ) is detected within 100 ps following laser excitation and intersystem crosses to the triplet ( $T_1$ ) state on the nanosecond time scale. The Raman spectrum of  $S_1$  is dominated by totally symmetric modes that can be correlated with ground state porphyrin modes. Depolarized modes are only weakly enhanced in  $S_1$ , which indicates that Jahn-Teller distortion in this state is essentially absent. By contrast, depolarized modes are prominent in the spectrum of  $T_1$  and indicate significant Jahn-Teller distortion, in agreement with previous metalloporphyrin  $T_1$  work from this (Walters, V. A., de Paula, J. C., Babcock, G. T., Leroi, G. E. *J. Am. Chem. Soc.* **1989**, 111, 8300-8302) and other (Kumble, R., Hu, S., Loppnow, G. R., Vitols, S. E., Spiro, T. G., *J. Phys. Chem.* **1993**, 97, 10521-10523) laboratories. These observations confirm theoretical predictions that the excited states are influenced by Jahn-Teller effects, but that configuration interaction minimizes the distortion in the  $S_1$  state.

## I. INTRODUCTION

Light induced charge separation in the photosynthetic reaction center is initiated by photoexcitation of a chlorophyll complex into its first excited singlet ( $S_1$ ) state.<sup>1</sup> To understand this critical biological process better, more insight into the electronic structure and conformation of singlet excited porphyrin-like molecules is essential. Time-resolved resonance Raman scattering is an ideal technique for providing this insight and has been used recently to characterize the vibrational properties of electronically excited porphyrins.<sup>2-4</sup> However, due to a limited time resolution, this approach could only focus on relatively long-lived excited states like the  $T_1$  and d,d states of metalloporphyrins,<sup>2-4</sup> and the  $S_1$  and  $T_1$  states of free-base derivatives.<sup>2,4</sup> Moreover, dynamic processes, such as vibrational relaxation of electronically excited macrocycles, could not be studied at all. These latter issues are likely to be of fundamental importance in understanding the details of the photosynthetic process.<sup>5</sup> To increase the time resolution of the Raman technique we have developed picosecond pump-probe methods<sup>6</sup> that allow us to monitor the time evolution of a metalloporphyrin in its excited state manifold. Here, we present our initial results on Raman scattering from excited electronic states of Zn(II) octaethylporphyrin (ZnOEP).<sup>7,8,9</sup> In the  $S_1$  state the number and symmetry of the bands indicate weak or absent Jahn-Teller distortion. ZnOEP in the  $T_1$  state, in agreement with previous work on the ZnTPP  $T_1$  state,<sup>2</sup> shows relatively strong enhancement of depolarized modes. The latter observation indicates Jahn-Teller distortion and shows that metalloporphyrin excited states of different spin multiplicity exhibit qualitatively different Jahn-Teller effects.

## II. MATERIALS AND METHODS

To induce the  $S_1$  state, we excited ZnOEP dissolved in tetrahydrofuran (THF) or pyridine at the maximum of its Q(0,0) absorption band. The Raman spectrum of the sample was probed in the blue with a second laser pulse. A pyrromethene 567 dye laser (Coherent 702) generated pulses (7 ps full-width-half-maximum) at 572 nm. The laser is synchronously pumped by the second harmonic of a mode-locked Nd:YAG (Coherent Antares 76-s). The laser setup used for these experiments is fully documented in Chapter 2 under “Experimental Apparatus”. The third harmonic is used to pump a stilbene 420 dye laser with an output wavelength of 450 nm. The wavelength of 450 nm was chosen because the porphyrin has a maximum near this wavelength in the  $S_1$  state, whereas the absorption of the porphyrin in the ground state is very low. A cavity dumper on each dye laser is used to create a time delay of 790 ns between subsequent pulses and to increase the peak power of the individual pulses. Time delays between the pump and probe pulses were adjusted electronically or spatially by adjusting the path length of the pump pulse. The pulse energies of the pump and probe lasers used were 40 nJ and 25 nJ at the sample, respectively. A microscope objective was used to focus these beams to  $\sim 13\ \mu\text{m}$  spots on the sample. A low-pass filter (Andover blue dichroic, 50% transmittance at 515 nm) was used to prevent scattered light from the pump beam and fluorescence to enter the spectrometer. The Raman spectrum was dispersed by a single grating monochromator (Jobin Yvon HR640, 2400 grooves/mm grating) and detected with a CCD detector (Princeton Instruments, model LN/CCD 1152UV). The spectral resolution was  $7\ \text{cm}^{-1}$ .

To refresh the sample between laser pulses, we used a flowing liquid jet assembly

similar to that of Atkinson *et. al.*,<sup>10</sup> the experimental setup for which is fully described in Chapter 2 under “Flowing Liquid Jet Assembly”.

The nanosecond time-resolved pulsed Raman setup (Figure 3.1) used for triplet state evaluation has the same basic setup as that used earlier in the ZnTPP experiment by Walters *et. al.*<sup>2a</sup>, but will be briefly described below.<sup>11</sup>

Two Quanta Ray Q-switched Nd:YAG lasers (Quanta-Ray DCR2's, 1250 Charleston Road, Mountain View CA, 94043) with pulse widths of 10 ns and repetition rates of 10 Hz were controlled by a Stanford DG35 Delay Generator (Stanford Research Systems, 1290-D Reamwood Avenue, Sunnyvale CA 94089) that provides programmable triggering for the flash lamps and Q-switches to produce the desired time delays. The delay was continuously monitored with a photodiode and a Tektronix oscilloscope. A glass slide intersected the two spatially overlapped beams, and reflected approximately 5% of the intensity into the photodiode. The pump wavelength was generated from the second harmonic (532 nm) of the first laser. The probe wavelength (435.7 nm) was provided by pumping a H<sub>2</sub> Raman shifter with 532 nm from a second Quanta Ray Nd:YAG laser and separating the first anti-stokes wavelength with a pellin-broca prism.<sup>11</sup> A low temperature back-scattering arrangement was chosen to collect data with the sample in a spinning EPR tube.<sup>12</sup> A spherical lens (f = 2.5 inches) was used to focus these beams to ~100  $\mu$ m spots on the sample. The Raman scattering was collected in a 135° orientation and focused by collection mirrors (5 times magnification) into a triple grating spectrometer (SPEX 1877 Triplemate, 1800 grooves/mm grating blazed at 450 nm (SPEX industries, Inc., 3880 Park Avenue, Edison NJ, 08820) with a spectral resolution



**Figure 3.1**      **Instrumentation used for time-resolved nanosecond Raman experiments. HG: harmonic generators giving 2<sup>nd</sup> and 3<sup>rd</sup> harmonic wavelengths; Dye Laser: optionally used to generate wavelengths not accessible by Raman shifter; H<sub>2</sub> Raman shifter: 1st anti-stokes of 532 nm used (435.7 nm); PBP: Pellin-Broca prism used to separate the Stokes lines coming from the Raman shifter; 1459 Illuminator: mirrors used to direct Raman scatter into Spex 1877 Triplemate.**

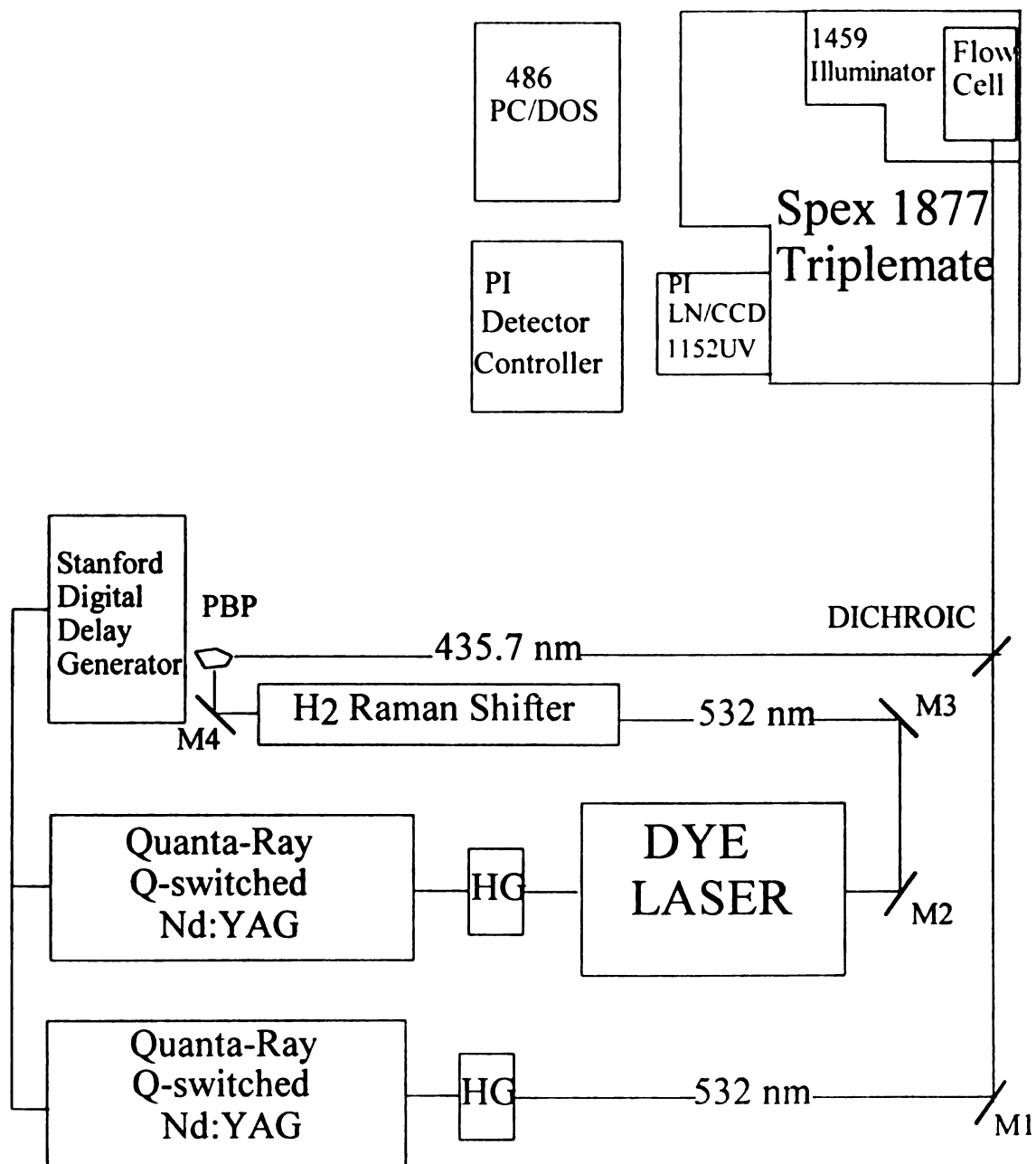


Figure 3.1

of  $8\text{ cm}^{-1}$ . The Raman intensity was detected with a CCD (Princeton Instruments, model LN/CCD 1152UV).

### III. RESULTS

Figure 3.2 shows Raman spectra of ZnOEP in tetrahydrofuran obtained by using the pump-probe arrangement described in Chapter 2. The excitation pulse preceded the probe pulse by 100 ps, 800 ps, 2 ns, and 27 ns, respectively. The spectra of the solvent THF and of the ground state are also shown in Figure 3.2. Figure 3.3 shows the time dependent difference spectra after subtracting out ground state features with a scaling constant and following procedures described in Chapter 2 under “Quasi-Simultaneous Accumulation”. Polarization dependent measurements were carried out to determine the symmetry species of the Raman modes. The Raman difference spectra in Figure 3.4 show the polarization dependence of ZnOEP obtained with the excitation pump pulse preceding the probe pulse by 100 ps. Likewise, the Raman difference spectra in Figure 3.5 show polarization dependence when the pump pulse is 27 ns prior to the probe pulse. The vibrational mode assignments based on these polarization measurements are listed in Table 3.1. At short time delays (100 ps, 800 ps), ZnOEP is in its  $S_1$  state and the spectrum is dominated by totally symmetric modes, although some weak nontotally symmetric modes are also visible. After 27 ns only the triplet state remains. At this time delay, the spectrum resembles that of Kumble *et. al.*<sup>2a</sup> obtained in a nanosecond pump-probe experiment, although some lineshape and intensity differences are apparent. These differences do not arise from the use of picosecond pulses in the present study. We have also taken excited

**Figure 3.2** Time resolved resonance Raman spectra of ZnOEP in THF in (a) low wavenumber region and (b) in the high wavenumber region. The pump and probe beams were at 572 nm and 450 nm, respectively. The time evolution of the Raman scattering is represented by spectra obtained at time delays between the pump and probe pulse of 100 ps, 800 ps, 2 ns, and 27 ns. The concentration of ZnOEP was  $5 \cdot 10^{-4}$  M. The spectra of the ground state (gs) and the solvent (dotted line) were obtained in the absence of the pump pulse.

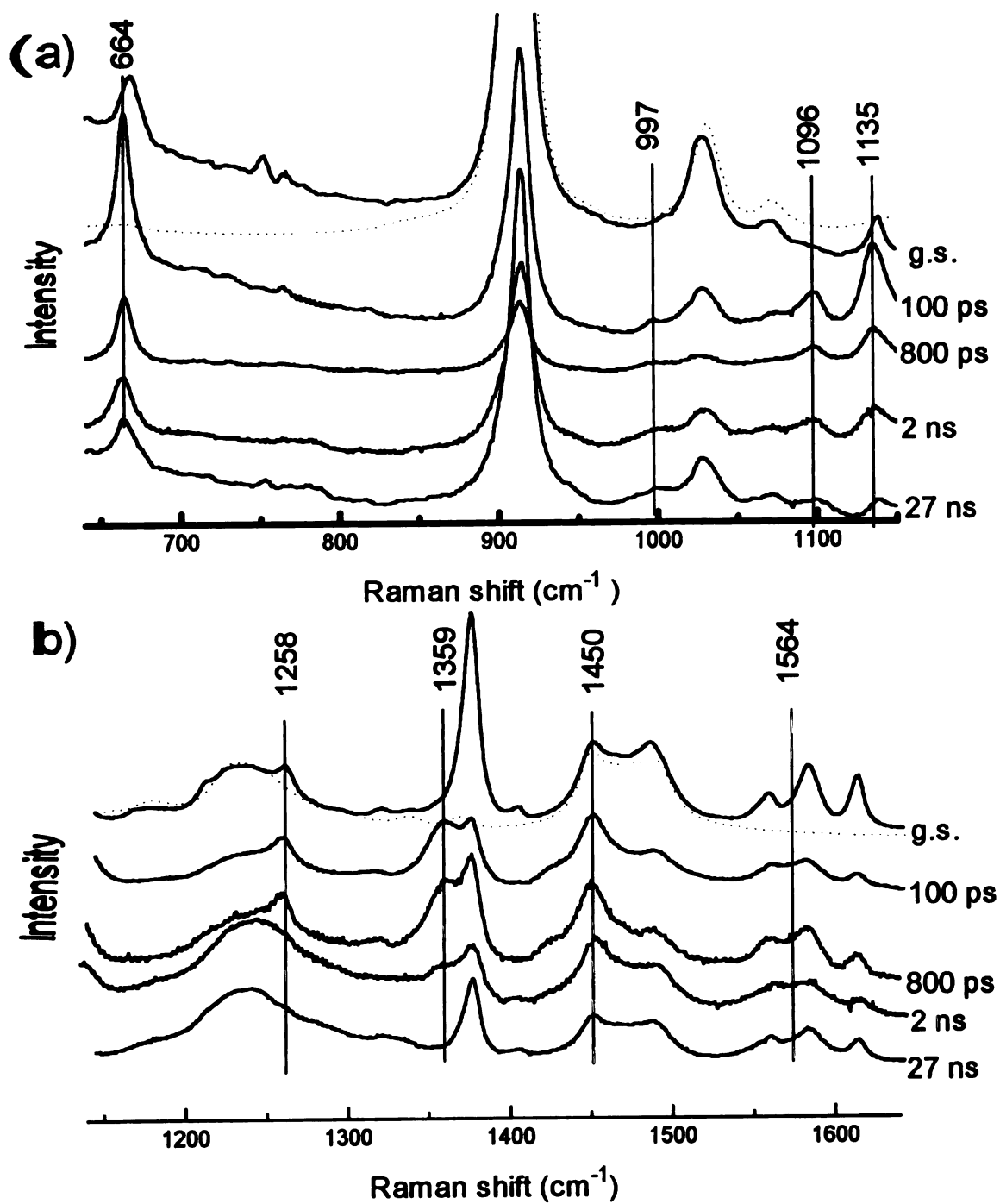


Figure 3.2

**Figure 3.3** Time resolved resonance Raman difference spectra of ZnOEP in THF in (a) low-wavenumber and (b) high-wavenumber range. Experimental spectra from Figure 3.2 were acquired “quasi-simultaneously”. The ground state features observed in Figure 3.2 at various delays for high and low frequencies have been subtracted out such that no negative peaks appear. The peak positions of the vibrational modes are collected in Table 3.1. The low intensities observed at  $669\text{ cm}^{-1}$  and  $753\text{ cm}^{-1}$  suggest that the intensities of ground state features in the excited state spectra are minimal.

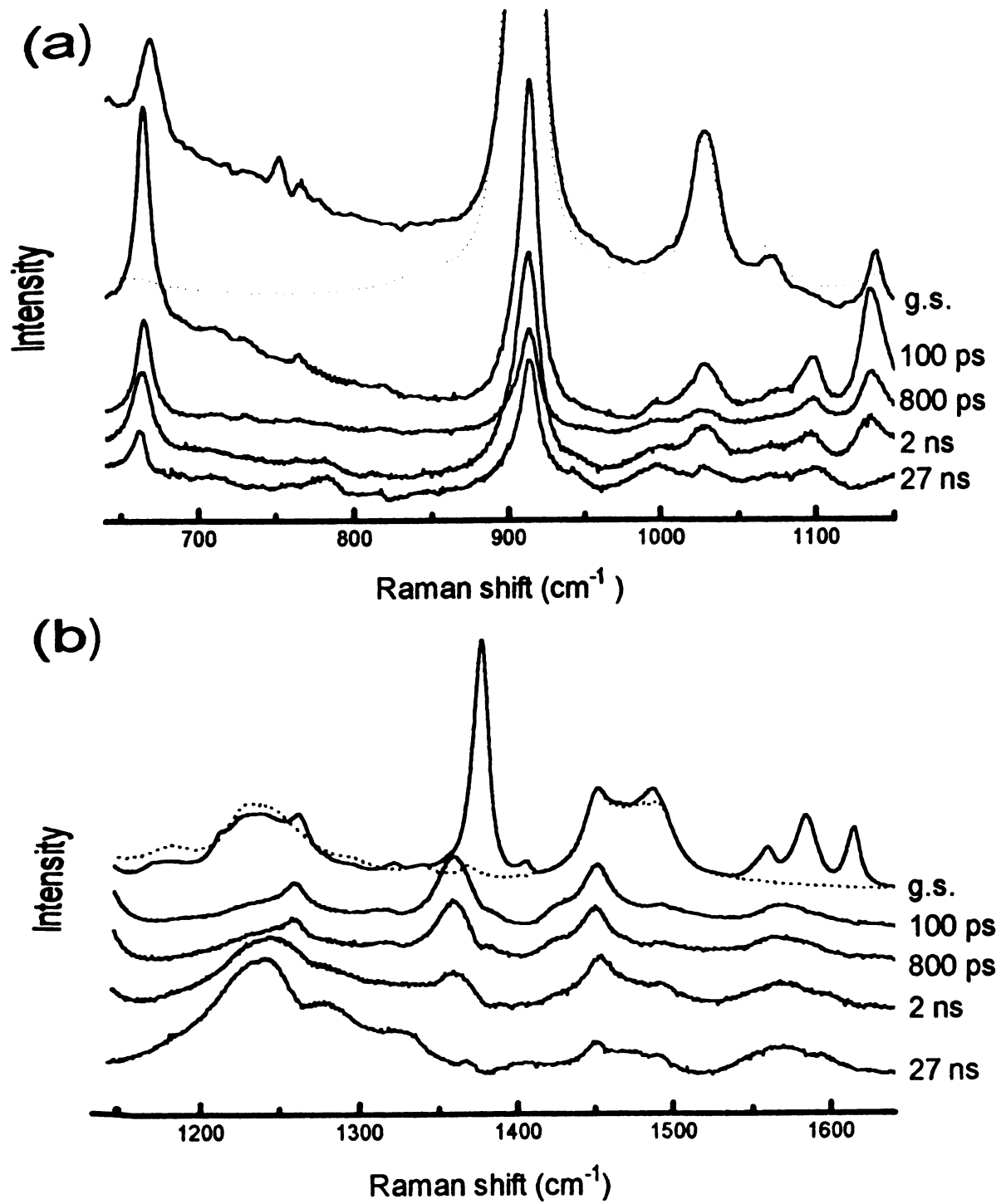


Figure 3.3

**Figure 3.4** Time-resolved resonance Raman difference spectra taken at 100 ps in (a) low and (b) high wavenumber regions. Spectra are shown for all polarizations, parallel polarization, and perpendicular polarization. Qualitative assignments to symmetries of vibrational modes are labeled as either totally symmetric (P) or nontotally symmetric (DP). Solvent spectra (dotted lines) are obtained in the absence of a pump pulse and peaks are marked by an asterisk.



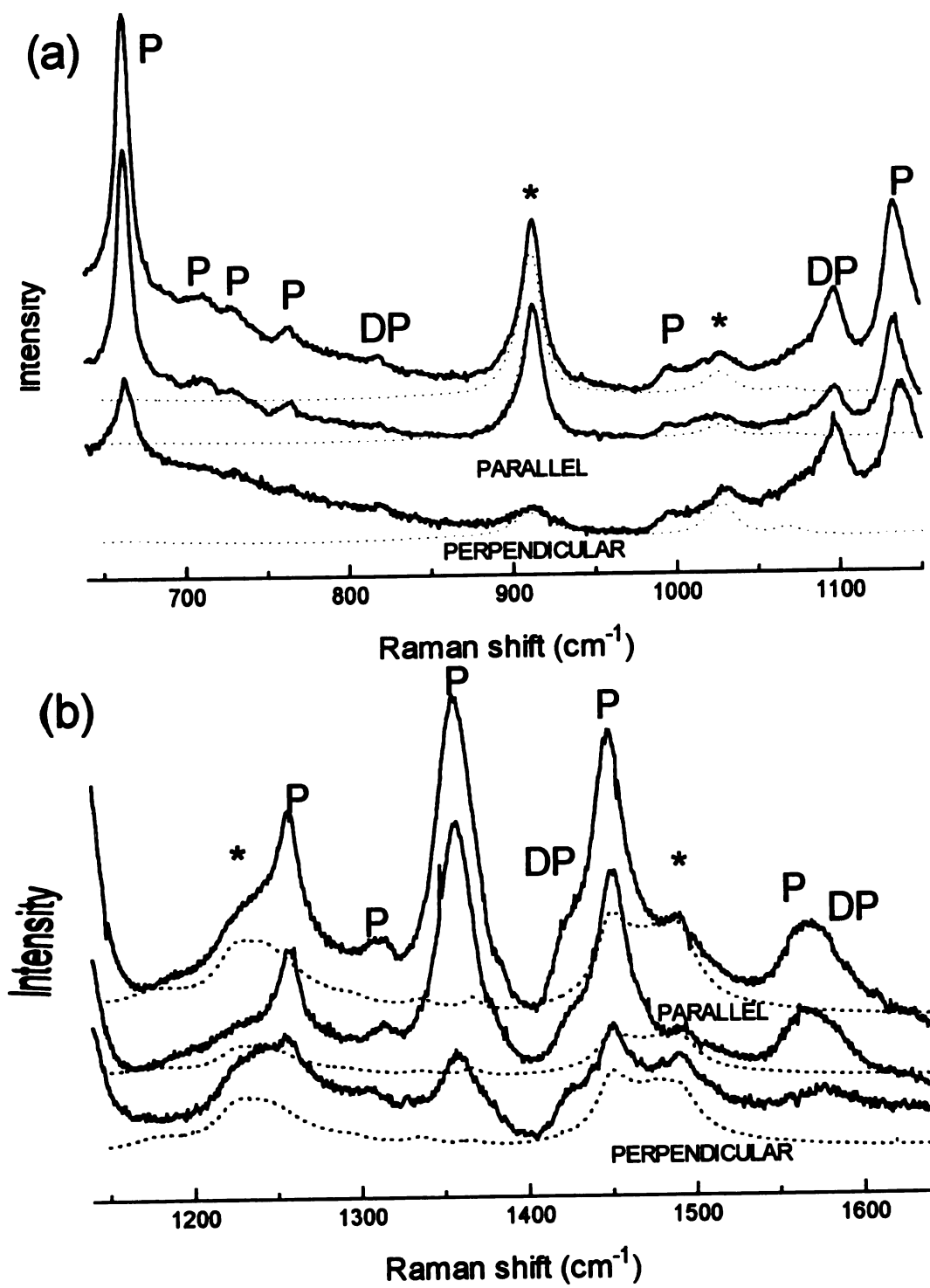


Figure 3.4

**Figure 3.5** Time-resolved resonance Raman difference spectra taken at 27 nanoseconds in (a) low and (b) high wavenumber regions. Spectra are shown for all polarizations, parallel polarization, and perpendicular polarization. Qualitative assignments to symmetries of vibrational modes are labeled as either totally symmetric (P) or nontotally symmetric (DP). Solvent spectra (dotted lines) are obtained in absence of a pump pulse and peaks are marked by an asterisk.

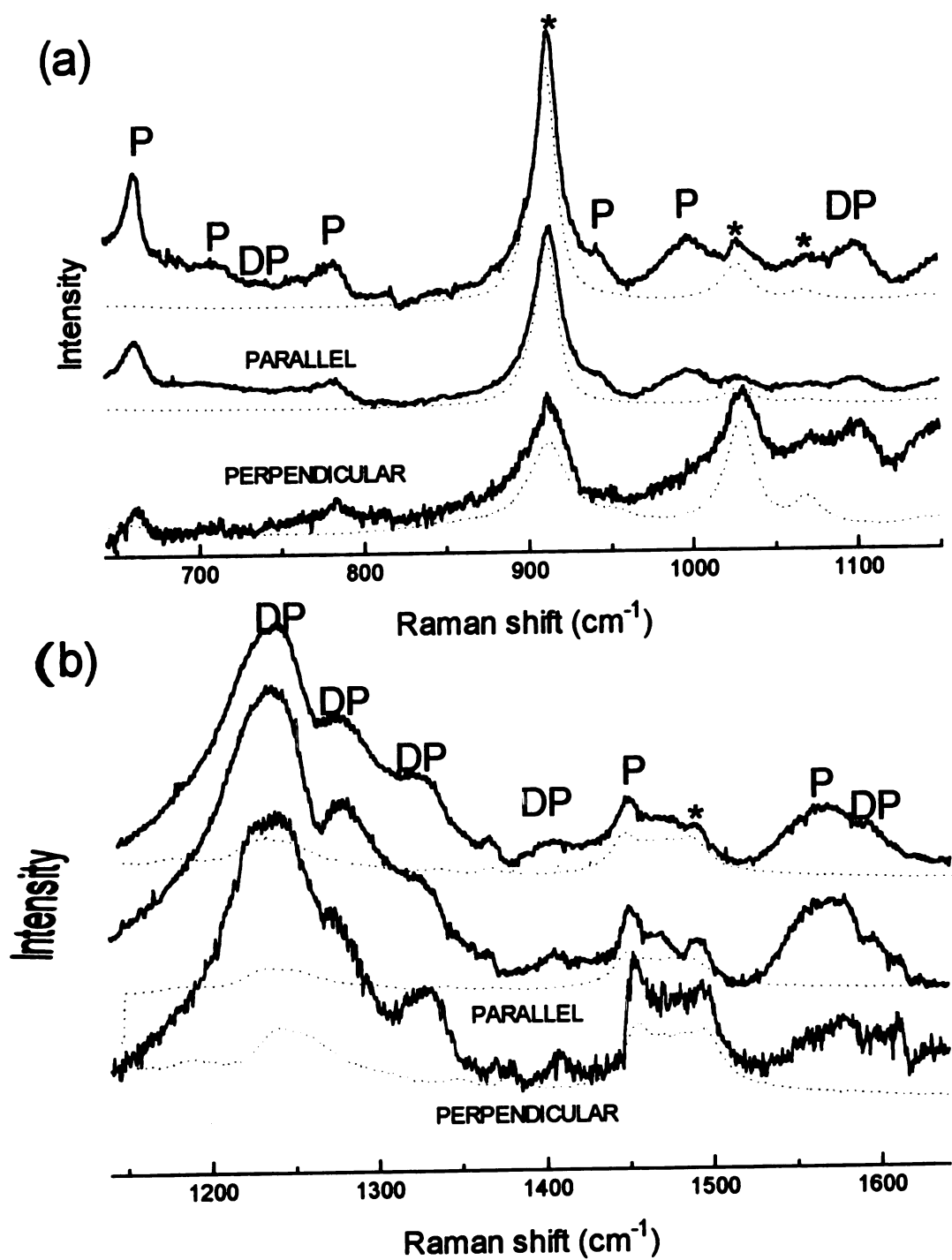


Figure 3.5

Table 3.1 Raman shifts, polarizations and assignments of the observed Raman modes of ZnOEP in its ground and  $S_1$  and  $T_1$  excited states in tetrahydrofuran and pyridine.

tetrahydrofuran			pyridine			$\rho^a$	assignment <sup>b</sup>	character <sup>b</sup>
$S_0$	$S_1$	$T_1$	$S_0$	$S_1$	$T_1$			
669	664	665	669	663	663	p	v <sub>7</sub>	$\nu(C_aN)$ , $\delta(C_aC_mC_a)$ , $\delta(C_aC_m)$
	710 <sup>c</sup>					p		
730 <sup>c</sup>	731 <sup>c</sup>	729 <sup>c</sup>	733 <sup>c</sup>	729 <sup>c</sup>		p		
753		753	752 <sup>c</sup>			dp		
765 <sup>c</sup>	764 <sup>c</sup>					p		
		781				p		
	817 <sup>c</sup>					dp		
1025 <sup>d</sup>	997	996	e	e	e	p	$\nu(C_1C_2)$	$\nu(C_1C_2)$
	1096	1097		1097	1096	dp		
1138	1135	1138	1135	1136	1135	p	v <sub>5</sub>	$\nu(C_aC_b)$ , $\nu(C_bC_1)$
1211			1210			dp	v <sub>13</sub>	$\delta(C_mH)$ , $\nu(C_aC_b)$
		1239			1240	dp		
1261	1258		1262	1258		p	CH <sub>2</sub> -twist	$\delta(C_bC_1H)$ , $\delta(C_2C_1H)$
		1276			1276	dp		
1320	1313		1319	1315		p	CH <sub>2</sub> -wag	$\delta(C_bC_1H)$ , $\delta(C_2C_1H)$
		1330				dp		
1375	1359		1373	1353		p	v <sub>4</sub>	$\nu(C_aN)$ , $\nu(C_aC_b)$
	1429 <sup>f</sup>			1429		dp		
1486	1450	1450	1484	1447		p	v <sub>3</sub>	$\nu(C_aC_m)$ , $\nu(C_bC_b)$
1558	1582 <sup>f</sup>	1582 <sup>f</sup>	1558			dp	v <sub>11</sub>	$\nu(C_bC_b)$
1584	1564	1564	1583	1564	1566	p	v <sub>2</sub>	$\nu(C_bC_b)$
1613			1611			dp	v <sub>10</sub>	$\nu(C_aC_m)$

<sup>a</sup> p, polarized; dp, depolarized. <sup>b</sup> From ref 12b. <sup>c</sup> Weak. <sup>d</sup> Evident at higher porphyrin concentrations. <sup>e</sup> Obscured by solvent modes. <sup>f</sup> Identified by polarization measurements.

st

p

n

a

n

o

3

P

v

s

s

P

S

R

S

C

state spectra of the  $T_1$  state obtained by using nanosecond Q-switched Nd:YAG lasers as pump and probe sources (Figure 3.6). The lineshapes and intensities from Figure 3.6 are nearly identical with the picosecond  $T_1$  results in Figure 3.4.

At a pump-probe time delay of 2 ns (Figure 3.2), modes characteristic of both  $S_1$  and  $T_1$  are seen. Overall, the temporal evolution of the singlet into the triplet, as monitored by the Raman spectra in Figure 3.2, shows excellent agreement with earlier optical work in which the lifetime of the singlet state was determined to be 2.5 ns.<sup>7</sup>

The  $S_1$  and  $T_1$  modes remain observable when we use pyridine as a solvent. Figure 3.7 shows Raman spectra of ZnOEP in pyridine with the excitation pulse preceding the probe pulse by 100 ps and 27 ns. Since pyridine has analogous vibrational frequencies with that of the pyrrole rings in porphyrins, the solvent features were subtracted out of all spectra involving ZnOEP dissolved in pyridine.

The scaling criteria for subtraction of solvent were similar to those used for subtraction of ground state features. Solvent modes that did not overlap in frequency with porphyrin modes were subtracted out such that no negative peaks appeared. This subtraction was done to the ground state spectrum in Figure 3.7b by using the  $1599\text{ cm}^{-1}$  solvent mode as the reference. This technique revealed ground state porphyrin modes such as the  $\nu_{13}$  ( $1211\text{ cm}^{-1}$ ),  $\nu_2$  ( $1582\text{ cm}^{-1}$ ), and  $\nu_3$  ( $1486\text{ cm}^{-1}$ ), modes that were previously buried under strong pyridine modes. Comparison with known ZnOEP spectra verified the validity of this approach.<sup>13</sup> This approach was then applied to the time-dependent high frequency spectra.

**Figure 3.6** Time-resolved resonance Raman difference spectra taken using nanosecond Q-switched Nd:YAG laser pulses as pump and probe. Spectra are shown for (a) ground state (g.s.), (b) time delay between pump and probe of 13 ns, (c) scaled difference spectrum, (d) parallel polarization, and (e) perpendicular polarization. The wavelength of the pump pulse was 532 nm, and the probe wavelength was 437.5 nm. The ground state spectrum was taken in the absence of a pump pulse. The concentration of ZnOEP was  $5 \cdot 10^{-3}$  M in THF.

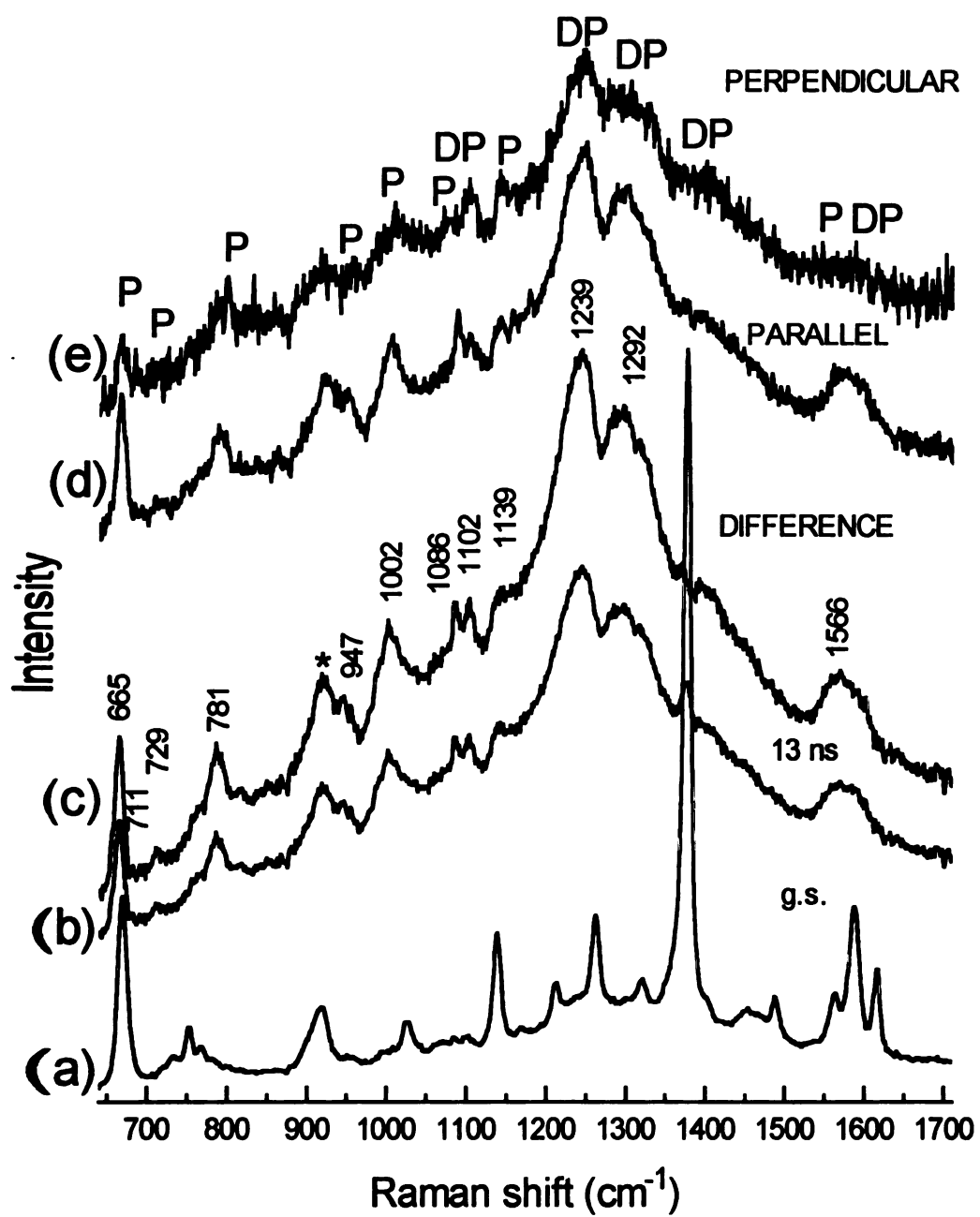


Figure 3.6



**Figure 3.7** Time-resolved resonance Raman difference spectra of ZnOEP in pyridine in (a) low-wavenumber and (b) high-wavenumber range. The ground state features observed in Figure 3.7 at various delays for high and low frequencies have been subtracted out such that no negative peaks appear by using techniques identical to that used in Figure 3.2. Solvent spectra acquired immediately after the experiment were used to subtract out the strong solvent features which obscure the 27 ns spectrum. The peak positions of the vibrational modes are collected in Table 3.1. Asterisks mark artifacts arising from subtraction of the pyridine solvent features.

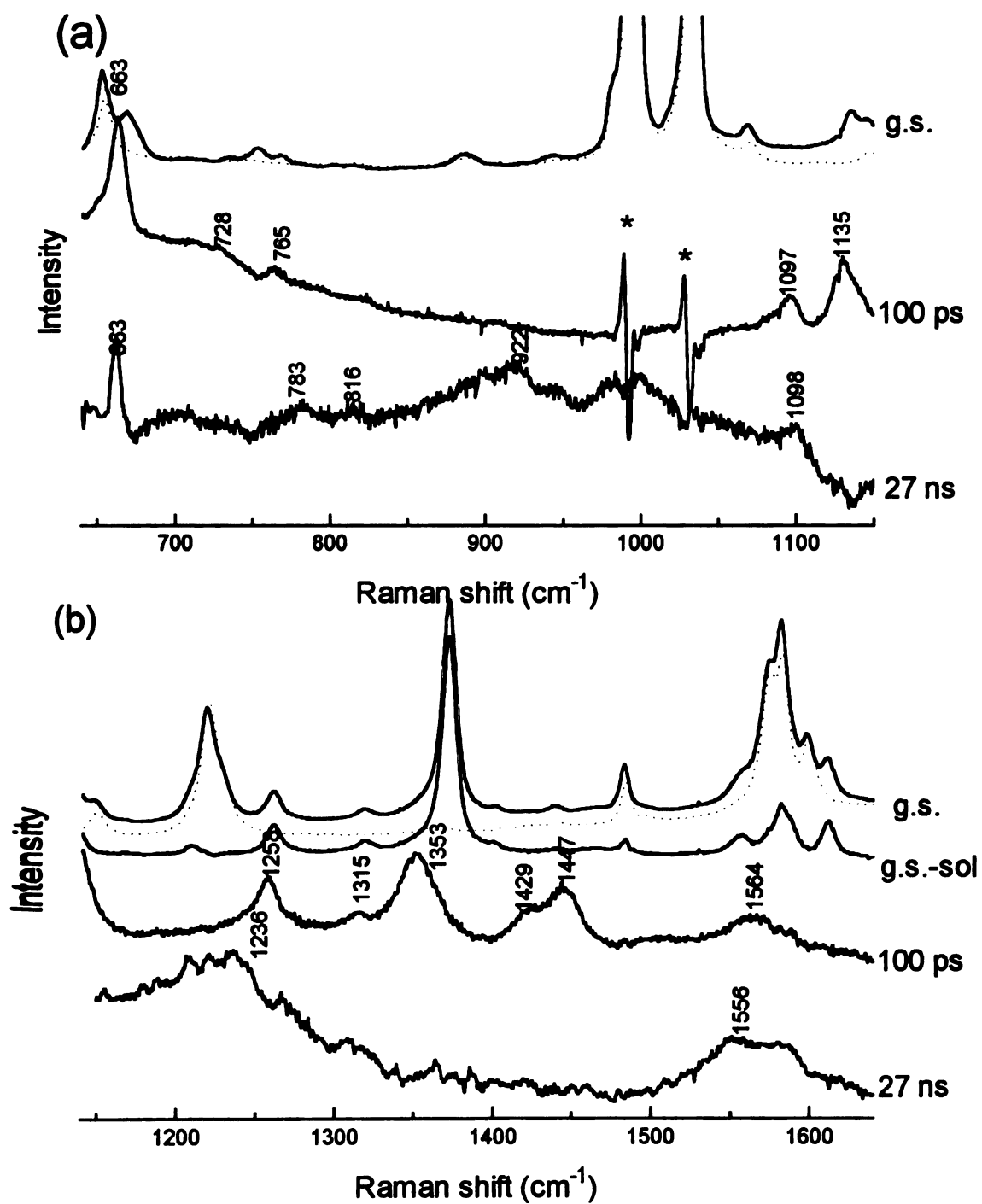


Figure 3.7

This same approach was used for the low frequency spectra in Figure 3.7a using the 991 and 1032  $\text{cm}^{-1}$  modes as the reference. However, the low frequency subtraction left derivative type features in these regions. These artifacts were unavoidable, probably due to the strong intensities of these solvent bands ( $\sim 10$  times the intensity of the strongest porphyrin modes).

The 100 ps spectrum reproduces the modes observed in the 100 ps and 800 ps spectra from Figure 3.2 quite closely. The slight differences in frequency and intensity may be attributed to coordination differences between the two solvents. (The 27 ns high frequency spectrum is somewhat obscured by strong pyridine scattering at 1219  $\text{cm}^{-1}$  and 1582  $\text{cm}^{-1}$ ).

Polarization dependent measurements on ZnOEP in pyridine were carried out and are displayed in Figure 3.8 and Figure 3.9. The Raman difference spectra in Figure 3.8 show the polarization dependence of ZnOEP with the excitation pump pulse preceding the probe pulse by 100 ps. Likewise, the Raman difference spectra in Figure 3.8 show polarization dependence when the pump pulse is 27 ns prior to the probe pulse. All spectra were solvent and ground state feature subtracted. The vibrational mode assignments based on these measurements are also listed in Table 3.1.

In Table 3.1, ZnOEP modes in the  $S_1$  and  $T_1$  states are labeled with reference to those reported for NiOEP.<sup>13</sup> Assignments for excited state vibrations were made by analogy to ground state vibrations. For totally symmetric modes this was facilitated by the one to one correlation that appears to exist between modes in the ground and excited state, respectively. For the  $S_1$  spectra, the depolarized modes are almost all of low

**Figure 3.8** Time-resolved resonance Raman difference spectra of ZnOEP in pyridine taken at 100 ps in (a) low and (b) high wavenumber regions. Spectra are shown for all polarizations, and parallel and perpendicular polarizations. Qualitative assignments to symmetries of vibrational modes are labeled as either totally symmetric (P), or nontotally symmetric (DP). Asterisks mark artifacts arising from subtraction of the pyridine solvent features.

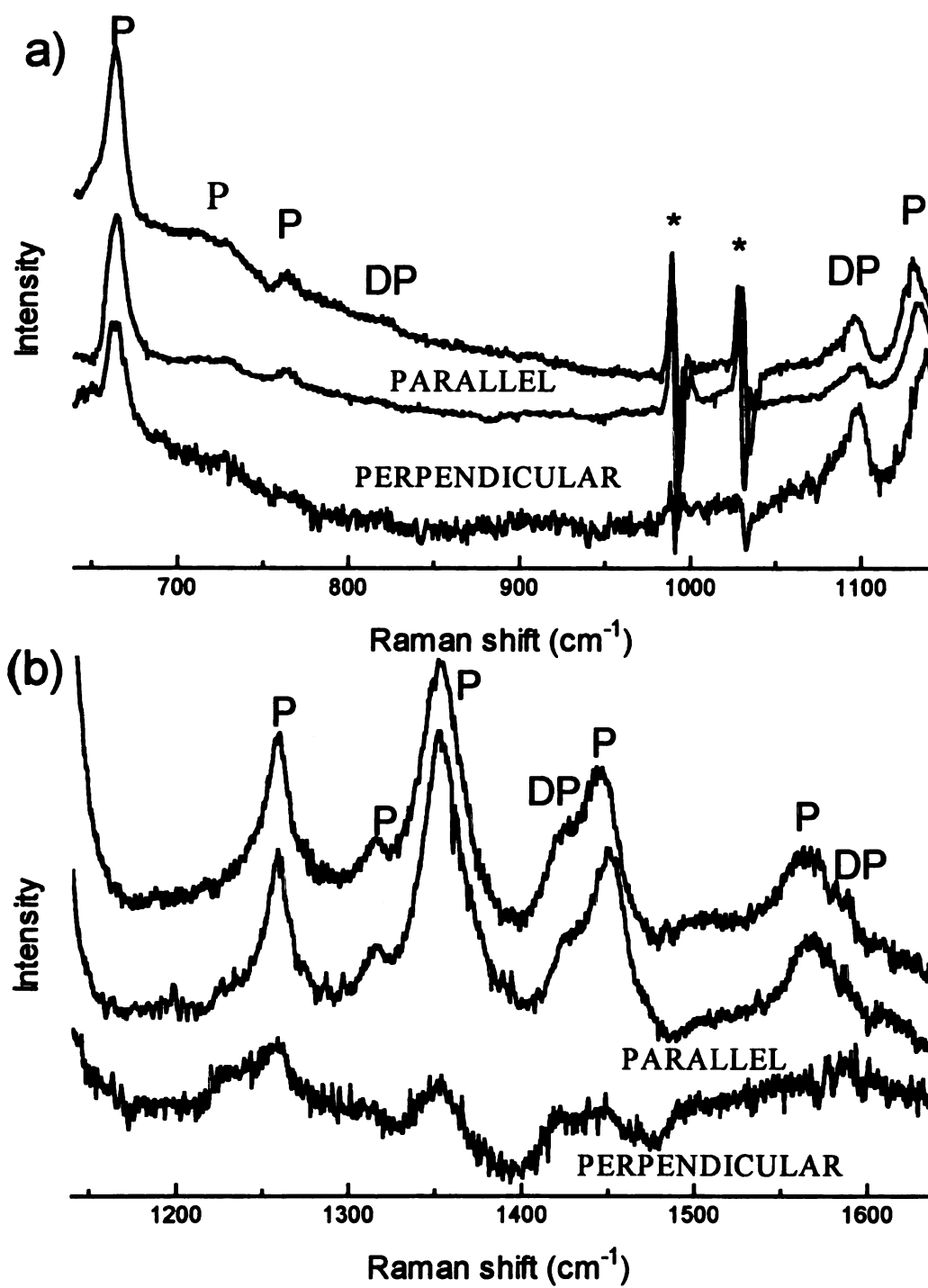


Figure 3.8

**Figure 3.9** Time-resolved resonance Raman difference spectra of ZnOEP in pyridine taken at 27 ns in (a) low and (b) high wavenumber regions. Spectra are shown for all polarizations, and parallel and perpendicular polarizations. Qualitative assignments to symmetries of vibrational modes are labeled as either totally symmetric (P), or nontotally symmetric (DP). Asterisks mark artifacts arising from subtraction of the pyridine solvent features.

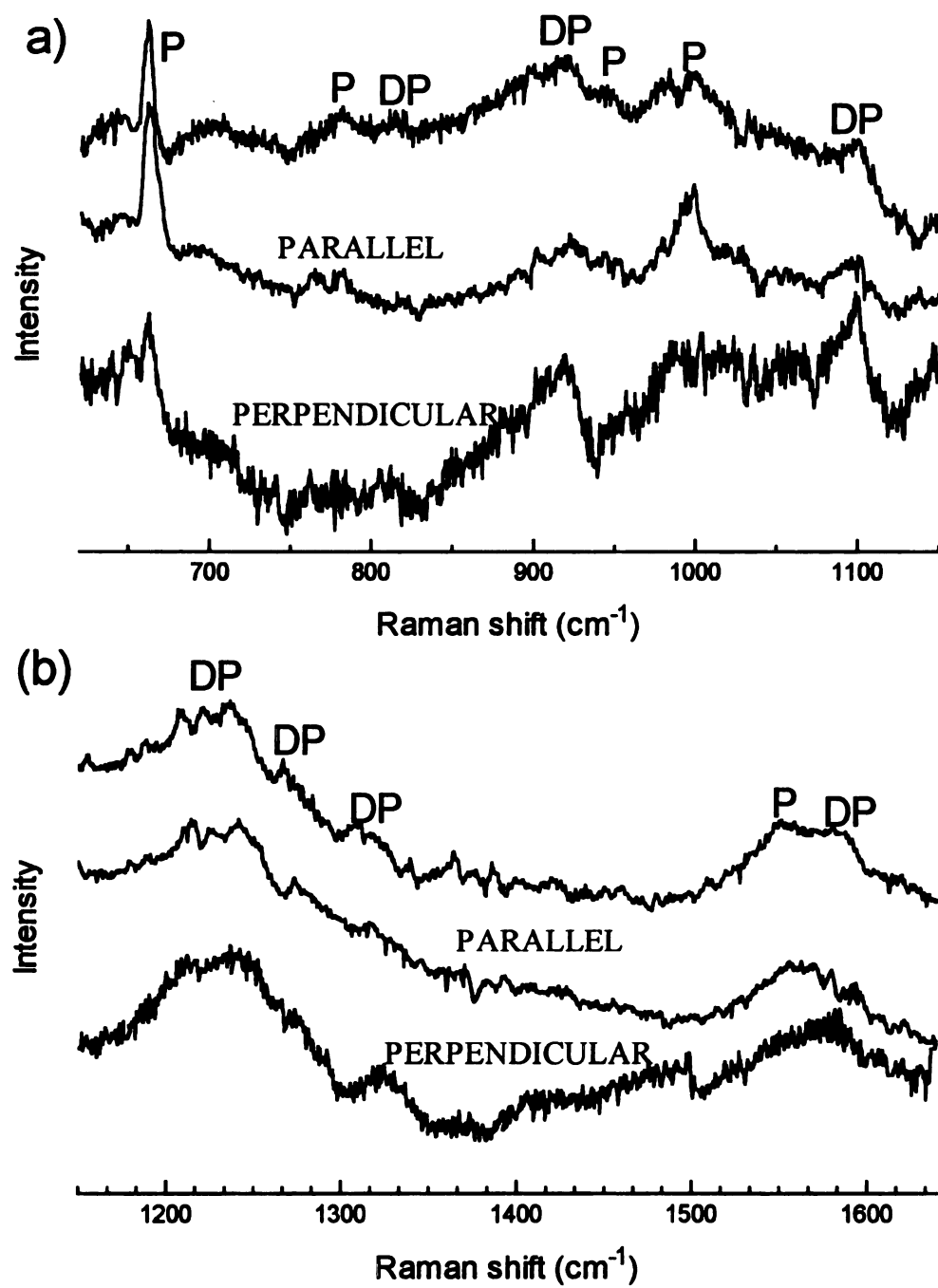


Figure 3.9

intensity, and some could only be identified by polarization measurements. We discuss the  $S_1$  spectrum below and then consider the  $T_1$  data briefly.

#### IV. DISCUSSION

The electronic configuration of metallooctaethylporphyrins in the ground excited singlet state is known to have an  $a_{1u}a_{1u}$  configuration. The lowest excited state configurations,  $^1(a_{1u},e_g)$  and  $^1(a_{2u},e_g)$ , are of nearly equivalent energies and both have  $E_u$  symmetry. Hence, they strongly mix via configuration interaction.<sup>14</sup> Molecular orbital calculations predict that the individual modes should show sensitivity to the electron occupancy of the  $a_{1u}$  and  $e_g$  orbitals.<sup>15</sup> Diagrams that depict the relative electron occupancy of these three molecular orbitals can be seen in Chapter 1, Figure 1.6. Modes involving primarily stretches of  $C_aC_m$ ,  $C_aC_b$ , or  $C_aN$  bonds are predicted by basic Gouterman molecular orbital theory to shift to lower frequencies in the  $S_1$  state, whereas modes comprising mostly  $C_bC_b$  stretches are predicted to shift to higher frequencies. Earlier work on both metalloporphyrin  $\pi$ -cation and  $\pi$ -anion radicals has demonstrated the generality of these orbital occupancy arguments in the assignment of vibrational modes and electronic state ordering.<sup>16</sup> In general, our assignments of the vibrational modes in  $S_1$  agree with predictions based on the orbital occupancy assignments above. An exception to this is the behavior of  $\nu_2$ , which apparently shifts to lower, rather than higher, frequency in the  $S_1$  state. Perng and Bocian<sup>16c</sup> observed similar behavior for some modes in the ZnOEP  $\pi$ -anion radical, that is, frequency shifts that were counter to those predicted for  $e_g$  orbital occupancy, and suggested that structural changes of the macrocycle in the anion



radical state were responsible. From the behavior of  $\nu_2$ , it appears that similar phenomena may occur to some extent in the  $S_1$  state.

As opposed to our previous work on the  $T_1$  state of ZnTPP,<sup>2a,b</sup> and that described below for  $T_1$  of ZnOEP, Jahn-Teller distortion occurs to only a minor extent, if at all, in the  $S_1$  state. This conclusion follows from our observations in Figure 3.3 and the frequency assignments in Table 3.1 that only weak enhancement of depolarized modes occurs, and that the number of totally symmetric modes does not increase relative to the ground state. This conclusion agrees with theoretical predictions that Jahn-Teller effects in the  $S_1$  state will be minimized by configuration interaction.<sup>17</sup>

In the  $T_1$  state, the Raman shifts of many modes coincide with those in the  $S_1$  state. The depolarized modes though, are significantly stronger than in the  $S_1$  state (Figure 3.3, Figure 3.4, and Table 3.1). The broad feature at  $1239\text{ cm}^{-1}$  with a shoulder at  $1276\text{ cm}^{-1}$  may be comprised of several underlying modes. The appearance and shape of this spectral feature was independent of whether tetrahydrofuran or pyridine was used as the solvent. Ethyl modes are expected to occur in this frequency range, and although they are not strongly enhanced in the ground state,<sup>13</sup> they may gain intensity in the excited state and account for the spectral congestion. The shift of  $\nu_2$  in the triplet state, as in  $S_1$ , doesn't follow the predictions based on the molecular orbital calculations. As in H<sub>2</sub>OEP and ZnTPP,<sup>2</sup>  $\nu_4$  is not strongly enhanced in the  $T_1$  state of ZnOEP. The enhancement of depolarized modes in the  $T_1$  state strongly suggests that Jahn-Teller distortion is present in this state, in agreement with the now general observation of structural rearrangement in triplet states of metalloporphyrin chromophores.<sup>2,18</sup>

To conclude, the observations presented here on the  $S_1$  and  $T_1$  states of ZnOEP test and confirm theoretical predictions that Jahn-Teller distortion is significantly more pronounced in the triplet than in the singlet state. This conclusion has possible ramifications for the initial steps in the photosynthetic process. Previous work on metalloporphyrin and metallochlorin cation radicals has shown that these are formed with little change in the normal coordinate composition and hence little nuclear rearrangement of the macrocycle.<sup>16a,16b,19</sup> Our demonstration here that the light-induced formation of the singlet state also proceeds in the absence of large nuclear rearrangements means that charge separation from this state to form the cation radical product state may occur with minimal reorganization energy.<sup>20,21</sup> Accordingly, the rate of the initial energy conversion step can be fast, as it is observed experimentally to be.<sup>1</sup>

## LIST OF REFERENCES

- (1) see, e.g.,: Research in Photosynthesis, *Proceedings of the IXth International Congress on Photosynthesis*; Murata, N., Ed.; Kluwer Academic Publishers: Dordrecht, 1992.
  
- (2) (a) Walters, V. A.; de Paula, J. C.; Babcock, G. T.; Leroi, G. E. *J. Am. Chem. Soc.* **1989**, 111, 8300-8302. (b) Nam, H. H.; Walters, V. A.; de Paula, J. C.; Babcock, G. T.; Leroi, G. E. In *Proceedings of the XIIth International Conference on Raman Spectroscopy*; Durig, J. R.; Sullivan, J. F., Eds.; Wiley and Sons: New York, 1990, p 618. (c) Reed, R. A.; Purello, R.; Prendegast, K.; Spiro, T. G. *J. Phys. Chem.* **1991**, 95, 9720-9727. (d) Sato, S.; Asano-Someda, M.; Kitagawa, T. *Chem. Phys. Lett.* **1992**, 189, 443-447. (e) Kumble, R.; Hu, S.; Loppnow, G. R.; Vitols, S. E.; Spiro, T. G. *J. Phys. Chem.* **1993**, 97, 10521-10523. (f) Kreszowski, D. H.; Babcock, G. T. *Biophys. J.* **1993**, 64, a276.
  
- (3) (a) Findsen, E. W.; Shelnutt, J. A.; Ondrias, M. R., *J. Phys. Chem.* **1988**, 92, 307-314. (b) Apanasevich, P. A.; Krugliyk, S. G.; Kvach, V. V.; Orlovich, V. A. in *Time Resolved Vibrational Spectroscopy V*; Takahashi, H., Ed.; Springer-Verlag: Berlin, 1992.
  
- (4) Bell, S. E. J.; Al-Obaidi, A. H. R.; Hegarty, M.; Hester, R. E.; McGarvey, J. J. *J. Phys. Chem.* **1993**, 97, 11599-11602.
  
- (5) (a) Rodriguez, J.; Holten, D., *J. Chem. Phys.* **1989**, 91, 3525-3531. (b) Rodriguez, J.; Holten, D., *J. Chem. Phys.* **1990**, 92, 5944-5949. (c) Bilsel, O.; Rodriguez, J.; Holten, D., *J. Phys. Chem.* **1990**, 94, 3508-3512. (d) Rodriguez, J.; Kirmaier, C.; Holten, D. *J. Chem. Phys.* **1991**, 94, 6020-6029. (e) Vos, M. H.; Rappaport, F.; Lambry, J.-C.; Breton, J.; Martin, J.-L. *Nature* **1993**, 363, 320-325.
  
- (6) For other or comparable methods to measure resonance Raman with picosecond time-resolution see, e.g., (a) Gustafson, T. L.; Iwata, K.; Weaver, W. L. in *Ultrafast Phenomena VII*; Harris, C. B.; Ippen, E. P., Mourou, G. A.; Zewail, A. H., Eds.; Springer-Verlag: New York, 1990. (b) Iwata, K.; Hamaguchi, H. *Chem. Phys. Lett.* **1992**, 196, 462-468. (c) Weaver, W. L.; Huston, L. A.; Iwata, K.; Gustafson, T. L. *J. Phys. Chem.* **1992**, 96, 8956-8961. (d) Butler, R. M.; Lynn, M. A.; Gustafson, T. L. *J. Phys. Chem.* **1993**, 97, 2609-2617.

- (7) Excited state absorption spectra and lifetimes on a picosecond time scale have been measured by Rodriguez, *et. al.*: Rodriguez, J.; Kirmaier, C.; Holten, D. W. *J. Am. Chem. Soc.* **1989**, 111, 6500-6501. The S<sub>1</sub> state of ZnOEP has an absorption maximum at 450 nm; the ground state absorption at this wavelength is low. With high yield, the S<sub>1</sub> state converts into the T<sub>1</sub> state, which has an absorption maximum at 435 nm.
- (8) Kreszowski, D. H.; Deinum, G.; Babcock, G. T. *Biophys. J.* **1994**, 66(2), a374.
- (9) Kreszowski, D. H.; Deinum, G.; Babcock, G. T. *J. Am. Chem. Soc.* **1994**, 116, 7463-7464.
- (10) Atkinson, G. H.; Brack, T. L.; Blanchard, D.; Rumbles, G. *Chem. Phys.* **1989**, 131, 1-15.
- (11) For a description of the nanosecond time-resolved Raman apparatus see the thesis of Varotsis, Constantinos, *Diss. Abstr. Int. B* 1991, 51(12) pp 52-54.
- (12) For a description of the low temperature back-scattering dewar see the thesis of Kean, Robert, *Diss. Abstr. Int. B* 1988, 48(7), pp 42-43.
- (13) (a) Abe, M.; Kitagawa, T.; Kyogoku, Y. *J. Chem. Phys.* **1978**, 69, 4526-4534. (b) Li, X.-Y.; Czernuszewicz, R. S.; Kincaid, J. R.; Stein, P.; Spiro, T. G. *J. Phys. Chem.* **1990**, 94, 47-61.
- (14) (a) Spellane, P. J.; Gouterman, M.; Antipas, A.; Liu, Y. C. *Inorg. Chem.* **1980**, 19, 386-391. (b) Shelnutt, J. A.; Ortiz, V. *J. Phys. Chem.* **1985**, 89, 4733-4739.
- (15) Gouterman, M. *J. Mol. Spectroscopy* **1961**, 6, 138-163. We used the coefficients of the frontier molecular orbitals in: Prendergast, K.; Spiro, T. G. *J. Phys. Chem.* **1991**, 95, 9728-9736.
- (16) (a) Oertling, W. A.; Salehi, A.; Chang, C. K.; Babcock, G. T. *J. Phys. Chem.* **1989**, 93, 1311-1319. (b) Czernuszewicz, R. S.; Macor, K. A.; Li, X.-Y.; Kincaid, J. R.; Spiro, T. G. *J. Am. Chem. Soc.* **1989**, 111, 3860-3869. (c) Perng, J.-H.; Bocian, D. F. *J. Phys. Chem.* **1992**, 96, 4804-4811.
- (17) (a) Gouterman, M. *Ann. N.Y. Acad. Sci.* **1973**, 206, 70-83. (b) Shelnutt, J. A.; Cheung, L. D.; Chang, R. C. C.; Yu, N.-T.; Felton, R. H. *J. Chem. Phys.* **1977**, 66, 3387-3398. (c) Cheung, L. D.; Yu, N.-T.; Felton, R. H. *Chem. Phys. Lett.* **1978**, 55, 527-530.

- (18) (a) Langhoff, S. R.; Davidson, E. R.; Gouterman, M.; Leenstra, W. R.; Kwiram, A. L. *J. Chem. Phys.* **1975**, 62, 169-176. (b) van der Waals, J. H.; van Dorp, W. G.; Schaafsma, T. J. in *The Porphyrins*; Dolphin, D., Ed.; Academic Press; New York, 1978, Vol 4, pp 257-312.
- (19) Salehi, A.; Oertling, W. A.; Fonda, H. N.; Babcock, G. T.; Chang, C. K. *Photochem. Photobiol.* **1988**, 48, 525-530.
- (20) Dutton, P. L.; Moser, C. C. *Proc. Natl. Acad. Sci. USA* **1994**, 91, 10247-10250
- (21) (a) Vos, M. H.; Lambry, J. C.; Robles, S. J.; Youvan, D. C.; Breton, J.; Martin, J. *Proc. Natl. Acad. Sci. USA*, **1991**, 88, 8885-8889. (b) Vos, M. H.; Rappaport, F.; Lambry, J.-C.; Breton, J.; Martin, J.-L. *Nature* **1993**, 363, 320-325.

## CHAPTER 4

# VIBRATIONAL ANALYSIS OF ZINC(II) OCTAETHYLPORPHYRIN IN THE LOWEST EXCITED SINGLET STATE

### ABSTRACT

Resonance Raman spectra of the lowest excited singlet state ( $S_1$ ) are reported for ZnOEP and its isotopomers ZnOEP- $d_4$  and ZnOEP- $^{15}N_4$ , as well as for ZnEtio and MgOEP. The Raman active vibrational modes in the  $S_1$  state of ZnOEP were assigned from depolarization ratios, isotopic shifts, and intensity correlations with ground state features. Downward frequency shifts of totally symmetric  $S_1$  porphyrin modes of ZnOEP reflect structural changes of the porphyrin macrocycle. These changes occur along totally symmetric normal modes as indicated by weak enhancement of depolarized modes and a 1:1 correlation between totally symmetric modes in the  $S_1/S_0$  states. This indicates the  $D_{4h}$  symmetry of the  $S_0$  molecule is retained and confirms our earlier conclusion that Jahn-Teller effects are negligible in the  $S_1$  state (Kreszowski, D. H.; Deinum, G.; Babcock, G. T. *J. Am. Chem. Soc.* **1994**, 116, 7463-7464). Based on frequency/core size relationships obtained for porphyrins in the ground state, we estimate that, upon excitation to  $S_1$ , the core size increases by about 0.1 Å. Calculations that include different excited state configurations predict small  $b_{1g}$  distortions in the  $S_1$  state that may be related to increased linewidths of the core modes that indicate inhomogeneity in the macrocycle structure.

## I. INTRODUCTION

The primary step of photosynthetic energy conversion involves charge separation in the reaction center where a chlorophyll complex is oxidized after excitation into its lowest excited  $\pi$ - $\pi^*$  singlet state ( $S_1$ ) by light absorption or by energy transfer from neighboring pigments.<sup>1</sup> The charge separation is stabilized by transfer of the electron to subsequent acceptors and by reduction of the oxidized chlorophyll by a secondary electron donor. Most critical in this process are the electronic and redox properties of the reaction center chlorophylls that are mediated by the protein environment and by exciton interactions between different chromophores.<sup>1,2</sup> More insight in the electronic and structural properties of chlorophylls and related macrocycles is a prerequisite for a better understanding of the structure and functioning of the reaction center. Resonance Raman spectroscopy has proven to be an excellent tool for studies of chlorophylls and the small structural changes of their macrocycles in the transient states, e.g., vide infra the  $S_1$ ,  $\pi$ -anion radical and  $\pi$ -cation radical.

However, not only the static properties of the reaction center are important. According to Marcus theory, the rates of electron transfer in photosynthesis<sup>3</sup> strongly depend on the reorganization energy associated with deformations of the pigments. Large deformations will reduce the rate of electron transfer, leading to less efficient photosynthesis.

Transient absorbance measurements on isolated photosynthetic reaction centers reveal that reorganization associated with low frequency vibrations up to about  $100\text{ cm}^{-1}$  persist on the time scale of charge separation.<sup>4</sup> These vibrations could not be clearly

related to chlorophyll modes and were tentatively attributed to modes involving the surrounding protein. Measurements by Zhu *et al.*<sup>5</sup> showed that, for the NO binding reaction to the heme of myoglobin, similar vibrations can be ascribed to the out-of-plane iron/histidine stretching mode at  $220\text{ cm}^{-1}$ . These latter results indicate that low frequency vibrational modes are coupled to reactions in these pigment-protein complexes.

To fit measurements of electron transfer rates in reaction centers using reorganization mode frequencies as a parameter,<sup>6</sup> high frequency vibrations are also expected to influence the electron transfer rate.<sup>2,7</sup> Higher frequencies, however, cannot be conveniently studied by time-resolved absorbance measurements because of the limited bandwidth of the laser flash. To study the coupling of high frequency vibrations to reactions directly, measurements should be performed in the frequency domain, i.e., using time-resolved Raman or infrared spectroscopy. Picosecond time resolved resonance Raman measurements<sup>8</sup> performed on, e.g.,  $S_1$  excited *trans*-stilbene and analogues have shown that depolarization ratios, linewidths, mode intensities and frequency positions can give valuable information about the dynamic processes occurring in transient excited states.

Some Raman experiments have been performed with intact photosystems,<sup>9</sup> but most work to date has been done with model porphyrins with a symmetry higher than that of chlorophyll. The higher symmetry of, e.g., Zn(II) octaethylporphyrin (ZnOEP) and Zn(II) tetraphenylporphyrin (ZnTPP), leads to Raman spectra that can be interpreted more easily and can provide bench marks against which analogous data for the lower symmetry macrocycles may be compared.



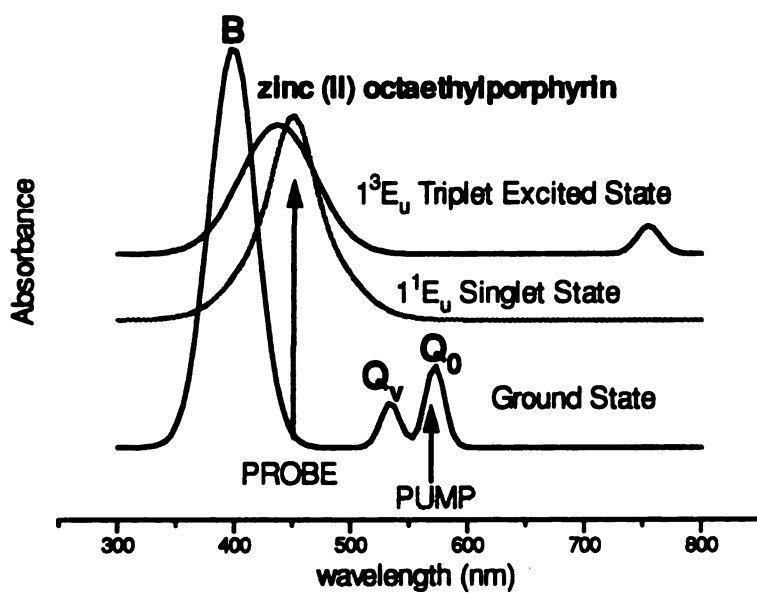
The ground state configurations of ZnOEP and ZnTPP retain a molecular symmetry of  $D_{4h}$  and the spectral properties can be explained by using the four orbital model of Gouterman.<sup>10</sup> According to that model two electronic transition states, the Q- and B-(Soret) states, arise from transitions from two nearly degenerate orbitals with  $a_{1u}$  and  $a_{2u}$  symmetry, respectively, to a degenerate pair of orbitals with  $e_g$  symmetry. Strong configuration interaction leads to a more intense band in the blue (Soret) and a less intense band in the red (Q). Gouterman orbitals depicting the relative electron occupancy of these three molecular orbitals can be seen in Chapter 1, Figure 1.6.<sup>10,46</sup> The absorption spectrum of ZnOEP and an energy level diagram are shown in Figure 4.1.

Because they are models for intermediates in the electron transport chain in the photosynthetic reaction center, a number of experiments have been performed on porphyrin  $\pi$ -cations and  $\pi$ -anions. It was shown that, upon oxidation of the porphyrin, an electron is removed from the  $a_{1u}$  or  $a_{2u}$  orbital, respectively, depending on whether the porphyrin is a metallo-OEP or a metallo-TPP.<sup>11,12</sup> Oxidation has little effect on the overall geometry of the macrocycle.<sup>13,14</sup> Measurements performed by Salehi *et al.*<sup>15</sup> on  $\pi$ -cations of metallomethyloctaethylchlorin (metallo-MeOECs), which have one reduced pyrrolic ring, showed a significant mode composition change due to the presence of this reduced pyrrolic ring, but they concluded, similar to the earlier conclusions for porphyrins,<sup>13,14</sup> that upon  $\pi$ -cation formation the general structure of the macrocycle remains the same.

Large frequency shifts have been reported for the modes of  $\pi$ -anions of metal-TPPs due to Jahn-Teller distortion of the ground state anion.<sup>16,17</sup> This distortion originates from the presence of one electron in degenerate orbitals.<sup>18</sup> In metallo-OEP  $\pi$ -

**Figure 4.1** a) Metalloporphyrin absorption characteristics for ground and excited states of zinc(II) octaethylporphyrin (ZnOEP) in methylene chloride. The  $S_1$  and  $T_1$  spectra are taken with reference to results of Rodriquez, J.; Kirmaier, C.; Holten, D. W. *J. Am. Chem. Soc.* **1989**, 111, 6500-6501. b) Energy level diagram representing observed energy levels for ZnOEP.

a)



b)

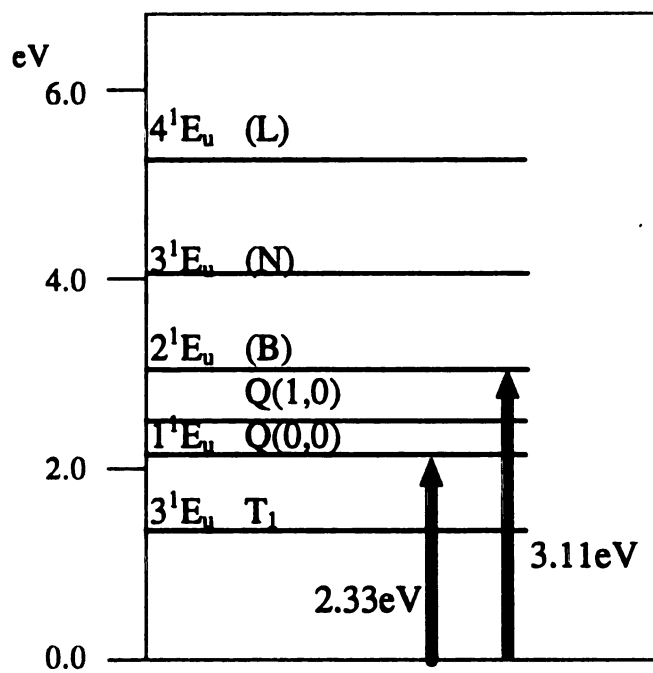


Figure 4.1

anions the shifts are only small and consequently Jahn-Teller effects are assumed to be much weaker.<sup>19</sup> This further indicates that the details of the macrocycle structure and electronics are influenced by the type and location of peripheral substituents.

Resonance Raman experiments performed with nanosecond lasers permitted studies of triplet states of metalloporphyrins.<sup>20,21</sup> As for the  $\pi$ -anion, the macrocycle of ZnTPP is Jahn-Teller distorted in the triplet state.<sup>20</sup> Because the lifetimes of the  $S_1$  excited states of free-base porphyrins are longer, nanosecond lasers could also be used to study their characteristics.<sup>22,23</sup> However, the results of the latter experiments have been interpreted only to a limited extent. Experiments with even higher time-resolution, picoseconds, have been performed on d-d states,<sup>24,25,26</sup> of nickel porphyrins and recently by us on the singlet excited state ( $S_1$ ) of ZnOEP.<sup>27,28,29</sup> Such types of experiments are especially important for unravelling photosynthesis since femto- or picosecond time resolution is necessary for more insight in dynamic processes of electronically excited macrocycles. Previous transient absorbance experiments showed that vibrational relaxation processes like those in reaction centers take place on a time scale of up to about 20 ps in model porphyrins.<sup>30</sup>

Here, we present results from extensive picosecond transient Raman experiments done on the model system ZnOEP, its isotopomers ZnOEP- $d_4$ , ZnOEP- $^{15}N_4$ , and Zn(II) etioporphyrin I (n.a.), and MgOEP. We especially focused our experiments on the structural changes, e.g., Jahn-Teller distortions, and will test whether these are important for the lowest excited singlet states ( $S_1$ ) of ZnOEP.

Combination of the isotopomer data and depolarization measurements was essential to assign the Raman active vibrational modes and to estimate changes of the macrocycle structure of ZnOEP in the  $S_1$  state. The Raman data on that state reveal frequency changes that indicate core size expansion but retention of  $D_{4h}$  symmetry, and suggest the relative absence of Jahn-Teller distortion in  $S_1$ . The directionality of the vibrational shifts in the  $S_1$  state of ZnOEP indicates that excitation to this state cannot simply be described by one electron promotion, but that several configurations need to be taken into account. To rationalize the shifts of the modes more quantitatively, we calculated natural orbitals, which are combinations of molecular orbitals that can describe electronic transitions involving configuration interaction. These calculations predict a small  $b_{1g}$  distortion of the porphyrin in the  $S_1$  excited state, which may be related to the experimentally observed increased width of the porphyrin core modes.

## II. MATERIALS AND METHODS

Zn(II) octaethylporphyrin (ZnOEP) and Mg(II) octaethylporphyrin (MgOEP) were purchased from Aldrich and used without further purification. Exchange of the hydrogen for deuterium in ZnOEP- $d_4$  was accomplished by using the  $D_2SO_4/D_2O$  method.<sup>31</sup> The  $N^{15}$ -labeled compound (ZnOEP- $^{15}N_4$ ) was prepared from  $Na^{15}NO_2$  and ethylpropionyl acetate.<sup>32</sup> Zinc(II)-Etioporphyrin-I (ZnEPI) was purchased from Midcentury Chemical Company (Posen, Illinois) and used as received. The solvent tetrahydrofuran (Baker Analyzed reagent) was used without further purification. The integrity of the porphyrins

were confirmed before and after the measurements by UV-visible absorption spectroscopy on a Perkin Elmer Lambda 5 spectrometer.

The experimental setup used for these experiments is that shown in Figure 2.1 (Chapter 2). Raman scattering was collected in a standard 90° orientation and focused by refractive optics into a single grating spectrometer (Jobin Yvon HR 640, 2400 grooves/mm grating blazed at 400 nm) with a spectral resolution of 7 cm<sup>-1</sup>. A charge-coupled device (Princeton Instruments, model LN/CCD 1152UV) cooled to -100°C was used for detection. A dye laser (Coherent 702) tuned to 450 nm with Stilbene 420 as the dye was used to generate the Raman spectra. This dye laser was synchronously pumped with the third harmonic of a mode locked Nd:YAG laser (Coherent Antares 76-s). The wavelength of 450 nm was chosen because the porphyrin has a maximum near this wavelength in the S<sub>1</sub> state,<sup>33</sup> whereas the absorption of the porphyrin in the ground state is very low. To excite the porphyrins at the maximum of the Q(0,0) band a second dye laser (Coherent 702) with pyrromethene 567 as the dye<sup>34</sup> was tuned to 572 nm for the zinc porphyrins, and 575 nm for MgOEP. This laser was pumped by the second harmonic of the Nd:YAG. Both dye lasers produce pulses of about 7 ps (FWHM). Cavity dumpers on the dye lasers were used to create a time delay of 790 ns between subsequent pulses and to increase the peak power of the individual pulses. The pulse energies of the pump and probe lasers were 80 nJ and 30 nJ, respectively. Most experimental setups use repetition rates between 50 Hz and several KHz rather than MHz.<sup>8,35</sup> Even though MHz repetition rates complicate the sample setup, an advantage is that high average laser powers can be used resulting in high signal-to-noise ratios. At low repetition rates, high average powers

lead to peak powers that are high enough to produce undesirable non-linear effects in the sample. Chapter 2 ( Flowing Liquid Jet Assembly) gives a more complete discussion about the relationship between pulse repetition rates and laser powers. A microscope objective (Newport M-5X) was used to focus these collinear beams to 15  $\mu\text{m}$  spots on the sample. A low-pass filter (Andover blue dichroic, 505FD64505, 50% transmittance at 515 nm) was used to prevent scattered light from the pump beam and fluorescence from entering the spectrometer. To refresh the sample between individual pulses a rapid flowing jet similar to that of Atkinson *et al.*<sup>36</sup> was used. Spectra were recorded with shutters in the probe and pump beam pathways, respectively, and were accumulated for two minute time periods. The shutters for the probe and pump beams were used as described in Chapter 2 under “quasi-simultaneous technique”. This permitted easy elimination of temporal instabilities from the laser or the sample jet during postprocessing of the data. Spectra of  $S_1$  excited state porphyrins were determined by a scaled subtraction of the contribution of ground state porphyrins from the raw data. Solvent contributions were also eliminated in a similar fashion. The uncertainties in most of the peak positions are about  $2\text{ cm}^{-1}$ . To determine the polarization of the Raman active vibrations, the Raman spectra were recorded with a dichroic sheet polarizer in front of the spectrometer.

### III. RESULTS

Raman spectra of ZnOEP (n.a.), ZnOEP- $d_4$ , ZnOEP- $^{15}\text{N}_4$ , ZnEPI (n.a.) and MgOEP (n.a.) in the ground state, without a pump pulse preceding the probe pulse at 450 nm, are shown in Figure 4.2. Raman spectra taken under the same conditions but detected

**Figure 4.2** Ground state Raman spectra of ZnOEP (n.a.), ZnOEP-*d*<sub>4</sub>, ZnOEP-<sup>15</sup>N<sub>4</sub>, ZnEPI (n.a.) and MgOEP (n.a.). The probe beam was at 450 nm. Each porphyrin was dissolved in tetrahydrofuran. The concentration for all porphyrins was  $5 \cdot 10^{-3}$  M, except ZnEPI, which was  $1 \cdot 10^{-3}$  M.



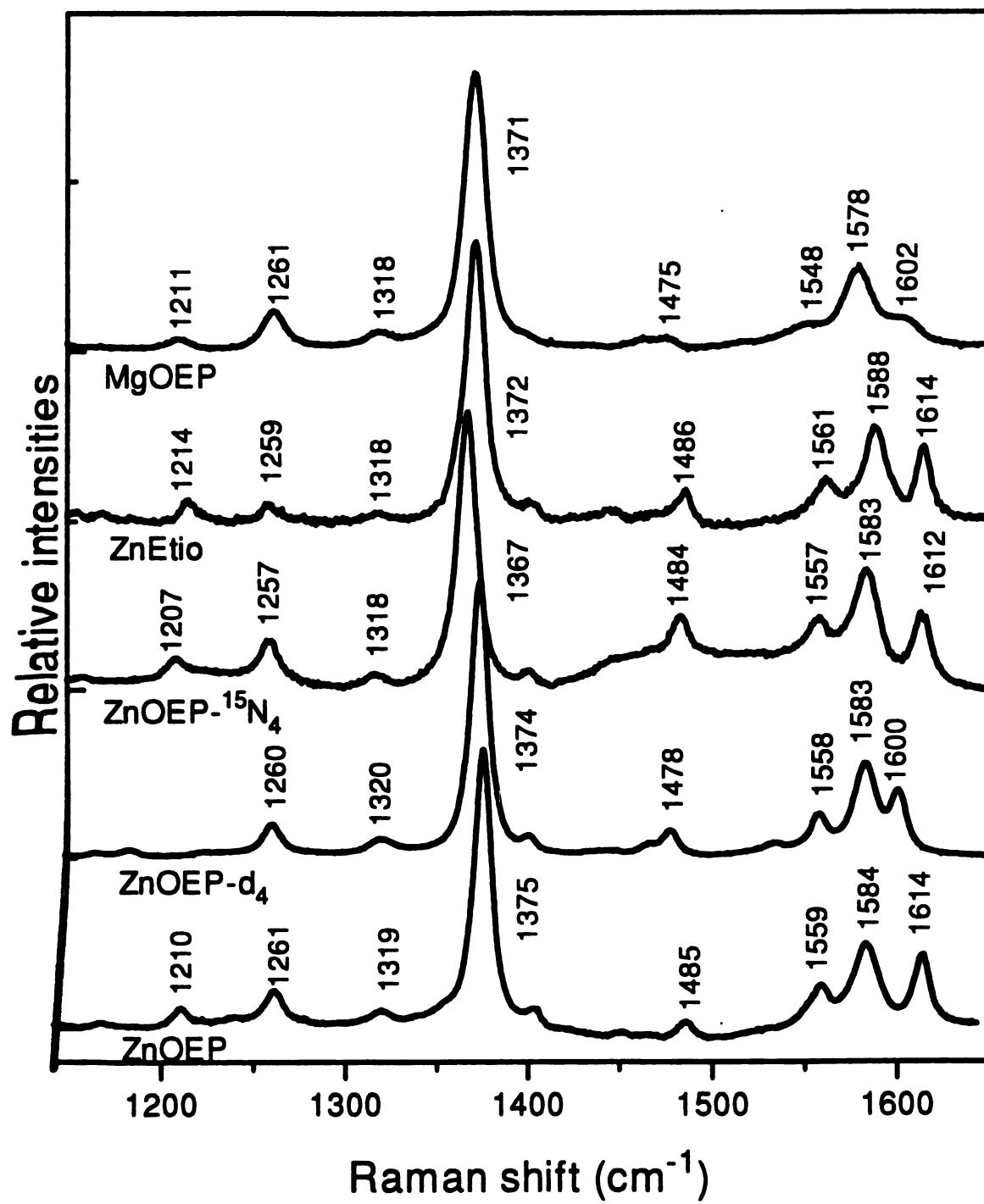


Figure 4.2

with a polarizer in front of the spectrometer are given in Figure 4.3. Raman frequencies and vibrational assignments for ZnOEP- $d_4$ , ZnOEP- $^{15}N_4$ , ZnEPI (n.a.) and MgOEP (n.a.) are given in Table 4.1, with Raman frequencies listed as isotopic shifts relative to ZnOEP(n.a.). Assignments for ground state ( $S_0$ ) Raman modes of ZnEPI, MgOEP, and ZnOEP and its isotopomers were made by analogy to those of NiOEP<sup>37</sup> and previously published results on ZnOEP.<sup>19</sup> The ground state Raman spectra of these porphyrins are very similar to previously published spectra obtained in resonance with the Soret absorption band. They are dominated by totally symmetric modes with only a few nontotally symmetric modes visible.

Raman difference spectra obtained with the pump pulse preceding the probe pulse by 100 ps are shown as difference spectra in Figure 4.4. These spectra were generated by subtracting out ground state and solvent contributions, which both are of about the same **size** as the difference spectra obtained. Previously, we showed that these spectra evolve in **time** parallel to transient absorbance changes that reflect the transition from the  $S_1$  state to **the** lowest triplet state ( $T_1$ ).<sup>27,28,33</sup> We also showed that the Raman spectrum is **independent** of whether pyridine or tetrahydrofuran is used as the solvent. At a delay time **of** 100 ps the modes observed belong exclusively to the  $S_1$  state. Determination of the **polarization** of these excited state modes was done with the spectra shown in Figure 4.5. It **shows** that the spectra taken at 100 ps, similar to the ground state spectra, are **dominated** by totally symmetric modes with only weakly enhanced nontotally symmetric **modes** visible.

In our earlier work we observed a 1:1 correlation between totally symmetric **modes** in the ground and  $S_1$  states of ZnOEP. This made vibrational assignments

**Figure 4.3** Parallel and perpendicular(---) Raman spectra of ZnOEP (n.a.), ZnOEP-*d*<sub>4</sub>, ZnOEP-<sup>15</sup>N<sub>4</sub>, ZnEPI (n.a.) and MgOEP (n.a.). Other than the polarizer, conditions were the same as those described in Figure 4.2.

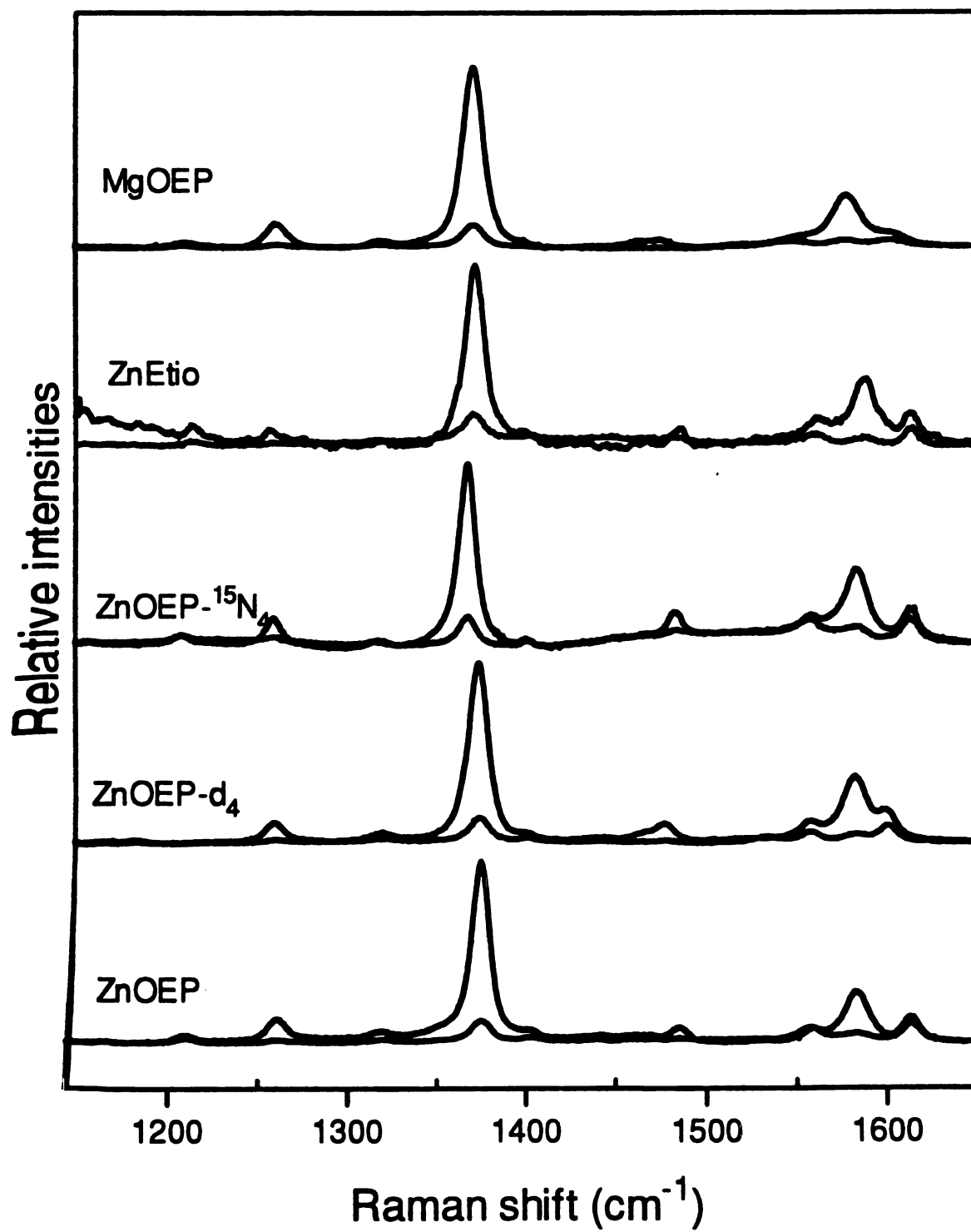


Figure 4.3

Table 4.1 Vibrational Frequencies ( $\text{cm}^{-1}$ ), isotope shifts ( $\text{cm}^{-1}$ ), and polarizations of ZnOEP, ZnEtio and MgOEP in the ground state, ( $S_0$ ), and the lowest excited singlet state, ( $S_1$ ).

S <sub>0</sub>					S <sub>1</sub>				MgOEP assignment
(n.a.)	ZnOEP d <sub>4</sub>	<sup>15</sup> N <sub>4</sub>	ZnEtio	MgOEP	(n.a.)	ZnOEP d <sub>4</sub>	<sup>15</sup> N <sub>4</sub>	ZnEtio	
1614 (.69)	-14 (.70)	-2 (.86)	0 (.67)	-12 (.92)					ν <sub>10</sub>
1584 (.15)	-1 (.12)	-1 (.15)	+4 (.11)	-6 (.08)	1567 (.20)	-8 (.14)	-2 (.17)	+3 p -7 p	ν <sub>2</sub>
1559 (.94)	-1 (.56)	-2 (1.0)	+2 (.53)	-11 (1.0)					ν <sub>11</sub>
1485 (.15)	-7 (.14)	-1 (.17)	+1 (.15)	-10 p	1450 (.10)	-8 (.30)	-1 (.10)	0 (.12) -14 (.23)	ν <sub>3</sub>
					1425 dp	-6 dp	-3 dp	-3 dp b	ν
1375 (.12)	-1 (.12)	-8 (.16)	-3 (.12)	-4 (.18)	1358 (.14)	-5 (.25)	-9 (.17)	-2 (.17) -5 (.27)	ν <sub>4</sub>
1319 (.33)	+1 (.33)	-1 (.39)	-1 a	-1 (.50)	1313 p	-2 p	+2 p	-2 a +1 a	ν <sub>CH2-wag</sub>
1261 (.12)	-1 (.13)	-4 (.15)	-2 p	0 (.18)	1258 (.14)	-1 (.22)	-3 (.17)	+1 (.18) -1 (.35)	ν <sub>CH2-twist</sub>
1210 (.67)		-3 (.81)	+4 dp	+1 (.67)					ν <sub>13</sub>

The polarization ratios are given in brackets. p, polarized; dp, depolarized; <sup>a</sup> based on the measurements it is not clear whether the mode is polarized or depolarized; <sup>b</sup>, a depolarized mode is present, but its precise location is obscured by the  $\nu_3$ ;

**Figure 4.4** Raman difference spectra of ZnOEP (n.a.), ZnOEP-*d*<sub>4</sub>, ZnOEP-<sup>15</sup>N<sub>4</sub>, ZnEPI (n.a.) and MgOEP (n.a.). The pump pulse was set at 572 nm, except for MgOEP, which used 575 nm, and preceded the probe pulse (450 nm) by 100 ps. Porphyrins were dissolved in tetrahydrofuran to approximately  $5 \cdot 10^{-4}$  M.

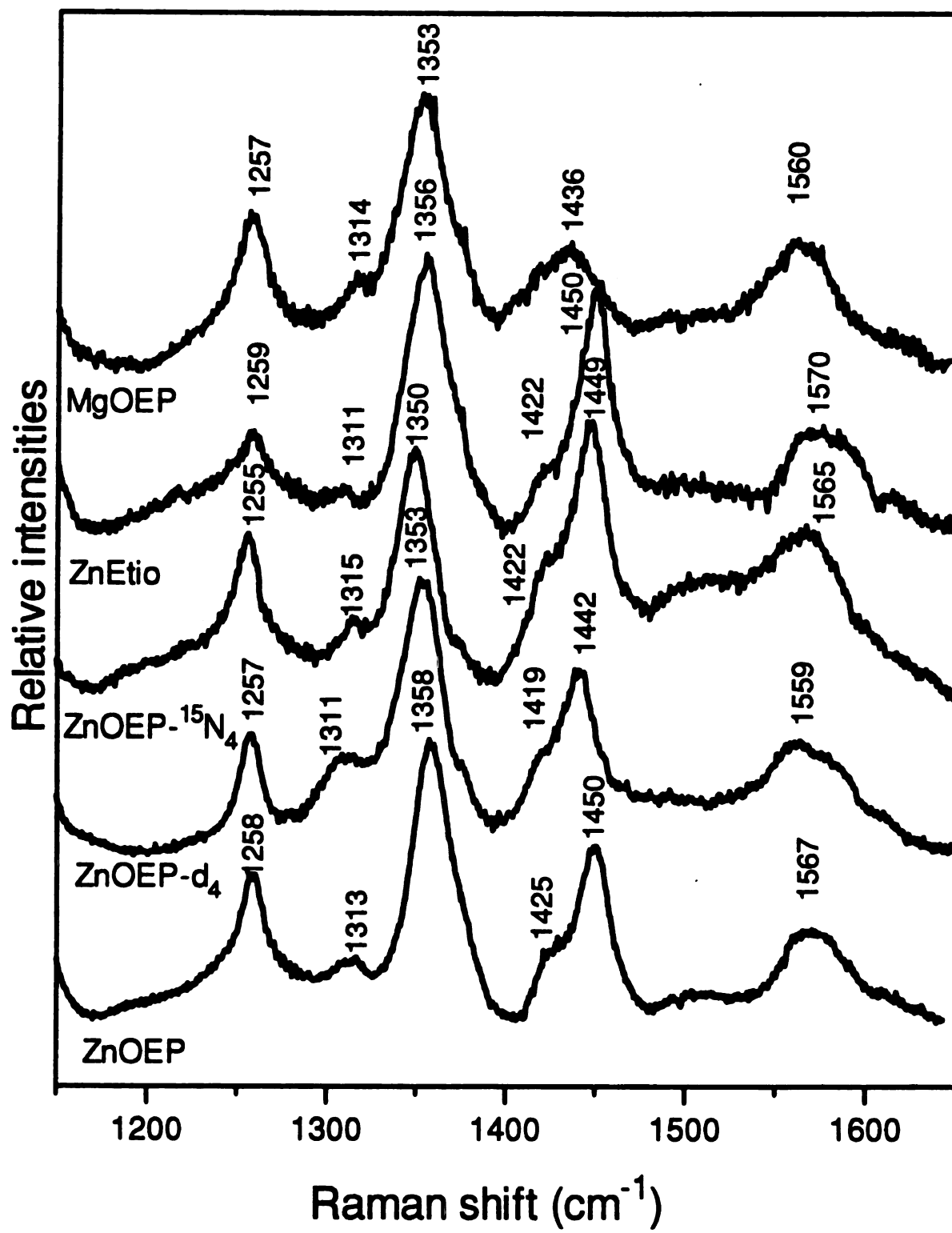


Figure 4.4

**Figure 4.5** Parallel and perpendicular(---) Raman difference spectra of ZnOEP (n.a.), ZnOEP-*d*<sub>4</sub>, ZnOEP-<sup>15</sup>N<sub>4</sub>, ZnEPI (n.a.) and MgOEP (n.a.). Other than the polarizer, conditions were identical to those used in Figure 4.4.



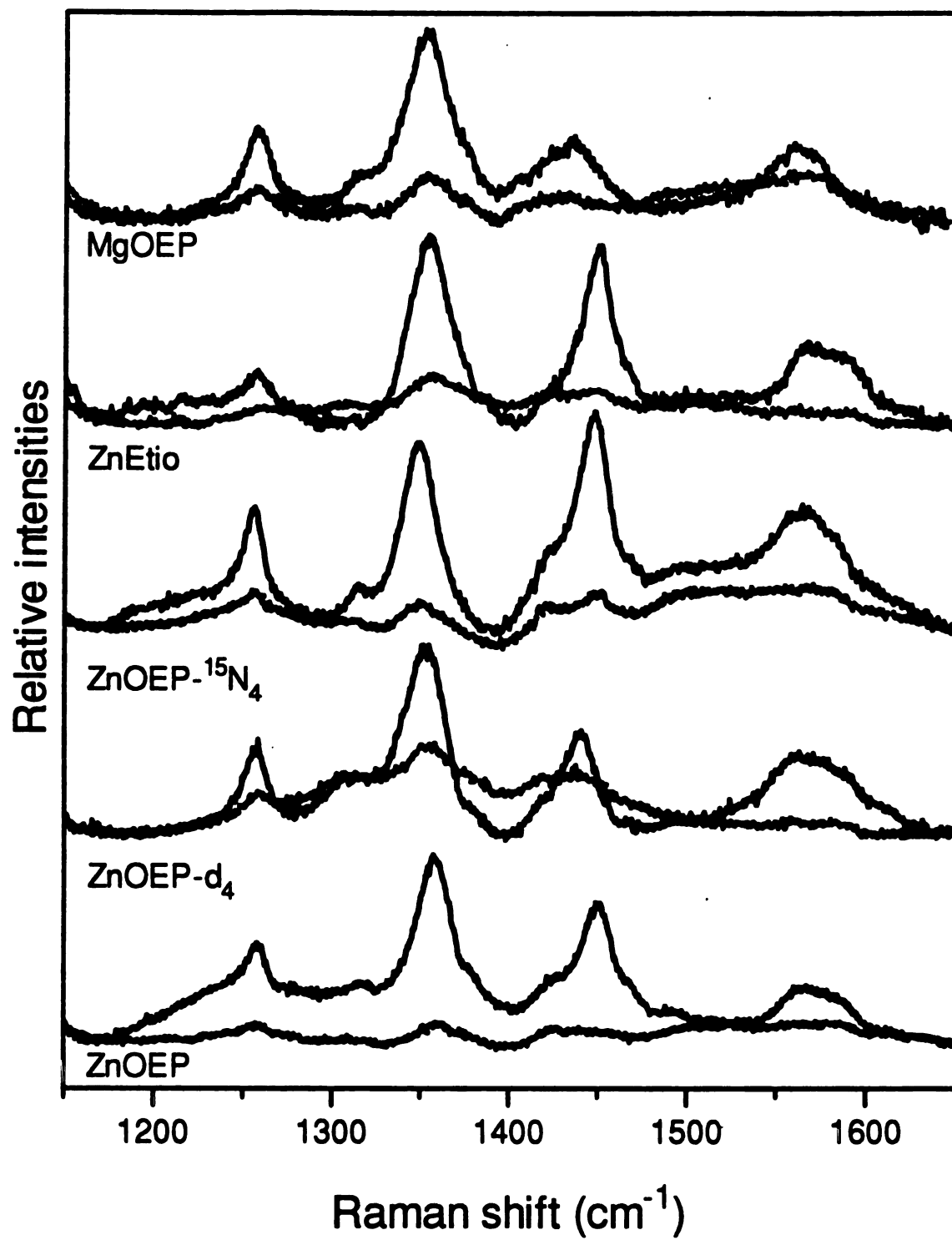


Figure 4.5

relatively straightforward by using direct analogy to ground-state vibrations. Shifts are observed for the  $\nu_2$  ( $-17\text{ cm}^{-1}$ ),  $\nu_3$  ( $-35\text{ cm}^{-1}$ ),  $\nu_4$  ( $-17\text{ cm}^{-1}$ ),  $\nu_{\text{CH}_2\text{-wag}}$  ( $-6\text{ cm}^{-1}$ ), and the  $\nu_{\text{CH}_2\text{-twist}}$  ( $-3\text{ cm}^{-1}$ ) bands. The relative intensity of individual peaks differ in the ground and excited states. In principle, peak intensities contain information about the higher excited state that is used for the resonance enhancement of the Raman scattering. However, a complicating factor is that the resonance enhancement depends on the wavelength if the excitation is not precisely at the 0,0 transition of the  $S_1$  state to the higher excited state.<sup>38</sup> The location of that transition is unknown for  $S_1$  excited ZnOEP and our excitation wavelength may differ significantly from it. Further, for the ground state, we are not in resonance with the 0,0 transition of the Soret band.

The difference spectra of ZnOEP- $d_4$ , ZnOEP- $^{15}\text{N}_4$ , ZnEPI (n.a.), and MgOEP (n.a.) in Figure 4.4 all preserve the same general features of the  $S_1$  state spectrum of ZnOEP. The small changes of the Raman shifts due to isotopic substitution are consistent with isotopic substitution and can be compared to those of the ground state. The Raman shifts of the isotopes facilitated the vibrational assignment of the modes in the  $S_1$  state (Table 4.1). The intensities of most of the isotopomer, ZnEPI and MgOEP modes are also very similar. Noteworthy is the low intensity of the  $\nu_3$  of MgOEP which is much weaker in both the ground and excited state than the  $\nu_3$  of ZnOEP. The same is true for the ethyl mode of ZnEPI at  $1259\text{ cm}^{-1}$  which is also relatively weak in both states. The preservation of the intensity features in both states indicates that the central atom or the peripheral substituents can perturb the porphyrin  $\pi$ -electron system in a similar fashion in different electronic states. Figure 4.6 shows the isotopic shifts in the excited state as a

**Figure 4.6**      **Relative isotopic shifts in ground and excited states**  
**(from Table 4.1).**

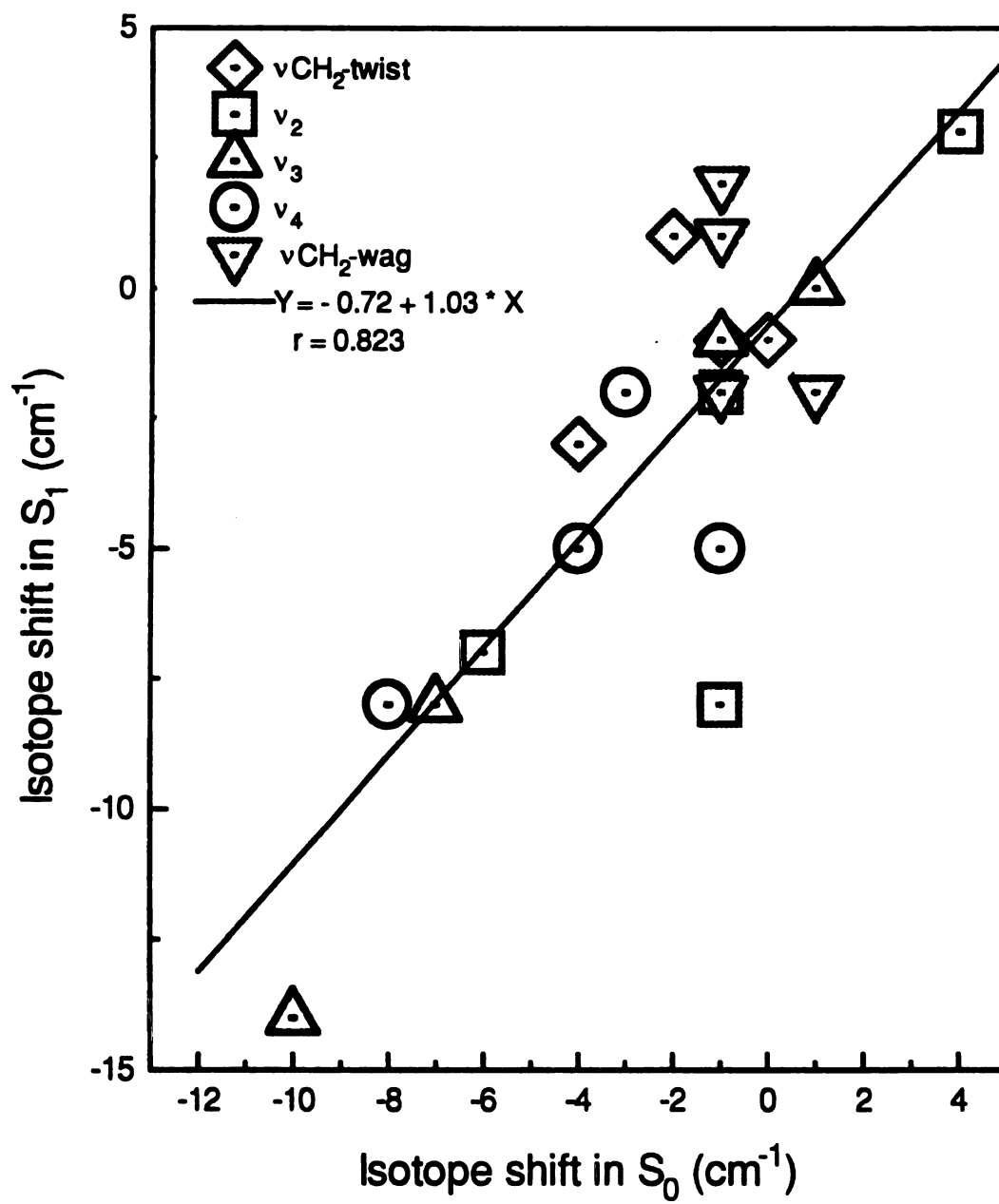


Figure 4.6

function of the isotopic shifts in the ground state. The magnitudes of the shifts are of the same size in both states. Some small differences exist in those of ZnOEP-*d*<sub>4</sub>. The shift for the  $\nu_2$  mode of this isotopomer is 7 cm<sup>-1</sup> larger in the S<sub>1</sub> state than in the ground state. This suggests a small normal mode change in the S<sub>1</sub> state. It should be mentioned, though, that in all S<sub>1</sub> state spectra the  $\nu_2$  is very broad and at the high frequency side may comprise a depolarized mode ( $\nu_{10}$ ?). A comparable argument is true for the MgOEP mode that shows a 4 cm<sup>-1</sup> larger shift for the S<sub>1</sub> state  $\nu_3$  mode. This mode is clearly obscured by a depolarized mode at about 1425 cm<sup>-1</sup>. The  $\nu_4$  mode of ZnOEP-*d*<sub>4</sub> is the only other mode for which the isotopic shift in the excited state differs from that in the ground state. In the former state the isotopic shift is 5 cm<sup>-1</sup>, whereas it is only 1 cm<sup>-1</sup> for the latter state. In general, though, the shifts in both states indicate that there are no significant normal mode changes upon excitation of the porphyrin to S<sub>1</sub>.

Table 4.1 shows that the depolarization values for excited state modes of the isotopomers are very comparable to the ground state values. Under D<sub>4h</sub> symmetry the totally symmetric modes are a<sub>1g</sub> and have a depolarization ratio of 1/8. If the symmetry is lowered to D<sub>2h</sub>, as in H<sub>2</sub>OEP,<sup>39</sup> the depolarization ratios of a<sub>g</sub> modes, corresponding to a<sub>1g</sub> under D<sub>4h</sub>, can be anywhere between 1/8 and 3/4.<sup>40</sup> Because the polarization values are almost unchanged in S<sub>1</sub>, our data do not support such a significant molecular distortion. If, e.g., the symmetry is reduced to D<sub>2h</sub>, the b<sub>1g</sub> modes become totally symmetric and can show reduced depolarization values. All the depolarized modes are, however, weak in S<sub>1</sub> and partly overlapping with other modes. Therefore, we were not able to determine depolarization values for these modes.

#### IV. DISCUSSION

Upon excitation at 450 nm the resonance Raman scattering of ZnOEP in the  $S_1$  state resembles the Soret excited resonance Raman spectrum of the  $S_0$  state.<sup>37</sup> Totally symmetric modes dominate both spectra. These modes gain enhancement via the Franck-Condon mechanism and their intensity is directly related to displacements along these modes within the excited state that is used for the resonance enhancement. The weakness of other modes besides the totally symmetric modes suggests that there is only a single electronic transition in the blue. Other transitions would lead to substantial Herzberg-Teller scattering. The presence of strong polarized modes only in the spectrum of the ZnOEP  $\pi$ -anion was explained analogously by Perng and Bocian.<sup>19</sup>

There are differences in intensities of the modes in the  $S_0$  and  $S_1$  state spectra, e.g., the  $\nu_4$  dominates the  $S_0$  state whereas its intensity is comparable to that of the other totally symmetric modes in the  $S_1$  state. This mode mainly comprises  $C_4N$  stretching and indicates that, when going from the  $S_0$  to the  $S_2$  state, there are significant electron density changes along this mode. When going to higher states from  $S_1$  the changes are smaller along this mode. The increase of the  $\nu_3$  and the  $\nu_{CH_2\text{-twist}}$  in  $S_1$  suggest that in the latter case there are more electron density changes along the periphery of the macrocycle. Another explanation for the increase of the  $\nu_3$  in the  $S_1$  state can be found in its potential energy distribution (PED). Li *et. al.*<sup>37b</sup> used normal mode calculations to explain the intensities of the  $\nu_3$  and  $\nu_2$  in the ground state by the mixing of  $C_bC_b$  and  $C_aC_m$  bond stretches in their PEDs. For the  $\nu_2$  this would lead to a relatively intense peak, but

apparently to weak  $\nu_3$  peak intensity. A small change of the normal mode in  $S_1$  could change the mixing and explain the more intense  $\nu_3$  in the  $S_1$  state.

The vibrational frequencies of the ethyl modes are almost unchanged in the  $S_1$  state. This indicates that upon excitation to  $S_1$  there is little change in electron density at the position of the ethyl groups and that for the  $S_0$  and  $S_1$  states the porphyrin localized orbitals of Gouterman's four orbital model are appropriate.<sup>10</sup> As mentioned above, for totally symmetric modes the resonance enhancement is directly related to the displacement along that normal coordinate. Our data indicate that transitions to higher excited states coincide with electron density changes at the ethyl groups. Similar observations were made with other peripheral substituents. The triplet spectrum<sup>20</sup> of Zn(II) tetraphenylporphyrin is dominated by a phenyl mode at  $1595\text{ cm}^{-1}$ . This mode occurs at almost the same frequency as in the ground state and is also unchanged upon addition of an electron to the  $e_g$  orbital (anion)<sup>16,41</sup> or removal of an electron from the  $a_{2u}$  orbital (cation).<sup>11</sup> These results indicate that for the lowest excited singlet or triplet states a porphyrin core localized model is valid, but that, for electronic transitions to higher excited states, the substituents have to be considered explicitly since there are significant electron density changes at the periphery of the macrocycle.

The depolarized modes appear to have lower intensity in the  $S_1$  state. These modes are enhanced by Jahn-Teller effects in higher excited states.<sup>8,42</sup> As mentioned above, we do not know the resonance enhancement spectrum and do not have a good calibration of the intensity of the  $S_1$  state Raman spectrum. It is therefore difficult to quantitatively compare the intensities in the ground and excited state. The decreased

intensity of depolarized modes is similar to the diminution observed by Perng and Bocian on the ZnOEP  $\pi$ -anion,<sup>19</sup> but a relationship between these observations is not clear, as for both cases it is not known which excited states are used for the resonance enhancement.

We can use the frequency shifts of ZnOEP in  $S_1$  to calculate the core size of the porphyrin in that state if we assume that the experimentally obtained frequency/core size relationships for ground state porphyrins still hold in the excited state. For many modes there is a linear relationship between their frequency and the core size.<sup>19,43,44,45</sup> The latter is defined as the distance between the central metal and the pyrrole nitrogen. The relationship for metal octaethylporphyrins obtained by Anderson *et al.*<sup>45</sup> predicts for ZnOEP in the  $S_1$  state a core size of 2.14, 2.13, or 2.19 Å, respectively, depending on whether the  $\nu_2$ ,  $\nu_3$ , or  $\nu_4$  is used as the core size marker. It is noted that these values are outside the calibrated range and that the error in the core size obtained with the  $\nu_4$  may be especially substantial, because, for this mode, the core size dependence is only weak. The core size of ZnOEP in the ground state is about 2.05 Å.<sup>14</sup> Excitation to the singlet excited state thus increases the core size by about 0.1 Å. This value is more than 10 times higher than that obtained by Prendergast and Spiro<sup>46</sup> from semiempirical calculations. The latter small core size increases were reflected by only small predicted frequency shifts. The 5 % increase of the core size in the  $S_1$  state is of similar order to core size increases reported previously when the oxidation state of the central ion is changed. Findsen *et al.*<sup>25</sup> reported a 3 % core size change upon photoinduced change of the metal oxidation state in nickel protoporphyrin IX. Furthermore, there is about a 3 % core size difference between high and low spin irons in six-coordinate heme complexes.<sup>14</sup> In these two



examples there is no redistribution of the porphyrin  $\pi$ -electron system. Therefore, a 5 % increase of the core size in the  $S_1$  state, where there is significant electron redistribution, is only small. According to our estimated core size increase the  $\nu_{10}$  would shift to about  $1575\text{ cm}^{-1}$ . It is therefore not surprising that no clear  $\nu_{10}$  was found in the data as this mode would probably be obscured by the  $\nu_2$  mode. Previously obtained linear relationships between core size and the frequencies of several modes were also found for metal-OEP cations,<sup>13</sup> although these relationships differ from those of ground state porphyrins. X-ray crystallography data did not indicate core size differences between cations and their neutral parents, whereas there are significant shifts in frequency. This indicates that frequency shifts may not necessarily reflect core size changes, but that they can also be caused by mode composition changes. In that case, however, we do not expect different modes to predict similar core size changes.

Transient absorption measurements by Rodriguez *et al.*<sup>33</sup> showed that the  $S_1$  state absorbs strongly between 400 nm and 500 nm and suggests similarity with the ground state absorption spectrum. They proposed that the absorption spectrum of  $S_1$  results from similar transitions as that of the  $S_0$  state and not from promotion of an electron in the  $e_g$  orbital to a higher orbital. Even though the intensities of the modes in the ground and excited states are different, the correlation that seems to exist for the intensities of some peaks corroborates their suggestion.

Measurements previously performed on ZnTPP triplets<sup>17,20</sup> showed an increase of the number of Raman active modes relative to the ground state and depolarized ground state modes that become polarized in the triplet state. This was attributed to a distortion

of the macrocycle along a nontotally symmetric coordinate due to Jahn-Teller effects. In general, macrocycle distortion will reduce the symmetry and increase the number of modes, because nontotally symmetric modes can become totally symmetric under reduced symmetry. ZnOEP in the  $S_1$  state does not show an increase of polarized  $a_{1g}$  modes nor a change of polarization of the nontotally symmetric  $b_{1g}$  modes. This leads to the conclusion that in the  $S_1$  state there is no significant change of symmetry of the porphyrin and that the  $D_{4h}$  symmetry of the ground state porphyrin is retained. A static Jahn-Teller distortion, as previously reported for the ZnTPP triplet, is therefore absent or negligible in  $S_1$  excited ZnOEP. It was shown before that Jahn-Teller effects in singlet excited states can be quenched by configuration interaction.<sup>18</sup>

Previously Sato *et al.*<sup>23</sup> published resonance Raman spectra of free-base OEP ( $H_2OEP$ ). Because of the long lifetime of the singlet state of  $H_2OEP$ , they performed their experiments with intense nanosecond laser flashes. These data were not analyzed extensively, but there are similarities between the Raman spectra of the ground states of ZnOEP and  $H_2OEP$ , even though this porphyrin has a lower symmetry ( $D_{2h}$ ) than ZnOEP. Differences are mainly in the modes around  $1600\text{ cm}^{-1}$ . These modes have become totally symmetric in the reduced symmetry of  $H_2OEP$  and consequently are more enhanced. In the  $S_1$  state there is a downshift of  $\nu_4$  by  $23\text{ cm}^{-1}$  which is comparable in size to the  $18\text{ cm}^{-1}$  downshift that we found for ZnOEP. In  $H_2OEP$  the intensity of the  $\nu_3$  is increased in the  $S_1$  state and is located at  $1445\text{ cm}^{-1}$  (in ZnOEP at  $1450\text{ cm}^{-1}$ ) and has probably shifted down significantly. It is noted that the authors did not identify this mode as the  $\nu_3$ , but this mode bears clear resemblance with the  $\nu_3$  of  $S_1$  excited ZnOEP. Sato *et al.* observed

a mode at  $1596\text{ cm}^{-1}$  in the  $S_1$  state and attributed this mode to  $\nu_2$ . Consequently they concluded that  $\nu_2$  shifts up in  $S_1$  excited  $\text{H}_2\text{OEP}$ , but judging from their data, it can also be argued that the  $\nu_2$  shifts down in frequency. We attribute modes at  $1255\text{ cm}^{-1}$  and  $1316\text{ cm}^{-1}$  to ethyl modes, that correspond to the  $1258\text{ cm}^{-1}$  and  $1318\text{ cm}^{-1}$  modes in  $S_1$  excited  $\text{ZnOEP}$ . As in  $\text{ZnOEP}$  these modes do not change in frequency in going from  $S_0$  to  $S_1$ . The  $\nu_{13}$  mode that is present in the  $S_0$  states of  $\text{ZnOEP}$  ( $1211\text{ cm}^{-1}$ ) and  $\text{H}_2\text{OEP}$  ( $1210\text{ cm}^{-1}$ ) cannot be identified in the  $S_1$  state of  $\text{H}_2\text{OEP}$ . Here, we do not present modes at frequencies lower than  $1200\text{ cm}^{-1}$ , but previously<sup>27,28</sup> we reported Raman spectra obtained at lower frequencies. Modes at  $1138$  and  $1096\text{ cm}^{-1}$  in  $S_1$  excited  $\text{ZnOEP}$  seem correlated to modes at  $1121$  and  $1076\text{ cm}^{-1}$  of  $\text{H}_2\text{OEP}$ . It is noteworthy that for both  $\text{H}_2\text{OEP}$  and  $\text{ZnOEP}$  the modes at  $1076$  and  $1096\text{ cm}^{-1}$ , respectively, cannot be clearly related to ground state modes. It thus seems that the  $S_1$  excited states of  $\text{H}_2\text{OEP}$  and  $\text{ZnOEP}$  have a number of common characteristics. This is important because  $S_1$  excited  $\text{ZnOEP}$  is potentially subject to Jahn-Teller effects,<sup>20</sup> whereas  $\text{H}_2\text{OEP}$  is not because the degeneracy of the  $e_g$  orbitals is lifted in the lower symmetry. As shown for  $\text{ZnTPP } \pi\text{-anion}^{11,16}$  and for  $\text{ZnTPP triplet}$ ,<sup>20</sup> Jahn-Teller effects can lead to large frequency shifts. Similar shifts for both  $\text{ZnOEP}$  and  $\text{H}_2\text{OEP}$  further indicate that Jahn-Teller effects are small for  $S_1$  excited  $\text{ZnOEP}$ . They also suggest that the influence of the central metal on the shift is only small.

The two highest occupied molecular orbitals ( $a_{1u}$  and  $a_{2u}$ ) of metalloporphyrins are almost accidentally degenerate. It was shown that for metallo-OEPs the energy of the  $a_{1u}$  orbital is slightly higher than that of the  $a_{2u}$  orbital. The HOMO of  $\text{ZnOEP}$  is therefore  $a_{1u}$ . Previously,<sup>27,28</sup> we explained our data by assuming that the electronic configurations of

ZnOEP changes from  $a_{1u}a_{1u}$  to  $a_{1u}e_g$  upon excitation into the first excited singlet state. For a more accurate description, several configurations should be taken into account for the  $S_1$  state. Since the  $a_{1u}$  and  $a_{2u}$  orbitals are almost accidentally degenerate, excitation to  $S_1$  cannot be described by one electron promotion, but is more properly described by promoting about 0.6 electron from the  $a_{1u}$  orbital to the  $e_{gx}$  orbital and 0.4 electron from the  $a_{2u}$  orbital to the  $e_{gx}$  orbital.<sup>47,48</sup> To gain more quantitative insight into electron redistribution in the porphyrin macrocycle upon excitation to  $S_1$ , we used results from calculations on metalloporphyrin by Sekino and Kobayashi<sup>47</sup> to generate plots of porphyrin natural orbitals.<sup>49</sup> These natural orbitals are combinations of molecular orbitals that describe the electron populations in a given electronic transition. The calculations and application theory for these natural orbitals are discussed fully within Chapter 5.

The relative sizes of the atomic orbital coefficients used for calculations on the molecular orbitals  $a_{1u}$ ,  $a_{2u}$ , and the degenerate orbitals  $e_{gx}$  and  $e_{gy}$  are shown in Figure 1.6.<sup>47</sup> The composite orbital diagrams for singlet electronic states are shown in Figure 5.3. Electron density changes after excitation to  $S_1$  and  $S_2$ , respectively, are shown in Figure 5.5 and Figure 5.6. Likewise, bond strengths (Figure 5.7 and Figure 5.8) and changes therein (Figure 5.10 and Figure 5.11) can be estimated with atomic orbital coefficients. It should be noted that these electron distribution changes that occur upon promotion of a single electron are small compared to the the absolute electron population. As indicated by the overall weakening of the bonds, the calculations predict an overall expansion of the core, in agreement with our experimental observations. More specifically, the calculations predict the largest changes at the  $C_cC_m$  bonds. Of the

observed modes,  $\nu_3$  has the largest contribution of  $C_a C_m$  stretching, and also shows the largest downshift in  $S_1$ . The full benefits of natural orbitals as a tool in interpreting excited state Raman spectra are discussed in Chapter 5. Interestingly, after excitation there is a small  $b_{1g}$  distortion of the porphyrin. The distortion is a result of the different contributions of the  $a_{1u}$  and  $a_{2u}$  orbitals to the electronic transition. If these orbitals are accidentally degenerate, the transition can be described as originating from 0.5 electron promotion from each of these orbitals, and there will be no distortion in that case. All our data indicate that the distortion is not reflected by a significant symmetry change of the molecule as this would have increased the number of Raman active modes. Based on resonance enhancement profiles of depolarized modes Shelnutt *et al.*<sup>50</sup> argued that the  $S_1$  state of nickel etioporphyrin I is weakly distorted by dynamic Jahn-Teller effects. This distortion may well be related to predicted geometry change as calculated.

Besides the calculations, we can also use results obtained on  $\pi$ -cation and  $\pi$ -anion radicals of ZnOEP and ZnTPP, the latter with the  $a_{2u}$  orbital as the HOMO, to predict frequency shifts of the vibrational modes in  $S_1$  based on the structures of the  $a_{1u}$ ,  $a_{2u}$ , and  $e_g$  orbitals. In Table 4.2 we test whether the vibrational shifts in the  $S_1$  state of a porphyrin cannot simply be described as a summation of shifts induced by addition of an electron to the  $e_g$  orbital (anion) and shifts induced by loss of an electron from the  $a_{1u}$  or  $a_{2u}$  orbital (cation). Assuming that the orbital occupancies of ZnTPP and ZnOEP  $\pi$ -cations are purely  $a_{2u}$  and  $a_{1u}$  respectively, we can predict the shifts in the  $S_1$  state to be  $0.6(\Delta\text{ZnOEP}^- + \Delta\text{ZnOEP}^+) + 0.4(\Delta\text{ZnTPP}^+ + \Delta\text{ZnTPP}^-)$ . The results are presented in Table 4.2. Since no proper data for  $\text{ZnTPP}^+$   $\pi$ -cation has been reported, we used data of  $\text{CuTPP}^+$  instead.

Table 4.2 Predictions based on shifts of vibrational frequencies of ZnTPP and ZnOEP anions, and ZnOEP and CuTPP cations compared with the measured values of shifts in the  $S_1$  state.

vibrational mode	$\Delta\text{CuTPP}^{+b}$ (cm-1)	$\Delta\text{ZnTPP}^{-c}$ (cm-1)	$\Delta\text{ZnOEP}^{+d}$ (cm-1)	$\Delta\text{ZnOEP}^{-e}$ (cm-1)	calc. $\Delta S_1^f$ (cm-1)	meas. $\Delta S_1$ (cm-1)
$\nu_2$	-32	-14	+19	0	-7	-20
$\nu_3$	$\sim 0^a$	-31	-8	-3	-19	-36
$\nu_4$	-10	-4	-34	-7	-30	-16

<sup>a</sup> no value has been reported for  $\nu_3$ , and the average of the shifts of the  $\nu_{10}$  and  $\nu_{11}$  modes is used; <sup>b</sup> from Czernuszewicz, R. S.; Macor, K. A.; Li, X.-Y.; Kincaid, J. R.; Spiro, T. G. *J. Am. Chem. Soc.* 1990, 111, 3860-3869. <sup>c</sup> from Atamian, M.; Donohoe, R. J.; Lindsey, J. S.; Bocian, D. F. *J. Phys. Chem.* 1989, 93, 2236-2243. <sup>d</sup> from Oertling, W. A.; Salehi, A.; Chung, Y. C.; Leroy, G. E.; Chang, C. K.; Babcock, G. T. *J. Phys. Chem.* 1987, 91, 5887-5898. <sup>e</sup> taken from Perng, J.-H.; Bocian, D. F. *J. Phys. Chem.* 1992, 96, 4804-4811. <sup>f</sup> calculated as  $(\Delta\text{ZnOEP}^+ + \Delta\text{ZnOEP}^-) + (\Delta\text{CuTPP}^+ + \Delta\text{ZnTPP}^-)$ .

Earlier data for ZnTPP<sup>+</sup> by Yamaguchi *et al.*<sup>51</sup> seems not completely reliable, because the frequency shifts of their cations are very different from data published later on.<sup>11</sup> For CuTPP<sup>+</sup> there is no observed  $\nu_3$  and we used the averaged values of  $\nu_{10}$  and  $\nu_{11}$ , modes with similar stretching contributions. Gouterman's model does not address the substituent modes. Therefore, they are not included in the table. Table 4.2 shows that, though there are quantitative differences between predicted and measured frequencies, the directions of the shifts agree. However, if configuration interaction is neglected and it is assumed that for ZnOEP one electron is promoted from the  $a_{1u}$  orbital to the  $e_g$  orbital as has been suggested in literature,<sup>46</sup> the shift of the  $\nu_2$  would be opposite to what is found experimentally. It should be noted that the metallo-TPP anion radicals are subject to Jahn-Teller distortion,<sup>11</sup> whereas these effects are only small in  $S_1$  excited porphyrins.<sup>18</sup> This will partly be responsible for the large shifts of some of the anion modes. Predictions based on semiempirical calculations of porphyrin structures in excited states by Prendergast and Spiro<sup>46</sup> predict frequency shifts much smaller than we observed. They included geometry optimization but no configuration interaction in their calculations, and calculated only minor changes of the porphyrin core geometry with consequently only small predicted shifts of the normal modes.

We will now discuss the change of the linewidths in the  $S_1$  state. An increase in linewidth can be caused by different dephasing or by structural inhomogeneity of the porphyrin sample in  $S_1$ . In the former case, modes are expected to be Lorentzian, whereas in the latter case the lines have Gaussian shapes. The differences between these shapes are mainly in the wings of the modes, and are difficult to assess if several modes overlap. The

$\nu_4$ , however, is reasonably isolated with a shape that resembles a Gaussian most. The linewidth broadening is thus due to inhomogeneous effects. Due to anharmonicity, an inhomogeneity can be caused by vibrational population relaxation in the  $S_1$  excited state manifold. It then, however, should disappear on the same time picosecond timescale as the excited vibrations. Spectra obtained at 100 ps, 800 ps, and 2 ns all have the same linewidths (see Chapter 2, Figure 2.1),<sup>28</sup> and indicate that the latter relaxation processes, which occur within tens of picoseconds,<sup>30</sup> are not responsible for the inhomogeneity. The broader modes, therefore, originate from a structural heterogeneity. Courtney *et al.*<sup>26</sup> observed narrower linewidths in the d,d excited state of nickel(II) protoporphyrin IX dimethyl ester and attributed this to nonplanar distortions in the ground state of nickel porphyrins.<sup>52</sup> They suggested that, in the excited state, the conformational heterogeneity of the macrocycle was less, leading to narrower modes. Our data indicates that for ZnOEP the conformational heterogeneity increases when going to the excited state. It is possible that this is a reflection of the theoretically predicted nontotally symmetric distortion of the porphyrin macrocycle.



## LIST OF REFERENCES

- (1) see e.g., Research in Photosynthesis, *Proceedings of the IXth International Congress on Photosynthesis*; Murata, N.; Ed.; Kluwer Academic Publishers: Dordrecht, 1992.
- (2) Lin, X.; Murchison, H. A.; Nagarajan, V.; Parson, W. W.; Allen, J. P.; Williams, J. C. *Proc. Natl. Acad. Sci. USA* **1994**, 91, 10265-10269.
- (3) Dutton, P.L.; Moser, C. C. *Proc. Natl. Acad. Sci. USA* **1994**, 91, 10247-10250.
- (4) (a) Vos, M. H.; Lambry, J. C.; Robles, S. J.; Youvan, D. C.; Breton, J.; Martin, J. *Proc. Natl. Acad. Sci. USA*, **1991**, 88, 8885-8889. (b) Vos, M. H.; Rappaport, F.; Lambry, J.-C.; Breton, J.; Martin, J.-L. *Nature* **1993**, 363, 320-325.
- (5) Zhu, L.; Sage, J. T.; Champion, P. M. *Science* **1994**, 266, 629-632
- (6) Jortner, J. *J. Chem. Phys.* **1976**, 64, 4860-4867.
- (7) Gunner, M. R.; Dutton, P. L. *J. Am. Chem. Soc.* **1989**, 111, 3400-3412.
- (8) (a) Gustafson, T. L.; Iwata, K.; Weaver, W. L. in *Ultrafast Phenomena VII*; Harris, C. B.; Ippen, E. P.; Mourou, G. A.; Zewail, A. H., Eds.; Springer-Verlag: New York, 1990. (b) Hayashi, H.; Kolczkowski, S. V.; Noguchi, T.; Blanchard, D.; Atkinson, G. H. *J. Am. Chem. Soc.* **1990**, 112, 4664-4670. (c) Noguchi, T.; Kolczkowski, S.; Gartner, W.; Atkinson, G. H. *J. Phys. Chem.* **1990**, 94, 4920-4926. (d) Hayashi, H.; Brack, T. L.; Noguchi, T.; Tasumi, M.; Atkinson, G. H. *J. Phys. Chem.* **1991**, 95, 6797-6802. (e) Noguchi, T.; Hayashi, H.; Tasumi, M.; Atkinson, G. H. *J. Phys. Chem.* **1991**, 95, 3167-3172. (f) Iwata, K.; Hamaguchi, H. *Chem. Phys. Lett.* **1992**, 196, 462-468. (g) Weaver, W. L.; Huston, L. A.; Iwata, K.; Gustafson, T. L.; *J. Phys. Chem.* **1992**, 96, 8956-8961. (h) Butler, R. M.; Lynn, M. A.; Gustafson, T. L. *J. Phys. Chem.* **1993**, 97, 2609-2617. (i) Reid, R. J.; Doig, S. J.; Wickham, S. D.; Mathies, R. A. *J. Am. Chem. Soc.* **1993**, 115, 4754-4763. (j) Reid, P. J.; Lawless, M. K.; Wickham, S. D.; Mathies, R. A. *J. Phys. Chem.* **1994**, 98, 5597-5606. (k) Hamaguchi, H.; Gustafson, T. L. *Ann. Rev. Phys. Chem.* **1994**, 45, 593-622.

- (9) (a) Donohoe, R. J.; Dyer, R. B.; Swanson, B. I.; Violette, C. A.; Frank, H. A.; Bocian, D. F. *J. Am. Chem. Soc.* **1990**, 112, 6716-6720. (b) Moënné-Loccoz, P.; Robert, B.; Ikegami, I.; Lutz, M. *Biochemistry* **1990**, 29, 4740-4746. (c) Mattioli, T. A.; Hoffmann, A.; Robert, B.; Schrader, B.; Lutz, M. *Biochemistry* **1991**, 30, 4648-4654. (d) Shreve, A. P.; Cherepy, N. J.; Franzen, S.; Boxer, S. G.; Mathies, R. A. *Proc. Natl. Acad. Sci. USA* **1991**, 88, 11207-11211. (e) Palaniappan, V.; Aldema, M. A.; Frank, H. A.; Bocian, D. F. *Biochemistry* **1992**, 31, 11050-11058. (f) Cherepy, N. J.; Shreve, A. P.; Moore, L. J.; Franzen, S.; Boxer, S. G.; Mathies, R. A. *J. Phys. Chem.* **1994**, 98, 6023-6029.
- (10) Gouterman, M. *J. Mol. Spectr.* **1961**, 6, 138-163.
- (11) Czernuszewicz, R. S.; Macor, K. A.; Li, X.-Y.; Kincaid, J. R.; Spiro, T. G. *J. Am. Chem. Soc.* **1990**, 111, 3860-3869.
- (12) Oertling, W. A.; Salehi, A.; Chung, Y. C.; Leroi, G. E.; Babcock, G. T. *J. Phys. Chem.* **1989**, 93, 1311-1319.
- (13) Oertling, W. A.; Salehi, A.; Chung, Y. C.; Leroi, G. E.; Chang, C. K.; Babcock, G. T. *J. Phys. Chem.* **1987**, 91, 5887-5898.
- (14) Spaulding, L. D.; Chang, C. C.; Yu, N.-T.; Felton, R. H. *J. Am. Chem. Soc.* **1975**, 97, 2517-2524.
- (15) Salehi, A.; Oertling, W. A.; Fonda, H. N.; Babcock, G. T.; Chang, C. K. *Photochem. Photobiol.* **1988**, 48, 525-530.
- (16) Atamian, M.; Donohoe, R. J.; Lindsey, J. S.; Bocian, D. F. *J. Phys. Chem.* **1989**, 93, 2236-2243.
- (17) Reed, R. A.; Purello, R.; Prendergast, K.; Spiro, T. G. *J. Phys. Chem.* **1991**, 95, 9720-9727.
- (18) Gouterman, M. *Ann. N. Y. Acad. Sci.* **1973**, 206, 70-83.
- (19) Perng, J.-H.; Bocian, D. F. *J. Phys. Chem.* **1992**, 96, 4804-4811.
- (20) Walters, V. A.; de Paula, J. C.; Babcock, G. T.; Leroi, G. E. *J. Am. Chem. Soc.* **1989**, 111, 8300-8302.
- (21) Kumble, R.; Hu, S.; Loppnow, G. R.; Vitols, S. E.; Spiro, T. G. *J. Phys. Chem.* **1993**, 97, 10521-10523.
- (22) Bell, S. E. J.; Al-Obaidi, A. H. R.; Hegarty, M.; Hester, R. E.; McGarvey, J. J. *J. Phys. Chem.* **1993**, 97, 11599-11602.

- (23) Sato, S.; Asano-Someda, M.; Kitagawa, T. *Chem. Phys. Lett.* **1992**, 189, 443-447.
- (24) Apanasevich, P. A.; Kruglik, S. G.; Kvach, V. V.; Orlovich, V. A. in *Time Resolved Vibrational Spectroscopy V*; Takahashi, H., Ed.; Springer-Verlag: Berlin, 1992.
- (25) Findsen, E. W.; Shelnutt, J. A.; Ondrias, M. R. *J. Phys. Chem.* **1988**, 92, 307-314.
- (26) Courtney, S. H.; Jedju, T. M.; Friedman, J. M.; Alden, R. G.; Ondrias, M. R. *Chem. Phys. Lett.* **1989**, 164, 39-44.
- (27) Kreszowski, D. H.; Deinum, G.; Babcock, G. T. *Biophys. J.* **1994**, 66(2), a374.
- (28) Kreszowski, D. H.; Deinum, G.; Babcock, G. T. *J. Am. Chem. Soc.* **1994**, 116, 7463-7464.
- (28) Deinum, G.; Kreszowski, D. H.; Chang, C. K.; Babcock, G. T. *submitted to J. Am. Chem. Soc.*
- (30) (a) Rodriguez, J.; Holten, D. *J. Chem. Phys.* **1989**, 91, 3525-3531. (b) Rodriguez, J.; Holten, D. *J. Chem. Phys.* **1990**, 92, 5944-5949. (c) Bilsel, O.; Rodriguez, J.; Holten, D. *J. Chem. Phys.* **1990**, 94, 3508-3512. (d) Rodriguez, J.; Kirmaier, C.; Holten, D. *J. Chem. Phys.* **1991**, 94, 6020-6029.
- (31) Fuhrhop, J.-H.; Smith, K. M. In: *Porphyrins and Metalloporphyrins*; Smith, K. M., Ed.; Elsevier: Amsterdam, 1975, pp 765-766, 816-817.
- (32) Paine, J. B.; Kirshner, W. B.; Maskowitz, D. W.; Dolphin, D. *J. Org. Chem.* **1976**, 41, 3857.
- (33) Rodriguez, J.; Kirmaier, C.; Holten, D. *J. Am. Chem. Soc.* **1989**, 111, 6500-6506.
- (34) O'Neil, M. P. *Optics Letters* **1993**, 18(1), 37-38.
- (35) (a) Iwata, K.; Hamaguchi, H. *Chem. Phys. Lett.* **1992**, 196, 462-468. (b) Butler, R. M.; Lynn, M. A.; Gustafson, T. L. *J. Phys. Chem.* **1993**, 97, 2609-2617. (c) Iwata, K.; Yamaguchi, S.; Hamaguchi, H. *Rev. Sci. Instrum.* **1993**, 64, 2140-2146. (d) Qian, J.; Schultz, S. L.; Bradbun, G. R.; Jean, J. M. *J. Phys. Chem.* **1993**, 97, 10638-10644. (e) Yamaguchi, S.; Hamaguchi, H. *Chem. Phys. Lett.* **1994**, 227, 255-260.
- (36) Atkinson, G. H.; Brack, T. L.; Blanchard, D.; Rumbles, G. *Chem. Phys.* **1989**, 131, 1-15.

- (37) (a) Abe, M.; Kitagawa, T.; Kyogoku, Y. *J. Chem. Phys.* **1978**, 69, 4526-4534. (b) Li, X.-Y.; Czernuszewicz, R. S.; Kincaid, J. R.; Stein, P.; Spiro, T. G. *J. Phys. Chem.* **1990**, 94, 47-61.
- (38) Babcock, G. T.; Callahan, P. M.; Ondrias, M. R.; Salmeen, I. *Biochemistry* **1981**, 20, 959-966.
- (39) Merchán, M.; Orti, E.; Roos, B. O. *Chem. Phys. Lett.* **1994**, 221, 136-144.
- (40) (a) McClain, W. M.; *J. Chem. Phys.* **1971**, 55, 2789-2796. (b) Siebrand, W.; Zgierski, M. Z. in *Excited States*; Lim, E. C. Ed.; Academic Press: New York, 1979, Vol 4., pp 1-136.
- (41) Yamaguchi, H.; Soeta, A.; Toeda, H.; Itoh, K. *J. Electroanal. Chem. Interfacial Electrochem.* **1983**, 159, 347-359.
- (42) Cheung, L. D.; Yu, N.-T.; Felton, R. H. *Chem. Phys. Lett.* **1978**, 55, 527-529.
- (43) Shelnut, J. A.; Majunder, S. A.; Sparks, L. D.; Hobbs, J. D.; Medforth, C. J.; Senge, M. O.; Smith, K. M.; Miura, M.; Luo, L.; Quirke, M. E. *J. J. Raman Spectr.* **1992**, 23, 523-529.
- (44) Sparks, L. D.; Anderson, K. K.; Medforth, C. J.; Smith, K. M.; Shelnut, J. A. *Inorg. Chem.* **1994**, 33, 2297-2302.
- (45) Anderson, K. K.; Hobbs, J. D.; Luo, L.; Stanley, K. D.; Quirke, J. M. E.; Shelnut, J. A. *J. Am. Chem. Soc.* **1993**, 115, 12346-12352.
- (46) Prendergast, K.; Spiro, T. G. *J. Phys. Chem.* **1991**, 95, 9728-9736.
- (47) Sekino, H.; Kobayashi, H. *J. Chem. Phys.* **1987**, 86, 5045-5052.
- (48) (a) Pettke, J. D.; Maggiora, G. M.; Shipman, L. L.; Christofferson *J. Mol. Spectr.* **1978**, 71, 64-84. (b) Edwards, W. D.; Zerner, M. C. *Can. J. Chem.* **1985**, 63, 1763-1772
- (49) Levine, I. N. in *Quantum Chemistry*; Levine, I. N., Ed.; Allyn and Bacon: Massachusetts, 1983, Vol III, pp 383-384.
- (50) Shelnut, J. A.; Cheung, L. D.; Chang, R. C. C.; Yu, N.-T.; Felton, R. H. *J. Chem. Phys.* **1978**, 66, 3387-3398.
- (51) Yamaguchi, H.; Nakano, M.; Itoh, K. *Chem. Phys. Lett.* **1982**, 1397-1400.

- (52) Shelnutt, J. A.; Majunder, S. A.; Sparks, L. D.; Hobbs, J. D.; Medforth, C. J.; Senge, M. O.; Smith, K. M.; Miura, M.; Luo, L.; Quirke, M. E. J. *J. Raman Spectr.* **1992**, 23, 523-529

## CHAPTER 5

### STRUCTURAL PREDICTIONS FROM NATURAL ORBITAL CALCULATIONS

#### ABSTRACT

The Gouterman approach has been successfully used to interpret bond displacements observed in triplet excited state Raman spectra of metalloporphyrins. This was done through direct comparison of frequency shifts with atomic electron density changes in individual molecular orbitals. However, configuration interaction between nearly degenerate electronic states of metalloporphyrins makes the Gouterman approach inadequate for discussing excited singlet state Raman spectra. Therefore, natural orbitals have been constructed to account for this configuration interaction. This chapter briefly discusses the selection of the *ab initio* study used to generate these natural orbitals. The quantum mechanical calculations necessary for generation of these orbitals are presented. Pictorial representations for the  $S_1$ ,  $T_1$ ,  $S_2$ , and  $T_2$  states, kindred to the original Gouterman molecular orbital diagrams, are given and represent both atom electron densities and bond orders of adjacent atoms. Both diagrams are necessary for more quantitative interpretation of the spectra presented in Chapter 4. The  $S_1$  and  $S_2$  states are estimated to undergo a minimal  $b_{1g}$  distortion that disappears only under accidentally degenerate conditions. Relative to singlet excited states, the  $T_1$  and  $T_2$  states undergo large nonuniform changes in electron densities. These composite orbitals illustrate the inhibition of Jahn-Teller distortions by significant configuration interaction.

## I. INTRODUCTION

Once the picosecond Raman experiments detailed in Chapter 2 through Chapter 4 were completed, complications arose in interpreting the Raman features observed for singlet excited states of zinc(II) octaethylporphyrin and its associated isotopomers. Triplet excited state studies of metalloporphyrins<sup>1-5</sup> frequently invoked Gouterman molecular orbitals (MO) to explain the Raman shifts and intensity enhancements observed in the  $T_1$  state.<sup>6</sup> These arguments were based upon theoretical changes in atomic orbital coefficients when a single electron from the HOMO state ( $a_{1u}$  or  $a_{2u}$ ) is promoted into the LUMO ( $e_{gx}$  or  $e_{gy}$ ) (Figure 1.6). This approach was particularly convenient when the atom electron densities were expressed in diagrams. These Gouterman MO's were simple pictorial descriptions of atomic orbital coefficients (atomic orbital electron densities) originally adapted from MO calculations on porphine done by Longuet-Higgins *et al.* (see Figure 1.6 for Gouterman molecular orbital diagrams).<sup>7</sup> Research studies such as those done by Walters *et al.*,<sup>1</sup> and Reed *et al.*<sup>2</sup> effectively used these orbitals to make qualitative arguments about directional shifts in the  $T_1$  state of zinc tetraphenylporphyrin. To a lesser degree, other studies by Sato *et al.*<sup>3</sup> and Bell *et al.*<sup>5</sup> have rationalized  $T_1$  frequency shifts in lower symmetry free base porphyrins  $H_2OEP$  and  $H_2TPP$  by invoking Gouterman orbitals. This approach becomes clearly inappropriate for interpreting excited singlet state Raman spectra, since configuration interaction between the  $a_{1u}e_g$  and  $a_{2u}e_g$  transitions results in mixing of the molecular orbitals. Ideally, a fictional orbital could be envisioned that would include this configuration interaction, while retaining the same basic simplicity of Gouterman orbitals. Therefore, by knowing the extent of configuration interaction for

metalloporphyrin, we constructed so called “natural” orbitals<sup>8</sup> that enabled predicting electron occupancy changes that occur upon transition to the S<sub>1</sub>, S<sub>2</sub>, T<sub>1</sub>, and T<sub>2</sub> excited states. Natural orbitals are defined strictly in quantum-mechanical terms and their characteristics are summarized as follows. A composite wavefunction ( $\psi$ ) can be written that describes a given electronic state of a porphyrin (in this case metalloporphyrin). This wavefunction can be expressed in terms of linear combinations of MO wavefunctions ( $\phi_i$ ). These MO wavefunctions are called natural orbitals when the density matrix of  $\psi$ ,  $\gamma(1/1')$ , has the form

$$\gamma(1/1') = \sum_i b_i \phi_i^*(1) \phi_i(1')$$

where the  $b_i$ 's reflect relative contributions of each natural orbital to the composite wavefunction. Essentially, the natural orbitals reflect the individual electronic transitions that combine to form the electronic state, and their relative contributions to the composite wavefunction density matrix are determined by the extent of configuration interaction. If calculated values for atomic orbital coefficients are known, composite orbital diagrams can not only predict directional frequency shifts of Raman bands, but also relative magnitudes of electron occupancy changes. Hence, these orbitals also have quantitative predictive value. We foresee future applications for rationalizing Raman intensity patterns as well as inhomogeneities and symmetry changes in excited states.

Since several semi-empirical<sup>9-12,19</sup> and *ab initio*<sup>13-16,17,18</sup> molecular orbital calculations have already been done on D<sub>4h</sub> porphyrins, it made sense to choose one such



study and apply its results towards the generation of these natural orbitals. Our selection criteria for an appropriate study involved convenience in using the data as well as accuracy and complete information. Essentially, we needed a complete set of atomic orbital coefficients that can be used to generate molecular orbitals, and wave functions that describe the extent of configuration interaction between the molecular orbitals.

The initial molecular orbital calculations done on porphine by Longuet-Higgins *et al.* ( Longuet-Higgins H. C.; Rector, C. W.; Platt, J. R. *J. Chem. Phys.* **1950**, 18(9), 1174-1181) in 1950 were initially very appealing since their calculations contain atomic orbital coefficients for  $b_{1u}$  and  $b_{2u}$  orbitals as well as the  $a_{1u}$ ,  $a_{2u}$ ,  $e_{gx}$  and  $e_{gy}$  orbitals and were the original basis of the Gouterman MO's.<sup>6,7</sup> The molecular orbital diagrams, kindred to the original Gouterman orbitals, but including the lowest unoccupied  $b_{1u}$  and  $b_{2u}$  orbitals, are shown in Figure 5.1. These additional orbitals would have been very useful in discerning the influence of higher unoccupied molecular orbitals upon excited state Raman spectra. However, this study was rejected for natural orbital generation since several weaknesses became rapidly apparent. Longuet-Higgins *et al.* recognized the presence of configuration interaction in the electronic absorption spectrum but did not account for it in the calculations, and therefore swayed electron occupancy values at the  $C_a$  and  $C_b$  positions. Furthermore, the electronegativities of the carbon and nitrogen atoms were treated as equivalent. That likewise influenced the relative electron occupancies at the  $C_m$  and N positions. Hence, we needed to involve more recent calculations.

In 1978, Petke *et al.* ( Petke, J. D.; Maggiora, G. M.; Shipman, L. L.; Christofferson, R. E. *J. Mol. Spectrosc.* **1978**, 71, 64-84) did more comprehensive *ab initio* calculations on magnesium porphine that considered the configurational

**Figure 5.1** Molecular orbitals for the HOMO,  $a_{2u}$  and  $a_{1u}$ , LUMO,  $e_{gx}$  and  $e_{gy}$ , and the next two lowest unoccupied states,  $b_{1u}$  and  $b_{2u}$ , of porphine as defined by Longuet-Higgins, H. C.; Rector, C. W.; Platt, J. R. *J. Chem. Phys.* **1950**, 18(9), 1174-1181.

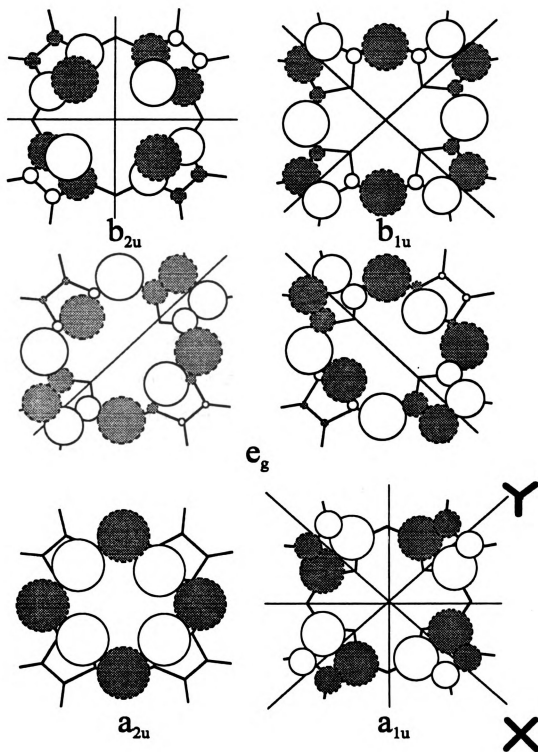


Figure 5.1

compositions of degenerate  $\pi\pi^*$  states.<sup>17</sup> Interestingly, their calculations for electron populations and bond orders for the  $S_1$  and  $T_1$  states agreed very well qualitatively with our experimental results for ZnOEP. Bond electron density changes between ground and excited states did agree with observed frequency shifts in the  $S_1$  state. However, there is no documentation of the atomic orbital coefficients used, so we could not use these results. Additionally, the study did not extend into higher excited states, which limits comparisons to only the lowest singlet and triplet excited states.

Sekino and Kobayashi ( Sekino, H.; Kobayashi, H. *J. Chem. Phys.* **1987**, 86(9), 5045-5052) carried out similar *ab initio* calculations on metalloporphin in 1987. Unlike earlier studies, even those including configuration interaction,<sup>16,17</sup> Sekino and Kobayashi found good reproduction of energy levels for excited states.<sup>18</sup> They attributed their success to a screened potential term that incorporates instantaneous polarization effects in their MO calculations. This term can vary appreciably between distinct electronic states.<sup>18</sup> Additionally, their study presented complete atomic orbital coefficients for the  $a_{1u}$ ,  $a_{2u}$ ,  $e_{gx}$  and  $e_{gy}$  orbitals, and potential wave functions that expressed the extent of configuration interaction for the five lowest singlet and triplet excited states. Their molecular orbital coefficients for the  $a_{1u}$ ,  $a_{2u}$ ,  $e_{gx}$  and  $e_{gy}$  orbitals were previously displayed in Figure 1.6 (Chapter 1). For these reasons, their results were optimal for creating natural orbitals. It should be noted that semi-empirical studies have also been done, notably a MNDO/3 study on zinc porphine by Prendergast and Spiro (Prendergast, K.; Spiro, T. G. *J. Phys. Chem.* **1991**, 95, 9728-9736), where geometry optimization was used without inclusion of configuration interaction.<sup>19</sup> Their calculated atomic orbital coefficients did agree to within

10% of Sekino and Kobayashi values, except for the  $C_b$  values which were generally higher than the *ab initio* calculations. However, Prendergast and Spiro's MNDO/3 calculations predicted core size changes of 0.025 Å in the  $S_1$  state, whereas our experimental results show core size expansion of 0.1 Å (see Chapter 4 for calculation of core size expansion).<sup>20,21</sup> Consequently, as a result of the core size and atomic orbital coefficients differences, the frequency shifts predicted by Prendergast and Spiro for electronic states of zinc porphine strongly disagree with our experimental values for ZnOEP. Therefore, the *ab initio* results of Sekino and Kobayashi were selected to modify Gouterman molecular orbitals.

## II. CALCULATIONS

The composite diagrams compare electron distributions of specific atoms in the  $S_0$  ground state of a metalloporphyrin with electron distributions of the same atoms in electronically excited states. To draw these diagrams, the composite wavefunction representing the relevant electronic state must be comprised of linear combinations of natural orbitals that depict individual electronic transitions. Natural orbital contributions to the composite wavefunction depend upon the extent of CI. Table 5.1 shows MO orbital assignments and energies for metalloporphyrin as calculated by Sekino and Kobayashi.<sup>18</sup> Since electronic symmetry rules permit *ungerade-gerade* or *gerade-ungerade* electronic transitions, configuration interaction (CI) can take place between several molecular orbitals of appropriate symmetries. The two lowest  $\pi\pi^*$  excited states of the  $D_{4h}$  metalloporphyrin are known to come almost exclusively from  $1a_{1u}4e_g$  and  $3a_{2u}4e_g$

Table 5.1 Molecular orbital energies of metalloporphin.<sup>a</sup>

<b>Orbital</b>	<b>E/eV</b>
4a <sub>2u</sub>	2.93
6e <sub>g</sub>	2.80
3b <sub>1u</sub>	2.31
2a <sub>1u</sub>	2.11
5e <sub>g</sub>	1.10
3b <sub>2u</sub>	-0.28
2b <sub>1u</sub>	-1.15
4e <sub>g</sub>	-3.21
3a <sub>2u</sub>	-9.25
1a <sub>1u</sub>	-9.58
3e <sub>g</sub>	-11.51
2b <sub>2u</sub>	-12.08
2a <sub>2u</sub>	-12.19
2e <sub>g</sub>	-12.23
1b <sub>1u</sub>	-12.44
1b <sub>2u</sub>	-15.63
1e <sub>g</sub>	-15.88
1a <sub>2u</sub>	-16.10

<sup>a</sup>calculations by Sekino, H.; Kobayashi, H. *J. Phys. Chem.* **1987**, 86, 5045-5052

orbital interactions,<sup>22</sup> although higher transitions could be included in the CI with proper atomic orbital coefficients. The two electronic transitions considered for CI calculations are both of  $E_u$  symmetry and form two degenerate pairs of orbital transitions that can be expressed in the following manner:

$$\begin{array}{llll}
 E_u(x,y) & 1a_{1u}4e_{gy} & (o,o) \times (e,o) & = (o,e) \\
 & 1a_{1u}4e_{gx} & (o,o) \times (o,e) & = (e,o) \\
 E_u(x,y) & 3a_{2u}e_{gy} & (e,e) \times (e,o) & = (e,o) \\
 & 3a_{2u}e_{gx} & (e,e) \times (o,e) & = (o,e)
 \end{array}$$

For our calculations we considered only the  $E_{ux}$  complement of the degenerate transition pair, and the appropriate screened potential wavefunctions are shown in Table 5.2. The parentheses represent the symmetry of the orbitals under consideration in (x,y) directions. For example,  $1a_{1u}4e_{gy}$  involves promoting one electron from the  $a_{1u}$  orbital, which is antisymmetric about both the x and y axes, to the  $e_{gy}$  orbital, which is symmetric about the x-axis, but antisymmetric about the y-axis (Figure 5.1). The transition dipole is along the y-axis and is permitted due to its symmetry change. The degenerate complement to this transition is the  $1a_{1u}4e_{gx}$  which utilizes the x-axis transition dipole. Configuration interaction for *ungerade-gerade* and *gerade-ungerade* transitions can be expressed in simple bra-ket form when we introduce  $\lambda$  as the configuration parameter.

$$|o,e\rangle = |a_{1u}e_{gy}\rangle + \lambda |a_{2u}e_{gx}\rangle \quad |e,o\rangle = |a_{1u}e_{gx}\rangle + \lambda |a_{2u}e_{gy}\rangle$$

Table 5.2      Screened potential wavefunctions of low-lying excited state metalloporphin.<sup>a</sup>

$1\ ^1E_{ux} = 0.6373\ ^1(3a_{2u} \rightarrow 4e_{gx}) - 0.7612\ ^1(1a_{1u} \rightarrow 4e_{gy}) + \dots$
$2\ ^1E_{ux} = 0.7597\ ^1(3a_{2u} \rightarrow 4e_{gx}) + 0.6383\ ^1(1a_{1u} \rightarrow 4e_{gy}) + \dots$
$1\ ^3E_{ux} = 0.4171\ ^3(3a_{2u} \rightarrow 4e_{gx}) - 0.8718\ ^3(1a_{1u} \rightarrow 4e_{gy}) + \dots$
$2\ ^3E_{ux} = -0.8813\ ^3(3a_{2u} \rightarrow 4e_{gx}) + 0.4539\ ^3(1a_{1u} \rightarrow 4e_{gy}) + \dots$

<sup>a</sup> calculations by Sekino, H.; Kobayashi, H. *J. Phys. Chem.* **1987**, *86*, 5045-5052



Since these two transitions are degenerate, we did calculations based only on the  $|o,e\rangle$  transition with the additional limitation that we were considering configuration interaction (CI) only within the four orbitals  $a_{1u}$ ,  $a_{2u}$ ,  $e_{gx}$  and  $e_{gy}$ . In other words, this is a two state CI model, where the  $|o,e\rangle$  transition is composed of a mixture of two electron configurations,  $|1\rangle$  and  $|2\rangle$ , that express electron population among the four molecular orbital wavefunctions:

$$|1\rangle = 1a_{1u}^2 3a_{2u}^1 4e_{gx} \quad |2\rangle = 1a_{1u}^1 3a_{2u}^2 4e_{gy}$$

Fundamentally, the two possible electron occupancies shown above,  $|1\rangle$  and  $|2\rangle$ , are the natural orbitals that sum up to form the overall singlet excited state wavefunction ( $^1E_{ux}$ ). Their relative electron contributions to  $^1E_{ux}$  are determined by the configuration parameter ( $\lambda$ ). Before tracing the procedure derived by Professor J. F. Harrison of Michigan State University Department of Chemistry and used for generating natural orbitals to express  $^1E_{ux}$ , remember what we were looking for: molecular orbital diagrams. The Gouterman orbital diagrams that we wished to emulate typically display relative electron occupancy amidst individual  $p_z$  (out-of-plane) atoms in the delocalized porphyrin ring. Hence, to draw our diagrams effectively,  $^1E_{ux}$  must be written explicitly in terms of atomic orbital wavefunctions. This required breaking down the natural orbitals,  $\phi_1$  and  $\phi_2$ , into linear combinations of MO wavefunctions,  $\phi_1$ ,  $\phi_2$ ,  $\phi_3$ ,  $\phi_4$  that can be expressed as slater determinants. The slater determinants are themselves products of the molecular

orbital wavefunctions  $1a_{1u}$ ,  $3a_{2u}$ ,  $4e_{gx}$ , and  $4e_{gy}$ , which in turn are merely linear combinations of the  $p_z$  atomic orbitals. The  $p_z$  atomic orbital electron densities can then be drawn in Gouterman-type diagrams. These diagrams, which are called composite diagrams since they are essentially composed of natural orbitals, reflect relative delocalized  $\pi$  electron occupations at and between individual atoms. The following equations trace the generation of natural orbitals for the lowest excited singlet state. Other excited electronic states can be derived using identical methodology.

The lowest excited singlet state wavefunction can be expressed as a combination of natural orbital wavefunctions due to transitions  $|1\rangle$  and  $|2\rangle$  and then written in normalized form:

{Eqn. 5.1}

$$^1E_{ux} = \frac{|1\rangle + \lambda|2\rangle}{\sqrt{1 + \lambda^2}}$$

The natural orbital wavefunctions for the two possible electron promotions are expressed completely when  $A$ , the antisymmetry operator, and spin functions  $\alpha$  and  $\beta$  are taken into consideration.

{Eqns. 5.2}

$$|1\rangle = A1a_{1u}^2 3a_{2u}^1 4e_{gx} \left( \frac{\alpha\beta - \beta\alpha}{\sqrt{2}} \right) \quad |2\rangle = A1a_{1u}^1 3a_{2u}^2 4e_{gy} \left( \frac{\alpha\beta - \beta\alpha}{\sqrt{2}} \right)$$

$|1\rangle$  and  $|2\rangle$  are wavefunctions that can be expanded into slater determinants ( $\varphi$ ) to fulfill the antisymmetry requirement for a many-electron molecule,<sup>23</sup> but first let:

$$1a_{1u} = a \quad 3a_{2u} = b \quad 4e_{gx} = x \quad 4e_{gy} = y$$

Then the determinants are:

{Eqns. 5.3}

$$\varphi_1 = Aa\alpha a\beta b\alpha\alpha\beta \quad \varphi_2 = Aa\alpha a\beta b\beta x\alpha \quad \varphi_3 = Ab\alpha b\beta a\alpha y\beta \quad \varphi_4 = Ab\alpha b\beta a\beta y\alpha$$

For indistinguishability of promoted electrons to remain true, the following must hold:

$$Ab\alpha\alpha\beta = \left( \frac{b\alpha\alpha\beta - x\beta b\alpha}{\sqrt{2}} \right) \quad Ab\beta x\alpha = \left( \frac{b\beta x\alpha - x\alpha b\beta}{\sqrt{2}} \right).$$

These two terms can be summed or subtracted and the wave functions separated from the spin functions.

$$Ab\alpha\alpha\beta \oplus Ab\beta x\alpha = \left[ \frac{bx(\alpha\beta + \beta\alpha) - xb(\alpha\beta + \beta\alpha)}{\sqrt{2}} \right]$$

$$Ab\alpha\alpha\beta - Ab\beta x\alpha = \left[ \frac{bx(\alpha\beta - \beta\alpha) - xb(\beta\alpha - \alpha\beta)}{\sqrt{2}} \right]$$

$$= \left( \frac{bx + xb)(\alpha\beta - \beta\alpha)}{\sqrt{2}} \right)$$

These determinants are incorporated into the individual natural orbitals ( $\phi_1$  and  $\phi_2$ ), and the electronic state wavefunction ( $\psi$ ) ( $^1E_{ux}$  in this case).

{Eqns. 5.4}

$$\frac{(\phi_1 - \phi_2)}{\sqrt{2}} = |1\rangle \quad \frac{(\phi_3 - \phi_4)}{\sqrt{2}} = |2\rangle$$

$$\psi = \frac{|1\rangle + \lambda |2\rangle}{\sqrt{1 + \lambda^2}} = \frac{\phi_1 + \lambda \phi_2}{\sqrt{1 + \lambda^2}}$$

The electron occupancy probability ( $\gamma(1/1')$ ) ( or density matrix) is simply the integrated conjugate product of the electronic state wavefunction from equation 5.4.

{Eqns 5.5}

$$\gamma(1/1') = 4 \int \psi^*(1,2,3,4) \psi(1',2,3,4) d\tau(2,3,4)$$

$$= 4 \frac{\int (\phi_1 + \lambda \phi_2)(\phi_1 + \lambda \phi_2) d\tau(2,3,4)}{1 + \lambda^2}$$

$$= \left( \frac{4}{1 + \lambda^2} \right) \left\{ \int \phi_1 \phi_1 d\tau + \lambda^2 \int \phi_2 \phi_2 d\tau \right\}$$

where all the cross terms cancel out since natural orbitals  $\phi_1$  and  $\phi_2$  always differ by two orbitals. Expansion of the integral product of natural orbital  $\phi_1$  into its Slater determinant wavefunctions ( $\varphi$ ) yields:

{Eqn. 5.6}

$$\int \phi_1 \phi_1 d\tau = \int \frac{(\phi_1 - \phi_2)}{\sqrt{2}} \left( \frac{\phi_1 - \phi_2}{\sqrt{2}} \right) d\tau = 0.5 \int \phi_1 \phi_1 d\tau + 0.5 \int \phi_2 \phi_2 d\tau$$

The cross terms for the determinants  $\varphi_1$  and  $\varphi_2$  also cancel out since they differ by two orbital spins. Expansion of these determinants into their composite spin functions yields

$$0.5 \int \varphi_1 \varphi_1 d\tau = \frac{1}{2 \cdot 4} (a\alpha(1)a\alpha(1') + a\beta(1)a\beta(1') + b\alpha(1)b\alpha(1') + x\beta(1)x\beta(1'))$$

Integration over the spin variables produce.

$$0.5 \int \varphi_1 \varphi_1 d\tau = \frac{1}{2 \cdot 4} (2a(1)a(1') + b(1)b(1') + x(1)x(1'))$$

Similar results can be obtained for the determinant  $\varphi_2$  and the results used to solve equation 5.6.

$$0.5 \int \phi_2 \phi_2 d\tau = \frac{1}{2 \cdot 4} (2a(I)a(I') + b(I)b(I') + x(I)x(I'))$$

$$\int \phi_1 \phi_1 d\tau = \frac{(2a(I)a(I') + b(I)b(I') + x(I)x(I'))}{4}$$

Likewise, the integral  $\phi_2^* \phi_2$  can be calculated and incorporated into equations 5.5 to express electron probability,  $\gamma(1/1')$ , solely in terms of MO wavefunctions and the configuration interaction parameter.

{Eqns. 5.7}

$$\int \phi_2 \phi_2 d\tau = \frac{(2b(I)b(I') + a(I)a(I') + y(I)y(I'))}{4}$$

$$\begin{aligned} \gamma(1/1') &= \left( \frac{1}{1 + \lambda^2} \right) \{ 2aa + bb + xx + \lambda^2 (2bb + aa + yy) \} \\ &= \left( \frac{1}{1 + \lambda^2} \right) \{ (2 + \lambda^2)aa + (2\lambda^2 + 1)bb + xx + \lambda^2 yy \} \end{aligned}$$

The probability distribution should reflect the  $\pi$  electron population of the  $a_{1u}$ ,  $a_{2u}$ ,  $e_{gx}$ , and  $e_{gy}$  orbitals in metalloporphin, as indeed it does upon normalization.

$$0.5 \int \gamma(1/1) dv = \left( \frac{1}{1 + \lambda^2} \right) \{ (2 + \lambda^2) + (2\lambda^2 + 1) + 1 + \lambda^2 \}$$

$$\left( \frac{1}{1 + \lambda^2} \right) \{ 4 + 4\lambda^2 \} = 4$$

We next employ the coefficients of equations 5.7 to show electron occupation changes in the  $S_1$  state of this natural orbital. The normalization shows that the natural orbitals do not change in total electron count, rather, relative populations shift according to the configuration parameter.

{Eqn. 5.8}

$$\begin{array}{ll} 1a_{1u} & (2 + \lambda^2)/(1 + \lambda^2) \quad 3a_{2u} \quad (2\lambda^2 + 1)/(1 + \lambda^2) \\ 4e_{gx} & 1/(1 + \lambda^2) \quad 4e_{gy} \quad \lambda^2/(1 + \lambda^2) \end{array}$$

The configuration parameter can be calculated by taking the ratio of the transition coefficients for the screened potential wavefunctions derived by Sekino and Kobayashi.<sup>18</sup> For example, when we consider the  $^1E_{ux}$  state

$$\lambda = \frac{-0.7612}{0.6373} = -1.1944$$

the molecular orbital occupancies from equations 5.8 become 1.4121 electrons for  $1a_{1u}$ , 1.5879 electrons for  $3a_{2u}$ , 0.4121 electrons for  $4e_{gx}$ , and 0.5879 electrons for  $4e_{gy}$ . This contrasts with the ground state, where the electron occupancy resides completely in  $1a_{1u}$  and  $3a_{2u}$  orbitals (2.0 electrons each).

The total electron densities can be expressed among the molecular orbitals for both ground and excited states where  $\vec{R}$  represents coordinates x,y,z.

$$\rho_{s_1}(\vec{R}) = 1.4121\rho(1a_{1u}) + 1.5879\rho(3a_{2u}) + 0.4121\rho(4e_{gx}) + 0.5879\rho(4e_{gy})$$

$$\rho_{s_0}(\vec{R}) = 2\rho(1a_{1u}) + 2\rho(3a_{2u})$$

$$\Delta\rho_{s_1-s_0} = -0.5879\rho(1a_{1u}) - 0.4121\rho(3a_{2u}) - 0.4121\rho(4e_{gx}) - 0.5879\rho(4e_{gy})$$

$\rho$  represents the molecular orbital summation of electron densities over the 24 atomic orbitals in metalloporphin. Remember that the four electrons we have been discussing are the  $\pi$  electrons involved in  $\pi\pi^*$  transitions, so naturally the atomic orbitals comprising these MO's come from  $p_z$  orbitals on each individual carbon atom. These MO densities can be written explicitly to express every atomic orbital. For example, consider the  $1a_{1u}$  MO.

$$\rho_{1a_{1u}} = \left( \sum_{i=1}^{24} p_i c_{i,1a_{1u}} \right)^2$$

$$\rho_{1a_{1u}} = \left( \sum_{i,j}^{24} c_{i,1a_{1u}} c_{j,1a_{1u}} p_i p_j \right)$$

The  $c_i$  values are the atomic orbital coefficients provided by Sekino and Kobayashi, and are the familiar values associated with Gouterman-type MO pictorials (Figure 1.6).<sup>18,6</sup>



The overall expression for the electron density matrices for the ground ( $\rho_{S_0}$ ) and singlet excited ( $\rho_{S_1}$ ) states can be written as the summation of electron densities from  $a_{1u}$ ,  $a_{2u}$ ,  $e_{gx}$ , and  $e_{gy}$  molecular orbitals. Contributions from the MO's are weighted by the configuration parameter as expressed in equations 5.7 and 5.8.

{Eqns. 5.9}

$$\rho_{S_0}(\vec{R}) = 2 \sum_{i=1}^{24} \sum_{j=1}^{24} (c_{i,1a1u} c_{j,1a1u} + c_{i,3a2u} c_{j,3a2u}) p_i p_j$$

$$\rho_{S_1}(\vec{R}) = \sum_{i=1}^{24} \sum_{j=1}^{24} \left\{ 1.4121 c_{i,1a1u} c_{j,1a1u} + 1.5879 c_{i,3a2u} c_{j,3a2u} + \right. \\ \left. 0.5879 c_{i,4e_{gx}} c_{j,4e_{gx}} + 0.4121 c_{i,4e_{gy}} c_{j,4e_{gy}} \right\} p_i p_j$$

### III. RESULTS AND DISCUSSION

The approach used to express natural orbital electron density for the  $S_1$  state (equations 5.9) was also applied to the  $S_2$ ,  $T_1$ , and  $T_2$  states. Gouterman originally displayed his four-orbital model pictorially with spheres that reflected the size of atomic orbital electron densities.<sup>6</sup> I have taken a similar approach, under the following conditions. Atoms are labeled in Figure 5.2. In all figures, spheres are arbitrarily scaled with respect to the largest value in a given set. The numbers to the right of the figures represent arbitrary scaling up to 1. The independent atom electron densities for the  $S_0$ ,  $S_1$ ,  $S_2$ ,  $T_1$ , and  $T_2$  orbitals are one set (Figure 5.3 and Figure 5.4). Figure 5.5 and Figure 5.6 are atomic orbital density differences with respect to ground state  $S_0$  and define a second set. The bond densities of individual electronic states comprise another set (Figure 5.7,

**Figure 5.2**      **Labeling sequence used for natural orbital calculations.**

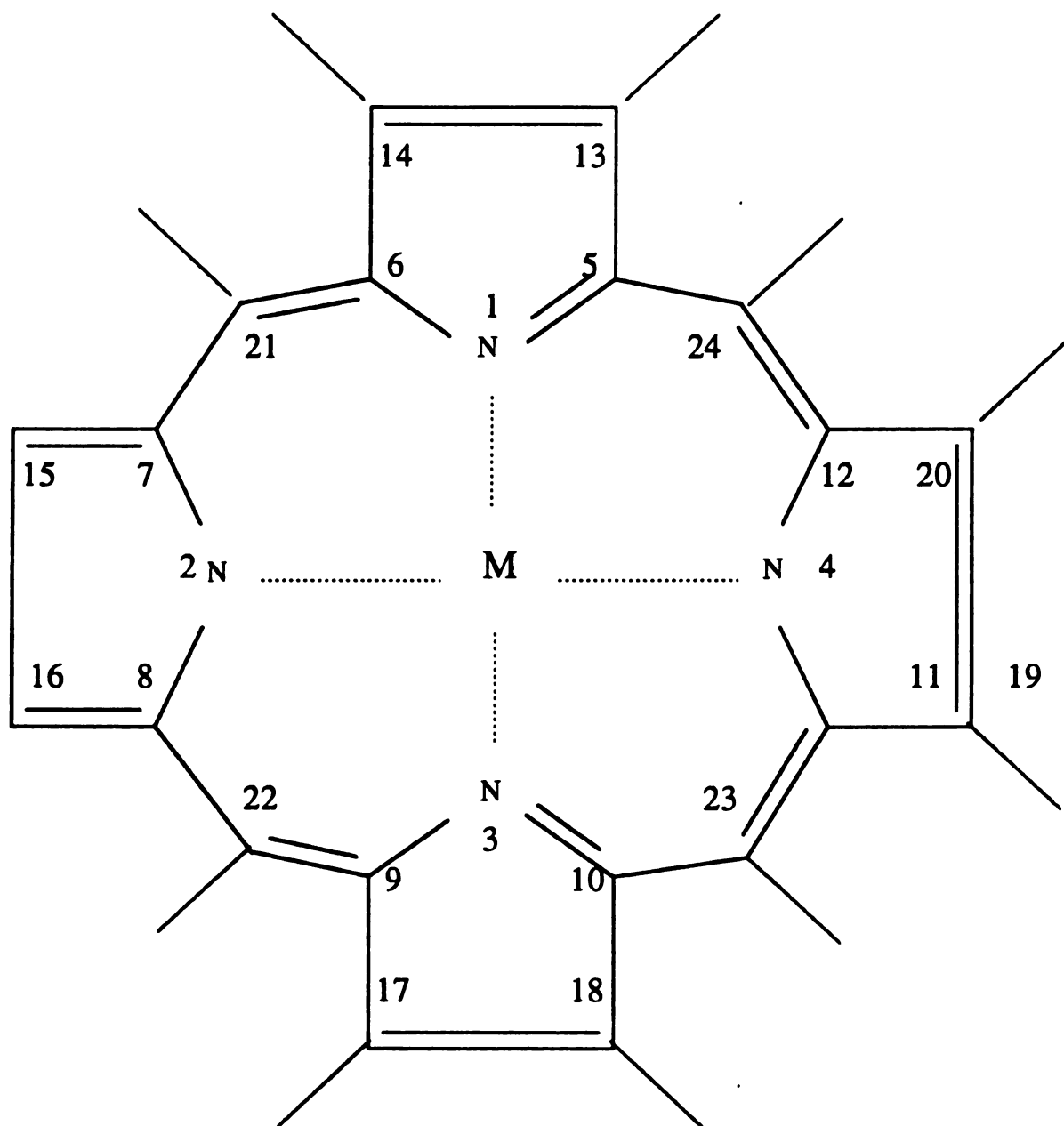
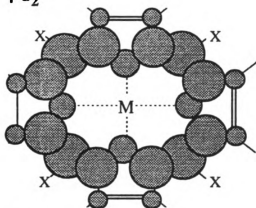


Figure 5.2

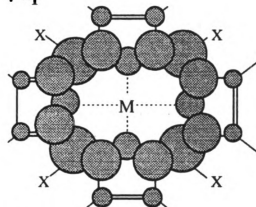
**Figure 5.3**      **Composite orbital diagrams for atom electron densities of singlet states of metalloporphin.**

# SINGLET STATE ATOM ELECTRON DENSITIES

 $\rho_{s_2}$ 


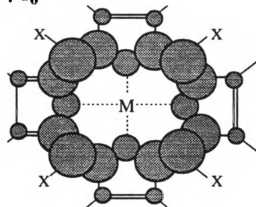
$N_1$	0.30
$N_2$	0.27
$C_{a1}$	0.66

$C_{a2}$	0.68
$C_{b1}$	0.13
$C_{b2}$	0.14
$C_m$	0.82

 $\rho_{s_1}$ 


$N_1$	0.30
$N_2$	0.32
$C_{a1}$	0.63

$C_{a2}$	0.61
$C_{b1}$	0.14
$C_{b2}$	0.13
$C_m$	0.90

 $\rho_{s_0}$ 


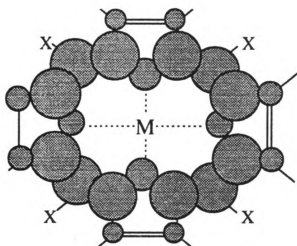
$N$	0.30
$C_a$	0.67

$C_b$	0.11
$C_m$	0.88

Figure 5.3

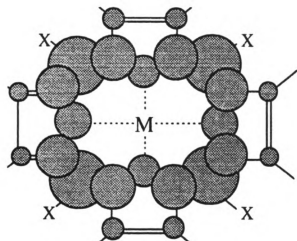
**Figure 5.4**      **Composite orbital diagrams for atom electron densities of triplet states of metalloporphin.**

# **TRIPLET STATE ATOM ELECTRON DENSITIES**

 $\rho_{T_2}$ 


$N_1$	0.30
$N_2$	0.21
$C_{a1}$	0.69

$C_{a2}$	0.76
$C_{b1}$	0.12
$C_{b2}$	0.17
$C_m$	0.73

 $\rho_{T_1}$ 


$N_1$	0.30
$N_2$	0.39
$C_{a1}$	0.60

$C_{a2}$	0.53
$C_{b1}$	0.14
$C_{b2}$	0.10
$C_m$	1

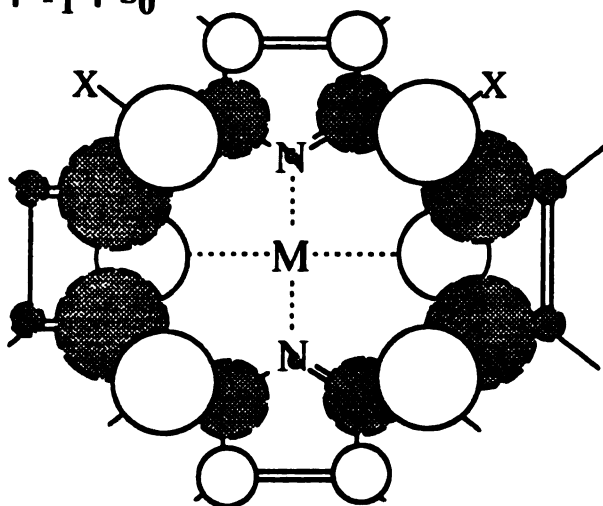
Figure 5.4

**Figure 5.5**      **Composite orbital difference diagrams for atom electron densities of lowest excited states of metalloporphin.**



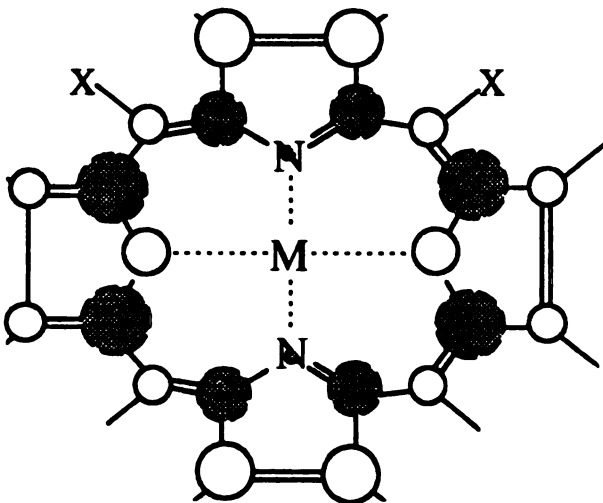
## LOWEST EXCITED STATE ELECTRON DENSITY CHANGES

$\rho_{T_1} - \rho_{S_0}$



$N_1$	-0.01
$N_2$	+0.58
$C_{a1}$	-0.42
$C_{a2}$	-0.87
$C_{b1}$	+0.24
$C_{b2}$	-0.07
$C_m$	+0.74

$\rho_{S_1} - \rho_{S_0}$



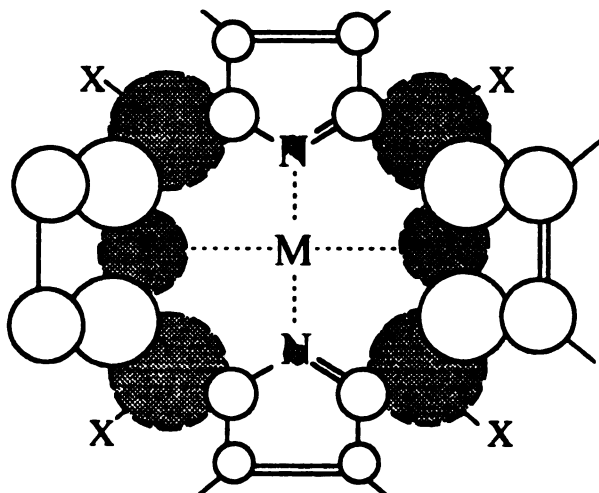
$N_1$	-0.01
$N_2$	+0.15
$C_{a1}$	-0.19
$C_{a2}$	-0.32
$C_{b1}$	+0.22
$C_{b2}$	+0.10
$C_m$	+0.09

Figure 5.5

**Figure 5.6**      **Composite orbital difference diagrams for atom electron densities of second lowest excited states of metalloporphin.**

## SECOND LOWEST EXCITED STATE ELECTRON DENSITY CHANGES

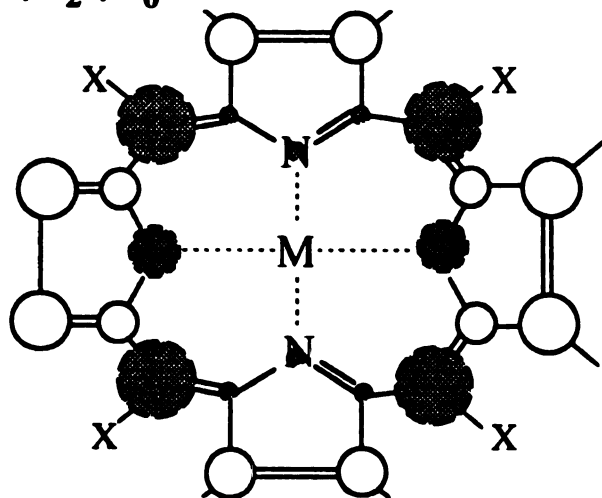
$\rho_{T_2} - \rho_{S_0}$



$N_1$	-0.03
$N_2$	-0.57
$C_{a1}$	+0.19

$C_{a2}$	+0.61
$C_{b1}$	+0.11
$C_{b2}$	+0.40
$C_m$	-1

$\rho_{S_2} - \rho_{S_0}$



$N_1$	-0.02
$N_2$	-0.18
$C_{a1}$	-0.02

$C_{a2}$	+0.11
$C_{b1}$	+0.17
$C_{b2}$	+0.25
$C_m$	-0.42

Figure 5.6

**Figure 5.7** Composite orbital bond order diagram for the singlet ground state of metalloporphin.

## GROUND STATE BOND ELECTRON DENSITIES

$\rho_{s0}$

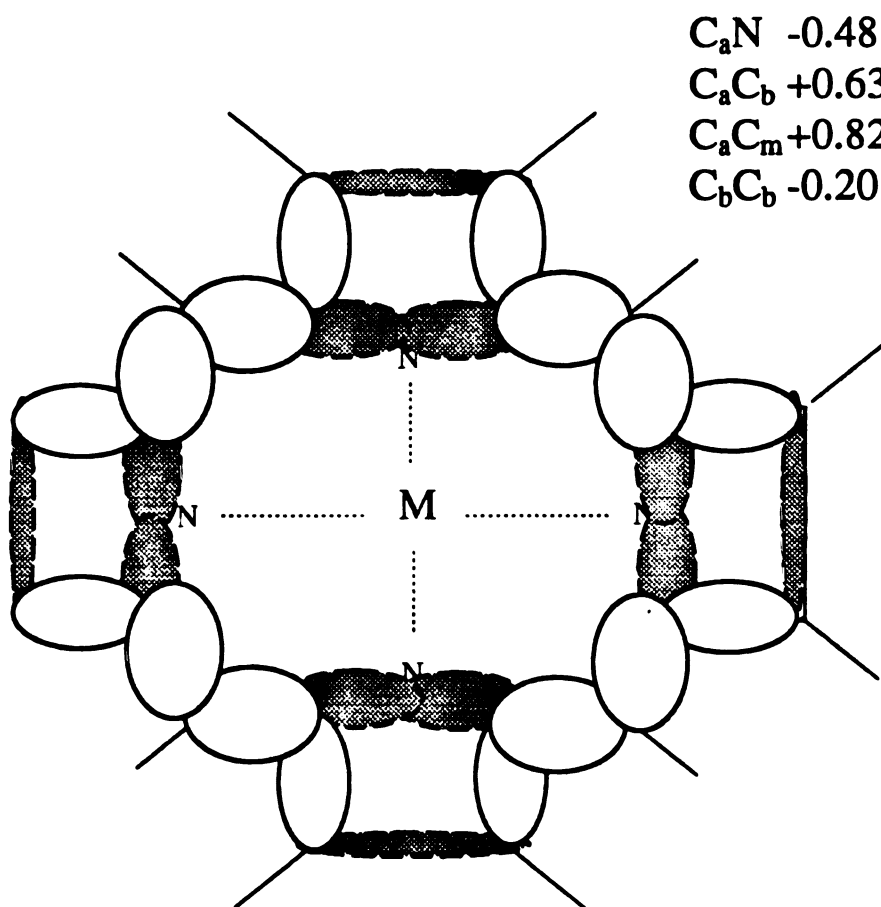
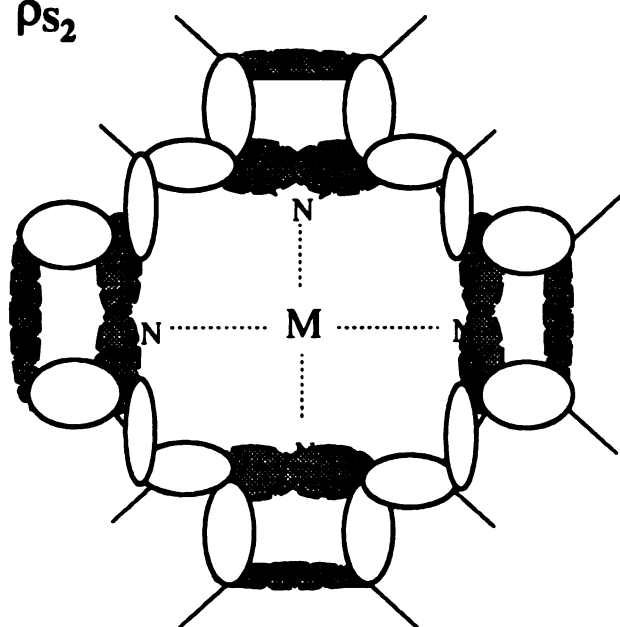


Figure 5.7

**Figure 5.8** Composite orbital bond order diagrams for the two lowest singlet excited states of metalloporphin.

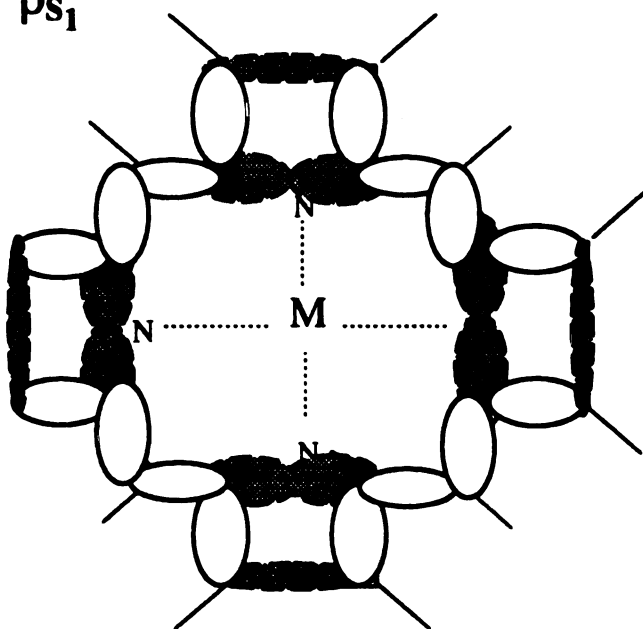
## SINGLET STATE BOND ELECTRON DENSITIES

$\rho_{s_2}$



$Ca_1N_1$	-0.57
$Ca_2N_2$	-0.51
$Ca_1Cb_1$	+0.63
$Ca_2Cb_2$	+0.73
$Ca_1C_m$	+0.57
$Ca_2C_m$	+0.37
$Cb_1Cb_1$	-0.27
$Cb_2Cb_2$	-0.33

$\rho_{s_1}$



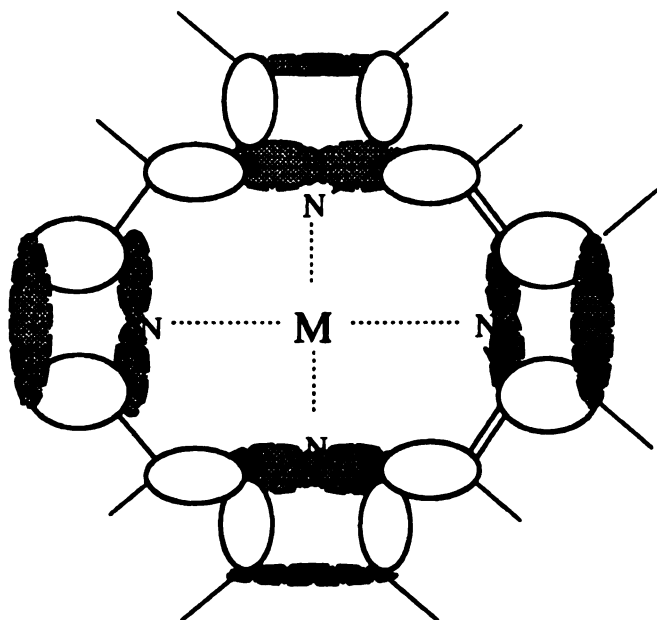
$Ca_1N_1$	-0.55
$Ca_2N_2$	-0.62
$Ca_1Cb_1$	+0.66
$Ca_2Cb_2$	+0.55
$Ca_1C_m$	+0.44
$Ca_2C_m$	+0.65
$Cb_1Cb_1$	-0.30
$Cb_2Cb_2$	-0.23

Figure 5.8

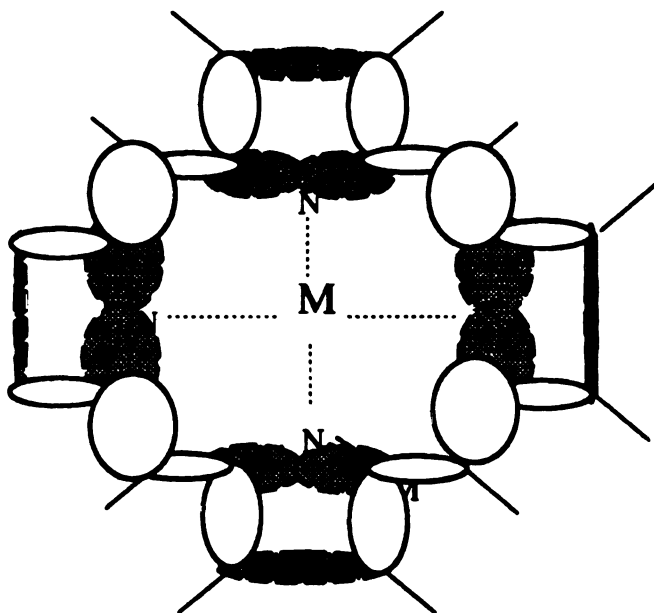
**Figure 5.9** Composite orbital bond order diagrams for the two lowest triplet excited states of metalloporphin.



# TRIPLET STATE BOND ELECTRON DENSITIES

 $\rho_{T_2}$ 


$C_{a1}N_1$	-0.61
$C_{a2}N_2$	-0.37
$C_{a1}C_{b1}$	+0.59
$C_{a2}C_{b2}$	+0.95
$C_{a1}C_m$	+0.72
$C_{a2}C_m$	+0.05
$C_{b1}C_{b1}$	-0.23
$C_{b2}C_{b2}$	-0.45

 $\rho_{T_1}$ 


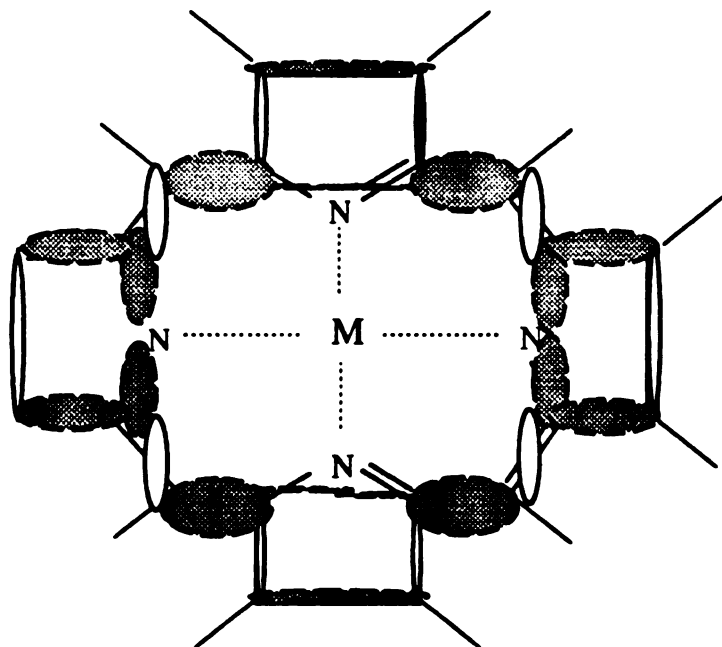
$C_{a1}N_1$	-0.51
$C_{a2}N_2$	-0.76
$C_{a1}C_{b1}$	+0.70
$C_{a2}C_{b2}$	+0.31
$C_{a1}C_m$	+0.27
$C_{a2}C_m$	+1
$C_{b1}C_{b1}$	-0.35
$C_{b2}C_{b2}$	-0.11

Figure 5.9

**Figure 5.10** Composite orbital bond order difference diagrams for the lowest singlet and triplet excited states of metalloporphin.

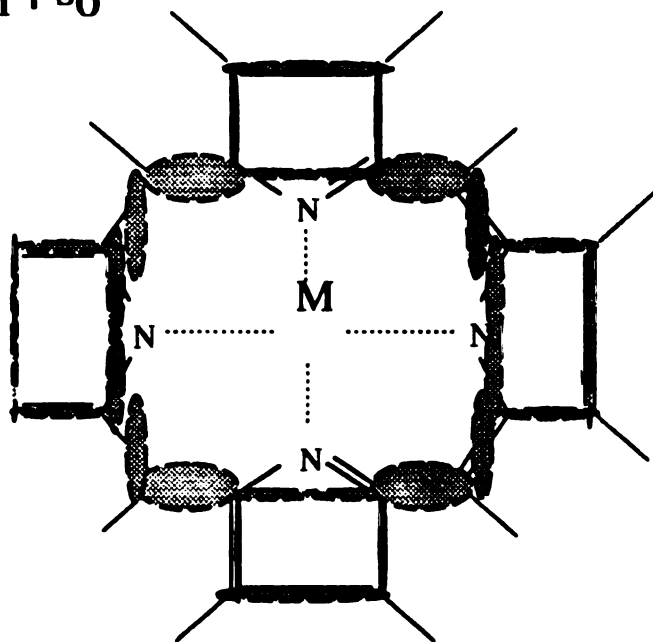
## LOWEST EXCITED STATE ELECTRON DENSITY CHANGES

$\rho_{T_1} - \rho_{S_0}$



$Ca_1N_1$	-0.04
$Ca_2N_2$	-0.36
$Ca_1Cb_1$	+0.09
$Ca_2Cb_2$	-0.42
$Ca_1C_m$	-0.71
$Ca_2C_m$	+0.23
$Cb_1Cb_1$	-0.14
$Cb_2Cb_2$	+0.13

$\rho_{S_1} - \rho_{S_0}$



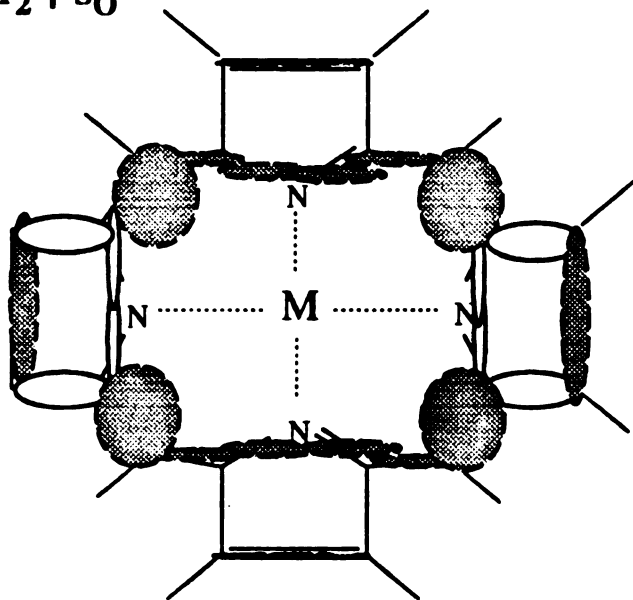
$Ca_1N_1$	-0.09
$Ca_2N_2$	-0.18
$Ca_1Cb_1$	+0.04
$Ca_2Cb_2$	-0.11
$Ca_1C_m$	-0.49
$Ca_2C_m$	-0.23
$Cb_1Cb_1$	-0.13
$Cb_2Cb_2$	-0.04

Figure 5.10

**Figure 5.11** Composite orbital bond order difference diagrams for the second lowest singlet and triplet excited states of metalloporphin.

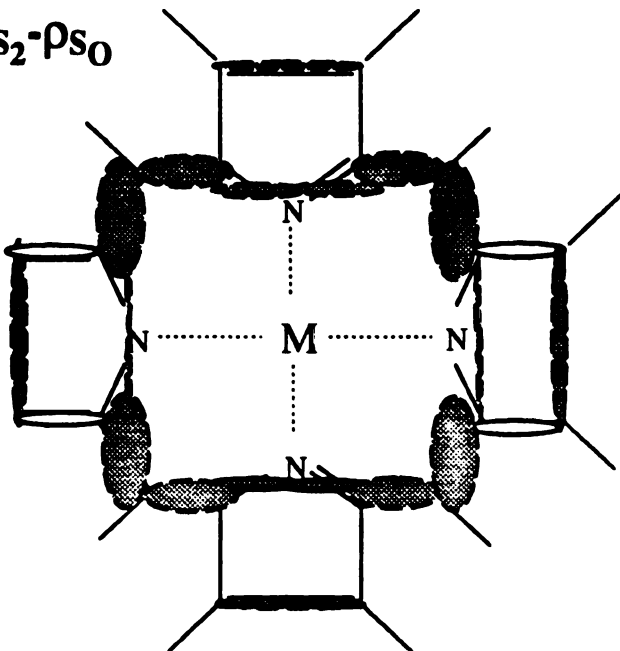
## SECOND LOWEST EXCITED STATE ELECTRON DENSITY CHANGES

$\rho_{T_2} - \rho_{S_0}$



$Ca_1N_1$	-0.17
$Ca_2N_2$	+0.14
$Ca_1Cb_1$	-0.05
$Ca_2Cb_2$	+0.42
$Ca_1C_m$	-0.13
$Ca_2C_m$	-1
$Cb_1Cb_1$	-0.03
$Cb_2Cb_2$	-0.32

$\rho_{S_2} - \rho_{S_0}$



$Ca_1N_1$	-0.12
$Ca_2N_2$	-0.04
$Ca_1Cb_1$	-0.01
$Ca_2Cb_2$	+0.14
$Ca_1C_m$	-0.32
$Ca_2C_m$	-0.58
$Cb_1Cb_1$	-0.08
$Cb_2Cb_2$	-0.17

Figure 5.11

Figure 5.8, and Figure 5.9). Figure 5.10 and Figure 5.11 are bond density differences with respect to the ground state ( $S_0$ ) and are considered a separate set. Each set provides slightly different information about the electronic states so we consider each group separately.

The atom electron densities in Figure 5.3 and Figure 5.4 were essential for generation of Figure 5.5 and Figure 5.6, but also provided some insight on their own. For all natural orbitals, electron population resides mainly within the inner ring, chiefly at the  $C_a$  and  $C_m$  positions. Electron distribution changes upon promotion to the  $S_1$ ,  $T_1$ ,  $S_2$ , and  $T_2$  states are small in comparison to the absolute electron population. The changes that do occur, however, suggest a redistribution of electrons to the periphery, primarily  $C_b$  orbitals. The  $S_1$  and  $T_1$  states have distribution changes that are associated with the dominant contribution of electron promotion from the  $1a_{1u}$  to  $4e_{gy}$  orbitals. Likewise, the  $S_2$  and  $T_2$  states have comparable directional changes that can be correlated to their primary  $3a_{2u}$  to  $4e_{gx}$  electron promotion.

These changes become more apparent in Figure 5.5 and Figure 5.6. The  $S_1$  natural orbital in Figure 5.5 shows relatively uniform electron redistribution from  $C_a$  atoms to surrounding atoms. For the  $S_1$  state increased electron density was observed at the  $N_2$ ,  $C_m$ , and both  $C_b$  positions, while the largest decreases in density occur at the  $C_a$  positions. The  $T_1$  state observed similar changes at the same positions, but the changes in atomic orbital densities are much larger, particularly at the  $C_m$  and  $N_2$  positions. The  $S_2$  and  $T_2$  states in Figure 5.6, however, show decreased populations at the  $N_2$  and  $C_m$  positions, with increased populations at the  $C_a$  and  $C_b$  positions. A small  $b_{1g}$  distortion is present in

the singlet excited states, that only disappears in cases of accidental degeneracy between the  $a_{2u}$  and  $a_{1u}$  orbitals. This distortion becomes more dominant in the triplet states. Clearly, absence of Jahn-Teller effects in singlet excited states is strictly true only for accidentally degenerate  $a_{1u}$  and  $a_{2u}$  orbitals, although the Raman data on metallooctaethylporphyrins suggest no direct observation of Jahn-Teller modes (see Chapter 4).<sup>20,24,25</sup>

Despite this clear correlation with experimental evidence describing the impact of configuration interaction upon Jahn-Teller distortions,<sup>26-29</sup> these atom electron density diagrams do not directly address actual bond order changes. So at this point we have no more insight than we have with the frequently used Gouterman orbitals as applied to triplet excited states. Indeed, atom electron densities indicate increased electron populations at the  $C_b$  positions, which could suggest upward frequency shifts of  $C_bC_b$  modes in Raman spectra. Yet, as mentioned previously, our experimental results show negative frequency shifts for the  $\nu_2$  (Chapter 3 and Chapter 4).<sup>20,24,25</sup> For these reasons, natural orbitals were next applied to bond orders.

As seen in the calculation section, computation of bond densities involved atomic orbital coefficient products of adjacent porphyrin atoms. In order to relate the atom electron density results to bond orders, we recall that the coefficient products imply nonequal sharing of  $\pi$  electrons between adjacent atoms for a given natural orbital. Thus, comparison of predictions from atom electron densities and bond electron densities can be difficult. As an example of how to interpret these results, we consider the  $C_{b1}C_{b1}$  bond in the  $S_1$  state. The  $C_{b1}C_{b1}$  bond was chosen as an example as this eliminates nonequal

sharing between atoms, since the two atomic orbital coefficients magnitudes are identical.<sup>18</sup> The electron bond density for  $S_0$  in Figure 5.7 is negative, -0.20, thus this is antibonding in nature. Bond order changes for  $S_1-S_0$  in Figure 5.10 show a value of -0.13. This suggests an increase in antibonding character, which can occur by increased electron population of an antibonding orbital. Now refer back to Figure 5.5. We see that the atom density change at the  $C_{b1}$  position in the  $S_1-S_0$  orbital is positive and describes an increased electron occupancy. Thus, the atom electron density and bond density diagram predictions are consistent. However, in the absence of these bond order diagrams, we cannot predict whether the increased electron occupancy at  $C_{b1}$  implies a bond lengthening or bond shortening at the  $C_bC_b$  position. Thus, bond order orbitals became a necessity.

The relative electron bond orders in Figure 5.7, Figure 5.8, and Figure 5.9 were used for generation of Figure 5.10 and Figure 5.11. The  $S_0$  natural orbital has equal contributions to bond electron density from the  $1a_{1u}$  and  $3a_{2u}$  molecular orbitals. Consequently, bond densities at the  $C_aC_b$  and  $C_bC_b$  positions have predominantly  $a_{1u}$  characteristics, and show bonding and antibonding bonds, respectively. Bond densities at  $C_aN$  and  $C_aC_m$  are predominantly  $a_{2u}$  in character, and are antibonding and bonding. Note that this bonding/antibonding label refers only to the four electrons within the  $\pi$  orbitals, not the entire porphyrin. Consistent with atom electron densities, these figures show relatively small electron redistribution upon promotion of a single electron. Similar to atom electron density results, larger changes are predicted for  $T_1$  and  $T_2$  states, and the relative changes are best seen with difference diagrams. Figure 5.10 is a good example of the utility of these calculations as a predictive tool for interpreting experimental data. The  $S_1-S_0$  diagram forecasts bond length expansion at the  $C_aC_m$ ,  $C_aN$ , and  $C_bC_b$  positions, and



contrasting changes at the  $C_aC_b$  position. This diagram also estimates relative bond expansions where  $C_aC_m > C_aN > C_bC_b$ . These predictions can be compared to observed Raman frequency shifts for the  $\nu_3(C_aC_m, C_bC_b)$ ,  $\nu_2(C_aN, C_aC_b)$ , and  $\nu_4(C_bC_b)$  modes in the  $S_1$  state of ZnOEP (Chapter 4).<sup>20</sup> To do this, we must assume the normal coordinate compositions of these ground state modes are similar to those calculated for NiOEP.<sup>29</sup> Since the isotope data suggests no great mode composition changes in the  $S_1$  state (Chapter 4 and Figure 4.6), the correlation between observed experimental frequency shifts of  $-35\text{ cm}^{-1}$ ,  $-20\text{ cm}^{-1}$ , and  $-17\text{ cm}^{-1}$  and natural orbital predictions is valid. The  $b_{1g}$  distortion noted earlier, when discussed in terms of nonuniform bond expansion/contraction, can explain the source of line broadening in the Raman spectra of higher excited states.<sup>29,31</sup> This distortion becomes stronger once the porphyrin enters the triplet state. Similar to the atom electron density results, the  $T_1-S_0$  diagram in Figure 5.10 shows large bond order changes characteristic of Jahn-Teller distortion. The  $C_{a2}N_2$ ,  $C_{a2}C_{b2}$ , and  $C_{a1}C_m$  bond orders decrease appreciably, indicating a general bond lengthening in these three regions of the macrocycle. Conversely, the  $C_{a2}C_m$  and  $C_{b2}C_{b2}$  bond orders become positive, suggesting bond compression as the porphyrin elongates in the x direction. These predictions suggest that the modes most affected by stretching and compressing in the  $T_1$  state are the  $\nu_4$  and  $\nu_3$  modes. Unfortunately, time-resolved Raman results for the  $T_1$  state of ZnOEP could not clearly resolve these peaks (Chapter 3).<sup>4,24,25</sup> Similar deformities of the porphyrin are predicted for the  $S_2$  and  $T_2$  states (Figure 5.11), but in the y-axis direction. The relative deformities of porphyrins in  $S_1$ ,  $T_1$ ,  $S_2$ , and  $T_2$  states are drawn schematically in Figure 5.12. The lowest and second lowest excited

Figure 5.12 Metalloporphin bond density changes in first and second excited states. Positive values suggest bond compression, whereas negative values suggest bond stretching.

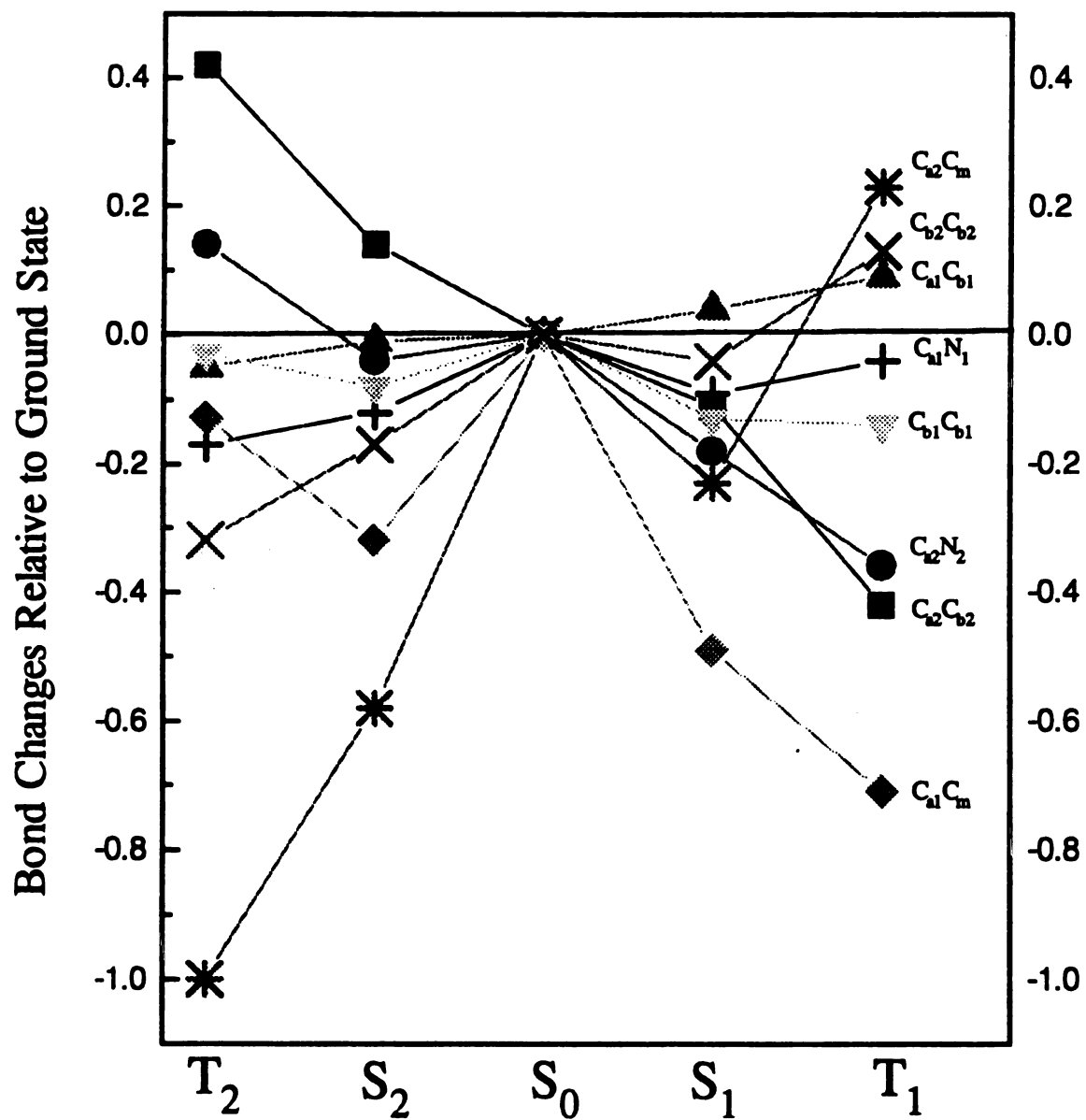


Figure 5.12

states are related in somewhat of a mirror image pattern. This is a direct reflection of the excited state configurations used within the screened potential wavefunctions (Table 5.1 and Table 5.2).<sup>18</sup> For  $S_1$ , the largest implied stretch is at  $C_{a1}C_m$  positions, whereas for  $S_2$  the largest stretch is at  $C_{a2}C_m$ . Transition to the triplet state causes large changes in bond densities at specific positions that deviate noticeably from the singlet state bond densities. For the  $T_1$  state, bond compression appears particularly strong at the  $C_{a2}C_m$  and  $C_{b2}C_{b2}$  positions, while bond stretching appears at  $C_{a2}N_2$ ,  $C_{a2}C_{b2}$ , and  $C_{a1}C_m$ . The  $T_2$  state observes compression at  $C_{a1}C_m$ ,  $C_{a2}C_{b2}$ , and  $C_{a2}N_2$  positions, and bond stretching at  $C_{a2}C_m$  and  $C_{b2}C_{b2}$ . The relative distortions in the  $S_1$ ,  $T_1$ ,  $S_2$ , and  $T_2$  states can be visualized with the porphyrin structures in Figure 5.13.

#### IV. FUTURE WORK

Since this is a project that I undertook only at the very end of my graduate career, I will discuss two areas where these natural orbitals can be applied. One such application would be experimental studies of  $D_{4h}$  porphyrins with more or less CI relative to ZnOEP. The amount of CI in porphyrins can be easily gauged by the relative intensity of Q band/Soret band absorption peaks in the ground electronic state spectrum. Correlations could then be drawn between the predicted  $b_{1g}$  distortions in singlet states of different porphyrins and observed line broadening effects in  $S_1$  Raman spectra. For example, metallotetraphenylporphyrins (MTPP) are porphyrins with generally stronger CI than their metallooctaethylporphyrin (MOEP) counterparts. The Raman spectra of MTPP excited electronic states can be accessed in a manner similar to that done for the MOEP's.<sup>1,2,5</sup> However, the initial experiments to detect excited singlet states of zinc and tin

Figure 5.13 Representative distortions in  $S_1$ ,  $T_1$ ,  $S_2$ , and  $T_2$  excited electronic states.

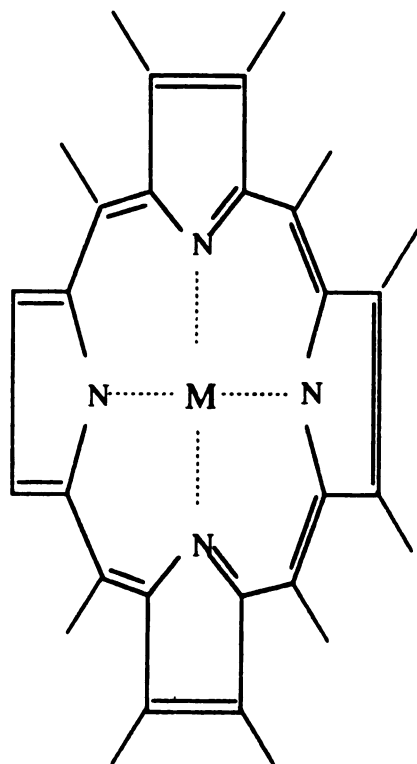
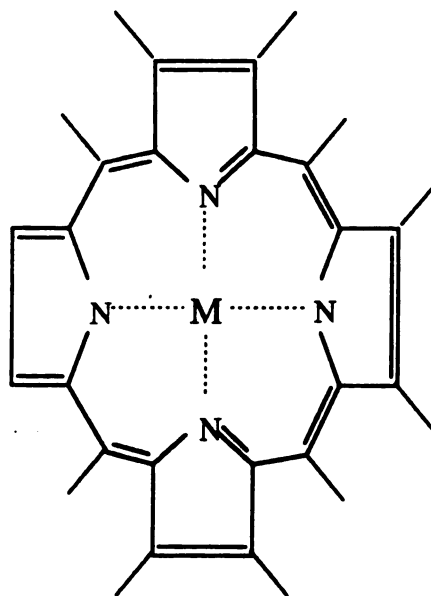
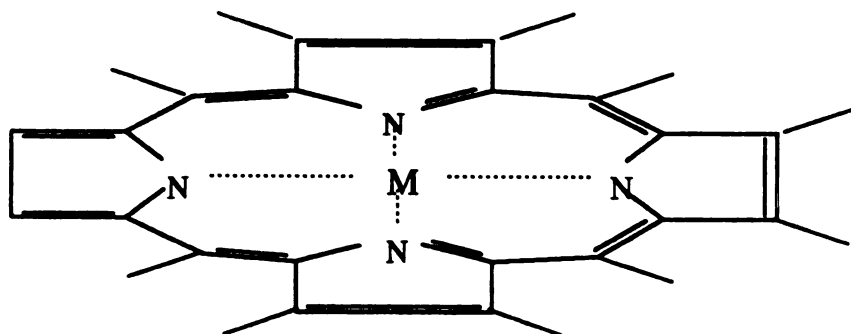
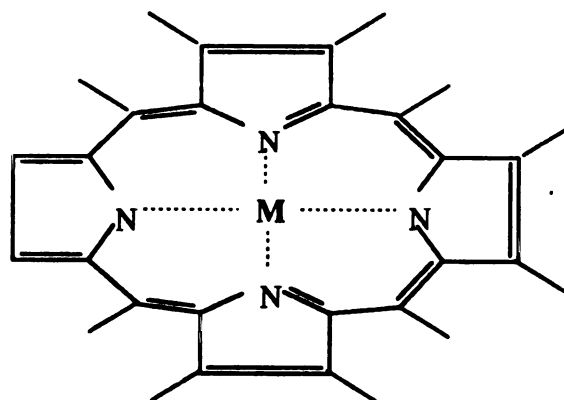
**T<sub>2</sub>****S<sub>2</sub>****T<sub>1</sub>****S<sub>1</sub>**

Figure 5.13

tetraphenylporphyrin via time-resolved Raman spectroscopy have given incomplete results.<sup>32</sup> Another feasible application is using these natural orbitals to predict chlorin/chlorophyll and metallochlorin transitions. Marcus theory predicts that the rate of electron transfer in photosynthesis is strongly dependent on reorganization energy, so strong deformations in singlet excited states could intuitively reduce the rate of electron transfer. Knowing the amount of CI, natural orbitals could be used to predict deformations in these lower symmetry excited states. Since CI is noticeably weaker in the electronic absorption spectra of chlorins (and chlorophylls), due to symmetry, CI may perhaps even be ignored. Preliminary experiments on chlorins suggest that singlet state Raman spectra of metallochlorins may well be very different than those of metalloporphyrins.<sup>33,34,35</sup>

## LIST OF REFERENCES

- (1) Walters, V. A.; de Paula, J. C.; Babcock, G. T.; Leroi, G. E. *J. Am. Chem. Soc.* **1989**, 111, 8300-8302.
- (2) Reed, R. A.; Purello, R.; Prendergast, K.; Spiro, T. G. *J. Phys. Chem.* **1991**, 95, 9720-9727.
- (3) Sato, S.; Asano-Someda, M.; Kitagawa, T. *Chem. Phys. Lett.* **1992**, 189, 443-447.
- (4) Kumble, R.; Hu, S.; Loppnow, G. R.; Vitols, S. E.; Spiro, T. G. *J. Phys. Chem.* **1993**, 97, 10521-10523.
- (5) Bell, S. E. J.; Al-Obaidi, A. H. R.; Hegarty, M.; Hester, R. E.; Mcgarvey, J. J. *J. Phys. Chem.* **1993**, 97, 11599-11602.
- (6) Gouterman, M. *J. Mol. Spectroscopy* **1961**, 6, 138-163.
- (7) Longuet-Higgins, H. C.; Rector, C. W.; Platt, J. R. *J. Chem. Phys.* **1950**, 18(9), 1174-1181.
- (8) Levine, I. N. in *Quantum Chemistry*; Levine, I. N., Ed.; Allyn and Bacon: Massachusetts, 1983, Vol III, pp 383-384.
- (9) Kobayashi, H. *J. Chem. Phys.* **1959**, 30, 1362-1373.
- (10) (a) Weiss, C. Jr.; Kobayashi, H.; Gouterman, M.; *J. Mol. Spectroscopy* **1965**, 16, 415. (b) Rawlings, D. C.; Davidson, E. R.; Gouterman, M. *Theor. Chim. Acta.* **1982**, 61, 227.
- (11) (a) Maggiora, G. M. *J. Am. Chem. Soc.* **1973**, 95, 6555. (b) Loew, G. H.; Rohmer, M.-M. *J. Am. Chem. Soc.* **1980**, 102, 3655. (c) Loew, G.; Goldblum, A. *J. Am. Chem. Soc.* **1980**, 102, 3657.
- (12) (a) Edwards, W. D.; Zerner, M. C. *Int. J. Quantum. Chem.* **1983**, 23, 1407-1419. (b) Edwards, W. D.; Zerner, M. C. *Can. J. Chem.* **1985**, 63, 1763-1778.



- (13) (a) Dedieu, A.; Rohmer, M.-M.; Bernard, M.; Veillard, A. *J. Am. Chem. Soc.* **1976**, 98, 3717. (b) Rohmer, M.-M.; Dedieu, A.; Veillard, A. *Chem. Phys.* **1983**, 77, 449.
- (14) (a) Spangler, D.; Mckinney, R.; Christofferson, R. E.; Maggiora, G. M.; Shipman, L. L. *Chem. Phys. Lett.* **1975**, 36, 427. (b) Spangler, D.; Maggiora, G. M.; Shipman, L. L.; Christofferson, R. E. *J. Am. Chem. Soc.* **1977**, 99, 7470-7478. (c) Christofferson, R. E. *Int. J. Quantum Chem.* **1979**, 16, 573.
- (15) (a) Obara, S.; Kashiwagi, H. *J. Chem. Phys.* **1982**, 77, 3155. (b) Saito, M.; Kashiwagi, J. *J. Chem. Phys.* **1985**, 82, 15.
- (16) (a) Petke, J. D.; Maggiora, G. M.; Shipman, L. L.; Christofferson, R. E. *Photochem. Photobiol.* **1979**, 30, 203 (b) **1980**, 31, 243 (c) **1980**, 32, 399 (d) **1981**, 33, 663 (e) **1982**, 36, 383. (f) **1978**, 73, 311.
- (17) Petke, J. D.; Maggiora, G. M.; Shipman, L. L.; Christofferson, R. E. *J. Mol. Spectroscopy* **1978**, 71, 64-84.
- (18) Sekino, H.; Kobayashi, H. *J. Chem. Phys.* **1987**, 86(9) 5045-5052.
- (19) Prendergast, K.; Spiro, T. G. *J. Phys. Chem.* **1991**, 95, 9728-9736.
- (20) Deinum, G.; Kreszowski, D. H.; Chang, C. K.; Babcock, G. T. *submitted to J. Am. Chem. Soc.*
- (21) Anderson, K. K.; Hobbs, J. D.; Luo, L.; Stanley, K. D.; Quirke, J. M. E.; Shelnutt, J. A. *J. Am. Chem. Soc.* **1993**, 115, 12346-12352.
- (22) Gouterman, M. in *The Porphyrins*; Gouterman, M., Ed.; Academic: New York, 1978, Vol III, p 1.
- (23) Levine, I. N. in *Quantum Chemistry*; Levine, I. N., Ed.; Allyn and Bacon: Massachusetts, 1983, Vol III, pp 249-250.
- (24) Kreszowski, D. H.; Deinum, G.; Babcock, G. T. *Biophys. J.* **1994**, 66(2), a374.
- (25) Kreszowski, D. H.; Deinum, G.; Babcock, G. T. *J. Am. Chem. Soc.* **1994**, 116, 7463-7464.
- (26) Perrin, M. H.; Gouterman, M.; Perrin, C. L. *J. Chem. Phys.* **1969**, 50, 4137.
- (27) Gouterman, M. *Ann. N. Y. Acad. Sci.* **1973**, 206, 70-83.

- (28) Shelnutt, J. A.; Cheung, L. D.; Chang, R. C. C.; Yu, N.-T.; Felton, R. H. *J. Chem. Phys.* **1977**, *66*, 3387-3398.
- (29) Cheung, L. D.; Yu, N.-T.; Felton, R. H. *Chem. Phys. Lett.* **1978**, *55*, 527-530.
- (30) (a) Abe, M.; Kitagawa, T.; Kyoguku, Y. *J. Chem. Phys.* **1978**, *69*, 4526-4534. (b) Li, X.-Y.; Czernuszewicz, R. S.; Kincaid, J. R.; Stein, P.; Spiro, T. G. *J. Phys. Chem.* **1990**, *94*, 47-61.
- (31) Courtney, S. H.; Jedju, T. M.; Friedman, J. M.; Alden, R. G.; Ondrias, M. R. *Chem. Phys. Lett.* **1989**, *164*, 39-43.
- (32) Unpublished data for singlet excited states of zinc(II) tetraphenylporphyrin and tin(IV) tetraphenylporphyrin (Cl<sub>2</sub>) showed strong interference in Raman spectra from broadband fluorescence centered around 442 nm, that coincided with excitation into excited electronic states. Preliminary fluorescent studies with variable pump laser intensities suggested possible two-photon processes.
- (33) Salehi, A.; Oertling, W. A.; Fonda, H. N.; Babcock, G. T.; Chang, C. K. *Photochem. Photobiol.* **1988**, *48*, 525-530.
- (34) Procyk, A. D.; Bocian, D. F. *Annu. Rev. Phys. Chem.* **1992**, *43*, 465-496.
- (35) Unpublished data for singlet and triplet excited states of zinc(II) methyloctaethylchlorin suggests different features and more similarity between the two excited states than was true for metalloporphyrins.

## APPENDIX

## APPENDIX A

### SPECTRUM BASIC SOURCE CODES USED FOR DATA PROCESSING

#### SEPARATE.PRO

```
rem Separate.pro
rem Created: 06/08/93 by Doug Kreszowski
rem This program reads a file of frames, separates
rem even frames from odd frames, and stores each separately.
print "SEPARATE",0,0,0,15
let dcolor = 12
rem new c.g.r.
rem suspend macro if running
let tmp = suspendmacro
let tmp = setbasicrunflag(1)
float starttime
float timefactor
int errorflag
rem errorflag set to 1 if error occurs, otherwise 0
let errorflag = 0
let startframe = getpivar(49)
let startwindow = getpivar(50)
let repcont = getpivar(74)
rem:: start at first unused curve in window if flag is set
to do so
rem:: replay "1=2" with flag when available.
let curvenumber = 1
STRING infile, outfileOdd, outfileEven
let infile = repname
let outfileOdd = "
let outfileEven = "
inp infile, outfileOdd, outfileEven
open infile for input as 1
open outfileOdd for output as 2
open outfileEven for output as 3
long strips
long numframes
rem read strips per frame from file header
let strips=header(1,6)
rem read total number of strips from header
let numframes=header(1,5)
rem calculate total number of frames = total strips/strips
rem per frame
let numframes=numframes/strips
```

---

```

rem read from header the type of data stored 0-float, 1-
rem long, 2-int
let datatype=header(1,3)
rem read from header whether file is scrambled (scram=0) or
rem unscrambled
let scram=header(1,7)
rem read in x-axis
let linecount=header(1,4)
    rem:: Read spectral direction from header.
let specdir = header( 1, 8 )
let errexit = 0
if strips < 1 then
    let errexit = 1
    beep
    print "Error: strips < 1",0,0
endif
if numframes <= 0 then
    let errexit = 1
    beep
    print "Error: Number of frames <= 0",0,0
endif
if errexit = 0 then
    rem check for a wavelength calibration file
    int wcfile
    let wcflag = getwcfilename(1, wcfile )
    let ytflag = ythead(1, timefactor, starttime)
    if wcflag+ytflag = 0 then
        rem CLEAR Wavelength Calibration
        let tmp = initwavcal
        let tmp = wavcaltype( 1, 1.0 )
        let tmp = makewavcal( 1 )
    endif
    print "                                ",0,0,0,14
    print "                                "
    print "                                ",95,40,0,14
rem set default color when in 256 mode
if maxcolors > 16 then
    let tmp = setcolor(dcolor)
endif
    rem Don't allow more than 9 strips to be replayed
    let totalwindows = 2
    if totalwindows > 9 then
        print "too many strips to replay in this program.",0,0
        let errorflag=1
    endif
    rem validate startframe
    if startframe > numframes then
        let currentframe = numframes
    else
        if startframe < 1 then
            let currentframe = 1
        else
            let currentframe = startframe

```

---

```

endif
endif
if errorflag = 0 then
  int EvenData
  int OddData
  let tmp = setarray( EvenData, datatype, strips,
                      linecount, 0, 0, 0 )
  let tmp = setarray( OddData, datatype, strips,
                      linecount, 0, 0, 0 )
  float SumOddData(strips, linecount)
  float SumEvenData(strips, linecount)
  let SumOddData = 0.0
  let SumEvenData = 0.0
  rem check if spectral direction is right to left
  if specdir = 1 then
    int rs
    let tmp = setarray(rs, datatype, strips,
                      linecount, 0, 0, 0)
  endif
  rem set the number of windows to the number of
  rem strips per window
  if iswindow(totalwindows) = 0 then
    let tmp = setscreen(1,totalwindows)
  endif
  for i=startwindow to totalwindows
    if getwindowsize(i) # linecount then
      while iscurve(i,1) = 1
        let tmp = delcurve(i,1)
      wend
      rem if windows size changes then we must start
      rem at curve 1
      rem if you want another result use recallm.rep
      let curvenumber = 1
      let tmp=windowsize(i,linecount)
    endif
  next i
  let tmp=setscreen(4,0)
  print "name = ",0,0,0,14
  print repname
  print "total frames = ",95,40,0,14
  print numframes
  print " strips = "
  print strips
  print " lines = "
  print linecount
  rem for 1 frame/1 strip and set to MANUAL MODE
  if numframes = 1 then
    Print " Number of frames=1"
  endif
  rem make sure frames is even
  let frames = (numframes/2) * 2
  for index = 1 to frames step 2
    let tmp=seekframe(1,index)

```

---

```

read 1, OddData
let tmp=seekframe(1,index+1)
read 1, EvenData
if scram = 0 then
    let OddData=unscramble(OddData)
    let EvenData=unscramble(EvenData)
endif
rem check if spectral direction is right to
rem left
if specdir = 1 then
    let tmp = reverse(OddData,rs)
    let OddData = rs
    let tmp = reverse(EvenData,rs)
    let EvenData = rs
endif
rem Sum up odds and Evens.
let SumOddData = SumOddData + OddData
let SumEvenData = SumEvenData + EvenData
print "frame = ",0,30,0,14
print index,0,40,0,15
next index
let w(1,1) = SumOddData
let w(2,1) = SumEvenData
write 2, SumOddData
print "                                ",95,40,0,14
write 3, SumEvenData
print "                                ",95,40,0,14
let tmp=transfer(1,2)
rem set x-axis size
let a=setheader(2, 0, linecount)
rem set accumulation to # stripes added to program
let a=setheader(2, 2, 1)
rem set data type to float (0)
let a=setheader(2, 3, 0)
rem set x-dimension
let a=setheader(2, 4, linecount)
rem set total number of stripes in file
let a=setheader(2, 5, 1)
rem set the number of stripes in the new frame
let a=setheader(2, 6, 1)
rem set the unscramble flag
let a=setheader(2, 7, 1)
rem set the reverse flag
let a=setheader(2, 8, 0)
endif rem: End of "if errorexit = 0 then"
ENDIF
close 1
close 2
rem restart macro if it was running
let tmp = restartmacro

```

---

**QUARTILES.PRO**

```

rem Quartiles.pro
rem Created: 08/11/93 by Doug Kreszowski
rem This program reads a file of frames, separates
rem and stores these frames into four different files
print "QUARTILES:DHK",0,0,0,15
let dcolor = 12
rem new c.g.r.
rem suspend macro if running
let tmp = suspendmacro
let tmp = setbasicrunflag(1)
float starttime
float timefactor
int errorflag
rem errorflag set to 1 if error occurs, otherwise 0
let errorflag = 0
let startframe = getpivar(49)
let startwindow = getpivar(50)
let repcont = getpivar(74)
rem:: start at first unused curve in window if flag is set
rem:: to do so
rem:: replay "1=2" with flag when available.
let curvenumber = 1
STRING infile, outfile1,outfile2,outfile3,outfile4
let infile = repname
let outfile1="
let outfile2="
let outfile3="
let outfile4="
inp infile,outfile1,outfile2,outfile3,outfile4
open infile for input as 1
open outfile1 for output as 2
open outfile2 for output as 3
open outfile3 for output as 4
open outfile4 for output as 5
long strips
long numframes
rem read strips per frame from file header
let strips=header(1,6)
rem read total number of strips from header
let numframes=header(1,5)
rem calculate total number of frames = total strips/strips
rem per frame
let numframes=numframes/strips
rem read from header the type of data stored 0-float, 1-
rem long, 2-int
let datatype=header(1,3)
rem read from header whether file is scrambled (scram=0) or
rem unscrambled
let scram=header(1,7)

```

---



```

rem read in x-axis
let linecount=header(1,4)
  rem:: Read spectral direction from header.
let specdir = header( 1, 8 )
let errorexit = 0
if strips <1 then
  let errorexit = 1
  beep
  print "Error: strips < 1",0,0
endif
if numframes <= 0 then
  let errorexit = 1
  beep
  print "Error: Number of frames <= 0",0,0
endif
if errorexit = 0 then
  rem check for a wavelength calibration file
  int wcfile
  let wcflag = getwcfilename(1, wcfile )
  let ytflag = ythead(1, timefactor, starttime)
  if wcflag+ytflag = 0 then
    rem CLEAR Wavelength Calibration
    let tmp = initwavcal
    let tmp = wavcaltype( 1, 1.0 )
    let tmp = makewavcal( 1 )
  endif
  print "                                ",0,0,0,14
  print "                                "
  print "                                ",95,40,0,14
rem set default color when in 256 mode
if maxcolors > 16 then
  let tmp = setcolor(dcolor)
endif
  rem Dont't allow more then 9 strips to be replayed
  let totalwindows = 4
  if totalwindows > 9 then
    print "too many strips to replay in program.",0,0
    let errorflag=1
  endif
  rem validate startframe
  if startframe > numframes then
    let currentframe = numframes
  else
    if startframe < 1 then
      let currentframe = 1
    else
      let currentframe = startframe
    endif
  endif
  if errorflag = 0 then
    int Firstdata
    int Seconddata
    int Thirddata

```

---

```

int FourthData
let tmp=
    setarray(Firstdata,datatype,strips,linecount,
              0, 0, 0)
let tmp=
    setarray(Seconddata,datatype,strips,linecount, 0,
              0, 0)
let tmp=
    setarray(Thirddata,datatype,strips,linecount, 0,
              0, 0 )
let tmp=
    setarray(Fourthdata,datatype,strips,linecount, 0,
              0, 0 )
float Sumfirstdata(strips, linecount)
float Sumseconddata(strips, linecount)
float Sumthirddata(strips, linecount)
float SumfourthData(strips, linecount)
let Sumfirstdata = 0.0
let Sumseconddata = 0.0
let SumThirddata = 0.0
let SumfourthData = 0.0
rem check if spectral direction is right to left
if specdir = 1 then
    int rs
    let tmp = setarray(rs, datatype, strips,
                        linecount, 0, 0, 0)
endif
rem set the number of windows to the number of
rem strips per win
if iswindow(totalwindows) = 0 then
    let tmp = setscreen(1,totalwindows)
endif
for i=startwindow to totalwindows
    if getwindowsize(i) # linecount then
        while iscurve(i,1) = 1
            let tmp = delcurve(i,1)
        wend
        rem if windows size changes then we must start
        rem at curve 1
        rem if you want another result use recallm.rep
        let curvenumber = 1
        let tmp=windowsize(i,linecount)
    endif
next i
let tmp=setscreen(4,0)
print "name = ",0,0,0,14
print rephrase
print "total frames = ",95,40,0,14
print numframes
print " strips = "
print strips
print " lines = "
print linecount

```

---

```

rem for 1 frame/1 strip and set to MANUAL MODE
if numframes = 1 then
Print " Number of frames=1"
endif
rem make sure frames is even
let frames = (numframes/4) * 4
for index = 1 to frames step 4
  let tmp=seekframe(1,index)
  read 1, Firstdata
  let tmp=seekframe(1,index+1)
  read 1, Seconddata
  let tmp=seekframe(1,index+2)
  read 1, Thirddata
  let tmp=seekframe(1,index+3)
  read 1, Fourthdata
  if scram = 0 then
    let Firstdata=unscramble(Firstdata)
    let Seconddata=unscramble(Seconddata)
    let Thirddata=unscramble(Thirddata)
    let Fourthdata=unscramble(Fourthdata)
  endif
  rem check if spectral direction is right to
  rem left
  if specdir = 1 then
    let tmp = reverse(Firstdata, rs)
    let Firstdata = rs
    let tmp = reverse(Seconddata,rs)
    let Seconddata = rs
    let tmp = reverse(Thirddata, rs)
    let Thirddata = rs
    let tmp = reverse(Fourthdata, rs)
    let Fourthdata = rs
  endif
  rem Sum up odds and Evens.
  let Sumfirstdata = Sumfirstdata + Firstdata
  let Sumseconddata = Sumseconddata + Seconddata
  let Sumthirddata = Sumthirddata + Thirddata
  let Sumfourthdata = Sumfourthdata + Fourthdata
  print "frame = ",0,30,0,14
  print index,0,40,0,15
next index
let w(1,1) = Sumfirstdata
let w(2,1) = Sumseconddata
let w(3,1) = Sumthirddata
let w(4,1) = Sumfourthdata
write 2, Sumfirstdata
print " ",95,40,0,14
write 3, Sumseconddata
print " ",95,40,0,14
write 4, Sumthirddata
print " ",95,40,0,14
write 5, Sumfourthdata
print " ",95,40,0,14

```

---

```

    let tmp=transfer(1,2)
    rem set x-axis size
    let a=setheader(2, 0, linecount)
    rem set accumulation to # stripes added to program
    let a=setheader(2, 2, 1)
    rem set data type to float (0)
    let a=setheader(2, 3, 0)
    rem set x-dimension
    let a=setheader(2, 4, linecount)
    rem set total number of stripes in file
    let a=setheader(2, 5, 1)
    rem set the number of stripes in the new frame
    let a=setheader(2, 6, 1)
    rem set the unscramble flag
    let a=setheader(2, 7, 1)
    rem set the reverse flag
    let a=setheader(2, 8, 0)
    endif rem: End of "if errexit = 0 then"
ENDIF
close 1
close 2
rem restart macro if it was running
let tmp = restartmacro

```

### **FRMEDIT.PRO**

```

REM FRMEDIT
rem Adaptation of REPLAY.PI modified by Doug Kreszowski
rem 08/11/93.
PRINT "FRAMEEDITOR:DHK/08/11/93",0,0,0,15
rem This program replays frames, displaying each stripe in
rem its own window. Thus it CAN NOT be used with frames
rem larger than 10 strips. It takes control of your keyboard
rem and redefines the following keys. This program then
rem selection of frames to save in a second output file.
rem PgDn - backup frames by 10.
rem PgUp - advance frames by 10.
rem HOME - Goto 1st frame.
rem END - Goto last frame.
rem UP ARROW - advance 1 frame.
rem DOWN ARROW - backup 1 frame.
rem ESC - leave program.
rem filename - name of file to read data from
rem startframe - frame to start at
rem S- command to save frame
rem set a default color if display is in 256 mode
let dcolor = 12
rem new c.g.r.

```

---

```

rem suspend macro if running
let tmp = suspendmacro
let tmp = setbasicrunflag(1)
float starttime
float timefactor
int errorflag
rem errorflag set to 1 if error occurs, otherwise 0
let errorflag = 0
let startframe = getpivar(49)
let startwindow = getpivar(50)
let repcont = getpivar(74)
  rem:: Start at first unused curve in window if flag is set
rem:: to do so
  rem:: replay "1 = 2" with flag when available
let curvenumber = 1
if 1 = 2 then
  let curvenumber = 1
  while iscurve( startwindow, curvenumber ) = 1
    let curvenumber = curvenumber + 1
  wend
endif
STRING infile,outfile
let infile=repname
let outfile="      "
inp infile,outfile
open infile for input as 1
open outfile for output as 2
rem open file as input assign filr to file handle number
long strips
long numframes
rem read strips per frame from file header
let strips=header(1,6)
rem read total number of strips from header
let numframes=header(1,5)
rem calculate total number of frames = total strips / strips
per frame
let numframes=numframes/strips
rem read from header the type of data stored 0-float, 1-
rem long, 2-int
let datatype = header(1,3)
rem read from header whether file is scrambled (scram=0) or
rem unscram
let scram=header(1,7)
rem read in x axis
let linecount = header(1,4)
  rem:: Read spectral direction from header
let specdir = header( 1, 8 )
let errorexit = 0
if strips <= 0 then
  let errorexit = 1
  beep
  print "Error: strips <= 0",0,0
endif

```

---

```

if numframes <= 0 then
    let errexit = 1
    beep
    print "Error: Number of frames <= 0",0,0
endif
rem:: Don't do anything else if we have a strips or
rem:: numframes error.
if errexit = 0 then
    int wcfile
    rem chk for a wavelength calibration file
    let wcflag = getwcfilename(1, wcfile )
    rem chk for a YT_FILE and set Wavelength Calibration
    let ytflag = ythead(1, timefactor, starttime)
    rem reset x-axis if no wavelength calibration or YT
    rem involved
    if wcflag+ytflag = 0 then
        rem CLEAR Wavelength Calibration
        let tmp = initwavcal
        let tmp = wavcaltype( 1, 1.0 )
        let tmp = makewavcal( 1 )
    endif
    print "                                ",0,0,0,14
    print "                                "
    print "                                ",95,40,0,14
    rem set default color when in 256 mode
    if maxcolors > 16 then
        let tmp = setcolor(dcolor)
    endif
    let totalwindows = strips + startwindow - 1
    rem Don't allow more than 10 strips to be replayed
    if totalwindows > 10 then
        print " too many strips to replay this program.",0,0
        let errorflag=1
    endif
    rem validate startframe
    if startframe > numframes then
        let currentframe = numframes
    else
        if startframe < 1 then
            let currentframe = 1
        else
            let currentframe = startframe
        endif
    endif
    if errorflag = 0 then
        int s
        let tmp = setarray( s, datatype, strips, linecount,
                                0, 0, 0 )
        rem check if spectral direction is right to left.
        if specdir = 1 then
            int rs
            let tmp = setarray(rs, datatype, strips,
                                linecount, 0, 0, 0)

```

```

endif
rem set the number of windows to the number of
rem strips per window.
if iswindow(totalwindows) = 0 then
    let tmp = setscreen(1,totalwindows)
endif
for i=startwindow to totalwindows
    if getwindowsize(i) # linecount then
        while iscurve(i,1) = 1
            let tmp = delcurve(i,1)
        wend
        rem if window size changes then we must start at
        rem curve 1.
        rem if you want another result use recallm.rep
        let curvenumber = 1
        let tmp=windowsize(i,linecount)
    endif
next i
let tmp=setscreen(4,0)
print "name = ",0,0,0,14
print repname
print "total frames = ",95,40,0,14
print numframes
print "  strips = "
print strips
print "  lines = "
print linecount
rem initialize some variables for later use
let lastkey=0
let done = 0
let inkey = 77
let actionflag = 1
rem for 1 frame/1 strip and set to MANUAL MODE
if numframes = 1 then
    if strips = 1 then
        let repcont = 0
    endif
endif
getkbd
while done = 0
    if repcont = 1 then
        rem look for ALT-M manual mode
        if inkey = 12800 then
            let repcont = 0
            rem: currentframe was incremented
            rem: before checking for ALT-M so
            rem: decrement it before going into
            rem: manual mode.
            if currentframe = 1 then
                let currentframe = numframes
            else
                let currentframe = currentframe - 1
            endif
        endif
    endif

```

---

```

else
    rem continous replay is picked
    rem read in frame
    let tmp=seekframe(1,currentframe)
    read 1, s
    if scram = 0 then
        let s=unscramble(s)
    endif
    rem check if spectral direction is right
    rem to left.
    if specdir = 1 then
        let tmp = reverse(s,rs)
        let s = rs
    endif
    rem chk if YT file and update
    rem calibration.
    if ytflag # 0 then
        if currentframe = 1 then
            let tmp = ythead(1,timefactor,
                               starttime)
        else
            let tmp =ytaddoffset(timefactor)
        endif
    endif
    rem set each window to a stripe in frame
    for j=1 to strips
        let w(startwindow + j - 1,
              curvenumber) = s(j)
    next j
    print "frame = ",0,30,0,14
    print currentframe,0,40,0,15
    print " "
    if currentframe < numframes then
        let currentframe = currentframe + 1
    else
        let currentframe = 1
    endif
    rem chk for only 1 frame and set to
    rem manual.
    if numframes = 1 then
        let repcont = 0
    endif
endif
else
    rem manual replay picked
    if inkey > 0 then
        rem look for ALT-A auto mode
        if inkey = 7680 then
            let repcont = 1
        endif
        Rem look for S key
        If inkey = 8051 Then
            let tmp=seekframe(1,currentframe)

```

---



```

        let tmp=writeframe(2,s)
    endif
    REM check for DOWN ARROW
    IF inkey = 20480 THEN
        LET currentframe = currentframe-1
        IF currentframe < 1 THEN
            let currentframe = numframes
        ENDIF
        LET actionflag = 1
    ENDIF
    rem look for END
    if inkey = 20224 then
        let currentframe = numframes
        let actionflag = 1
    endif
    rem look for HOME
    if inkey = 18176 then
        let currentframe = 1
        let actionflag = 1
    endif
    rem look for PgDn
    if inkey = 20736 then
        let currentframe = currentframe - 10
        if currentframe < 1 then
            let currentframe = numframes
        endif
        let actionflag = 1
    endif
    rem look for PgUp
    if inkey = 18688 then
        let currentframe = currentframe + 10
        if currentframe > numframes then
            let currentframe = 1
        endif
        let actionflag = 1
    endif
    rem check for UP ARROW
    if inkey = 18432 then
        let currentframe=currentframe+1
        if currentframe > numframes then
            let currentframe = 1
        endif
        let actionflag = 1
    endif
    rem if a function was requested
    if actionflag # 0 then
        rem read in frame
        let tmp=seekframe(1,currentframe)
        read 1, s
        if scram = 0 then
            let s=unscramble(s)
        endif
    
```

---

```

rem check if spectral direction is
rem right to left.
if specdir = 1 then
    let tmp = reverse(s,rs)
    let s = rs
endif
rem chk if YT file and update
rem calibration.
if ytflag # 0 then
    let tmp = ythead(1,timefactor,
                    starttime)
    if currentframe # 1 then
        let tmp = ytaddoffset
                    (timefactor*
                    (currentframe-1))
    endif
endif
rem set each window to a stripe in
rem frame.
for j=1 to strips
    let w(startwindow + j - 1,
        curvenumber ) = s(j)
next j
print "frame = ",0,30,0,14
print currentframe,0,40,0,15
print " "
print "name = ",0,0,0,14
print repname
print "total frames = ",95,40,0,14
print numframes
print " strips = "
print strips
print " lines = "
print linecount
let actionflag = 0
endif
endif
endif
rem get key from keyboard
let inkey=getkey
rem check for ESCAPE
if inkey = 283 then
    let done = 1
endif
rem look for ?, Q or q - and display"replay.hlp"
if (inkey=13631)or(inkey=4177)or(inkey=4209)then
    let tmp=helpdisplay(1)
endif
wend
if getpivar( 23 ) = 1 then
    let tmp = cpyimageptr( 4, s, getcurrentimage )
endif
endif
endif

```

---

```
    rem:: End of "if errexit = 0 then"
endif
    rem:: File was opened before errexit check, so must be
    rem:: closed here.
close 1
    rem:: If we're NOT error exiting, we've locked the
    keyboard, so release it
if errexit = 0 then
    rem:: check if spectral direction is right to left.
    if specdir = 1 then
        erase rs
    endif
    releasekbd
endif
print "                                ",95,40,0,14
rem new c.g.r.
rem restart macro if it was running
let tmp = restartmacro
close 2
```

---

MICHIGAN STATE UNIV. LIBRARIES



31293014203180